IntechOpen

Superconductors
New Developments

Edited by Alexander Gabovich

SUPERCONDUCTORS – NEW DEVELOPMENTS

Edited by **Alexander Gabovich**

Superconductors - New Developments
http://dx.doi.org/10.5772/58655
Edited by Alexander Gabovich

Contributors

Luis De Los Santos Valladares, Shi-Xue Dou, Wenxian Li, Peter Brusov, Akira Sugimoto, Alexander Gabovich, Yuta Sakai, Jun Akimitsu, Toshikazu Ekino, Omar Augusto Hernández-Flores, Carolina Romero-Salazar, Vadim Loktev, Mario Santos, Yuriy Pogorelov, Dario Daghero, Mauro Tortello, Chung-Li Dong, Chi-Liang Chen, Michael I. Faley, Leandro Alves, Guoxing Miao

© The Editor(s) and the Author(s) 2015
The moral rights of the and the author(s) have been asserted.
All rights to the book as a whole are reserved by INTECH. The book as a whole (compilation) cannot be reproduced, distributed or used for commercial or non-commercial purposes without INTECH's written permission.
Enquiries concerning the use of the book should be directed to INTECH rights and permissions department (permissions@intechopen.com).
Violations are liable to prosecution under the governing Copyright Law.

Individual chapters of this publication are distributed under the terms of the Creative Commons Attribution 3.0 Unported License which permits commercial use, distribution and reproduction of the individual chapters, provided the original author(s) and source publication are appropriately acknowledged. If so indicated, certain images may not be included under the Creative Commons license. In such cases users will need to obtain permission from the license holder to reproduce the material. More details and guidelines concerning content reuse and adaptation can be foundat http://www.intechopen.com/copyright-policy.html.

Notice

Statements and opinions expressed in the chapters are these of the individual contributors and not necessarily those of the editors or publisher. No responsibility is accepted for the accuracy of information contained in the published chapters. The publisher assumes no responsibility for any damage or injury to persons or property arising out of the use of any materials, instructions, methods or ideas contained in the book.

First published in Croatia, 2015 by INTECH d.o.o.
eBook (PDF) Published by IN TECH d.o.o.
Place and year of publication of eBook (PDF): Rijeka, 2019.
IntechOpen is the global imprint of IN TECH d.o.o.
Printed in Croatia

Legal deposit, Croatia: National and University Library in Zagreb

Additional hard and PDF copies can be obtained from orders@intechopen.com

Superconductors - New Developments
Edited by Alexander Gabovich

p. cm.

ISBN 978-953-51-2133-6

eBook (PDF) ISBN 978-953-51-6382-4

We are IntechOpen, the world's leading publisher of Open Access books

Built by scientists, for scientists

3,800+
Open access books available

116,000+
International authors and editors

120M+
Downloads

Our authors are among the

151
Countries delivered to

Top 1%
most cited scientists

12.2%
Contributors from top 500 universities

WEB OF SCIENCE™

Selection of our books indexed in the Book Citation Index in Web of Science™ Core Collection (BKCI)

Interested in publishing with us?
Contact book.department@intechopen.com

Numbers displayed above are based on latest data collected.
For more information visit www.intechopen.com

Meet the editor

Alexander M. Gabovich graduated cum laude from the Physical Department of Kiev State University in 1969. He majored theoretical physics, with emphasis on the nuclear physics. Dr. Gabovich obtained his PhD in Physics and Mathematics from the Institute of Physics of the Ukrainian National Academy of Sciences (Kiev) in 1976, and Doctor's degree in Physics and Mathematics from the Institute of Low Temperature Physics and Engineering of the Ukrainian National Academy of Sciences in 1990 (Kharkov). Dr. Gabovich is leading Research Associate of Crystal Physics Department, Institute of Physics of the Ukrainian National Academy of Sciences (Kiev). His research interests are: superconductivity, phase transitions, electronic properties of surfaces, biophysics. Dr. Gabovich authored and co-authored more than 300 scientific and tutorial publications.

Contents

Preface

Superconductivity is developing steadily and new perspective materials appear each year. Electrodynamics of superconductors is also a vigorously evolving field of science. A lot of books on superconductivity can be found in libraries and on Internet.

This book is a collection of chapters dealing with various old and new problems of the superconducting state. It includes 8 experimental and 4 theoretical chapters written by well-known specialists and young researchers. Oxides, pnictides, chalcogenides and intermetallic compounds are described here. The superconducting order parameter symmetry is discussed and consequences of the actual non-trivial symmetry are studied. Impurity and tunneling effects are among topics covered by the chapters.

I hope the book will be useful for undergraduates, postgraduates and professionals.

Dr. Alex Gabovich
Institute of Physics
Kiev, Ukraine

Experiment

Chapter 1

Superconductivity and Physical Properties in the $K_xMoO_{2-\delta}$

L. M. S. Alves, B. S. de Lima, M. S. da Luz and
C. A. M. dos Santos

Additional information is available at the end of the chapter

http://dx.doi.org/10.5772/59672

1. Introduction

In a normal metallic conductor the electrical resistivity decreases until it reaches a lower limit (≈0) when heat energy is removed from the system. In these materials electrons are scattered by the lattice and obey Fermi-Dirac statistics [1]. The behaviour of a gas of identical particles at low temperature depends on the spin of the particle. Fermions are formed by half-integral spin, and obey Pauli's exclusion principle, wherein two of them cannot have the same quantum numbers [1]. However many metals, alloys and compounds exhibit the electrical resistivity dropping suddenly to zero and exclude magnetic flux completely when cooled down to a sufficiently low temperature [1]. This phenomenon is known as superconductivity. It was observed first by Kamerlingh Onnes in 1911, a couple of years after the first liquefied helium [2]. At a critical temperature T_C, the material undergoes a phase transition from a normal state to a superconducting state. At that point an electron-electron attraction arises mediated by phonons and the pairs formation of electron is favourable. Electron pairs are named Cooper pairs [3,4]. Cooper pairs are a weakly bound pair of electrons, each having equal but opposite spin and angular momentum.

It is interesting to note that when a superconductor is cooled below its critical temperature its electronic properties change appreciably, but its crystalline structure remains the same, as revealed by X-ray or neutron diffraction studies. Furthermore, the formation mechanism of photons that depends on the thermal vibrations of the atoms remains the same in the superconducting phase as in the normal state. This means that superconductivity is not associated with any remarkable change in the crystalline structure of the specimens. However, although superconductivity is not a property of particular atoms, it does depend strongly on their arrangement. The conduction electrons themselves must be responsible for the superconduct-

INTECH
open science | open minds

© 2015 The Author(s). Licensee InTech. This chapter is distributed under the terms of the Creative Commons Attribution License (http://creativecommons.org/licenses/by/3.0), which permits unrestricted use, distribution, and reproduction in any medium, provided the original work is properly cited.

ing behaviour. A feature that illustrates an important characteristic of these superconducting electrons is that the transition from the normal to the superconducting state is very sharp [3,4]. This could only happen if the electrons in a superconductor become condensed into a coherent, ordered state, which extends over long distances compared to the distances between the atoms. A superconducting state is more ordered than the normal state in a metal. This means that it has a lower entropy, the parameter that measures the amount of disorder in a system. In an analogous way, the entropy of a solid is lower than that of a liquid at the same temperature; solids are more ordered than liquids. So, when a material turns to a superconducting state, the superconducting electrons must be condensed into an ordered state compared to normal electrons.

But what happens if, in a material, the electronic interaction leads to the formation of Cooper pairs but in a disordered state? If this were so then any local variations from collective action between the electrons would broaden the transition over a much wider temperature range or transition could not be noticed. Thus, despite the existence of the Cooper pairs, the state formed would be unconventional metallic but not superconductor. Due to the existence of bosonic particles in the crossover from weak coupling Bardeen-Cooper-Schrieffer (BCS) pairing to a Bose-Einstein condensate (BEC) of tightly bound pairs, this unconventional metallic phase is conveniently called Bose metal [5,6]. The Bose metal has been characterized as a system without long-range order. This new state of the matter has attracted a lot of attention over the past decades due to occurrence of a metal-insulator transition in low dimensional systems [5,6]. Experiments have shown that this transition can be induced by disorder or by applying external magnetic field. When a sufficiently high magnetic field is applied in the material the Cooper pairs are completely localized turning its electrical conductivity to zero and leading to an insulating state. Within this framework a scale law was proposed to identify a Bose metal-insulator transition (BMIT). So, this transition can be analysed in terms of two-parameter scaling, as follows:

$$RT^{1+2/z} / \delta^{2\beta} = f\left(\delta T^{\frac{1}{zV}} \right), \tag{1}$$

where R is the electrical resistance and T is the temperature. $\beta = V(z+2)/2$, z and V are critical exponents, and $\delta = H - H_c$ the deviation of the variable parameter (magnetic field) from the critical values [5]. H_c is the critical magnetic field where the BMIT occurs. Such a transition has been recently observed in semimetals as graphite and bismuth [7], and also in the quasi one-dimensional $Li_{0.9}Mo_6O_{17}$ [8]. Theoretical analysis has suggested that the BMIT in graphite is associated with the transition between Bose metal and excitonic insulator state, whereas in $Li_{0.9}Mo_6O_{17}$ this transition is discussed in terms of localized bosons in a low dimensional system, which could be related to the Luttinger liquid (LL) state.

Another interesting subject to consider is that superconductivity and magnetism are two different ordered states into which substances can condense at low temperatures, and in general these states are opposite to each other [1]. It has generally been believed that the

conduction of electrons in a metal cannot be both ferromagnetically ordered and superconducting. In conventional superconductors, local magnetic moments break up the spin singlet Cooper pairs, and hence strongly suppress superconductivity, an effect known as pair-breaking [3,4]. However, since the 1970s several studies on the interplay between superconductivity and magnetism have arisen in the scientific community. Namely, a coexistence between ferromagnetism and Bose metal state has been demonstrated for both highly oriented pyrolitic graphite and graphite sulphur composites [9]. Actually, the authors' assumed the observation of metal-insulator crossover in both cases might be related to a Bose metal-insulator transition [9].

This chapter will report results about recent studies on the $K_xMoO_{2-\delta}$ system, which has suggested that K doping in the MoO_2 matrix causes defects leading to a magnetic ordering temperature and superconducting critical temperature (T_C) ratio ranging from 7 to 18 in this compound [10]. These are the highest ratios reported so far for a magnetic superconductor. Furthermore, anomalous metallic behaviour has been reported in this compound [11]. The study of the anomalies provides important conclusions, such as the temperature dependence of the electrical resistance is described by a power law of the type $R(T) = R_0 + CT^{\alpha}$, where α is found to be near 0.5. This value of α can be interpreted according to the theory of LL. Anderson and Ogata [12] proposed a theoretical description based on the model of the Luttinger liquid (LL) in which the electrical resistivity of a one-dimensional conductor must be described by a power law of the type $\varrho(T) = \varrho_0 + CT^{\alpha}$ where the residual resistivity is ϱ_0, C is a constant and not universal α is provided in the anomalous exponent model [12,13]. This result suggests a mechanism for one-dimensional metallic conduction in the $K_xMoO_{2-\delta}$ system. Furthermore, the LL theory suggests that the interaction between the conduction electrons is attractive to positive α and smaller than one. Measurements of several samples with different amounts of potassium confirm the value of α near 0.5 for all of them. With the goal of increasing the understanding of the physical properties of $K_xMoO_{2-\delta}$ at low temperatures, especially the anomaly shown in the electrical resistivity curves below ~70K, magnetoresistance measurements as a function of temperature were performed. Under applied magnetic field the electrical resistance changes to larger values, indicating a positive magnetoresistance. This behaviour is very similar to a Bose metal-insulator transition observed in semi-metals such as graphite-bismuth [7], thin films of MoGe [5] and to compounds with quasi-low-dimensional behaviour such as $Li_{0.9}Mo_6O_{17}$ [8]. This behaviour was interpreted according to the scaling theory. This theory implies the existence of Cooper pairs without long-range order, thus featuring a metallic state at absolute zero (Bose metal). This seems to agree with that observed by the LL theory and with the existence of superconductivity in the $K_xMoO_{2-\delta}$ system.

1.1. $K_xMoO_{2-\delta}$ crystalline structure

Polycrystalline samples of $K_xMoO_{2-\delta}$ with $0 \leq x \leq 0.30$ were prepared in pellet forms using appropriate amounts of Mo, MoO_3, and K_2MoO_4. The precursor K_2MoO_4 was obtained after heat treating K_2CO_3 and MoO_3 in air at 400°C for 24h followed by a treatment at 700°C for 24h. The pellets of $K_xMoO_{2-\delta}$ were sintered at 400°C for 1 day followed by 700°C for 3 days in a quartz tube under vacuum. Different heat treatments resulted in different potassium (x) and

oxygen contents due to the volatilization of atoms inside quartz tubes. X-ray diffractometry (XRD) analysis of the samples was performed using a Shimazu diffractometer (XRD 6000) with CuK ϱ radiation and Ni filter. The 2 data were collected from 10° to 90° using step of 0.058 and counting time of 1 s.

Figure 1 shows the x-ray diffraction patterns of $K_xMoO_{2-\delta}$ (x = 0.05, 0.10, 0.20, and 0.30), the final Rietveld refinement, and the difference between both.

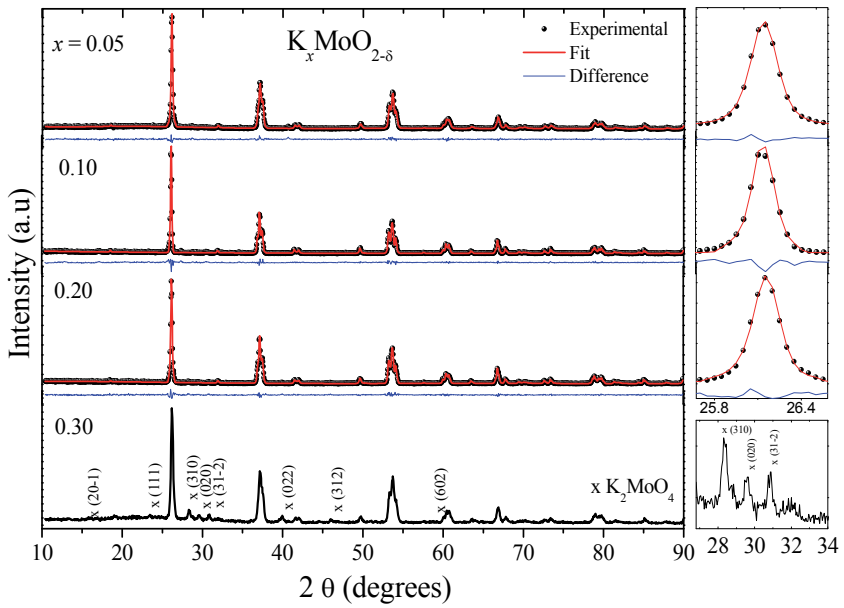

Figure 1. X-ray diffraction patterns for the samples of $K_xMoO_{2-\delta}$ with $x \leq 0.30$, Rietveld refinement and the difference between both. To right magnifications show the high quality of fit as well as the peaks belonging to impurities for the $K_{0.30}MoO_{2-\delta}$ sample.

Diffractograms of all samples with $x \leq 0.20$ reported in this work show only peaks of the MoO_2 phase related to the monoclinic structure ($P2_1/c$). The parameters, which represent the quality of the Rietveld refinement and summarizes the crystalline data description resulting from the final Rietveld refinement, are listed in the Table 1.

x	a (Å)	b (Å)	c (Å)	β (°)	χ^2	R_{wp}
0.05	5.600(8)	4.850(7)	5.619(6)	120.906(4)	1.419	0.1238
0.10	5.602(2)	4.854(3)	5.621(6)	120.926(3)	2.213	0.1570
0.20	5.604(3)	4.856(3)	5.623(8)	120.934(3)	1.526	0.1482

Table 1. Rietveld quality parameters refinement and crystal parameters to $K_xMoO_{2-\delta}$ samples with x between 0.05 and 0.20.

For $x \geq 0.3$ a second phase appears related to the precursor K_2MoO_4. Its x-ray diffractogram is shown in figure 1. The existence of impurity in this specimen means that the solubility limit was reached.

In figure 2 is shown the variation of lattice parameters as a function of the K contents (x) in the specimens.

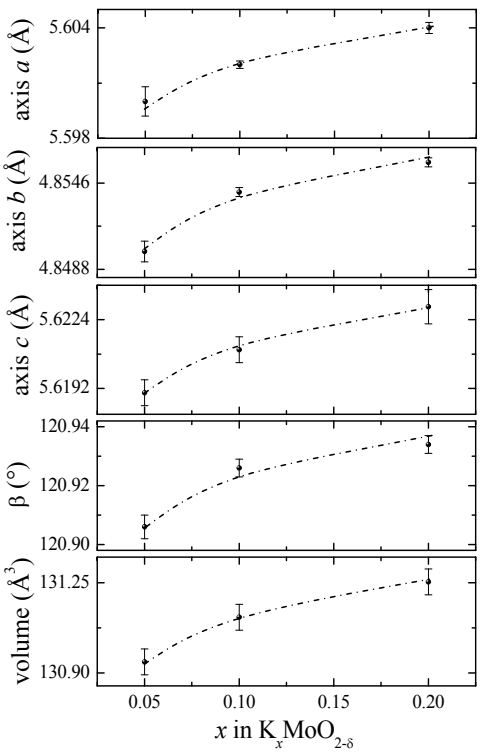

Figure 2. Lattice variation as a function of x in $K_xMoO_{2-\delta}$.

With increasing the amount of K one can observe a slight increase in unit cell volume, which is caused by the insertion of K in the crystalline lattice of MoO_2. For $x = 0.05$ the unit cell volume is 131.11 (5) A^3 and for $x = 0.20$ is 131.25 (5) A^3, which represent an increase of approximately 1% in the volume of the unit cell.

To expand the knowledge about the physical properties of the $K_xMoO_{2-\delta}$ compound was chosen for more detailed study the $K_{0.05}MoO_{2-\delta}$. So, in this part we will focus on the results for $x = 0.05$.

1.2. Interplay between superconductivity and ferromagnetism in $K_{0.05}MoO_2$

Magnetization curves as a function of the temperature measured in $K_{0.05}MoO_{2-\delta}$ sample with H = 10 and 200 Oe are shown in figure 3 performed under zero field cooled (ZFC) and field cooled (FC) regimes.

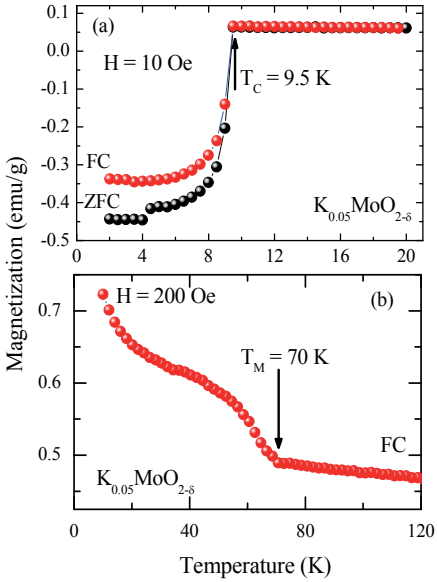

Figure 3. (a) ZFC and FC magnetization curves as a function of temperature for the $K_{0.05}MoO_{2-\delta}$ sample under applied magnetic fields H = 10 Oe. (b) FC magnetization curves as a function of temperature under H = 200 Oe showing the magnetic ordering near 70K [from reference 10].

Below T_C ~ 9.5 K the specimen undergoes a superconducting transition exhibiting a diamagnetic ordering. An estimation of the superconducting fraction through measurements with applied magnetic field of 10 Oe was calculated as ~ 0.4%. The low superconducting volume fraction is probably due to the appearance of the ferromagnetic ordering at higher temperatures (T_M = 70 K), which can be seen in the Figure 3 (b). The superconducting state appears below the ferromagnetic transition and the ratio between critical temperature is T_M / T_C ~7 [10].

To study in greater detail the relationship between the ferromagnetism and superconductivity several loops of magnetization as a function of applied magnetic field was obtained above and below T_C. The results are shown in Figure 4.

Hysteresis curves were obtained with applied magnetic field ranging from 0 to 10 kOe at a temperature of 2 K, as shown in Figure 4 (a). It was observed that for values of applied magnetic field up to 1 kOe, the magnetization curve is almost linear as a function of applied magnetic field and is reversible (blue curve) due to the Meissner effect. This result allows one to estimate the lower critical field (H_{C1}) as approximately 1.17 kOe [10]. It is quite difficult to estimate the value of the upper critical field (H_{C2}) due to the interplay between weak ferromagnetism and superconductivity. A rough estimation, considering the measurements at 2 K, allows us to assume a value of H_{C2} ~ 10 kOe, since the magnetic moment reaches saturation near to this field. With these values, it was found $\kappa = 4.1$ to 2 K in the sample with x = 0.05, indicating that the material is a type II superconductor [10]

In the inset of the figure 4 (a) is shown the M(H) at 20 K. We can observe clearly a ferromagnetic ordering very similar to that observed in magnetic superconductors such as

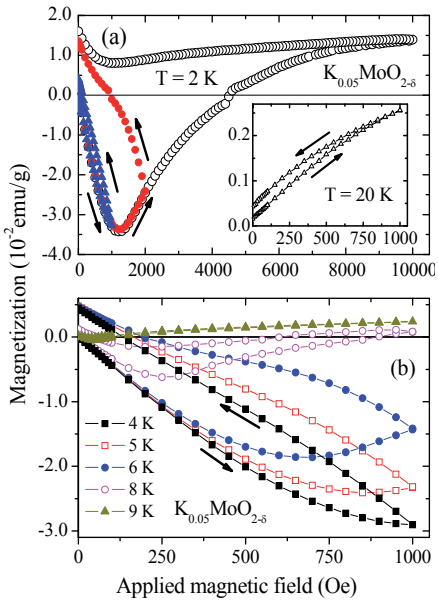

Figure 4. Magnetization curves as a function of magnetic field for $K_{0.05}MoO_{2-\delta}$ measured at (a) 2K using a maximum applied magnetic field of 1kOe (triangle), 2kOe (full circle), and 10kOe (open circle). (b) M versus H curves are shown at 4, 5, 6, 8, and 9K. Inset displays the M(H) curve at 20K [from reference 10].

$RuSr_2GdCu_2O_8$ [14]. In the figure 4 (b) is displayed the continuous disappearance of superconductivity when the temperature is increasing. At 9 K the superconductivity almost disappears, leaving only a weak positive magnetic component.

Figure 5 shows magnetization curves as a function of temperature for several samples with different starting compositions. The superconducting critical temperature of each sample is indicated by arrows on the figure.

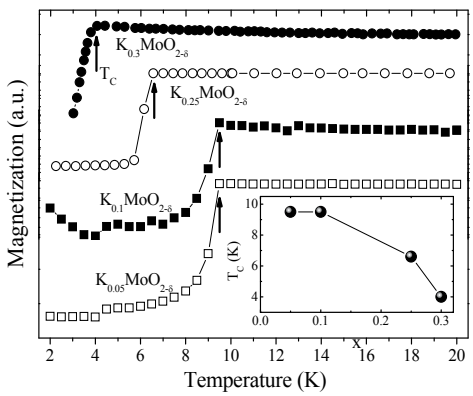

Figure 5. Diamagnetic transition for four samples with different starting compositions (*x*). Arrows indicate the superconducting T_C for each potassium composition. Magnetization curves are shifted and shown in arbitrary units for clarity. The inset shows the superconducting T_C as a function of the starting composition for the $K_xMoO_{2-\delta}$ compound [10].

The inset shows the variation in superconducting critical temperature (T_C) as a function of initial amount of potassium in the $K_xMoO_{2-\delta}$. The result shows also a systematic decrease of the T_C with the increasing of the amount of K. However, the lower limit of doping with K that exhibits superconductivity is still to be determined. Recently, Parker *et al.* have reported superconductivity near 12 K for non-doped $MoO_{2-\delta}$ [15].

1.3. Unconventional metallic behaviour

Figure 6 shows the electrical resistance as a function of temperature below 80 K for $K_{0.05}MoO_{2-\delta}$.

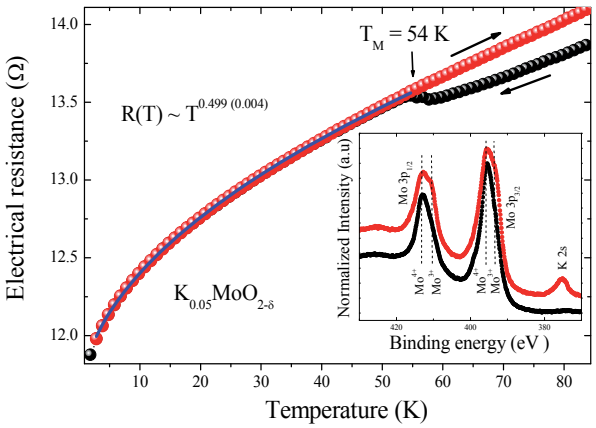

Figure 6. Electrical resistance as a function of temperature below ~ 80 K for $K_{0.05}MoO_{2-\delta}$. The blue line is a representation of the fit by power law with anomalous exponent α. The inset shows the core level photoemission spectra for the MoO_2 and $K_{0.05}MoO_{2-\delta}$ near the Mo $3p_{1/2}$, Mo 3 $p_{3/2}$, and K 2s peaks [from reference 10].

The electrical resistance temperature dependence for $K_{0.05}MoO_2$ sample shown in figure 6 exhibits a anomalous metallic behaviour. The blue line is the best fit using the power law such as $R(T) = R_0 + CT^{\alpha}$. The anomalous exponent (α) indicated for the electrical resistance as a function of temperature is the best value found by the fit obtained by the method of least squares. This value of α suggests that the one-dimensional conduction mechanism is described by Luttinger liquid theory, with attractive interaction between electrons [8,12-13]. Furthermore, this result confirms the $\alpha \sim 0.5$ that has also been observed for several another samples of this system [16], showing that the anomalous metallic behaviour is characteristic of this material.

The inset of figure 6 shows the core level photoemission spectroscopy for MoO_2 and $K_{0.05}MoO_{2-\delta}$. The Mo 3p spectrum of the undoped sample shows two main structures associated with the Mo $3p^{1/2}$ and Mo $3p^{3/2}$ core levels, which are split due to spin-orbit effects. In the $3p_{3/2}$ region, the peak around 395.5 eV is assigned to Mo^{4+} ($4d^2$) states, but there is also a very small Mo^{3+} ($4d^3$) contribution at about 393.4 eV. The later can be associated with the covalent Mo-O bond character, which is also supported by the relatively small charge transfer satellite, at around 425 eV. Nevertheless, a small oxygen deficiency in MoO_2 cannot be ruled out, as well. In the $3p^{1/2}$ region, the corresponding binding energies of the Mo^{4+} and Mo^{3+} states are

413.0 and 410.9 eV, respectively. The spectrum of the potassium-doped sample shows a new structure at 376 eV, assigned to the K 2s core level. More importantly, the peaks due to the Mo^{3+} states in the Mo 3p core level increase and become more prominent. This relative increase indicates that the potassium ions, when incorporated into the MoO_2 structure, are effectively doping the Mo 4d band with electrons, from a nominal $4d^2$ to $4d^3$. The extra charge introduced in the Mo 4d band by the potassium ions would lead to an effective magnetic moment and might be the origin of magnetism in this material. A similar effect, namely, extra charge induced by the presence of ligand vacancies, was reported as the origin of ferromagnetism in other oxides with nonmagnetic ions. Similarly the electrical behaviour of the $K_xMoO_{2-\delta}$ can be also influenced by this mechanism, causing the appearance of anomalous resistive electrical behaviour [10,11].

1.4. Bose-metal insulator transition

With the goal of increasing the understanding of the physical properties of $K_xMoO_{2-\delta}$ at low temperatures, especially the anomaly observed in the curves of electrical resistivity below ~ 70K and its relation to the existence of superconductivity, we report in this section magneto-resistance versus temperature for a sample of composition $K_{0.05}MoO_{2-\delta}$.

Figure 7 shows the electrical resistance as a function of temperature in a zero magnetic applied field as well as in 7 T. The results show an anomalous metallic behaviour at zero applied field. Under the applied magnetic field the electrical resistance changes to higher values indicating a positive magnetoresistance. At zero magnetic field one can observe an anomalous behaviour, in which the electrical resistance decreases as the temperature decreases. As already discussed, this behaviour differs from conventional metal-like behaviour in which the electrical resistance should reach a saturation state at low temperatures.

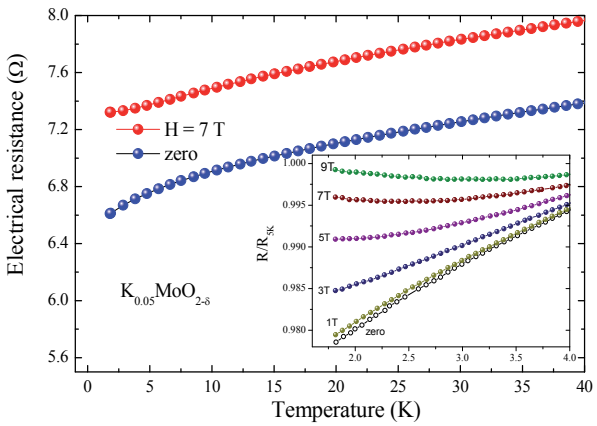

Figure 7. Electrical resistance as a function of temperature for $K_{0.05}MoO_{2-\delta}$ sample under H = 0 and 7 T. The inset shows the suppression of electrical anomalous behaviour below 70K. Furthermore, it displays a reduced electrical resistance *R(T)/R(5K)* as a function of temperature for $K_{0.05}MoO_{2-\delta}$ sample under several values of applied magnetic field [from reference 17].

It is important to note in figure 7 that the anomalous metallic behaviour disappears at very low temperatures ($T < 5$ K) when magnetic field is increased. This result has attracted attention, and to obtain further information about the influence of the magnetic field on the electrical resistance behaviour at low temperatures the magnetic field dependence of the electrical resistance in the temperature range of 1.8 K to 5 K was measured. The results are shown in the inset of figure 7, which are plotted in terms of reduced temperature $R(T)/R(5K)$ for a better comparison. At a lower applied magnetic field ($H \leq 5T$), electrical resistance as a function of temperature shows a metallic behaviour. At a higher applied magnetic field the electrical resistance first decreases to a minimal value, and below this temperature the electrical resistance starts to increase, leading to an insulating electrical behaviour. This behaviour is reminiscent of the transition from Bose metal to insulator (BMIT) reported for semi-metals such as graphite-bismuth [7], thin films of MoGe [5] and for compounds with quasi-one-dimensional characteristics, such as $Li_{0.9}Mo_6O_{17}$ for example [8].

The critical magnetic field where the Bose metal-insulator transition occurs is better observed by the crossover in the isotherms shown in the Figure 8.

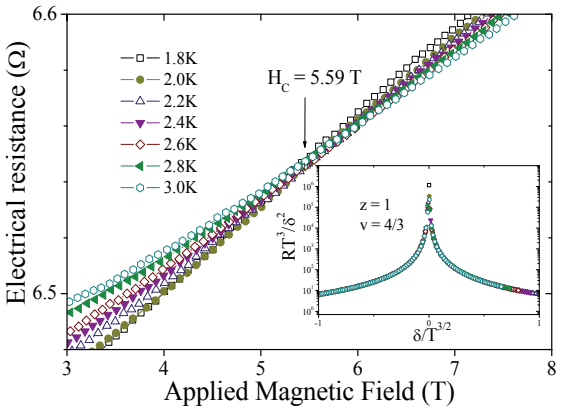

Figure 8. Isotherms showing H_C = 5,59 T. In the inset we can see the Bose metal-insulator transition scaling showing the collapse near HC = 5.59 T [from reference 17].

For applied magnetic field lower than the critical value (H_C = 5.59 T), the system behaves in the classical model of magnetoresistance as in metallic systems, expressed by $\Delta R(B)/R \sim H^n$ with n = 2 (typical exponent for metals) [1] for all ranges of temperature. For applied magnetic fields higher than the critical value the system deviates from this classical model with values between $1 < n < 2$, which features an insulating state (for detail see reference 17). The exponents obtained (n = 1 and n = 2) are similar to the values reported for graphite and bismuth (n = 1.25 to 1.30) [7], and for the organic conductor $(TMTSF)_2PF_6$ (n = 1.25 to 1.50) [18].

To better characterize the transition from a metal to an insulating state induced by a applied magnetic field, the scaling theory proposed by Das and Doniach [5] was used. This theory implies the existence of Cooper pairs tightly bound and without long-range order, thus featuring a metallic state at absolute zero (Bose metal). Within this context, these authors proposed a scaling law used to characterize the transition from Bose metal to insulator based on two scaling parameters *Vez*. In the inset the result of this scaling to a critical field H_C = 5.59 T and critical exponent $V = \frac{4}{3}ez = 1$ are shown.

The deviation of the Fermi liquid behaviour and a perfect correlation between the magnetoresistance data with the model proposed by Das and Doniach [5] suggests that, at low temperatures and zero applied magnetic field, the $K_{0.05}MoO_{2-\delta}$ compound shows the expected for a Bose metal. In this context one may suggest a possible correlation between the unconventional metallic behaviour observed in the curves R(T) below ~70 K with the existence of Cooper pairs tightly bounded without long-range order. This seems to corroborate with the observation of superconductivity in the $K_xMoO_{2-\delta}$ system [10-11,15].

2. Conclusions

This chapter reported the influence of defects in the crystalline structure on the properties of K-doped MoO_2. Potassium doping leads to superconductivity with critical temperatures up to 10 K and electrical resistance measurements displayed an anomalous behaviour below the temperature showing the manifestation of magnetism (T < 70 K). The study of the anomalies in the electrical behaviour provided important conclusions, such as the temperature dependence of the electrical resistance as described by a power law of the type $R(T) = R_0 + CT^{\alpha}$, where anomalous exponent (α) is found to be near 0.5. This value of α described by the theory of Luttinger liquid (LL) suggests a mechanism for one-dimensional metallic conduction. Furthermore, the LL theory suggests that the interaction between the conduction electrons is attractive to positive α and smaller than one. Under an applied magnetic field the electrical resistance changes to higher values indicating positive magnetoresistance. This behaviour is very similar to a Bose metal-insulator transition. This behaviour was interpreted according to the scaling theory proposed by Das and Doniach. This theory implies the existence of Cooper pairs tightly bound without long-range order, thus featuring a metallic state at absolute zero (Bose metal). This seems to agree with that observed by the LL theory and with the existence of superconductivity in the $K_xMoO_{2-\delta}$ system.

Acknowledgements

This material was based upon work supported by the FAPESP (2010/06637-2 and 2009/54001-2) and CNPq (08162/2013-7). J. J. Neumeier, J. B. Leão, R. J. O. Mossanek, and J. A. O. Aguiar are acknowledged for helping with several measurements and previous discussions.

Author details

L. M. S. Alves[1*], B. S. de Lima[1], M. S. da Luz[1,2] and C. A. M. dos Santos[1]

*Address all correspondence to: leandro_fisico@hotmail.com

1 Escola de Engenharia de Lorena, Universidade de São Paulo, Lorena, SP, Brazil

2 Universidade Federal do Triângulo Mineiro, Uberaba, MG, Brazil

References

[1] Kittel, C. Introduction to solid state physics, 8th Ed., p. 136 and 277 (Wiley, New York, 2005).

[2] Kamerlingh Onnes, H. Commun. Phys. Lab. Univ. Leiden. Suppl. 29 (Nova York, 1911).

[3] Bardeen, J., Cooper, L. N., and Schriffer, J. R. Microscopic theory of superconductivity. Phys. Rev., 106(1):162–164, Apr 1957.

[4] Bardeen, J., Cooper, L. N., and Schriffer, J. R. Theory of superconductivity. Phys. Rev., 108(5):1175–1204, Dec 1957.

[5] Das, D. and Doniach, S. Bose metal: Gauge-field fluctuations and scaling for field-tuned quantum phase transitions Phys. Rev. B 64, 134511 (2001).

[6] Phillips, P. and Dalidovich, D. The elusive Bose metal. Science 302, 243 (2003).

[7] Kopelevich, Y., Medina Pantoja, J. C., da Silva, R. R., and Moehlecke, S. Universal magnetic-field-driven metal-insulator-metal transformations in graphite and bismuth. Phys. Rev. B 73, 165128 (2006).

[8] dos Santos, C. A. M., da Luz, M. S., Yu, Yi-Kuo, Neumeier, J. J., Moreno, J., and White, B. D., Electrical transport in single-crystalline $Li_{0.9}Mo_6O_{17}$: A two-band Luttinger liquid exhibiting Bose metal behavior. Phys. Rev. B 77, 193106 (2008).

[9] Kopelevich, Y. Esquinazi, P. Torres, J. H. S., Moehlecke, S. Ferromagnetic and superconducting like behavior of Graphite. J. Low Temp. Phys. 119, 691-702 (2000).

[10] Alves, L. M. S., dos Santos, C. A. M., Benaion, S. S., Machado A. J. S., de Lima B. S., Neumeier, J. J., Marques, M. D. R., Albino Aguiar, J., Mossanek, R. J. O., and Abbate, M. Superconductivity and magnetism in the $K_xMoO_{2-\delta}$. J. Appl. Phys. 112, 073923 (2012).

[11] Alves, L. M. S., Damasceno, V. I., dos Santos, C. A. M., Bortolozo, A. D., Suzuki, P. A., Izario Filho, H. J., Machado, A. J. S., and Fisk, Z. Unconventional metallic behavior and superconductivity in the K-Mo-O system. Phys. Rev. B 81, 174532 (2010).

[12] Ogata, M., Anderson, P. W. Transport properties in the Tomonaga-Luttinger liquid. Phys. Rev. Letters 70, 3087 (1993).

[13] Pereira, R. G. Transport in ordered one-dimensional systems. Campinas: UNICAMP, 2004. 134p. Dissertation (Master in Physics) - Universidade Estadual de Campinas, Instituto de Física Gleb Wataghin, Campinas, São Paulo, 2004.

[14] Bernhard, C., Tallon, J. L., Niedermayer, Ch., Blasius, Th., Golnik, A., Brücher, E., Kremer, R. K., Noakes, D. R., Stronach, C. E., and Ansaldo, E. J. Coexistence of ferromagnetism and superconductivity in the hybrid ruthenate-cuprate compound $RuSr_2GdCu_2O_8$ studied by muon spin rotation and dc magnetization. Phys. Rev. B 59, 14099-14107 (1999).

[15] Parker, D., Idrobo, J. C., Cantoni, C., and Sefat, A. S. Evidence for superconductivity at T_C = 12 K in oxygen-deficient $MoO_{2-\delta}$ and properties of molybdenum arsenide and oxide binaries. Phys. Rev. B 90, 054505 (2014).

[16] Alves, L. M. S. Unconventional electrical behavior in the $K_xMoO_{2-\delta}$. 2010. 68 p. Dissertation (Master of Science) – Escola de Engenharia de Lorena, Universidade de São Paulo, Lorena-SP, Brazil, 2010.

[17] Alves, L. M. S., de Lima, B. S., da Luz, M. S.,dos Santos, C. A. M., Neumeier, J. J., and Yu, Yi-Kuo. A magnetic field tuned metal-insulator transition in unconventional metallic K-doped MoO_2. To be published.

[18] Danner, G. M.; Chaikin, P. M. Non-fermi-liquid behavior in transport in $(TMTSF)_2PF_6$. Phys. Rev. Letters 75, 4690, 1995.

Chapter 2

Characterization of the Electronic Structure of Spinel Superconductor $LiTi_2O_4$ using Synchrotron X-ray Spectroscopy

Chi-Liang Chen and Chung-Li Dong

Additional information is available at the end of the chapter

1. Introduction

Numerous studies on high-transition temperature (T_c) superconductivity were motivated primarily by the intention to explore the nature of cuprates. Experimental results, particularly those based on hard X-ray absorption spectra, show that Cu ions reveal a mixed valence and are accountable for high-T_c superconductivity. Recently discovered iron-based superconductors with perovskite blocking layers [i.e., LnFeAsO (Ln = lanthanide), $BaFe_2As_2$, KFeAs, FeSe, and FeAs] have received considerable attention similar to cuprate superconductivity, which was first explored in the 1980s. New superconducting compounds and non-cuprate superconductors with magnetic elements, particularly 3*d* transition metals, have been widely analyzed by various scholars. Spinel $LiTi_2O_4$ (LTO) is a titanium (Ti)-based superconductor that is considered an exotic BCS *s*-wave superconductor with a T_c of ~12 K [21]. This superconductor is regarded as such because it can be described using electron–phonon interaction within the framework of the BCS model [43]. Of the more than 200 typical compounds with an AB_2O_4 normal spinel structure, in which low-valent-state cation "A" occupies the tetrahedral (8a, T_d) interstitial sites and high-valent-state cation "B" occupies the octahedral (16d, O_h) sites, only a few exhibit superconductivity, including CuV_2S_4 (T_c = 4.5 K), $CuRhS_4$ (T_c = 4.8 K), and $CuRhSe_4$ (T_c = 3.5 K). LTO is the only known spinel oxide superconductor, and it has the highest T_c among superconductors with a spinel structure. The 3*d* transition metals occupying the O_h sites in spinel oxides may generally exhibit antiferromagnetism, ferromagnetism, and charge/orbital ordering. The nature of magnetic and electronic properties depends on the average valence of the cations. The closely related case of LiV_2O_4 (LVO), which is an isostructural compound, exhibits distinct physical properties. LVO is the closest neighbor to LTO, and it contains a mixed-valence system with an equal ratio of V^{3+} (S = 1) and V^{4+} (S = ½). LVO exhibits

INTECH
open science | open minds

© 2015 The Author(s). Licensee InTech. This chapter is distributed under the terms of the Creative Commons Attribution License (http://creativecommons.org/licenses/by/3.0), which permits unrestricted use, distribution, and reproduction in any medium, provided the original work is properly cited.

strong electronic correlation, resulting in a greatly enhanced effective mass. The resistivity of this compound displays a metallic character. Although LVO is not a superconductor, it exhibits a heavy fermionic behavior typically observed in a Ce-based (4*f* electron) system [2, 22].

Similar to cuprates [6, 33] and pnictides [9, 24], Ti-based superconductors (titanate) present the possibility of a mixed-valence state (with electronic configuration of $3d^{0.5}$, equal ratio of Ti^{3+} of spin $S = 1/2$ and Ti^{4+} with $S = 0$) in the ground state. Given that magnetic impurities can suppress the superconductivity of various materials, an investigation into whether the dilute doping of magnetic ions in LTO results in the complete suppression of superconductivity must be conducted. Such an undertaking may provide valuable insights into the mechanism of superconductivity. A previous research observed a rapidly suppressed superconducting T_c in magnetically doped system $LiTi_{1-x}M_xO_4$ (M = Cr and V) [19]. Among the explored dopants, vanadium (V) was determined to be more effective in decreasing T_c even at small proportions, and it was also observed in other 3*d* transition metals (e.g., Cr, Mn, Fe, etc.). The results of the study not only signified the magnetic influences and other mechanisms for T_c suppression, but also the charge density wave and structural distortion. For V-doped LTO, the T_c of LTO decreases with V at 2% proportion from ~13 K to ~5 K [18, 19, 24, 49]. These superconducting activities in such a series may unravel the mechanism of superconductivity. Material study on the atomic/electronic structure has essentially illuminated the understanding of its electron transportation properties. Studies have investigated the electronic structure of LTO [8, 39]. The decrease in superconductivity of V-doped LTO is discussed based on a pair-breaking mechanism [19] and a crystalline distortion from octahedral symmetry [34]. The change of Ti and V valence states is suggested to be thoroughly linked to their chemical and physical properties. Electron–electron interaction cannot be overlooked because magnetic ions occupy the structures [32]. In this event, the mechanism of superconductivity remains unknown.

The atomic and electronic structures of the novel spinel LTO superconductors have been investigated. X-ray spectroscopy, X-ray absorption near-edge structure (XANES) spectroscopy, and resonant inelastic soft X-ray scattering (RIXS) spectroscopy are powerful tools for obtaining information on the local orbital character of a specific element. These approaches are also used to probe occupied or unoccupied electronic states near the Fermi level (E_F) and the structural symmetry of mixed-oxide systems. However, these spectroscopic techniques are sensitive to atomic symmetry because edge-sharing charge and charge distribution induce electron–electron and electron-orbital interactions, which may be related to the magnetic nature of the transition metal systems.

XANES spectroscopy is a sensitive tool that can be employed to probe unoccupied electronic states above E_F and to analyze the structural symmetry of mixed-oxide systems [10, 12]. It can provide details on the electronic–orbital interaction from the transition metal 3*d*-O 2*p* hybridization states and the symmetry of the atomic structure. Therefore, the Ti L- and K-edges can be used to determine the valence states of Ti ions in $LiTi_{2-x}V_xO_4$ (LTVO). The V ions occupying and doped in the O_h site may distort the crystal structure of LTVO because of the bonding of O–Ti–O as well as the unoccupied states in the 3*d* orbitals [34].

RIXS spectroscopic technique is used to explore the electronic structure of materials and to associate the structure with the XANES spectrum. RIXS is a process that describes the de-

excitation of the final state of X-ray absorption, providing information on ground state via the excited intermediate states. Consequently, by tuning various excitation energies, certain RIXS features can be enhanced, allowing the separation of different electronic configurations in the mixed ground states [11, 30, 42]. The above conditions indicate that RIXS is a complementary tool compared with XANES. Unlike XANES, RIXS can be used to investigate a forbidden electronic transition (e.g., *d-d* or *f-f* excitation) because it involves two dipole-allowed transitions, given that its final state has symmetry similar to that of the initial state of the former. The RIXS of TM L-edge can reflect the 3*d* partial density of states and is regarded as a useful approach for analyzing the electron correlation among strongly correlated materials [31, 36, 45] as well as the charge transfer between TM 3*d* and O 2*p* orbitals.

In this research, XANES and RIXS spectra were applied to understand the influence of V doping on the atomic/electronic properties of the LTVO system and to discuss the basis of the quick suppression of superconductivity. The occupied or unoccupied states near E_F of a solid-state solution may be a useful starting point in obtaining fundamental information on the complicated behavior of materials, including ferrites, high-T_c superconductors, and strongly correlated and ladder systems. These properties demonstrate that magnetic behavior and atypical physical and chemical characteristics can be synthesized and analyzed. The obtained X-ray spectra reveal that the rapidly suppressed superconductivity is associated with the variation of Ti-O hybridization mainly at e_g bands rather than with the magnetic nature of the substituted V ion.

2. Experiments

All the LTVO samples were synthesized through conventional two-step solid-state reactions with highly pure oxides of TiO_2 (99%), Li_2CO_3 (99.99%), and V_2O_3 (99%) [19]. The samples were dried at 150 °C for at least 2 h. Additional Li_2CO_3 (5 mol%) was added into the samples to compensate for lithium evaporation at high temperature. These processes were performed in a dynamic vacuum environment. In the first step, a mixture of Li_2CO_3 and TiO_2 was pulverized and calcined at 750 °C for 8 h in ambient air. The mixture was pulverized and calcined again at 800 °C for 12 h to form the intermediate compound $Li_2Ti_2O_5$. In the second step, the stoichiometric powders of $Li_2Ti_2O_5$, Ti_2O_3, and V_2O_3 were mixed and ground and then cold-pressed into pellets. The pellets were wrapped with gold foil and sintered in an alumina crucible at 880 °C for 24 h in a dynamic vacuum environment at less than 10^{-5} torr. The final products were stored in an Ar-filled glove box or vacuum desiccator to prevent aging. Powder X-ray diffraction (XRD) patterns [19] with X-ray (Cu, K_α =1.5418 Å) radiation in a diffractometer (Philips PW3040/60) confirmed the phase purity of the product and showed the variation of the lattice parameter as a function of V dopant. Different proportions of the dopant up to 2% were selected to understand the effect of dilute doping. Oxygen stoichiometry was expected to remain constant for all small concentrations given that the preparations were all the same.

XANES spectra were obtained from the National Synchrotron Radiation Research Center (Taiwan) and were operated at 1.5 GeV with a current of 360 mA. The K-edge of Ti and V K-

edge of LTVO were measured with a wiggler beamline BL17C1 equipped with Si (111) crystal monochromators. The absorption spectra were recorded in the fluorescence-yield mode with a Lytle detector [27]. These hard X-ray absorption spectra, which could provide information on the unoccupied states with transition metal *p* state, were normalized to a unit step height in the absorption coefficient from below to above the edges. The oxide powders, namely, TiO_2, VO_2, Ti_2O_3, and V_2O_3, and standard metal foils were used for energy calibration and for comparing the electronic valence states. The XANES spectra at the Ti L- and O K-edges were determined at beamline BL20A in the total-electron-yield mode using an ultrahigh-vacuum chamber with pressure of ~5×10^{-9} torr. All spectra were normalized with the standard procedure.

The experiments for X-ray emission spectroscopy (XES) were conducted at beamline 7.0.1 at the Advanced Light Source, Lawrence Berkeley National Laboratory. The beamline is armed with a spherical grating monochromator and an undulator (period 5 cm in 99 poles) [3]. The RIXS spectra were recorded with a high-resolution grating spectrometer at grazing incidence with a 2D detector [17]. The resolution for Ti L emission spectra was about 0.4 eV. The monochromator resolution was set up similar to that of the emission measurements.

X-ray absorption at the Ti L-edge determined that the electron in the Ti 2*p* core level was excited to the unoccupied Ti 3*d* and 4*s* orbitals. XES recorded the signal from the decay process related to the partial densities of Ti 4*s* and 3*d* states. RIXS spectra were acquired by tuning different excitation energies according to the x-ray absorption spectral profile to measure XES. Sample current mode was employed to record XANES with an energy resolution of ~0.15 eV. Meanwhile, a high-resolution grazing-incidence grating spectrometer with a 2D multi-channel plate detector was used to record XES at a resolution of 0.6 eV [36].

3. Results and discussion

3.1. Structure of LTVO

The crystal structure of cubic spinel LTO, which belongs to the Fd3m space group, is illustrated in Fig. 1(a). The structure demonstrates that the lattice parameter of LTO is 8.404 Å (a = b = c) and contains eight AB_2O_4 units per unit cell. In general, a spinel structure has a total of 56 ions, 32 anions, and 24 cations per unit cell. The Li, Ti, and oxide ions are located at tetrahedral (T_d) A-sites, octahedral (O_h) B-sites, and 32e sites, respectively. The XRD patterns of $LiTi_{2-x}V_xO_4$ (x = 0, 0.05, 0.01, 0.015, and 0.02) are shown in Fig. 2(a). The result of the chemical analysis (determined with ICP-AES) is consistent with the nominal composition [19, 18, 24, 49]. These patterns reflect that the crystal structure is of pure spinel structure without an impure phase. The lattice parameter of LTVO samples displayed in Fig. 2(b) linearly decreases with the increasing concentration of the dopant. Doping V, which has a smaller ionic radius, induces a change in the lattice parameter when in a Ti site. This lattice shrinkage can be attributed to the fact that the ionic radius of V^{3+} (0.64 Å) is smaller than that of Ti^{3+} (0.67 Å) in the O_h site [29]. The rate of shrinkage of the lattice parameter is ~3.6 Å/at% based on the occupancy of O_h sites. This rate is also related to the bond length between the cations (Ti and V) and oxygen. Electronic

structure strongly depends on the hybridization states of the transition metal 3*d*-O 2*p* orbitals nearby E_F when electronic exchange normally occurs. Thus, the changed electronic structure around the transition metal ions greatly affects the oxidation state and physical properties of the latter. Considering these physical properties in AB_2O_4 with mixed-valence states require wide-ranging knowledge of their electronic structure, particularly the *p-d* hybridization and spin-orbital symmetry. Several experiments and theories show that AB_2O_4 exhibits strong electron–hole correlations because of the TM ions located in various sites [8, 39].

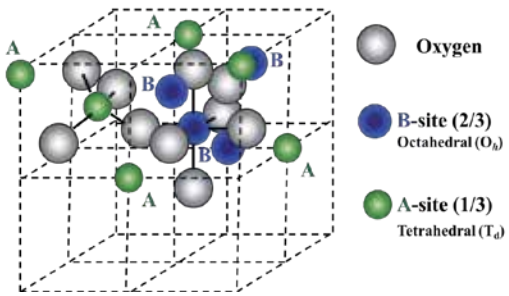

Figure 1. Crystal structure of LTO [Li (green), Ti (blue), and O (grey)].

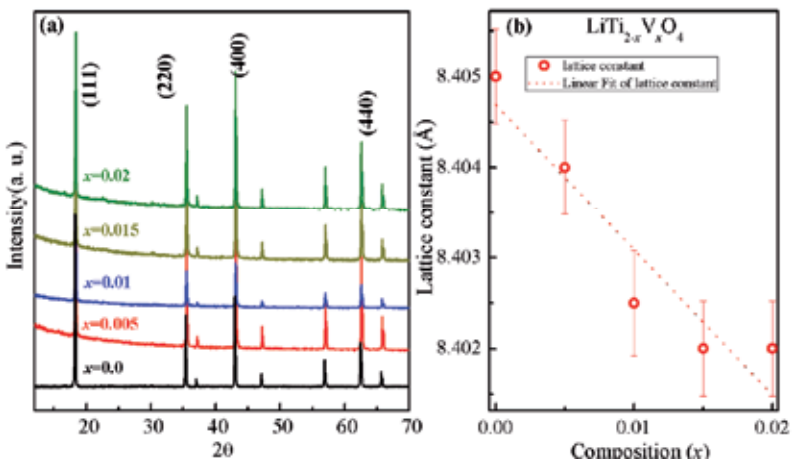

Figure 2. (a) Powder XRD patterns of LTVO crystals with $x = 0$, 0.005, 0.01, 0.015, and 0.02. The patterns are fitted to the Fd3m space group and are indexed. (b) Chemical composition of V dependence of the lattice constant of LTVO.

3.2. Resistive properties

The transport properties of the samples are specified in Fig. 3(a) with V doping of less than 0.025. The findings indicate that the superconducting T_c is suppressed with an increasing proportion of the dopant. Fig. 3(c) reveals that the resistivity of the samples gradually increases. The un-doped LTO has a superconducting T_c of ~12 K with a transition width ($\triangle T_c$) of ~0.4 K. Fig. 3(b) indicates that when the Ti ion is replaced with V ions, T_c exhibits an abrupt but linear suppression with respect to the level of doping. Given the magnetic pair-breaking effects [47],

the doped magnetic ions suppress superconductivity. Considerable research has been devoted to exploring cuprate [48]; Tarascon et al., 1987) and pnictide [41] superconducting systems based on resistivity measurements. For the LTO series, the effect of doping with both non-magnetic and magnetic impurities at both T_d and O_h sites on $(Li_{1-x}A_x)(Ti_{2-y}B_y)O_4$ [A = Mg and Mn; B = Al and Cr] compounds has been previously reported [26]. The substitution of non-magnetic ions (e.g., Mg^{2+} at the T_d site and Al^{3+} at the O_h site) slightly suppresses superconductivity similar to the case when Li^+ ions occupy the T_d site. However, the effect of superconductivity suppression is greater when the magnetic Mn^{2+} ions occupy the T_d site. The suppression of superconductivity is attributed to pair-breaking when the Cooper pairs are scattered with magnetic impurities. The effect of substituting Ti^{3+} with Cr^{3+} at the O_h site is even more significant.

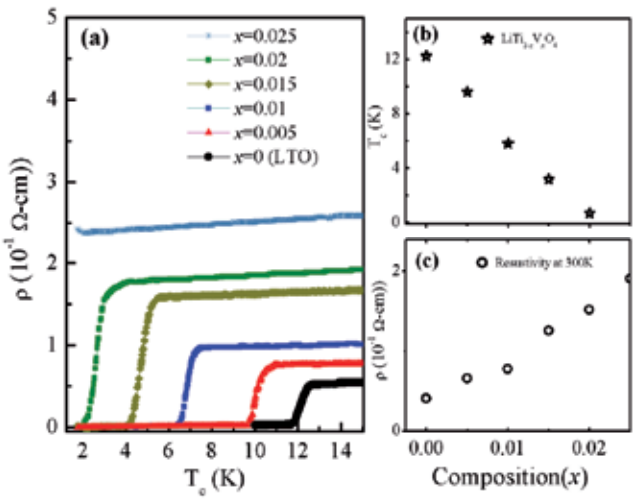

Figure 3. (a) Transport properties of LTO and LTVO samples at low temperature without magnetic field. (b) Chemical composition of V-dependence of superconducting T_c. (c) Resistivity at room temperature.

The resistivity near 300 K increases as x increases [Fig. 3(c)], indicating the extreme sensitivity of the transport properties to the electronic effect of 3*d* transition metals. The itinerant carrier density can be attributed to the cation (Ti^{3+}) in LTO. Similar to the reports of a previous study on Al-doped LTO [16], the results of the current study clarify the effect of carrier density on superconductivity, such that the resistivity increases with the level of doping in the normal state. Except for the semiconducting behavior at the normal state, a similar T_c has been determined in $LiTi_{1.7}$, $Al_{0.3}O_4$, and LTO samples [19]. This observation implies that T_c is slightly affected by substituting a considerable proportion of the trivalent non-magnetic ions. The ratio Ti^{4+}/Ti^{3+} in O_h symmetry can then be modulated with impurity doping to vary the superconducting properties of LTO. Electron–electron interaction may be a key factor in causing changes in the transport properties of the samples. By distorting the local symmetry of the spinel structure, V substitution will not only alter the valence of Ti, but the hole/electron effect as well. This phenomenon is discussed in the next section.

3.3. Electronic structure results based on x-ray spectra

With the aim to investigate the effects of V dilute doping on LTO, this research measures XANES and RIXS at Ti L-edges. As shown in the inset in Fig. 4(a), the Ti L-edge XANES spectra exhibit several well-resolved features because of the excitations of a 2*p* core electron into the Ti 3*d* empty states, that is, a transition from the ground state with configuration $2p^6 3d^n$ to an excited electronic configuration $2p^5 3d^{n+1}$ with numerous multiplet excitations. When the spin-orbital coupling is in the transition metal 2*p* state, the spectra reveal two prominent features located at the energy ranges of 455 eV to 461 eV and 461.2 eV to 468 eV, corresponding to the absorptions L_3 ($2p_{3/2} \rightarrow 3d$) and L_2 ($2p_{1/2} \rightarrow 3d$) edge respectively. These prominent features are due to a strong Coulombic interaction between the poorly screened Ti 3*d* electrons and the Ti 2*p* core hole [12]. L_2 edge features are normally broadened compared with the L_3 edge because of the lesser lifetime of the $2p_{1/2}$ core hole (i.e., a radiationless electron transition from energy level $2p_{3/2}$ to the $2p_{1/2}$), accompanied by the promotion of a valence electron into the unoccupied states (conduction band). In the O_h crystal field, the 3*d* band splits into t_{2g} (d_{xy}, d_{xz}, and d_{yz}) and e_g ($d_{x^2-y^2}$ and $3d_{3z^2-r^2}$) subbands [$\Delta = (e_g) - (t_{2g}) = 10$ Dq]. Given the O_h crystal-field splitting, the Ti L_3-edge feature possesses t_{2g} and e_g bands. The RIXS Ti 3*d* spectra of LTO and doped LTO (V 2 %) are exhibited with energy-loss scales in Fig. 4(a). Four distinct spectral features are observed in RIXS spectra. These features are as follows: elastic peak at the energy loss at zero, *d*–*d* excitations at about 4 eV, a broad-band feature at around 7 eV, and a large energy dispersed-feature above 10 eV. Letters *a* to *k* denote the different exciting energies based on the XANES spectra, as displayed in the inset of Fig. 4(a). For example, XES spectrum *b* is collected by tuning the incident photon energy at 457 eV in XANES. The inelastic scattering features ranging from 5 eV to 10 eV originate from the complicated charge-transfer excitation from O 2*p* to Ti 3*d* t_{2g} and e_g subbands [1, 31]. The low-energy inelastic scattering features absent in TiO_2 are observed at energy of less than 5 eV [36]. The spectra within this energy range significantly differ from that of TiO_2. The appearance of Ti^{3+} implies that an electron occupies the empty 3*d* t_{2g} orbitals, thus inducing the energy-loss features. Strong *d*-electron correlation is revealed because the relative intensities of peaks A_4 and B_4 (*d*-*d* excitations) are observed to be markedly different at varying excitation energies. An enhanced energy-loss peak is observed at 1 eV in spectrum *a*, and the intensity of this peak intensively drops when the excitation energy is tuned to a higher energy (peak *b* in XANES). With the increase of excitation energy at *c*, another intense peak at energy loss of about 2.9 eV is observed. An excitation energy tuned below the L_3 t_{2g} peak in the spectrum (letter *a*) enhances inelastic scattering A_4, which is uncommon. This enhanced inelasticity is not observed at either t_{2g} (*b*) or e_g (*d*) resonant energy. This phenomenon can be explained by considering the presence of Ti^{3+}, as revealed by the constant-initial-state absorption spectrum [3]. The spectral shapes in XANES spectra are similar for both LTO and LTVO, wherein spectral differences are slightly small. Given that the spectral change of XANES is small with V doping, the spectral deconvolution and specific electronic state can be measured separately from RIXS [11]. The result at a specific energy (*c*) in Figs. 4(b) and 4(c) indicates that an enhanced trivalent Ti contribution is observed at a dip quadrivalence within the spectrum (between t_{2g} and e_g). The Ti^{3+} t_{2g}- and e_g-resonance energies correspond to the excitation energies 456 and 457.5 eV respectively. [3].

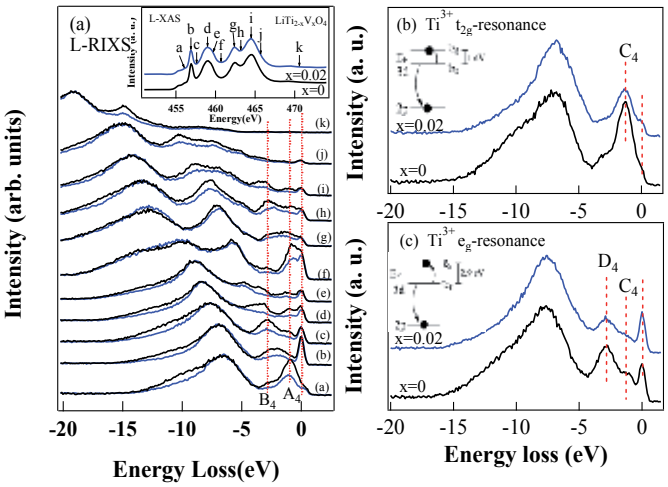

Figure 4. (a) Ti L-RIXS spectra of LTVO (x = 0 and 0.02) recorded with several excitation energies labeled with letters *a* to *k* in the Ti XANES L-edge spectrum. Ti L_3 RIXS spectra at (b) Ti^{3+} t_{2g}-resonance and at (c) Ti^{3+} e_g-resonance. The insets of (b) and (c) display the energy diagram of the *d-d* excitation.

When excitation energy is tuned to the t_{2g} resonance, the low-energy-excited feature C_4 at ~1 eV demonstrated in Figs. 4(b) and 4(c) is resonantly enhanced. This feature corresponds to the electron-hole pairs within the t_{2g} band. When the spectrum is acquired with energy at about e_g resonance energy [Fig. 4(c)], the intensity of peak D_4 increases. Such an increase can be attributed to the transition between the occupied t_{2g} and the unoccupied e_g states. The presence of this RIXS feature indicates a strong electron–electron association. The *d-d* excitation peak at an energy loss of about 2.9 eV corresponds to the crystal-field splitting (i.e., 10 Dq) and refers to the ground state without the core hole. The comparison of the spectra of each set shows that the intensity of the loss feature decreases with the increasing concentration of dopant (x = 0.02). Hence, fewer electrons are distributed in the t_{2g} band. In a previous study on TiO_2 [31], no obvious feature was exhibited in the region located below the elastic signal (peak). The change in intensity is due to the variation of the incompletely filled t_{2g} band arising from the V doped effect. This result forcefully indicates that the Ti valence is enhanced when V is doped. The active Ti ions in LTO have a formal oxidation state trivalence and quadrivalence, which display nearly 0.5 electrons in the 3*d* orbital, and possess a lesser electronic density. Doping with V reduces the number of Ti 3*d* electrons, suggesting an increase in the formal oxidation number of the Ti ion. The Ti ions show a mixed-valence state and contain some t_{2g} electrons in LTO. With no t_{2g} electron, *d-d* excitation is absent because no electron subsists in t_{2g} to be excited to the t_{2g}/e_g unoccupied state. A little variation in valence of Ti is then reflected in the RIXS spectra. The diminution or absence of features in the energy range from 0 eV to 5 eV indicates a decrease in *d–d* transitions. More electrons occupy the t_{2g} orbital when the oxidation number of Ti changes from trivalence to quadrivalence. The probability of exciting the t_{2g} electron into the unoccupied states (t_{2g} or e_g) is therefore increased. Only RIXS can observe the *d-d* excitations (t_{2g}-t_{2g} and t_{2g}-e_g) in the spectra. The significance of observing this *d-d* excitation is that the t_{2g} occupation number changes with V doping, whereas the number of t_{2g} electrons decreases with V doping. Therefore, the significant RIXS spectrum can observe this kind of valence change.

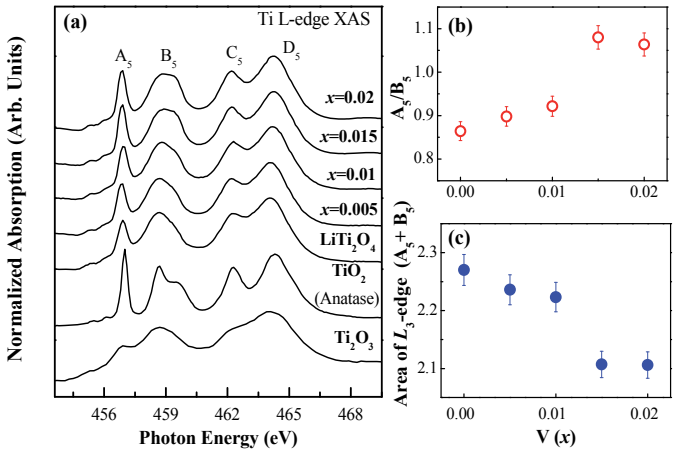

Figure 5. (a) XANES Ti $L_{3,2}$-edge spectra for LTVO (x = 0.005 to 0.02), LTO (x = 0), Ti_2O_3, and anatase TiO_2. (b) Integrated area ratio of A_5/B_5. This ratio increase implies the presence of $3d^0$ states. (c) Total area of L_3-edge (A_5+B_5) decreases with the increase of V concentration

Complementary information is also acquired for this research by thoroughly analyzing the XANES Ti $L_{3,2}$-edge spectra. The spectra of $LiTi_{2-x}V_xO_4$ (or LTVO) (x = 0 to 0.02) are presented in Fig. 5(a). The white line shapes of the spectra of LTO (undoped) and slight V doping (x = 0.005) in LTO are similar. The A_5 and C_5 features (B_5 and D_5) are previously assigned as the t_{2g} (e_g) states of the 10 Dq crystal-field-split in 3*d* orbitals. This O_h crystal-field splitting is ~1.8 eV at LTO, but increases from 1.8 eV to 2.0 eV when the V concentration increases from x = 0.005 to x = 0.02. This phenomenon reveals the distortion of O_h symmetry when Ti is replaced with slight V doping. This finding is consistent with the powder XRD results and the theoretical calculations [12, 13, 15]. Moreover, the results specify that B_5 peak broadens with its gradual V doping. As previously reported [12, 13, 15], and according to the Jahn-Teller distortion with $\Delta E_{J\text{-}T}$ energy splitting in the e_g band, the e_g orbitals point directly toward the Ti 2*p* orbitals of the octahedrally coordinated O atoms. In general, e_g band is sensitive to the local environment, producing a changed bonding distance and a O–Ti–O angle in the presence of V doping. These e_g-related peaks are also broader than the t_{2g} peak because of the larger hybridization between e_g orbitals and O ligand states, and because of the associated effects of solid-state broadening [12]. The e_g feature appears as a narrow and symmetric profile in LTO, representing symmetric octahedrally coordinated Ti–O bonds. This feature becomes broad and asymmetric upon doping, suggesting a distortion. In particular, distortion may arise from the uneven Ti-O bonds in the O_h symmetry. The e_g peak at the side with greater energy originates from the short Ti-O bonds because of the increase in hybridization (relative to the long Ti-O bonds); hence, the intensity ratio of the high-energy to low-energy e_g peaks is increased with V doping. This result implies that long Ti–O bonds become shorter [17]. An enhancement in the integrated area under A_5 peak implies the increase in unoccupied states of Ti 3*d* states, thereby indicating that the Ti valence increases with slight V doping. From the Ti–O bond, the electronic configuration of Ti exhibits a combination of $3d^0$ ($t_{2g}{}^0e_g{}^0$) and $3d^1$ ($t_{2g}{}^1e^0$) in the ground state. Fig. 5(b) shows

the integrated area of ratio A_5/B_5, which clearly increases with V doping. Consequently, the more intense A_5 (t_{2g}) feature implies a higher oxidation number and exhibits the presence of Ti^{4+} ($3d^0$) [28, 40]. Moreover, the area of the L_3-edge that corresponds to (A_5+B_5) progressively decreases when V concentration increases [Fig. 5(c)] because V replaces Ti. This trend is in good agreement with the XRD results [18]. A small but actual increase in Ti valence with slight V doping is observed in XANES Ti $L_{3,2}$-edge spectra. Such an increase is significantly obvious in the Ti L-RIXS spectra.

The pre-edge features of Ti K-edge XANES spectra are displayed in Fig. 6(a). These spectral features at K-edge are due to the transitions from the Ti 1*s* core level to the 4*p*-derived final states based on the dipole selection rule. The pre-edge features are a combination of strongly hybridized Ti 4*sp* and 3*d* and O 2*p* orbitals. Quadrupole-allowed transitions generally occur at the pre-edge region in the transition metal oxides, which correspond to the contribution from 3*d* orbitals through 4*sp*-3*d* hybridization [14, 25, 37]. The inset of Fig. 6(a) reveals that a Gaussian function is subtracted from the original Ti K-edge spectrum for a detailed comparison of the pre-edge spectra. Fig. 4(a) shows the Ti K-edge spectra of LTO and LTVO (0.005 to 0.02). As marked by the black arrow in Fig. 6(a), the spectra of LTVO with a small concentration of x from 0.005 to 0.01 are similar to that of LTO with the same photon energy at the main peak A_6. The Ti valence performs to maintain +3.5 owing to the smaller concentration of V doping. Nevertheless, the intensity of the pre-peak spectrum increases relative to that of pure LTO as the doping level is increased to $x = 0.015$ and $x = 0.02$. Meanwhile, as directed by the red arrow in Fig. 6(a), chemical shift is also observed as V concentration increases. Fig. 6(b) displays the pre-edge region between 4969 and 4977 eV, as well as the three main features (i.e., C_6, D_6, and E_6) in XANES Ti K-edge spectra of TiO_2 (anatase, Ti^{4+}) and LTVO ($x = 0$, 0.02) samples. The origin of the splitting of pre-peaks is caused by local excitations (1*s* to 3*d* t_{2g} and e_g) [5, 14, 38, 46]. Conversely, the greatest contribution to this splitting is suggested to be the corner- and edge-sharing Ti octahedra that yield non-local, intersite hybrid excitations. The next-nearest neighbor 3*d* states (t_{2g} and e_g) are related Ti 4*p* states that absorb atom via the anion O 2*p* states [7, 23, 44]. The local structure of Ti for LTO and LTVO also possesses O_h symmetry; hence, the pre-peak region (A_6 and B_6) can be described in terms of a similar scenario [23, 44, 7]. The intensity of these pre-peaks varies with V concentration. In the V-doped LTO, the substitution of V for Ti slightly decreases the lattice parameter [18]. A reduced bond length (Ti–O–Ti) subsequently increases the overlap of the first-nearest-neighbors and the absorbing atom (e.g., Ti 4*p*-Ti 3*d* orbitals) mediated by O ion. Therefore, these pre-peaks are closely related to the increase in the number of the first-nearest-neighbor unoccupying the Ti 3*d* states. These intersite hybrid peaks intensities increase with the increase of V concentration. The inset of Fig. 6(b) shows that the variation in the area under the pre-peak suggests that the 3*d* unoccupied states are altered via the interaction of the Ti 4*p*-O 2*p*-Ti 3*d* states. These results strengthen the conclusion that Ti is in mixed-valence states between LTO and LTVO [14, 24]. The analysis of the spectra of LTO and LTVO ($x = 0.02$) reveals that pre-peaks A_6 and B_6 are stronger in LTVO than in LTO, attended by a chemical shift of the main peak to higher energy. Therefore, Ti valence is increased when V is doped. The average valence of Ti in the case of doped LTVO ($x = 0.015$ and 0.02) is approximately +3.6, which is obtained with a simple calculation and a fit of the ratio of areas under the spectral lines.

The O K-edge XANES spectra [Fig. 6(c)] provide useful information about the unoccupied density of states in TMO because of the covalent mixing between O and TM ions. The two pre-edge features are at about 530 eV to 536 eV because of the strong hybridizations in Ti 3*d*–O 2*p* states, and correspond to the t_{2g} and e_g states of Ti 3*d* orbitals respectively. The intensity of the t_{2g} and e_g peaks at the O K-edge changes is similar to an increased peak ratio t_{2g}/e_g in Ti L-edge XANES. In sum, the above results specified by the XANES and RIXS spectra strongly confirm that the valence of Ti is increased when the doping level of x increases. Thus, the Ti-O hybridization and electron–electron correlation are modified when a slight doping of V ions completely suppresses the superconductivity of LTO.

Previous studies have indicated that LTO is a spinel superconductor, whereas spinel LVO reveals a heavy fermionic behavior with a Curie-Weiss spin susceptibility and a large electronic specific heat. Conduction arises on a Ti sublattice via the t_{2g} orbitals with a narrow bandwidth (2 eV to 3 eV), displaying possible strong electronic correlations. The origin of the physics and electronic properties of the spinel structure are yet to be resolved. Our current research demonstrates the role of 3*d* electrons in the properties of LTO and LTVO. The full solid solution of $LiTi_{2-x}V_xO_4$ ($0 \le x \le 2$) has been investigated [24]. The replacement of V ions for Ti site modifies the bandgap and *d* electron/hole exchange in Ti energy levels in order to maintain electrical neutrality. Several mechanisms for understanding the quickly suppressed superconductivity with a slight doping of LTVO have been proposed. The slight doping of LTVO may incur two major electronic effects. The first one is a simple pair-breaking effect with electron spin $S = 1$ on superconductivity [20, 24]. The second one refers to the effect of carrier doping on electron correlation via band filling. The 3*d* electrons of V are assumed to hybridize the Ti conduction electrons, making them itinerant. A simple magnetic pair-breaking of electron spins induced by additional impurity is commonly assumed to be responsible for suppressing superconductivity based on the localized moments of 3*d* electrons of V [24]. The localized magnetic moment per V atom is estimated to be 1.7 μB in the V^{4+} state with $S = 1/2$ [24]. The XANES measurements at V K-edges plotted in Fig. 7 show that V is more likely to be in state 3+ (Bordage et al., 2110), which contains a d^2 electronic configuration and is supposed to offer a weak magnetic moment probably because of the antiparallel orientation of the electron spins. The decreased V magnetic moment is also obvious in $LiZnV_2O_4$ [35]. A second possible reason for a weak magnetic moment is the decreased charge carriers at Ti t_{2g} bands. In this case, V electrons are expected to be localized at the Ti conduction electrons. If the Ti ions in LTO possess oxidation numbers 3+ and 4+, then ~0.5 (t_{2g}) electrons are expected to be in the conduction band. This condition results in the observation of a *d-d* excitation within the energy range of 0 eV to 5 eV owing to the presence of electrons in the t_{2g} occupied state that are excited to either the t_{2g} or e_g unoccupied state. The number of electrons occupying the t_{2g} orbital is expected to decrease if the oxidation number of Ti increases from trivalence to quadrivalence because of the doping of V ions. The spectra in RIXS reveal a significant variation in the *d-d* excitation feature, which suggestively decreases when LTO becomes LTVO, even with slight doping of V ions. This situation shows the decreased Ti 3*d* occupied states with the increase of x concentration. The Ti t_{2g} occupation number is then altered upon V doping. This valence variation is small in XANES Ti K- or L-edges spectra, but weighty in RIXS spectra. The results, particularly the reflection of the decreased intensities of t_{2g}-t_{2g}, and t_{2g}-e_g transitions from the RIXS spectra,

support the role of these electronic states in rapidly suppressing T_c in slight V doping. Accordingly, the findings of this research support the conclusion that the decreased density of the states of Ti 3*d* electrons at E_F is responsible for rapidly suppressing superconductivity.

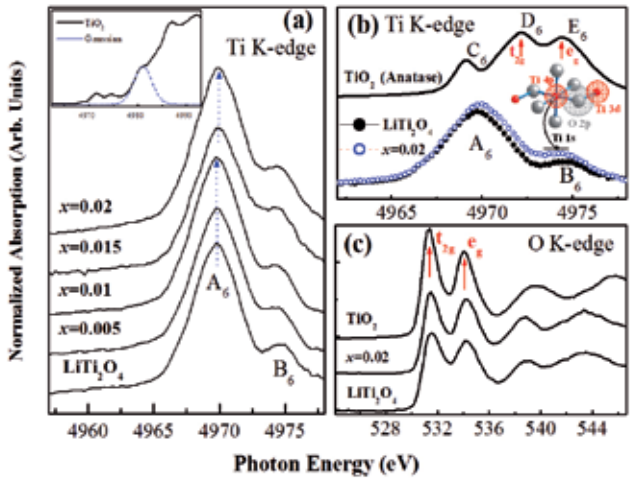

Figure 6. (a) XANES Ti K-edge spectra of LTVO (x = 0 to 0.2) and Anatase-TiO_2 in the pre-edge region. The inset shows that a Gaussian function was subtracted from the original TiO_2 spectrum. (b) Detailed comparison of the pre-edge region for LTO and LTVO (x = 0.02). (c) XANES O K-edge spectra shown with two main peaks in the pre-edge region corresponding to the hybridization of Ti 3*d* (t_{2g} and e_g)-O 2*p* states.

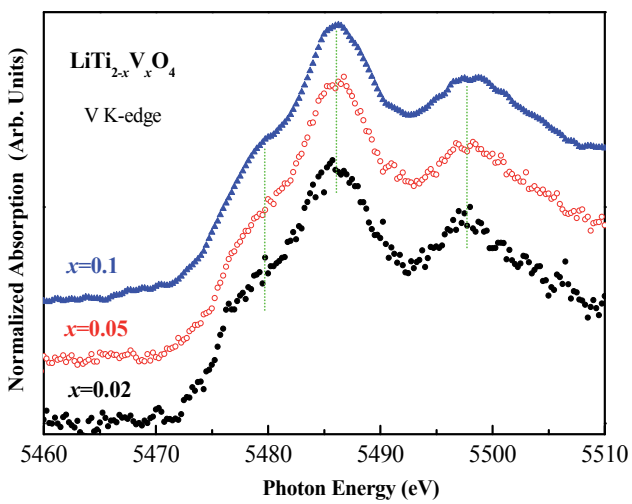

Figure 7. XANES V K-edge of LTVO (x = 0.02) compared with the larger doping of LTVO (x = 0.05 and 0.1). No significant variation is observed in the spectra

4. Conclusion

The results on the effect of V doping on the atomic and electronic structures of LTVO, XAS, and RIXS spectra reveal that the valence of V ions remains constant, but the hybridization of Ti-O considerably varies. In particular, the results show the mixed valency nature of Ti ions and a significant variation in the hybridization of Ti 3d-O 2p states. The sharp decrease in the superconductivity of V-doped samples is ascribed to the electron–orbital interaction arising from the hybridization of TM and O orbitals. Low-energy excitation because of d-d excitation indicates that electron correlation and Ti oxidation number are enhanced, which support the XAS observation. Meanwhile, the observed properties of superconductivity are attributed to an altered density of the states of Ti 3d electrons and Ti-O hybridization. The Ti electronic configuration and lattice distortion induce the rapidly suppressed superconductivity and are attributed to hybridization rather than to the magnetic nature of the substituted ion. This research also demonstrates that RIXS is a powerful tool for investigating the electronic states and electron correlations of Ti compounds, in which the XANES spectral features are subdued.

Author details

Chi-Liang Chen[1,2] and Chung-Li Dong[1,2]

1 Institute of Physics, Academia Sinica, Nankang, Taipei, Taiwan

2 National Synchrotron Radiation Research Center (NSRRC), Hsinchu, Taiwan

References

[1] Agui, A.; Uozumi, T.; Mizumaki, M. & Käämbra, T. (2009). Intermetallic charge transfer in $FeTiO_3$ probed by resonant inelastic soft x-ray scattering. *Physical Review B*, 79: 092402.

[2] Anisimov, V. I.; Korotin, M. A.; Zölfl, M.; Pruschke, T.; Hur, K. Le & Rice, T. M. (1999). Electronic Structure of the Heavy Fermion Metal LiV_2O_4. *Physical Review Letters*, 83: 364.

[3] Augustsson, A.; Henningsson, A.; Butorin, S. M.; Siegbahn, H.; Nordgren, J. & Guo, J.-H. (2003). Lithium ion insertion in nanoporous anatase TiO_2 studied with RIXS. *The Journal of Chemical Physics*, 119: 3983.

[4] Bordage, A.; Balan, E.; de Villiers, J. P. R.; Cromarty, R.; Juhin, A.; Carvallo, C.; Calas, G.; Sunder Raju, P. V. & Glatzel, P. (2011). V oxidation state in Fe–Ti oxides by high-energy resolution fluorescence-detected x-ray absorption spectroscopy. *Physics and Chemistry of Minerals*, 38: 449-458.

[5] Brydson, R.; Sauer, H.; Engel, W.; Thomass, J. M.; Zeitler, E.; Kosugi, N. & Kuroda, H. (1989). Electron energy loss and x-ray absorption spectroscopy of rutile and anatase: a test of structural sensitivity. *Journal of Physics: Condensed Matter*, 1: 797.

[6] Bussmann-Holder; Müller, K. A. & Keller, H. (2007). High T_c Superconductors and Related Transition Metal Oxides ISBN 3540710221.

[7] Cabaret, D; Bordage, A; Juhin, A; Arfaoui, M. & Gaudry, E. (2010). First-principles calculations of x-ray absorption spectra at the K-edge of 3*d* transition metals: an electronic structure analysis of the pre-edge. *Phys. Physical Chemistry Chemical Physics*, 12: 5619-5633.

[8] Cava, R. J.; Murphy, D. W.; Zahurak, S.; Santoro, A. & Roth, R. S. (1984). The crystal structures of the lithium-inserted metal oxides $Li_{0.5}TiO_2$ anatase, $LiTi_2O_4$ spinel, and $Li_2Ti_2O_4$. *Journal of Solid State Chemistry*, 53: 64-75.

[9] Chen, C. L. & Dong, C. L. (20012). SUPERCONDUCTOR-Materials, Properties and Applications, 2012 ISBN: 979-953-307-798-6 Chapter 2 'X-ray spectroscopy studies of the iron chalcogenides', 21-44.

[10] Chen, C. L.; Yeh, K. W., Huang, D. J., Hsu, F. C.; Lee, Y. C., Huang, S. W., Guo, G. Y.; Lin, H. J.; Rao, S. M. & Wu, M. K. (2008). Orbital polarization of the unoccupied states in multiferroic $LiCu_2O_2$. *Physical Review B*, 78: 214105.

[11] Dallera, C.; Grioni, M.; Shukla, A.; Vankó, G.; Sarrao, J. L.; Rueff, J. P. & Cox, D. L. (2002). New Spectroscopy Solves an Old Puzzle: The Kondo Scale in Heavy Fermions. *Physical Review Letters*, 88: 196403.

[12] De Groot, F. M. F.; Fuggle, J. C.; Thole, B. T. & Sawatzky, G. A. (1990). 2*p* x-ray absorption of 3d transition-metal compounds: A atomic multiplet descriptiom including the crystal field. *Physical Review B*, 42: 5459. (1990). $L_{2,3}$ x-ray-absorption edges of d^0 compounds: K^+, Ca^{2+}, Sc^{3+}, and Ti^{4+} in O_h (octahedral) symmetry. *Physical Review B*, 41: 928.

[13] De Groot, F. M. F.; Faber, J. C.; Michile, J. J. M.; Czyzyk, M. T.; Abbate, M. & Fuggle, J. C. (1993). Oxygen 1*s* x-ray absorption of tetravalent titanium oxides: A comparison with single-particle calculations. *Physical Review B*, 48: 2074

[14] Durmeyer, O.; Kappler, J. P.; Beaurepaire, E.; Heintz, J. M. & Drillon, M. (1990). TiK XANES in superconducting $LiTi_2O_4$ and related compounds. *Journal of Physics: Condensed Matter*, 2: 6127

[15] Finkelstein, L. D.; Zabolotzky, E. I.; Korotin, M. A.; Shamin, S. N.; Butorin, S. M.; Kurmaev, E. Z. & Nordgren, J. (2002). Vacant states of TiO_2 with rutile structure and their reflection in different-type x-ray absorption spectra. *X-ray Spectrometry*, 31: 414-418.

[16] Fazileh, F.; Gooding, R. J.; Atkinson, W. A. & Johnston, D. C. (2006). Role of Strong Electronic Correlations in the Metal-To-Insulator Transitionin Disordered $LiAl_yTi_{2-y}O_4$. *Physical Review Letters*, 96: 046410.

[17] Harada, Y.; Kinugasa, T.; Eguchi, R.; Matsubara, M.; Kotani, A.; Watanabe, M.; Yagishita, A. & Shin, S. (2000). Polarization dependence of soft-x-ray Raman scattering at the L edge of TiO_2. *Physical Review B*, 61: 12854.

[18] Hsu, F. C. Liao, Y. C.; Yan, D. C.; Gu, S. Y.; Wu, M. K.; Tang, H. Y. & Perng, T. P. (2007). Observation of metal–insulator transition in vanadium-doped superconducting $Li(Ti_{2-x}V_x)O_4$. *Physica C*, 460-462: 546-548.

[19] Hsu, F. C. (2009), Investigation of the electrical, magnetic and thermal properties of spinel $LiTi_{2-x}M_xO_4$ (M=V and Cr). Department of Materials Science and Engineering, *National Tsing Hua University, Taiwan.* Ph. D. Thesis.

[20] Itoh, Y,; Moritsu, N. & Yoshimura, K. (2008). Emergence of Antiferromagnetic Correlation in $LiTi_{2-x}V_xO_4$ via ^{7}Li NMR. *Journal of the Physical Society of Japan*, 77: 123713.

[21] Johnston, D. C. (1976). Superconducting and normal state properties of $Li_{1+x}Ti_{2-x}O_4$ spinel compounds. I. Preparation, crystallography, superconducting properties, electrical resistivity, dielectric behavior, and magnetic susceptibility. *Journal of Low Temperature Physics*, 25: 145-175

[22] Johnston, D. C.; Swenson,C. A. & Kondo, S. (1999). Specific heat (1.2–108 K) and thermal expansion (4.4–297 K) measurements of the 3*d* heavy-fermion compound LiV_2O_4. *Physical Review B*, 59: 2627.

[23] Joly, Y; Cabaret, D.; Renevier, H. & Natoli, C. R. (1999). Electron Population Analysis by Full-Potential X-Ray Absorption Simulations. *Physical Review Letters*, 82: 2398.

[24] Kichambare, P. Kijima, N.; Honma, H., Ebisu, S. & Nagata, S. (1996). Suppression of superconductivity in $Li(Ti_{1-x}V_x)_2O_4$. *Journal of Physics and Chemistry of Solids*, 57: 1615-1620.

[25] Kucheyev, S. O.; van Buuren, T.; Baumann, T. F.; Satcher, J. H.; Willey, Jr., T. M.; Meulenberg, R. W., Felter, T. E.; Poco, J. F.; Gammon, S. A. & Terminello L. J. (2004). Electronic structure of titania aerogels from soft x-ray absorption spectroscopy. *Physical Review B*, 69: 245102.

[26] Lambert, P. M.; Edwards, P. P. & Harrison, M. R. (1990). Magnetism, superconductivity, and the metal-nonmetal transition in the spinel $LiM_xTi_{2-x}O_4$; M = Al^{3+}, Cr^{3+}. *Journal of Solid State Chemistry*, 89: 345-360.

[27] Lytle, F. W., Greegor, R.B., Sandstrom, D.R., Marques, E.C., Wong, J., Spiro, C.L., Huffman, G.P. & Huggins, F. E. (1984). Measurement of soft x-ray absorption spectra with a fluorescent ion chamber detector. Nuclear Instruments and Methods in Physics Research Section A: Accelerators, Spectrometers, Detectors and Associated Equipment, 226:542-548.

[28] Le Fèvre, P.; Danger, J.; Magnan, H.; Chandesris, D.; Jupille, J.; Bourgeois, S.; Arrio, M. A.; Gotter, R.; Verdini, A. & Morgante, A. (2004). Stoichiometry-related Auger

lineshapes in titanium oxides: Influence of valence-band profile and of Coster-Kronig processes. *Physical Review B*, 69: 155421.

[29] Lide, D. R. (2007-2008) CRC handbook of Chemistry and Physics, 88th edition, Taylor & Francis Group.

[30] Maddox, B. R.; Lazicki, A.; Yoo, C. S.; Iota V.; Chen, M.; McMahan, A. K.; Hu, M. Y.; Chow, P.; Scalettar, R. T. & Pickett, W. E. (2006). 4*f* delocalization in Gd: Inelastic x-ray scattering at ultrahigh pressure. *Physical Review Letters*, 96: 215701.

[31] Matsubara, M.; Uozumi, T.; Kotani, A.; Harada, Y. & Shin, S. (2002). Polarization dependence of resonant x-ray emission spectra in $3d^n$ transition metal compounds with n = 0, 1, 2, 3. *Journal of the Physical Society of Japan*, 71: 347-356.

[32] Massidda, S.; Yu, J. & Freeman, A. J. (1988). Electronic structure and properties of superconducting $LiTi_2O_4$. *Physical Review B*, 38: 11352.

[33] Merz, M.; Nücker, M.; Schweiss, P.; Schuppler, S.; Chen, C. T.; Chakarian, V.; Freeland, J.; Idzerda, Y. U,; Kläser M.; Müller-Vogt, M. & Wolf, Th. (1998). Site-Specific X-Ray Absorption Spectroscopy of $Y_{1-x}Ca_xBa_2Cu_3O_{7-y}$: Overdoping and role of apical oxygen for high temperature superconductivity. *Physical Review Letters*, 80: 5192.

[34] Millis, A. J. (1998). Lattice effects in magnetoresistive manganese perovskites. *Nature*, 392: 147.

[35] Muhtar; Takagi, F.; Kawakami, K. & Tsuda, N. (1988). Magnetic Susceptibility of Metal-Insulator System $Li_xZn_{1-x}V_2O_4$. *Journal of the Physical Society of Japan*, 57: 3119-3127.

[36] Nordgren, J.; Bray, G.; Cramm, S.; Nyholm, R.; Rubensson, J. E. & Wassdahl, N. (1989). Soft x-ray emission spectroscopy using monochromatized synchrotron radiation (invited). *Review of Scientific Instruments*, 60: 1690.

[37] Poumellec, B.; Marucco, J. F. & Touzelin, B. (1987). X-ray-absorption near-edge structure of titanium and vanadium in $(Ti,V)O_2$ rutile solid solutions. *Physical Review B*, 35: 2284.

[38] Parlebas, J. C.; Khan, M. A.; Uozumi, T.; Okada, K. & Kotani, A. (1995). Theory of many-body effects in valence, core-level and isochromat spectroscopies along the 3*d* transition metal series of oxides. *Journal of Electron Spectroscopy and Related Phenomena*, 71: 117.

[39] Ra, W.; Nakayama, M.; Uchimoto, Y. & Wakihara, M. (2005). Experimental and computational study of the electronic structural changes in $LiTi_2O_4$ Spinel Compounds upon Electrochemical Li insertion reactions. *The Journal of Physical Chemisity B*, 109(3): 1130-1134.

[40] Richter, J. H.; Henningsson, A.; Sanyal, B.; Karlsson, P. G.; Andersson, M. P.; Uvdal, P.; Siegbahn, H.; Eriksson, O. & Sandell, A. (2005). Phase separation and charge localization in UHV-lithiated anatase TiO_2 nanoparticles. *Physical Review B*, 71: 235419.

[41] Rotter, M,; Tegel, M. and Johrendt, D. (2008). Superconductivity at 38 K in the Iron Arsenide $(Ba_{1-x}K_x)Fe_2As_2$. *Physical Review Letters*, 101: 107006.

[42] Rueff, J. P.; Hague, C. F.; Mariot, J. M.; Journel, L.; Delaunay, R.; Kappler, J. P.; Schmerber, G.; Derory, A.; Jaouen, N. & Kril,l G. (2004). f-state occupancy at the γ-α phase transition of Ce-Th and Ce-Sc alloys. *Physical Review Letters*, 93: 067402.

[43] Sun, C. P.; Lin, J. Y.; Mollah, S.; Ho, P. L.; Yang, H. D.; Hsu, F. C.; Liao, Y. C. & Wu, M. K. (2004). Magnetic field dependence of low-temperature specific heat of the spinel oxide superconductor $LiTi_2O_4$. *Physical Review B*, 70: 054519.

[44] Uozumi, T.; Okada, K.; Kotani,; Durmeyer, A. O.; Kappler, J. P.; Beaurepaire, E. & Parlebas, J. C. (1992). Experimental and Theoretical Investigation of the Pre-Peaks at the Ti K-Edge Absorption Spectra in TiO_2. *EPL (Europhysics Letters)*, 18: 85.

[45] Warwick, T.; Heimann, P.; Mossessian, D.; McKinney, W. & Padmore, H. (1995). Performance of a high resolution, high flux density SGM undulator beamline at the ALS (invited). *Review of Scientific Instruments*, 66: 2037.

[46] Wu, Z. Y.; Ouvrard, G.; Gressier, P. & Natoli, C. R. (1997). Ti and O K edges for titanium oxides by multiple scattering calculations: Comparison to XAS and EELS spectra. *Physical Review B*, 55: 10382.

[47] Xiao, G.; Cieplak, M. Z.; Xiao, J. Q. & Chien, C. L. (1990). Magnetic pair-breaking effects: Moment formation and critical doping level in superconducting $La_{1.85}Sr_{0.15}Cu_{1-x}A_xO_4$ systems (A=Fe, Co, Ni, Zn, Ga, Al). *Physical Review B*, 42: 8752(R)

[48] Xiao, G.; Streitz, F. H.; Gavrin, A.; Du, Y. W. & Chien C. L.(1987). Effect of transition-metal elements on the superconductivity of Y-Ba-Cu-O. *Physical Review B*, 35: 8782(R)

[49] Xu, F.; Liao, Y. C.; Wang, M. J.; Wu, C. T.; Chiu, K. F. & Wu, M. K. (2003). The Preparation Effect of Li_{1+x} Ti_2O_4 and Its Aging Effect. *Journal of Low Temperature Physics*, 131: 569-574.

Chapter 3

A Fluorine-Free Oxalate Route for the Chemical Solution Deposition of $YBa_2Cu_3O_7$ Films

Luis De Los Santos Valladares, Juan Carlos González, Angel Bustamante Domínguez, Ana Maria Osorio Anaya, Henry Sanchez Cornejo, Stuart Holmes, J. Albino Aguiar and Crispin H.W. Barnes

Additional information is available at the end of the chapter

http://dx.doi.org/10.5772/59359

1. Introduction

To date there has been intensive research, both theoretical and experimental, about epitaxial growth of high critical temperature superconductor (HTS) thin films [1, 2]. The term epitaxy (from the Greek roots *epi*, meaning "above", and *taxis*, meaning "order") appeared around 50 years ago and refers to the growth of an oriented film on a substrate which can be based on the same substrate material (homoepitaxy) or onto a different material (heteroepitaxy). $YBa_2Cu_3O_7$ (YBCO) is one most studied HTS [3,4]. It has an orthorhombic structure and it is superconductor below the critical temperature (T_C) around 90 K. The superconductivity mechanism in this material is related to the presence of CuO_2 planes and charge carriers reservoir planes in its crystalline structure [5]. The interest in developing superconducting YBCO films is to produce second generation superconducting tapes [6] which, under the absence of magnetic fields, can transport high electric current densities (~10^6 A/cm^2) at liquid nitrogen temperature (77 K).

To achieve the epitaxial growth, the crystal lattice of the substrate must match with that of YBCO, permitting a small difference between them (e.g. $a_{substrate}$ ~ 3.9 Å, a_{YBCO} ~ 3.8 Å). If the lattice constant of the substrate differs from that of YBCO, the epitaxial growth is not achieved, resulting in a small amount of grains oriented in the *c*-axis and hence in anisotropy of the critical current density and magnetic susceptibility.

The methods for synthesizing YBCO layers can be classified into two categories: in-situ and ex-situ. In the in-situ methods, the YBCO phase is formed during deposition. Some of them are:

INTECH
open science | open minds

© 2015 The Author(s). Licensee InTech. This chapter is distributed under the terms of the Creative Commons Attribution License (http://creativecommons.org/licenses/by/3.0), which permits unrestricted use, distribution, and reproduction in any medium, provided the original work is properly cited.

Pulsed laser deposition (PLD), liquid phase epitaxy (LPE) and metal organic chemical vapour deposition (MOCVD) [7-13]. In the ex-situ methods, the nucleation and growth of the YBCO film takes place after the deposition, by subsequent heat treatments [14,15]. The advantage of the in-situ techniques over the ex-situ ones are that they allow YBCO films with high J_C values, they can control thickness of the film and they can permit partially substitution of rare-earth elements during growing. Nevertheless, these techniques require sophisticated apparatus and high vacuum systems which make the technique expensive for commercial purposes. In contrast, the ex-situ techniques, in particular the Chemical Solution Deposition (CSD), are more attractive since they are cheap, fast and can provide large areas films and mass production. In this chapter, a fluorine-free CSD method is introduced for the fabrication of YBCO films on different substrates.

2. Chemical solution deposition technique for obtaining YBCO films

Chemical solution deposition is an ex-situ technique in which a chemical solution precursor is deposited on substrates to epitaxially grow YBCO layers [16,17]. It does not require expensive conditions or equipments such as high vacuum, irradiation or sputtering. In this technique, a solution precursor containing stoichiometric cations of Y, Ba and Cu (with ratio 1: 2: 3) is prepared, usually by sol gel, and directly deposited onto single crystals or templates which transfers their texture to the coating. The YBCO textured film is then obtained after heat treatments in oxidizing atmosphere [18, 19]. Therefore, this technique is cheap, fast and can provide large-area films. In the present work, depending on the Trifluoroacetate composition of the precursor solution, the CSD is classified into two routes: Trifluoroacetate and free-trifluoroacetates.

2.1. Trifluoroacetate metal-organic CSD route

The trifluoroacetate metal-organic (TFA-MOD) CSD route is promising for producing YBCO superconducting films with high critical current density (J_C) values [20-26]. This technique was introduced by Gupta et al. in 1988 in order to prevent the formation of $BaCO_3$ of the YBCO films usually obtained by CSD [27]. In fact, in other different CSD routes, $BaCO_3$ agglomerates at the grain boundaries affecting the J_C of the YBCO textured films. However, in the TFA-MOD BaF_2 forms during the decomposition of the organic compounds (during pyrolisis) and the YBCO films are then obtained via hydrolysis of BaF_2 [28].

In this technique, the precursor solution is prepared by mixing Y and Ba trifluoroacetates with Cu acetate (in molar ratio 1:2:3) in methanol [29] or water [30]. The organic components are eliminated by pyrolisis at around 400 °C, yielding in Y_2O_3, BaF_2 and CuO. These intermediate compounds are then transformed into YBCO tetragonal (non superconductor) by annealing at around 800 °C. The reaction follows the equation [31]:

$$0.5Y_2O_3 + 2BaF_2 + 3CuO + 2H_2O \rightarrow YBa_2Cu_3O_{7-x} + 4HF\uparrow \quad (1)$$

http://dx.doi.org/10.5772/59359

The superconducting YBCO (orthorhombic) is obtained by oxygenating the latest compound at high temperatures. Nevertheless, the release of the HF-gas product during heat treatments makes this technique hazardous for health and environment. Thus non-fluorine routes are necessary to be investigated.

2.2. Free-trifluoroacetate CSD routes

Chemical solution deposition routes which does not require the use of trifluoroacetates are vast. However, most of them result in YBCO films containing unreacted and/or secondary phases such as Y_2O_3, $BaCO_3$, Y_2BaCuO_5 (Y211), $BaCuO_2$, Cu_2BaO_2, etc. Table 1 list free-trifluoroacetates routes reported in the literature which do not require carbonate ingredients and without $BaCO_3$ formation. The routes are listed according to the employed reagents. In metal alkoxides routes the gelation rate of the precursor solution is adjusted by choosing the proper solvent. The solidification includes the hydrolysis and condensation of the alkoxides through which a polymeric product is formed [32]. However, since the rate of hydrolysis of Y and Ba are faster than that for Cu, different sized clusters results in the sol [33]. In the hydroxides route $Ba(OH)_2$ and Y-and Ba-trimethylacetates are reacted in propionic acid with amine solvent. Remarkably, it has been reported that this stock solution is stable in air and has a shelf life longer than 2 years [34-36]. On the other hand, the CSD based on nitrates, which is also known as polymer-assisted deposition (PAD) because of the use of polymers, obtains a homogeneous distribution of the metal precursors in the solution and the formation of uniform metal–organic films [37]. The formed NO and/or NO_2 can be easily eliminated leading in a high homogeneity of the precursor solution. In the following sections, a novel fluorine-free method, based on oxalates, for the CSD of YBCO films is described.

Route	Ingredients	Solvent	Substrate	Advantage	Disadvantage	Ref.
Metal alkoxides	$M(OR)_n$ where M=Y, Ba and Cu, and R=CH_3, CH_2O_5	H_2O, CH_3OH	Ni	It is possible to control the degree of gelation.	Inhomogeneity of the precursor gel.	[32]
Acetyl acetonates	APyP, where A= acetylacetone of Y, Ba and Cu, Py= pyridine, and P = acid	C_5H_5N, CF_3CO_2H, CH_3OH	MgO, YSZ	Smooth surface	Films composed of dispersed grains	[38]
Hydroxides	$Y(C_4H_9COO)_3$, $Ba(OH)_2$ and Cu- trimethyl acetate	Propionic acid / amine solvent	YSZ, $LaAlO_3$, MgO	Smooth surface without cracks	Difficult to reproduce	[34-36, 39-42]
Nitrates	$Y(NO_3)$, $Ba(NO_3)$ and $Cu(NO_3)$	$(CH_3)_2NC(O)H$	$SrTiO_3$, $LaAlO_3$	Homogeneous solution precursor	Requires rapid drying to prevent premature crystallization	[43]

Note: YSZ refers to Yttria-stabilized Zirconia ($Y:ZrO_2$)

Table 1. Classification of some free-trifluoroacetate CSD routes depending on the reagents reported in the literature and which do not result on YBCO films containing $BaCO_3$.

3. Substrates

Similar to the in-situ technique, CSD of YBCO superconducting layers also includes careful selection of substrates. To obtain high quality growth of YBCO, many considerations should be taking into mind, such as:

- The potential substrates should have lattice constant similar to that of YBCO orthorhombic so as to allow epitaxial growth.
- They must be highly insulating for eventual applications in electrical circuits.
- Ferromagnetic substrates must be discarded since they affect the diamagnetic properties of the YBCO superconducting film.
- They should have a high melting point since the fabrication of the film requires high temperatures (usually higher than 800 °C).

Some materials which meet well the requirements listed above and are: sapphire (Al_2O_3), magnesium oxide (MgO), cerium dioxide (CeO_2), yttrium oxide (Y_2O_3), lanthanum aluminate ($LaAlO_3$), strontium titanate ($SrTiO_3$) and Yttria-stabilized Zirconia (Y:ZrO_2, YSZ). The following sections describe the CSD of YBCO superconducting films onto the three latest substrates ($LaAlO_3$, $SrTiO_3$ and YSZ). The substrates used in this work (5 mm^2 area) were purchased from CrysTec Ltd. and their main characteristics are listed in Table 2. Note that from them, the YSZ substrate present the highest mismatch in lattice constant with respect to YBCO which, as it will be discussed below, influences in the crystallization, composition, texture and magnetic properties of the resulting YBCO film.

Material	Crystal structure	Lattice constant (nm)	Mismatch with YBCO (%)	Density at 25 °C (×10^3 kg/m^3)	Melting point (K)	Thermal expansion (K^{-1})
$LaAlO_3$	p.c.	0.3821	-0.83	6.51	2380	10×10^{-6}
$SrTiO_3$	c.p.	0.3905	+1.35	5.12	2353	9×10^{-6}
YSZ	Cubic	0.512	+32.88	5.90	2780	9.2×10^{-6}

Note: p.c: Pseudocubic (with microtwins parallel to (100)), c.p: Cubic perovskite structure.

Table 2. Some physical properties of the substrates used for the CSD of YBCO superconducting in this work.

4. Solution preparation and deposition

The first step of the CSD technique to obtain YBCO superconducting films is the preparation of the precursor solution. This solution is required to have homogeneously dispersed Y, Ba and Cu cations, suitable viscosity and without precipitation so as to achieve good adherence to the surface of the substrate and desired thickness of the resulting YBCO film.

http://dx.doi.org/10.5772/59359

Figure 1 provides a schematic representation of the manufacturing process of the YBCO film followed in this work. Initially a precursor solution is obtained by sol-gel similar to previous reports [44-48]. Stoichiometric amounts of yttrium, barium and copper acetates ($Y(OOCCH_3)_3.4H_2O$, $Ba(OOCCH_3)_2$ and $Cu(OOCCH_3)_2.2H_2O$ respectively) were mixed and completely dissolved in a solution of ethanol (C_2H_5OH) and oxalic acid ($H_2C_2O_4$) (1:1 ratio). The system was left to decant for about 12 h. The matrix was then dispersed and magnetically stirred at 250 rpm to achieve a homogeneous metathesis reaction (without the segregation of any particular constituents) between the acetate solution and the oxalic acid. The resulting precursor solution was a colloid based on Y, Ba and Cu oxalates. Single drops of this precursor were carefully dripped on the $LaAlO_3(100)$, $SrTiO_3(100)$ and YSZ(100) substrates with the help of a Fisher pipette. The samples were immediately dried in an oven at 40 °C. The last steps were repeated 7 times. The oxalate is formed by the reaction [49]:

$$Y_2(OOCCH_3)_3.H_2O + Ba(OOCCH_3)_2 + Cu(OOCCH_3)_2.H_2O + H_2C_2O_4 \rightarrow Y(C_2O_4).mH_2O\downarrow + Ba(C_2O_4).nH_2O\downarrow + Cu(C_2O_4)\downarrow \quad (2)$$

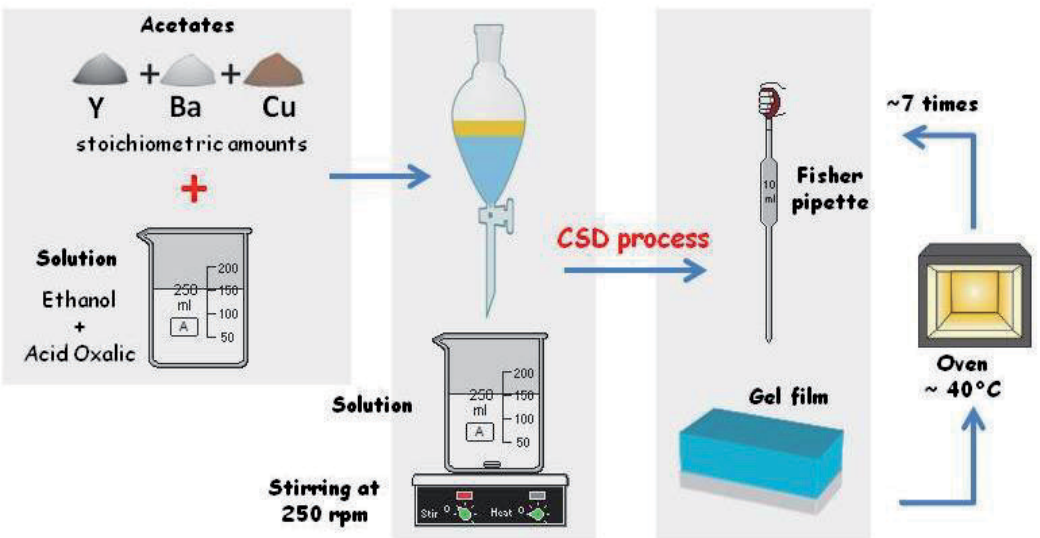

Figure 1. Schematic representation followed in this work for the fabrication of YBCO superconducting films on $LaAlO_3(100)$, $SrTiO_3(100)$ and YSZ(100) substrates by chemical solution deposition. Initially a precursor solution is obtained by reacting stoichiometric amounts of yttrium, barium and copper acetates in a solution of ethanol and oxalic acid (1:1 ratio). After decanting the solution for 12 h, it was dispersed by magnetic agitation to achieve a homogeneous metathesis reaction between acetate and oxalic acid. The resulting precursor solution was carefully dripped onto $LaAlO_3$, $SrTiO_3$ and YSZ substrates and they were immediately dried in an oven at 40 °C. The last two steps were repeated 7 times.

5. Heat treatments

$YBa_2Cu_3O_{7-x}$ has relatively strong oxygen-metal bonds, thus high temperatures heat treatments are required to rearrange the species in the precursor solution for a correct crystallization and crystal growth. The thermodynamic stability of YBCO limits the synthesis and the crystal growth parameters. For example synthesis at temperatures well below 900 ℃ result in x values from 0.7 to 1, leading the crystalline structure as tetragonal (non superconductor). Further oxidization at high temperatures is necessary to decrease x to ~ 0, from which cooling it below the phase transition range (~ 700 ℃ [50]) results in the orthorhombic structure (superconductor).

In this work, the crystallization and epitaxial growth of the YBCO layers were achieved by ex-situ heat treatments, as represented in Fig. 2. After drying the samples for 10 min, they were annealed at 860 °C in a tubular furnace (LENTON LTF-PTF Model 16/610) in low oxygen atmosphere for 12 h. The low oxygen atmosphere facilitates the liquid phase formation, which in turn influences the grain growth and interconnection between crystallites [51]. On the other hand, the slow heating rate (1 °C/min) permits the thermal decomposition to remove residual volatile hydrocarbons thus lowering the risk of trapping CO_2 bubbles in. Besides, it is expected that both, the slow rate and the high annealing temperature performed in this work also prevent the formation of $BaCO_3$ [52]. Thus, the chemical reaction during this process might described by [49]:

$$\begin{aligned} &Y_2(C_2O_4).H_2O + Ba(C_2O_4).nH_2O + Cu(C_2O_4) \\ &\rightarrow 0.5Y_2O_3 + 2BaO + 3CuO + n'.CO_2 + m'CO + x'.H_2O \end{aligned} \tag{3}$$

obtaining mixtures of yttrium, barium and copper oxides (Y_2O_3, BaO and CuO). At this stage, epitaxial growth of the crystallites occurs specially at the interface of the layer/substrate, together with a considerable decrease of the thickness of the film (as it is represented in the bottom part of the figure) [53]. Furthermore, the microstructure of the film might consist of irregular arrangement of porous together with groups of chemically bounded crystallites. The reaction is described by [49]:

$$\begin{aligned} &0.5Y_2O_3 + 2BaO + 3CuO + n'.CO_2 + m'CO + x'.H_2O \\ &\rightarrow YBa_2Cu_3O_{6.5} + n''CO_2\uparrow m''.CO_2\uparrow + x''.H_2O\uparrow \end{aligned} \tag{4}$$

Note also that at this stage the sample consists on $YBa_2Cu_3O_x$ (probably with x=6.5 [49], which is not a superconductor). The sintering of the YBCO superconducting ($YBa_2Cu_3O_7$, orthorhombic structure) is obtained after oxygenating the sample at higher temperatures than 800 ℃. For example, the represented oxygenation at 860 °C in Fig. 2 promotes the increase of the density of the layer and the epitaxial growth of the crystallites toward the surface, consuming other disoriented grains to a thermodynamically stable phase during this process. The sintering process of YBCO superconducting during oxygenation is thus described by [49]:

http://dx.doi.org/10.5772/59359

$$YBa_2Cu_3O_{6.5} + 0.25O_2 \rightarrow YBa_2Cu_3O_7 \quad (5)$$

Eventually, the samples were subsequently quenched to room temperature with an intermediate step at 600 °C so as to minimise the stress in the film.

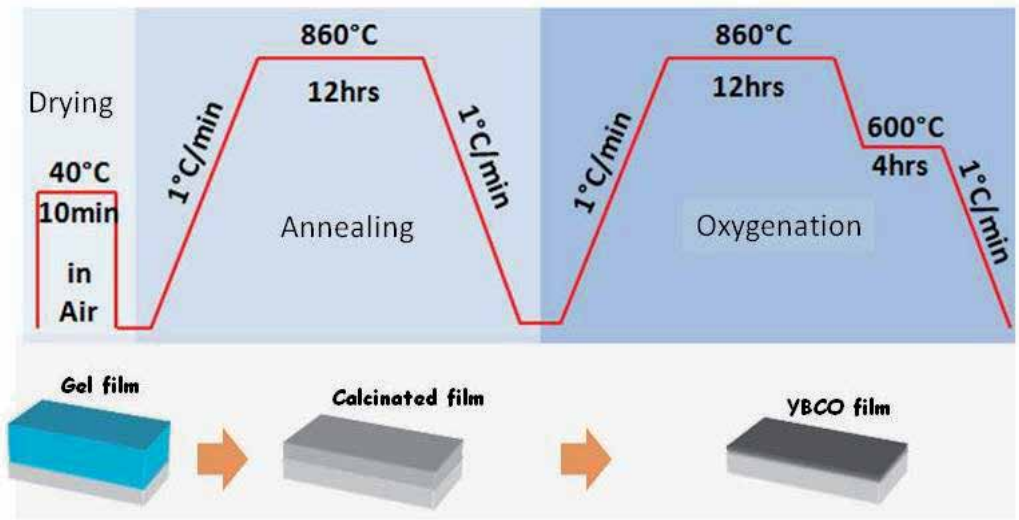

Figure 2. Schematic representation of the ex-situ heat treatments performed on CSD YBCO films. Initially the samples were dried at 40 °C for 10 min. Then they were annealed at 860 °C in oxygen flow for 12h. The slow heating rate (1 °C/min) released volatile hydrocarbons. Epitaxial growth of the crystallites occurs together with a considerably decrease of the thickness of the film. At this stage the sample consists on $YBa_2Cu_3O_x$ (with unknown x value). The sintering of the YBCO superconducting film is obtained after oxygenating the sample at 860 ℃.

6. Surface morphology

Figure 3 shows the surface morphology of the YBCO films on $LaAlO_3$, $SrTiO_3$ and YSZ substrates obtained by the oxalate CSD route and after oxygenation at three different temperatures: 820 840 and 860 °C. The results reveal that all the samples consist on granular films. In the case of the sample deposited on $LaAlO_3$ the YBCO grains are uniformly dispersed over the substrate surface, forming small groups. Previous results report that the average grain size formed is smaller than 100 nm [47]. In the case of the sample deposited on $SrTiO_3$, continuous films are clearly distinguished independently of the oxygenation temperature. However for the sample annealed at 820 °C, bright spots are spread on the surfaces. The light in the microscope might reflect in different directions when it is incident to some clusters or grains spread on the surface of the sample. Note also the formation of wide cracks (~ 5 μm) on the surface of the samples revealing parts of the underneath substrate. These cracks, which are typical for ceramic films under stress, together with some fringes formed on the surfaces (especially in the case of 860 °C annealing) suggest that the YBCO films strain during quench-

ing. The samples deposited on the YSZ substrates also present some cracks indicating stress during the quenching. However, the granular nature of the films is more pronounced than in the previous cases. On this substrate, the accumulation of grains is better appreciated in the film treated at 820 °C, whereas the surface softens at higher temperatures as it is clearly observed on the sample treated at 860 °C revealing the occurrence of melting. Furthermore, on all the samples, macro-segregation, leading to the formation of secondary phases and degradation of the epitaxy might occur as it is studied in more detail by XRD below.

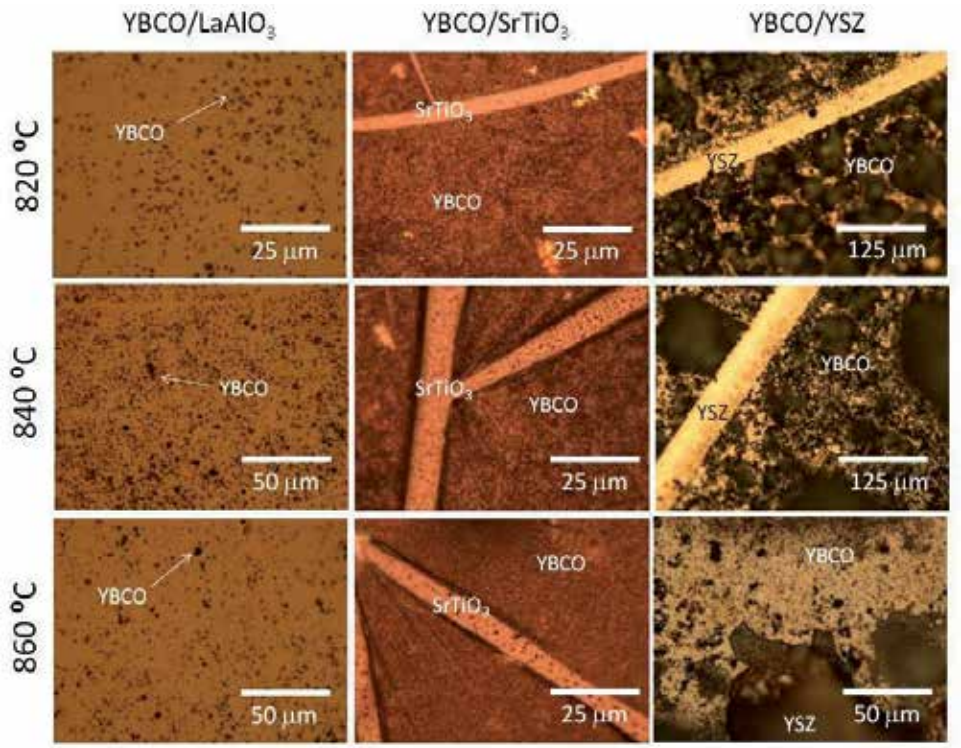

Figure 3. Optical microscopy images of the YBCO films obtained by the oxalate CSD route on $LaAlO_3$, $SrTiO_3$ and YSZ substrates after oxygenation at three different temperatures: 820, 840 and 860 °C. All the samples consist of granular films.

7. Crystallization

$YBaCu_3O_7$ films can grow in three different orientations: a) random, b) along the *a-b* plane and c) along the *c*-axis. In the case of YBCO films grown by the CSD technique, highly-randomly-oriented crystallites result if the fabrication has been performed without systematic control of the viscosity, homogeneity, cations ratio, etc during sol-gel and temperature, oxygen pressure, water pressure, etc during heat treatments. Fig. 4 depicts a representation of the crystallites in

http://dx.doi.org/10.5772/59359

an YBCO film oriented along the *a*-*b* plane and along the *c*-axis. For technological applications, a *c*-axis orientation growth of the YBCO film is preferable.

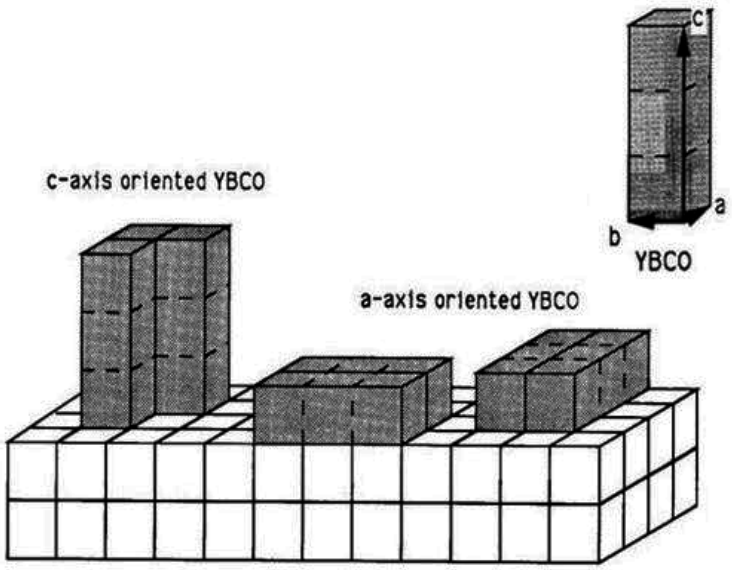

Figure 4. Schematic representation of the crystallites in an YBCO film oriented along the *a*-axis and along the *c*-axis.

The crystal orientation of YBCO thin films is commonly studied by X-ray diffraction. Fig. 5 shows the 4 representative angles (θ−2θ, ω, ϕ and Ψ) of the goniometer in a diffractometer. In the θ−2θ scans, by varying the angle of incidence θ, a diffraction pattern is recorded. The position and the intensity of the peaks are used for identifying the phase formation through their respective characteristic reflections. The ω scans are taken to check for a preferential film orientation normal to the substrate plane. In that case a strong peak from the θ−2θ scan is chosen, the detector is set and fixed to the corresponding value of the 2θ angle, as it is discussed in the next section. In this work, the crystallization of the films is studied by both, θ−2θ and ω scans. In a Bragg-Brentano geometry [54], YBCO films containing randomly oriented crystallites are identified by strong (103) reflections. Whereas YBCO films containing *a*-*b* and *c* oriented crystallites are recognized by high (005) and (200) reflections, respectively.

Figure 6 shows the X-ray diffractograms XRD, in semi-logarithmical scale, of the films grown on the three different substrates ($LaAlO_3$, $SrTiO_3$ and YSZ) obtained after annealing at 820, 840 and 860 °C. In all the cases, the strongest reflections are those (*h*00) corresponding to the substrate: (100), (200) and (300). Regarding the diffractions corresponding to YBCO, all the diffractograms present (00 ℓ) reflections: (002), (003), (00,4), (005), (006), and (007) indicating epitaxial growth of the film in the *c*-direction. Note that comparing to the samples annealed at 820 and 840 °C, the samples annealed at 860 °C present the highest (00 ℓ) reflections. Moreover, some (0*k*0) reflections, such as (010) and (020) are also detected, especially in the

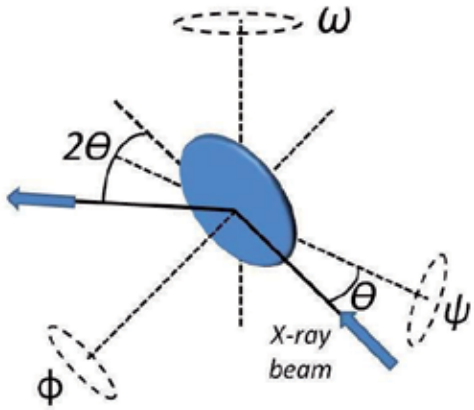

Figure 5. Four representative angles (θ–2θ, ω, ϕ and Ψ) of the goniometer in a typical diffractometer. In the θ–2θ scans, by varying the angle of incidence θ, a diffraction pattern is recorded. Whereas, the ω scans is performed over a strong peak from the θ–2θ scan. In this work, the crystallization of the films is studied by both, classical 2θ and ω scans.

diffractogram corresponding to the sample deposited on $LaAlO_3$, revealing that some crystallites grow in the *b*-direction.

On the other hand, since YBCO is a multi-cationic material, during the heat treatment at high temperatures the oxygen atoms can diffuse as they are weakly bounded to the structure, especially the oxygen atoms in the basal plane. Thus, in addition to the YBCO phase, other different stable phases can be formed according to the phase diagram. The stabilization in other structures depends on the number and arrangement of the vacant-sites of oxygen (tetrahedral or octahedral). Following the phase diagram of YBCO at 800 ℃ [55], these phases can be classified as: i) stable ($YBa_2Cu_3O_7$, $YBa_2Cu_4O_8$), ii) Secondary ($BaCuO_2$, $Y_2Cu_2O_5$, Y_2BaCuO_5, $BaCO_3$ etc), iii) unreacted (CuO, BaO, $BaCO_3$ and Y_2O_3) and iv) unstable ($BaCu_2O_2$, $Ba_2Cu_3O_{6-x}$). In the XRD presented in the figure, small reflections corresponding to the phases Y_2BaCuO_5 (Y211), Y_2O_3, $BaCuO_2$ and Cu_2BaO_2 were also detected. They are listed in Table 3. Note that in this work, no $BaCO_3$ has been detected on the XRD of the samples, indicating that the pyrolisis at 860 °C and slow rate (1 °C/min) is effective to prevent the formation of this unwanted phase. In contrast, reflections belonging to Y211 (also called 'green phase') were detected in the XRD for all the samples, suggesting that this phase might be formed during melting of the YBCO phase [56]. Y211 also acts as flux pinning centres improving the electrical and magnetic properties of the YBCO film [57]. Furthermore, the samples annealed at 820 °C present the majority amount of unreacted phases, indicating that this annealing temperature is not high enough to complete all the reaction. Besides, the less formation of secondary phases is obtained on the $LaAlO_3$ substrate while the sample containing more secondary phases is obtained on YSZ substrates. The latest suggests that as smaller is the mismatch in lattice constant to that of YBCO, there is better reaction between the coating components to form more pure YBCO. The presence of these unwanted phases affect the magnetic properties of the material, as we discuss in more detail below.

http://dx.doi.org/10.5772/59359

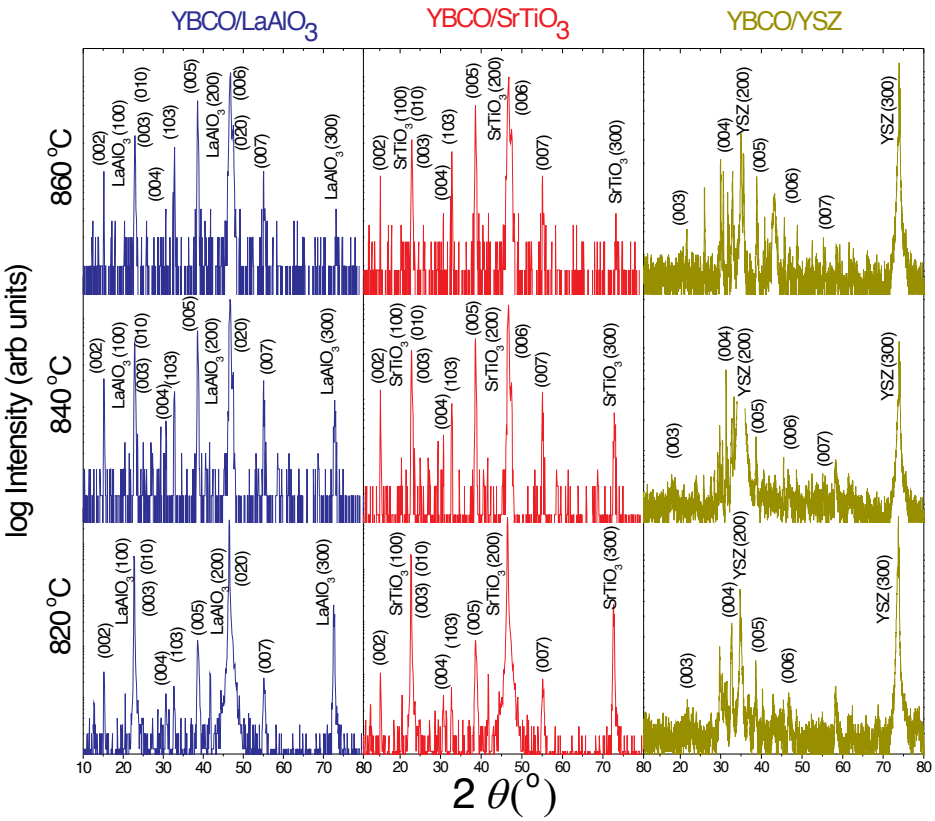

Figure 6. X ray diffractogram of YBCO films on $LaAlO_3$, $SrTiO_3$ and YSZ substrates obtained by the oxalate CSD route and annealing at 820, 840 and 860 °C. For all the cases, the strongest reflections are those (*h*00) corresponding to the respective substrates. The presence of the (00 ℓ) reflections corresponding to YBCO indicate crystallite growth in the *c*-direction. Some (0*k*0) reflections are also detected, especially in the diffractogram corresponding to the sample deposited on $LaAlO_3$, revealing that some crystallites grow in the *b*-direction.

For all the samples, the mean crystallite sizes and degree of epitaxy (f_c) for YBCO were calculated from the reflection (005) around 38.51°. The crystallite sizes were calculated with Scherrer's formula, neglecting peak broadening caused by residual stresses in the films [54]:

$$D = \frac{0.916\lambda}{\beta_{\mathrm{hkl}} \cos\theta_{hkl}} \tag{6}$$

where D is the average crystallite size, λ is the wavelength of the applied X-ray ($\lambda_{\mathrm{Cu\text{-}K\alpha 1}}$=0.154056 nm), θ_{hkl} is the Bragg's angle and β_{hkl} is the pure diffraction line broadening (in radians), which were easily found by measuring the full width at the half maximum (FWHM) of the reflection. The obtained values are listed in Table 3. Note that for all the samples, the crystallite size increases with temperature and the largest grains are obtained on the sample grown in YSZ substrates and annealed at 860 °C.

To calculate f_c, the (005) and (002) intensities ($I^{(005)}$ and $I^{(002)}$ respectively) were compared to those ones provided in the PDF-2 card 89-6049 ($I_{stand}^{(005)}$and $I_{stand}^{(002)}$ respectively) [58], following the relation:

$$\frac{I^{005}}{I^{200}} = \frac{f_c \cdot I_{stand}^{005}}{(1 - f_c) I_{stand}^{200}} \tag{7}$$

The f_c values are also listed in Table 3. Similar to the grain growth, f_c increases with annealing temperature, except for the samples grown on YSZ substrates. The highest f_c is also obtained on the sample grown on YSZ and annealed at 860 °C which is correlated with crystallite size and sharpest (005) reflections.

Overall, the increase of grain size and f_c values with annealing temperature observed in this work indicate that annealing promotes the epitaxial growth of the crystals orientated to (005) thus improving the crystallization of the CSD YBCO films, specially at higher temperatures.

Substrate	Annealing Temperature (°C)	Secondary Phases	Crystallite size (nm)	f_c
$LaAlO_3$	820	Y211, Y_2O_3, $BaCuO_2$,	25	0.60
	840	Y211, Y_2O_3	32	0.74
	860	Y211	33	0.88
$SrTiO_3$	820	Y211, Y_2O_3, $BaCuO_2$, Cu_2BaO_2	25	0.02
	840	Y211, Y_2O_3, $BaCuO_2$, Cu_2BaO_2	30	0.61
	860	Y211	35	0.64
YSZ	820	Y211, Y_2O_3, CuO, $BaCuO_2$	34	0.90
	840	Y211, Y_2O_3, CuO, $BaCuO_2$	36	0.86
	860	Y211, Y_2O_3, $BaCuO_2$	56	0.91

Table 3. Secondary phases, grain size and f_c values obtained from the (005) reflections from XRD of YBCO films grown in $LaAlO_3$, $SrTiO_3$ and YSZ substrates by CSD and annealing.

8. Texture

As mentioned in the previous section, X-ray diffraction can also provide qualitative information about the texture of the YBCO films. Figure 7 shows a schematic representation of inclined crystallites and their correspondent identification by ω-scans. The inclination (Fig. 7 (a)) is related to the out-of-plane deviation of the crystallites and it is also called out-of-plane texture (along the *z* axis). The ω− scans, also called rocking curves (Fig. 7 (b)), are obtained by scanning the ω angle as indicated in Fig. 5 above and the degree of out-of-plane texture is then deter-

http://dx.doi.org/10.5772/59359

mined by the FWHM value of the profile. If the rocking curve is the superposition of more than one profile, the components indicate different internal layers.

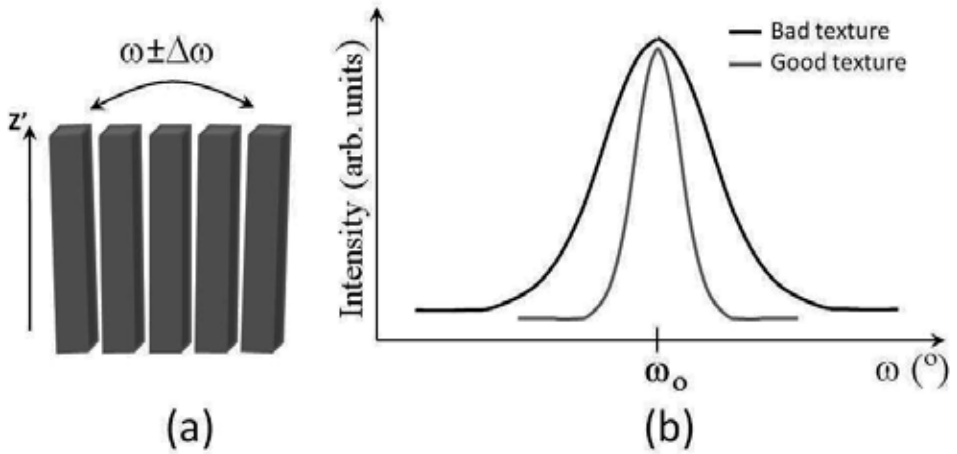

Figure 7. Schematic representation of: a) inclined crystallites and b) the correspondent identification by ω-scans by XRD.

Figure 8 shows the rocking curves corresponding to the (005) reflection of the YBCO films obtained by the oxalate CSD route on $LaAlO_3$, $SrTiO_3$ and YSZ substrates and after oxygenation at 860 °C. This reflection was chosen because its intensity is higher than the other (00ℓ) reflections and also because its position in the XRD plot (around 2θ=38.72°) is far away from any other reflection (see Fig 6). As mentioned above, the values of the FWHM ($\Delta\omega$) of the rocking curves represent the degree of inclination of the crystallites with respect to the normal of the plane substrate. The rocking curves corresponding to the sample deposited on $LaAlO_3$ can be fitted with two Gaussian functions, while the samples deposited on $SrTiO_3$ and YSZ can be fitted up to three Gaussian functions respectively. Each Gaussian function provide different $\Delta\omega$ values meaning that the films consist on multilayers of YBCO of different texture. The $\Delta\omega$ values are listed in Table 4. Since the texture of the films is strongly influenced by the substrate, the smaller $\Delta\omega$ values in each sample should correspond to layers close to the YBCO/substrate interface, whereas high $\Delta\omega$ values represent textures of layers close to the film surface. Note that the sample deposited on $LaAlO_3$ present only two layers with different texture although the inner layer presents the poorest texture (with $\Delta\omega$=0.45°) compared to those from the other samples. Despite the YBCO film deposited on $SrTiO_3$ contains three layers with different texture, the inner layer presents a better texture ($\Delta\omega$=0.35°) than the other samples. On the other hand, the relative high lattice mismatch between YBCO and YSZ (see Table 2) was expected to influence the texture of the deposited YBCO. In fact, the intermediate and outter-layers composing it are highly distorted ($\Delta\omega$=6° and 9° respectively) although the texture of the deepest layer is similar to the other samples. The effect of increasing $\Delta\omega$ from bottom to top layers is characteristic of films increasing in thickness, once a critical or threshold thickness is exceeded, the out-of-plane texture becomes negative.

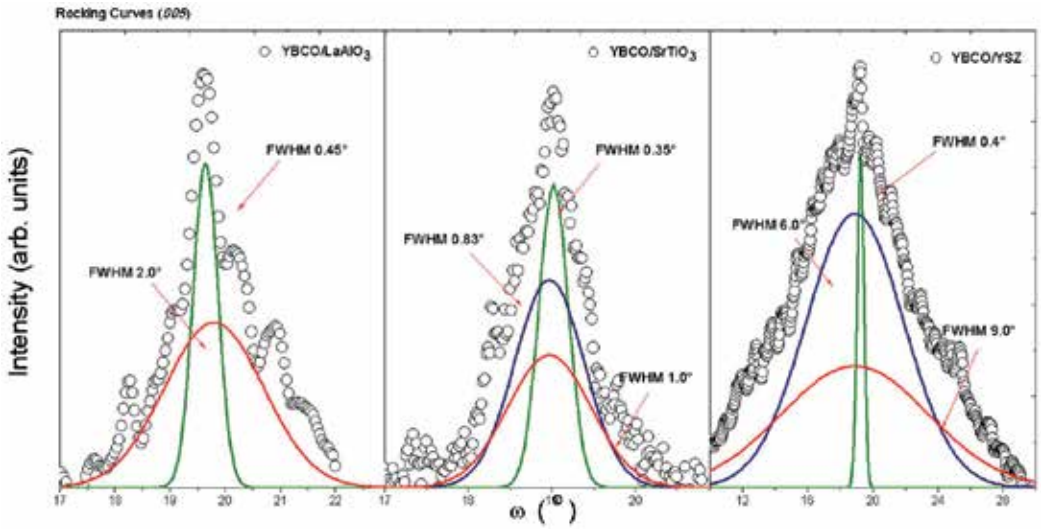

Figure 8. Rocking curves corresponding to the (005) reflection of the YBCO films obtained by CSD on $LaAlO_3$, $SrTiO_3$ and YSZ substrates, after oxygenation at 860 °C. The rocking curves corresponding to the sample deposited on $LaAlO_3$ can be fitted with two Gaussian functions, while the samples deposited on $SrTiO_3$ and YSZ can be fitted up to three Gaussian functions respectively. Each Gaussian function provides a different $\Delta\omega$ value which is listed in Table 4.

Position	$LaAlO_3$	$SrTiO_3$	YSZ
Close to the film/substrate interface	0.45°	0.35°	0.4°
Intermediate layer	-	0.83°	6.0°
Close to the surface	2.0°	1.0°	9.0°

Table 4. Full width at the half maximums (FWHM, $\Delta\omega$) of the rocking curves corresponding to the reflection (005) for YBCO films obtained by the oxalate CSD route on $LaAlO_3$, $SrTiO_3$ and YSZ substrates and after oxygenation at 860 °C.

9. Superconductivity

Figure 9 shows the magnetic moment vs. temperature of the YBCO films on $LaAlO_3$, $SrTiO_3$ and YSZ substrates obtained by the oxalate CSD route and oxygenation at 860 °C. The plots show the measurements taken in zero field cooling (ZFC) and field cooling (FC) modes for external magnetic field applied parallel to the film plane of 100 mT for films deposited on $LaAlO_3$ and $SrTiO_3$ and 50 mT for that deposited on YSZ. The superconducting property of the obtained films is demonstrated by the diamagnetic signals below the transition temperature T_C=90 K, thus confirming the formation of the superconducting YBCO. Note that the sample deposited on YSZ shows an up turn in the diamagnetic signal at low temperature, which can be attributed to other phases which are present in the sample. In fact, according to Table 3, this sample contains more secondary and unreacted phases than the other samples oxygenated at

http://dx.doi.org/10.5772/59359

860 °C. Therefore, the diamagnetic behaviour of the YBCO superconductor is screened by the paramagnetic response of those unwanted phases. The latest is better distinguished at the lowest temperatures in which the paramagnetic response tends to rise both, the ZFC and FC, branches to positive values of the magnetic moment.

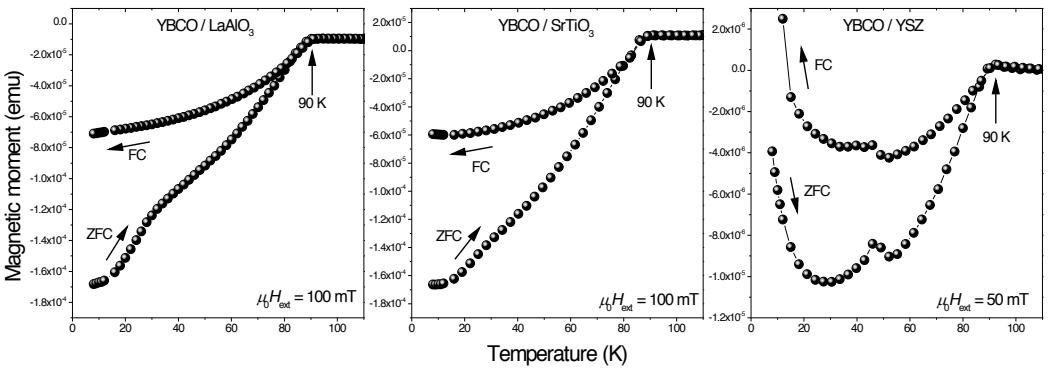

Figure 9. Magnetic moment vs. temperature of YBCO films on $LaAlO_3$, $SrTiO_3$ and YSZ substrates obtained by oxalate CSD and oxygenation at 860 °C. The magnetic measurements were taken in zero field cooling (ZFC) and field cooling (FC) modes. The superconducting property is demonstrated by the diamagnetic signals below the transition temperature 90 K. The samples deposited on $LaAlO_3$ and $SrTiO_3$ were measured under $\mu_0 H_{ext}$=100 mT while the sample deposited on YSZ was measured under $\mu_0 H_{ext}$=50 mT.

10. Conclusions

$YBa_2Cu_3O_7$ films were successfully deposited on $LaAlO_3$, $SrTiO_3$ and YSZ by the oxalate CSD route and heat treatments at 820, 840 and 860 °C. The preparation of the precursor solution does not require trifluoroacetates components. The obtained samples consist of granular YBCO films. X-ray diffraction reveals that all the samples contain crystallites oriented to (00 ℓ) indicating epitaxial growth of the film in the *c*-direction. Remarkably, similar to the trifluoroacetates CSD route, the oxalate route presented here does not form $BaCO_3$. However, small amounts of other phases, such as Y_2BaCuO_5 (Y211), Y_2O_3, $BaCuO_2$ and Cu_2BaO_2, were formed. The grain size and the degree of crystallinity values increase with annealing temperature leading in more epitaxial and pure YBCO films. Thus, the samples oxygenated at 860 °C present less unreacted and secondary phases, and higher (00 ℓ) reflections than the sample oxygenated at 820 and 840 °C. Rocking curves corresponding to the (005) reflection of these films can be fitted with more than one Gaussian functions meaning that they consist on multilayers of YBCO with different texture. Moreover, the relative high lattice mismatch between YBCO and YSZ was reflected in the texture of the corresponding grown YBCO layer. The superconducting property of the obtained films is demonstrated by their corresponding magnetic measurements confirming the formation of the superconducting YBCO with T_C=90 K. However, for the case of the sample deposited on YSZ its corresponding diamagnetic signal is distorted by the paramagnetic responses of the unwanted phases within this sample.

Acknowledgements

This work has been supported by the Con-Con program of the National University of San Marcos, Peru (Funding No. 121301041). The work in Cambridge was supported by the Engineering and Physical Science Research Council (EPSRC-RG63021). The work in Brazil has been supported by CNPq (307552/2012-8), CAPES (PNPD-230.007518/2011-11) and FACEPE (APQ-0589-1.05/08).

Author details

Luis De Los Santos Valladares[1*], Juan Carlos González[2], Angel Bustamante Domínguez[2], Ana Maria Osorio Anaya[3], Henry Sanchez Cornejo[2], Stuart Holmes[1], J. Albino Aguiar[4,5] and Crispin H.W. Barnes[1]

*Address all correspondence to: luisitodv@yahoo.es

1 Cavendish Laboratory, Department of Physics, University of Cambridge, J.J. Thomson Ave., Cambridge, United Kingdom.

2 Laboratorio de Cerámicos y Nanomateriales, Facultad de Ciencias Físicas, Universidad Nacional Mayor de San Marcos, Lima, Peru

3 Facultad de Química e Ingeniería Química, Universidad Nacional Mayor de San Marcos, Ciudad Universitaria, Lima, Peru

4 Departamento de Física, Universidade Federal de Pernambuco, Recife, Brazil

5 Programa de Pós-Graduação em Ciência de Materiais, Centro de Ciências Exatas e da Natureza, Universidade Federal de Pernambuco, Recife, Brazil

References

[1] G. Desgardin, I. Monot y B. Raveau, Supercond. Sci. Technol. 12 (1999) R115.

[2] E. K. Hollmannt, O. G. Vendik, A. G. Zaitsev y B.T. Melekh, Supercond. Sci. Technol. 7 (1994) 609.

[3] J. L. Mayo, Superconductivity: The Threshold of a New Technology, TAB Books, Inc., Blue Ridge Summit, Pasadena (1989).

[4] W. A. Harrison, Phys. Rev. B 38 (1988) 270.

[5] C. Poole, H.A. Farach, R.J. Creswick, R. Prozorov, Superconductivity, 2nd ed., Academic Pres, The Netherlands 2007.

[6] High performance YBCO-coated superconductors wires, MRS Bulletin 29 No 8 (2004).

[7] S. U. K. Nair, P. R. S. Warriary J. Koshy; Bull. Mater. Sci. 25, (2002) 95.

[8] D. P. Norton; Annu. Rev. Matter. Sci. 28, 299 (1998).

[9] R. Wondenweber, Supercond. Sci. Technol. 12 (1998).

[10] T. Manabe, I. Yamaguchi, S. Nakamura, W. Kondo, T. Kumagai, S. Mizuta, J. Mat. Res. 10 (1995) 1635-1643.

[11] J.A. Smith, M.J. Cima, N. Sonnenberg, IEEE Trans. Appl. Supercond. 9 (1999)1531-1534.

[12] K. Yamagiwa, T. Araki, Y. Takahashi, H. Hier, S.B. Kim, K. Matsumoto, J. Shibata, T. Hirayama, H. Ikuta, U. Mizutani, I. Hirabayashi, J. Crystal Growth 229 (2001) 353-357.

[13] T. Araki, I. Hirabayashi, Supercond. Sci. Techn. 16 (2003) R71-R94.

[14] K. Yamagiwa, T. Araki, Y. Takahashi, H. Hiei, S. B. Kim, K. Matsumoto, J. Shibata, T. Hirayama, H. Ikuta, U. Mizutani, I. Hirabayashi; J. Cryst. Growth 229, 353 (2001).

[15] O. Castano, A. Cavallaro, A. Palau, J. C. Gonzalez, M. Rossell, T. Puig, F. Sandiumenge, N. Mestres, S. Pinol, A. Pomar, X. Obradors; Supercond. Sci. Technol. 16, 45-53 (2003).

[16] R.W. Schwartz, Chem. Mater, 9 (1997) 2325-2340.

[17] W. Cui, J.L. Tanner, T.W. Button, J. Phys.: Conf. Series, 97 (2008) 012257.

[18] K. Knoth, S. Egel, C. Apettri, M. Falter, B. Schlobach, R. Huhne, S. Oswald, L. Schultz, B. Holzapfel, Current Op. Sold. Stat. Mat. Sci., 10 (2006) 205-216.

[19] A. Sheth, K. Trembath, J. Mat. Process. Tech., 123 (2002) 167-178.

[20] M.E. Gross, M. Hong, S.H. Liou, P.K. Gallagher, J. Kwo, Appl. Phys. Lett. 52 (1988) 160-162.

[21] M.L. Kullberg, M.T. Lanagan, W. Wu, R.B. Poeppel, Supercond. Sci. Technol. 4 (1989) 337-342.

[22] Y.L. Chen, J.V. Mantese, A.H. Hamdi, A.L. Mecheli, J. Mater. REs. 4 (1989) 1065-1070.

[23] K. Yamagiwa, H. Hiei, Y. Takahashi, S.B. Kim, K. Matsumoto, H. Ikuta, U. Mizutani, I. Hirabayashi, Physica C 334 (2000) 301-305.

[24] P.C. McIntyre, M.J. Cima, J.A. Smith, R.B. Hallock, M.P. Siegal, J.M. Phillips, J. Appl. Phys. 71 (1992) 1868-1877.

[25] P.C. McIntyre, M.J Cima, A. Roshko, J. Appl. Phys. 77 (1995) 5263-5272; S. Sathyamurthy, K. Salama, Physica C 329 (2000) 58-68.

[26] A. Malozemoff, S. Annavarapu, L. Fritzmeier, Q. Li, V. Prunier, M. Rupich, C. Thieme, W. Zhang, A. Goyal, M. Paranthaman, D.F. Lee, Supercond. Sci. Technol. 13 (2000) 473-476.

[27] A. Gupta, R. Jagannathan, E.I. Cooper, E.A. Giess, J.I. Landman, B.W. Hussey, Appl. Phys. Lett. 52 (1988) 2077-2079.

[28] P.C. McIntyre, M.J. Cima, J.A. Smith, R.B. Hallock, M.P. Siegal, J.M. Phillips, J. Appl. Phys., 71 (1992) 1868-1877.

[29] X.M. Cui, B.W. Tao, Z. Tian, J. Xiong, X.Z. Liu, Y.R. Li, Supercond. Sci. Technol. 19 (2006) L13-L15.

[30] S. Wang, L. Wang, B. Gu, J. Mater. Sci. Technol. 24 (2008) 899-902.

[31] X. Tang, Development of a fluorine-free chemical solution deposition route for rare-earth cuprate superconducting tapes and its application to reel-to-reel processing, PhD Thesis, Technical University of Denmark, Denmark, 2013.

[32] I.H. Mutlu, H. Acun, E. Celick, H. Turkmen, Physica C 451 (2007) 98-106.

[33] K.S. Mazdiyashi, C.T. Lynch, J.S. Smith, Inorg. Chem., 5 (1996) 342-346.

[34] B. Zhao, H.B. Yao, K. Shi, Z.H. Han, Y.L. Xu, D.L. Shi, Physica C 386 (2003) 348-352.

[35] J. Lian, H. Yao, D. Shi, L. Wang, Y. Xu, Q. Liu, Z. Han, Supercond. Sci. Technol. 16 (2003) 838-844.

[36] S. Shi, Y. Xu, H. Yao, Z. Han, J. Lian, L. Wang, A. Li, H.K. Liu, S.X. Dou, Supercond. Sci. Tech. 17 (2004) 1420-1425.

[37] Q.X. Jia, T.M. McCleskey, A.K. Burrell, Y. Lin, G.E. Collis, H. Wang, A.DQ. Li, S.R. Foltyn, Nature Matt. 3 (2004) 529.

[38] T. Manabe, I. Yamaguchi, H. Obara, S. Kosaka, H. Yamasaki, M. Sohma, T. Tsuchiya, S. Mizuta, T. Kumagai, Physica C 378-381 (2002) 1017-1023.

[39] D. Shi, Y. Xu, S.X. Wang, J. Lian, L.M. Wang, S.M. Mc Clellan, R. Buchanan, K.C. Goretta, Physica C 371 (2002) 97-103

[40] A.H. Li, M. Ionescu, H.K. Liu, D.L. Shi, X.L. Wang, X. Peng, E.W. Collings, Physica C 426-431 (2005) 1408-1414.

[41] H. Yao, B. Zhao, K. Shi, Z. Han, Y. Xu, D. Shi, S. Wang, L.M. Wang, C. Peroz, C. Villard, Physica C 392-396 (2003) 941-945.

[42] L. Lei, G.Y. Zhao, J.J. Zhao, H. Xu, IEEE Trans. Appl. Supercond. 20 (2010) 2286-2293.

[43] C. Apetrii, H. Schlorb, M. Falter, I. Lampe, L. Schultz, B. Holzapfel, IEEE Trans. Appl. Supercond. 15 (2005) 2642-2644.

[44] A. Bustamante Domínguez, A. M. Osorio, L. De Los Santos Valladares, H. Carhuancho, J.C. González, G.R.C. Cernicchiario, J.A. Feijoo Lévano, Advances in Science and Technology 47 (2006) 37-42.

[45] H.E. Sanchez, A. Bustamante Domínguez, A. Osorio Anaya, L. De Los Santos Valladares, J. Albino Aguiar, C.H.W. Barnes, J. Chem. Chem. Eng. 8 (2014) 547-511.

[46] A. Bustamante Domínguez, A.M. Osorio, L. De los Santos Valladares, J. Garcia, J.C. González, C.H.W. Barnes, Y. Azuma, Y. Majima, J. Albino Aguiar, J. Phys.: Conf. Ser. 507 (2014) 01005.

[47] A. Bustamante Domínguez, L. León Felix, J. Garcia, J. Flores Santibañez, L. De Los Santos Valladares, J.C. González, A. Osorio Anaya, M. Pillaca, Phys. Proc. 36 (2012) 526-531.

[48] J. García, A. Bustamante Domínguez, L. De Los Santos Valladares, J.C. González, L. León Felix, J. Flores Santibañez, A. Osorio Anaya, J. Albino Aguiar, Rev. Inv. Fis. 15 (2012) 121502102 (in Spanish).

[49] J.C. González, A. Osorio, A. Bustamante, Rev. Soc. Quim. Peru 77 (2011) 249 (in Spanish).

[50] J. Jorgensen, M. Beno, D. Hinks, L. Sodeholm, K. Volin, C. Segre, K. Zhang, M. Kleefisch, Phys. Rev. B 36 (1987) 3608.

[51] Z. Aslanoglu, Y. Akin, M.I. El-Kawni, W. Sigmund, Y.S. Hascicek, Physica C 384 (2003) 501-506.

[52] A. Bustamante Domínguez, L. De Los Santos Valladares, J. Flores Santibañez, R. Lozano, J. Palomino, G.R.C. Cernicchiario, Rev. Inv. Fis. 7 (2004) 30-33.

[53] J.C. González, L. De Los Santos Valladares, A.M. Osorio Anaya, J. Albino Aguiar, A. Bustamante Domínguez, Rev. Inv. Fis. 15 (2012) 121501104 (in Spanish).

[54] B. D. Cullity, Elements of X-ray Diffraction (Addison-Wesley Publishing Company, Inc. USA, 1956), pp.96-102.

[55] E. Brosha, F. Garzon, I. Raistrick, P. Davies, J. Am. Ceram. Soc. 78 (1995) 1745.

[56] M. Llosa, L. de los Santos Valladares, N. de la Cruz Centeno, A. Bustamante Domínguez, Rev. Inv. Fis. 7 (2004) 34-37 (in Spanish).

[57] F. Frangi, T. Higuchi, M. Deguchi, M. Murakmi, J. Matter. Res. 10 (1995) 2241-2250.

[58] Powder Diffraction Files PDF-2 of The International Centre for Diffraction Data® (ICDD®)-2001.

Chapter 4

Gap Structures of A-15 Alloys from the Superconducting and Normal-State Break-Junction Tunnelling

Toshikazu Ekino, Alexander M. Gabovich,
Akira Sugimoto, Yuta Sakai and Jun Akimitsu

Additional information is available at the end of the chapter

http://dx.doi.org/10.5772/59338

Introduction

A well-known A-15 compound Nb_3Sn was investigated by the break-junction tunnelling technique with high superconducting critical temperature $T_c \approx 18$ K. Relevant energy-gap values were measured at $T = 4.2$ K and these manifested as conductance peaks at bias voltages $2\Delta/e = 4$–6 mV. Here, T is temperature and $e > 0$ is the elementary charge. In addition to superconductivity-driven gap structures, reproducible humps were also detected at biases ±20–30 mV and ±50–60 mV for $T = 4.2$ K. Such hump features, complementary to coherent peaks at the superconducting-gap edges, apparently resemble the pseudo-gap manifestations inherent to high-T_c superconductors. These humps remain the only gap-related features above T_c. Possible origins of these structures are discussed with emphasis on the charge–density–wave (CDW) formation. CDWs are accompanied by periodic lattice distortions and are related to the structural phase transition discovered decades ago in Nb_3Sn. The current-voltage characteristics exhibit asymmetries, being probably a consequence of normal-metal junction shores or due to the vanishing symmetry of the junction conductance when CDWs are present in both electrodes.

PACS numbers: 74.55.+v, 74.70.Ad, 71.20.-b, 74.81.Fa, 81.30.Kf

Materials with A-15 (β-tungsten) crystal structure [1, 2] possessed the highest superconducting critical temperatures, T_c, over a long period of time until Cu-based superconducting ceramic oxides were discovered [3]. The compound Nb_3Sn is a representative material with $T_c \approx 18$ K among those inter-metallic alloy compounds and possesses stable metallurgical characteristics [1, 2]. Therefore, Nb_3Sn and some other older and newer materials, such as MgB_2 and Fe-based superconductors, are competitive with cuprates in technological applications of superconductivity [4–11].

INTECH
open science | open minds

© 2015 The Author(s). Licensee InTech. This chapter is distributed under the terms of the Creative Commons Attribution License (http://creativecommons.org/licenses/by/3.0), which permits unrestricted use, distribution, and reproduction in any medium, provided the original work is properly cited.

The crystal structure of Nb_3Sn (as well as of its A-15 relatives) is not a layered one as that of the copper-oxide or Fe-based high T_c superconductors. Instead, it includes orthogonal linear chains of Nb atoms along each principal cube axis direction [1, 2] (see Figure1). This quasi-one-dimensional feature served as a guide for the Labbe–Friedel model, which predicted structural anomalies driven by peculiarities of the normal-state electron density of states, $N(E)$, near the Fermi level (a cooperative Jahn–Teller effect). More involved Gor'kov model, taking into account *inter alia* the inter-chain correlations, also leads to the $N(E)$ singularity and a Peierls phase transition. Whatever the theoretical details, the primordial (high-temperature, high-T) electron spectrum in Nb_3Sn is unstable towards low-T phase transformation [12].

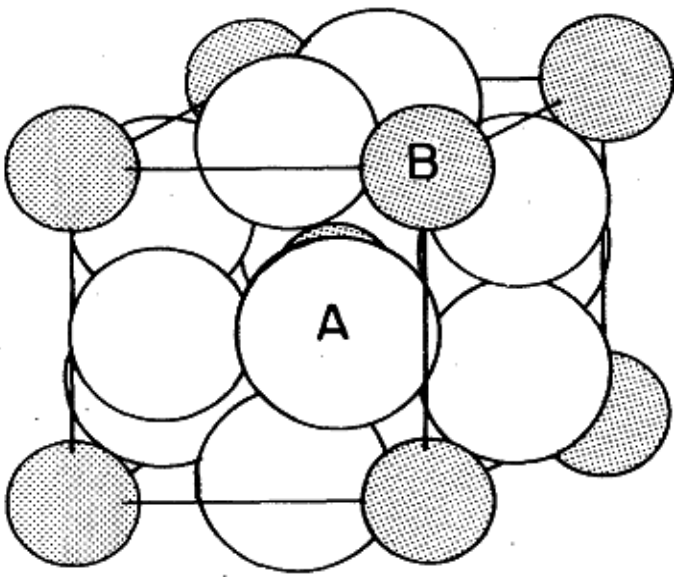

Figure 1. The A-15 crystal structure for the compound formula A_3B. In our case, A stands for Nb whereas B stands for Sn (taken from Ref. [1]).

In fact, A-15 cubic compounds, including Nb_3Sn, are well known to undergo tetragonal distortion below a certain temperature T_m, being higher than T_c. Hence, some part of the Fermi surface is gapped by CDWs, which is detrimental to superconductivity, because of the reduced electron density of states, which to a large extent determines T_c. The interplay between periodic lattice distortions accompanied by CDWs in the electron subsystem, on the one hand, and superconductivity, on the other hand, was intensively studied both experimentally and theoretically and applied to Nb_3Sn as a particular case [1, 2, 12–15].

The contest between superconducting and CDW (dielectric) order parameters should inevitably lead to a superposition of the corresponding energy gaps in the overall electron spectrum modified by both Cooper and electron–hole pairings. Any experimental technique measuring the gapped electron density of states below T_c or the convolution with its counterpart (if any) should be sensitive to the interplay between phenomena discussed above [15–17]. A typical

http://dx.doi.org/10.5772/59338

example of such a method is electronic quasi-particle tunnelling spectroscopy. Moreover, if multiple gaps of the same nature (usually, those are recognized as superconducting gaps) are inherent to the reconstructed electron spectrum or multiple gaps are generated by some kind of proximity effect, they would influence the tunnel conductance together [18–20]. Multiple superconducting gapping in Nb_3Sn was also suggested on the basis of heat capacity [21, 22] and point-contact conductivity [23] measurements. On the contrary, subsequent heat capacity studies were considered as manifestations of a single superconducting gap [24].

The origin of superconductivity and the gapping features in A-15 compounds have been explored by various methods. Namely, fabrication of corresponding tunnel junctions and electron tunnelling spectroscopic measurements were intensively carried out to probe the electron–phonon interaction in terms of the Fröhlich–Eliashberg function $\alpha^2F(\omega)$ and to extract the superconducting-gap values 2Δ [25–29]. Those junctions made for tunnelling spectroscopy purposes included artificial oxide barriers that might cause spurious features in the tunnelling spectra. On the other hand, pristine junctions of Nb_3Sn samples such as break junctions or cleaner direct contacts turned out to be of better quality so that the ambiguous influence of the barrier was avoided both in the tunnel [30] and point-contact [31] conductivity regimes. Those measurements revealed a single clear-cut superconducting gap and another feature at higher voltages most probably connected with the structural transition discussed above. In this chapter, tunnelling measurements of Nb_3Sn single crystals are presented using a break-junction technique that has been improved on the basis of previous work [30]. The experiments were carried out focusing on both the superconducting-gap characteristics and the electronic peculiarities of $N(E)$ emerging due to the structural (martensitic) transition intimately associated with CDWs. The latter could be due to the Peierls [1–3, 12] or excitonic (Coulomb) [32] transitions of the parent high-T state. In the mean-field approach, the coupled system of equations describing competing superconducting and electron–hole pairings is the same for any microscopic picture of the CDW pairing [13–15, 33]. Therefore, the consequences important for our subsequent analysis are similar for both kinds of electron–hole instabilities at this semi-phenomenological level, although one should bear in mind the necessity of the microscopic justification for any adopted model (see, e.g., electron band calculations [34, 35]). According to earlier findings in the point-contact measurements [31], we expected the manifestations of CDWs also in the quasi-particle conductance $G(V) = dI/dV$, where I denotes the quasi-particle tunnel current across the break junction. The quantity $G(V)$ in CDW superconductors is a complicated functional of the superconducting, Δ, and dielectric (CDW), Σ, energy gaps [15, 16, 33] being no more a simple convolution of the electron density of states as in the conventional Bardeen–Cooper–Schrieffer (BCS) model of superconductivity [36]. From the experimental point of view, tunnel conductances $G(V)$ distorted by CDW gapping are well known for a number of relevant materials [15, 16, 37, 38].

2. Experimental procedures

Nb_3Sn single crystal samples were grown by a standard vapour transport method. The temperature dependence of the electrical resistance for an Nb_3Sn crystal is shown in Figure 2.

It was measured using the break-junction configuration just before the breaking. To avoid any difficulty in forming a clean junction interface on the small surface area of the tiny crystalline piece, making such a break junction is the best method. A cryogenic fracture at 4.2 K of the crystal piece provides the crucial advantage of this technique. The fracture is performed by at first mounting the sample on the flexible substrate with four electrodes, subsequently stressed by an external bending force. Thus, a fresh and clean junction interface appears that can provide the undistorted gap features both for superconducting and semiconducting electron spectra including extremely surface-sensitive delicate compounds [38]. This junction design exhibits the symmetric superconductor–insulator–superconductor (SIS) geometry.

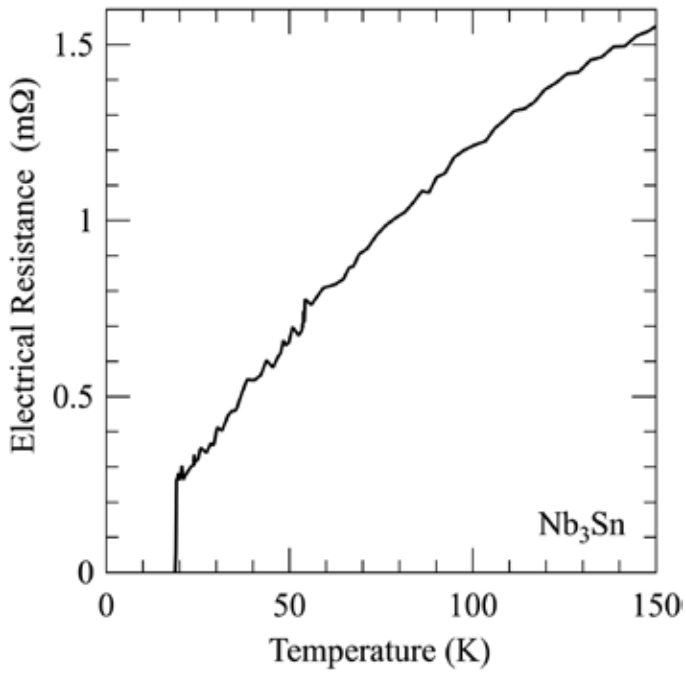

Figure 2. The temperature dependence of the electrical resistance, R (T), for Nb_3Sn used in the present break-junction measurements.

3. Results and discussion

The tunnelling conductance $G(V) = dI/dV(V)$ in the superconducting state at $T = 4.2$ K is shown in Figure 3 for several break junctions. The sharp and intensive gap-edge structure observed in Figure 3 (a) exhibits the *peak-to-peak* voltage interval $V_{p\text{-}p} \approx 8.6$ mV (corresponding to bias voltages $V_p \approx \pm 4.3$ mV) and very small zero-bias leakage. This is common to the *s*-wave BCS gap structure inherent to the SIS geometry of the break junction, for which $V_{p\text{-}p} = 4\Delta/e$. Here $e > 0$ is the elementary charge.

http://dx.doi.org/10.5772/59338

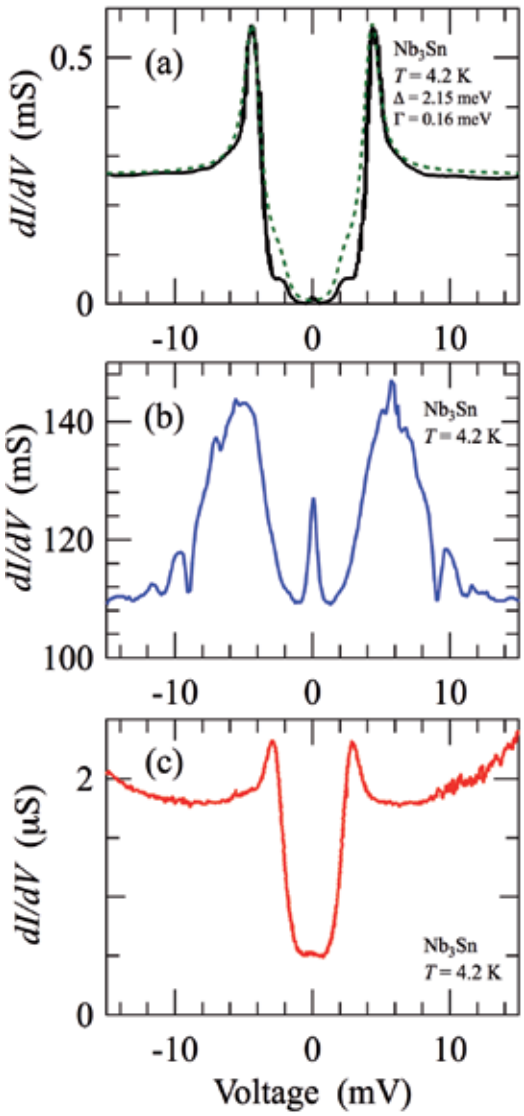

Figure 3. Conductance $G(V) = dI/dV$ obtained for different Nb_3Sn break junctions (a), (b) and (c). Tunnelling quasi-particle gap feature (a) is fitted with the broadened BCS density of states $N(E, \Gamma)$ (see the text). $G(V)$ of (b) is broadened showing much more conductance leakage as compared with (a). Substantial zero-bias leakage with asymmetric background conductance is seen in (c).

By employing the standard broadening in the quasi-particle density of states, $N(E,\Gamma) = |\mathrm{Re}\{(E-i\Gamma)/[\Delta^2-(E-i\Gamma)^2]^{1/2}\}|$, along with thermal smearing, the fitting procedure quantitatively reproduces the SIS spectral features. Here, Γ is a phenomenological broadening parameter [39]. Applying the fitting procedure, we emphasized on either the outer or the inner features of the gap structure. The resultant parameters Δ were similar in both cases, whereas Γ values describing the pair breaking caused by an identified reason varied conspicuously. The sub-

gap shoulders at ±2.3 mV in Figure 3 (a) correspond to ± Δ/e singularities as a result of the SIN admixture to $G(V)$. Here, N stands for the normal metal. In contrast to the SIS junction characteristics in Figure 3 (a), the gap peak in $G(V)$ of Figure 3 (b) is substantially broadened showing much more intensive conductance leakage as well as the high-bias conductance magnitude about 10^3 times larger than that for the junction of Figure 3 (a). The conductance leakage level reaches almost the normal-state high-bias value exhibiting also the Josephson or weak link peak at zero bias. This feature is no longer a standard tunnelling phenomenon appropriate to junctions with small transparencies [36]. Instead, the Andreev reflection at the interfaces should govern the current through the junction interface. At the same time, the wide conductance peaks at about ±5.5 mV corresponding to the values ±2Δ/e for an SIS junction do not differ much from their counterparts seen in Figure 3 (a). We rarely observed much smaller gap-peak energies. In fact, the shoulders at ±2.3 mV in Figure 3 (a) appear as the apparent but less enhanced gap-peak structures at the same bias positions in Figure 3 (c), where the substantial zero-bias leakage (~28% of the high-bias normal state) as well as the asymmetric conductance background above the gap voltages are evident. These features indicate that the tunnelling conductance of Figure 3 (c) is due to the accidental formation of an SIN junction corresponding to the peak positions of ±Δ/e, in which one side of the junction is a normal metal. Assuming the weak-coupling isotropic BCS gap to T_c ratio $2\Delta/k_BT_c \approx 3.5$, where k_B is Boltzmann constant, the observed gap values correspond to the local critical temperatures $T_c^* \approx 14.2$ K (a) and 18 K (b). The former value indicates the existence of the non-stoichiometric patch, nevertheless exhibiting almost textbook-coherent gap-edge peaks, while the latter value is close to the bulk T_c. The smaller gap value extracted from Figure 3 (a) and (c) most probably corresponds to the reported Sn-deficient phase [28], which is suggested to exist as a quite stable crystallographic phase of this compound. We note that in the present break-junction measurements, the observed maximum gap size shown in Figure 3 (b) demonstrates the almost BCS value, so that we could not find any apparent strong-coupling feature showing the typical ratios $2\Delta/k_BT_c \approx 4.3$–$4.4$ [10, 11, 28].

In Figure 4 (a), the conductance $G(V)$ is shown for two different break junctions at $T = 4.2$ K and bias voltages extended to higher regions of ±40 mV. The well-developed gap peaks, which are consistent with the results depicted in Figure 3 (a), are clearly seen. The intensive $G(V)$ peaks of the curve A are cut in order to magnify other important features. The reproducible appearance of the peaks at ±4.2–4.6 mV as is shown in Figure 4 (a) suggests that the cracking forming break junctions tends to occur along the defect phase of the crystal [28]. In curve A, outer peaks appear at values ≈ ±5.5 mV, which can be seen as shoulders in curve B. These features are consistent with the broad peaks corresponding to the bulk T_c as was discussed while describing Figure 3, thereby reflecting the inherent gap value of Nb_3Sn, although those coherent gap peaks are not very strong. The outer-bias peaks or shoulders in curves A or B appear when the zero-bias peak is present. Since zero-bias peaks are manifestations of the coherent Cooper-pair tunnelling and are not expected to appear in the distorted regions, the presence of this feature supports the idea that the break-junction interface is formed inside an optimal superconducting-phase patch of the inhomogeneous Nb-Sn composite displaying substantial gap distributions. Thus, multiple superconducting gaps are indeed observed in Nb_3Sn, being, however, a consequence of the spatial inhomogeneity and, probably, also certain

http://dx.doi.org/10.5772/59338

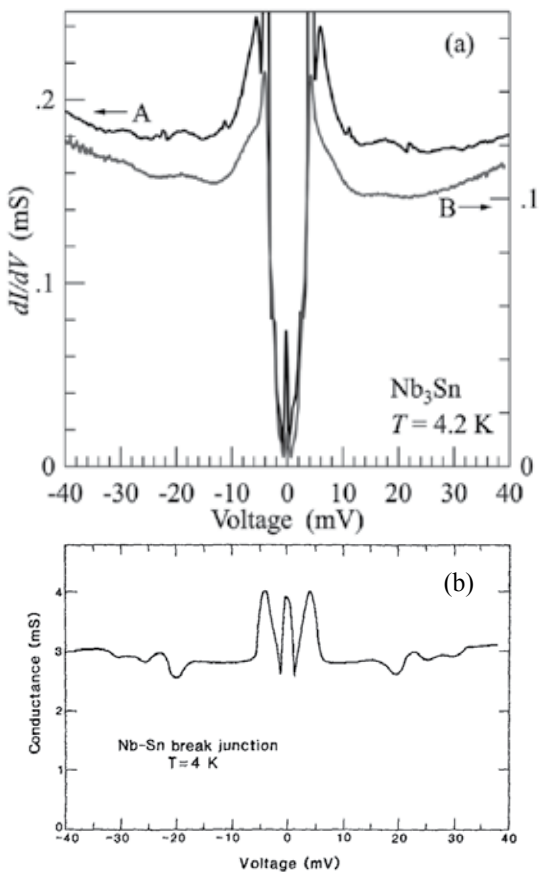

Figure 4. (a) $G(V)$ describing different Nb_3Sn break junctions. (b) The break-junction data of the superconducting Nb-Sn composite (taken from Ref. [30]).

proximity between different phases rather than features appropriate to a true two-gap superconductivity realized in the momentum-space [20].

In addition to the superconducting-gap structures at ≈ ±4.2–4.6 mV and ≈ ±5.5 mV, one can see the broad humps around ±20 mV as a third structure inherent to the curves A and B in Figure 4 (a). The hump bias positions and their ≈2–4% intensity increase against the background are similar for all curves represented. Such ±20 mV structures were also seen previously in Nb-Sn break junctions [30] and an example is shown for comparison in Figure 4 (b). In those data (Figure 6 of Ref. [30]), the peculiarities start at ±20 mV and extend up to biases of ±30 mV. Their subtle intensity could be associated with their possible origin as strong-coupling phonon features, phonons being the most probable Cooper-pair glue in Nb_3Sn. However, this explanation seems to be unlikely here because similar hump structures are observed together with the smaller ±4.3 mV superconducting-gap peaks, corresponding to the phase with a lower T_c, but in the absence of the larger ±5–6 mV ones, which are considered as the predominant gap features. Furthermore, although the strong-coupling feature of the electron–phonon interac-

tion should be concomitant with the ideal BCS-like gap structures, no such hump is observed along with the very distinct BCS gap structure of Figure 3 (a). On the other hand, it seems remarkable that the coexisting superconducting-gap and hump structures presented here are very similar to the tunnelling conductance patterns of the high-T_c copper-oxide superconductors observed at low T [16, 33], although the energy scales differ in both cases [27]. We note that a misleading interpretation of the outer structures as a strong-coupling effect was discussed earlier in the case of a 5*f*-electron superconductor [40].

We plot the temperature evolution of $G(V)$ in Figure 5 for a mechanically stable break-junction configuration. This is a representative selected among a number of trial measurements. The conductance $G(V)$ at each T, $G(V, T)$, is quite stable exhibiting almost no shift along the vertical $G(V)$ axis in the whole T range from 4.2 K to 20 K. It might be expected that thermal crystal lattice expansion would destroy the conventional smooth evolution with T of the $G(V)$ spectra, but in our case this possible disturbance is completely absent or cancels out. To be certain that this stability of spectra really takes place, we even sometimes measured $G(V)$ with the T-steps up to several tenths of Kelvin and no shift was noticed just the same. The microscopic origin of the observed mechanical stability still remains to be clarified, but it can be speculated that the exposed edges of the fractured crystal may accompany structural changes by possible surface reconstructions, which might serve as solid junction interfaces. In Figure 5, the well-defined gap-edge peaks clearly seen at $T = 6.4$ K are gradually suppressed and smeared when T increases and finally the sequence $G(V)$ tends to the curve of the shallow V-like shape at T about 17.4 K. This behaviour is quite common to the BCS superconductors.

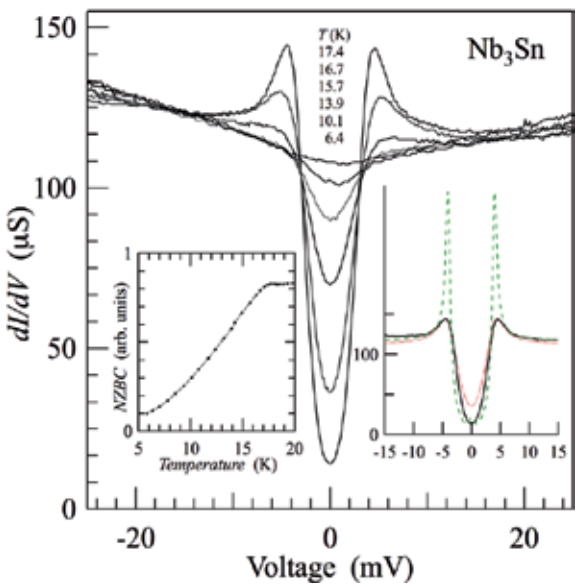

Figure 5. Temperature variations of $G(V)$ for an Nb_3Sn break junction. The left inset shows the temperature dependence of the normalized zero-bias conductance, $G(0)/G$ (±30 mV). The right inset shows the $G(V)$ fitting with $N(E, \Gamma)$ for the SIS junction (see the text).

http://dx.doi.org/10.5772/59338

To analyze the T-driven evolution of the gap characteristics more closely, we plot the T dependence of the fixed conductance at zero bias, $G(0, T)$, normalized by high-bias voltage value (V = 30 mV) in the left inset of Figure 5. It is noted that $G(0, T)$ changes drastically, while the conductance at 30 mV, $G(30\ \text{mV}, T)$, is kept almost constant. According to the BCS theory for isotropic superconductors, the quantity $G(0, T)$ is proportional to the thermally smeared convolution of two densities of states. Thus, $G(0, T)$ may serve as an estimate of the removed electronic states due to the superconducting-gap formation with decreasing T. For a typical SIS junction, however, the intensive Josephson peak and thermally excited states above and below the gap energy made it impossible to quantitatively measure the smooth $G(0, T)$. Nevertheless, in the left inset of Figure 5, the actual $G(0, T)$ can be of help to estimate the gap evolution because of the featureless zero-bias conductance similar to that for an SIN junction.

The critical temperature T_c of Nb_3Sn at the break-junction interface should be determined as ≈18 K from the behaviour of the zero-bias conductance $G(0, T)$, which is consistent with the temperature dependence of the electrical resistance, $R(T)$, in the Figure 2. The low-T gap combined with the found value $T_c \approx 18$ K gives the gap-to-T_c ratio $2\Delta(0)/k_BT_c \approx 2.8–2.9$, which is notably smaller than the weak-coupling BCS constant 3.5, not to talk about the strong-coupling values ~4.4 known from literature [10, 28]. After a closer look at the left inset of Figure 5, one can recognize that $G(0, T)$ has a very weak maximum below 18.3 K and exhibits a decrease with lowering T, the slope becoming steeper below 14–15 K. The latter threshold T value is consistent with the local BCS $T_c^* \approx 14–15$ K corresponding to $2\Delta = 4.2–4.6$ meV as was inferred from Figure 3 (a). This smaller gap is probably formed by the proximity effect in the junction region presumably due to the break-junction fracture of the local imperfect phase. The subtle rising of the peak in $G(0, T)$ with the decrease of T below ≈18.3 K, may correspond to the BCS coherence-factor manifestation below T_c due to the energy gap formation. The right inset shows the SIS conductance fitting results using the $N(E,\Gamma)$ with thermal smearing in order to determine accurately the gap value at 6.4 K [39]. We can recognize from these results that the fitted gap-peak position corresponding to the gap parameter Δ = 2–2.3 meV changes only slightly even if the broadening parameter Γ varies strongly in the range 0.12–0.46 meV.

Figure 6 displays the conductance curve $G(V)$ extended to the high-bias region. We can notice larger-V features in addition to the superconducting-gap-edge structures. The magnitude of $G(V)$ exhibits rather weak voltage dependence up to $|V| \approx 100$ mV. In the curve A of Figure 6, the width of the central superconducting-peak region is about 9 mV, which corresponds to the representative gap value 2Δ = 4.5 meV as has been already indicated and discussed in connection with Figures 3–5. The main and unconventional features of $G(V)$ shown in the curve A of Figure 6, which deserve to be emphasized, are the reproducible broadened humps of $G(V)$ centered at biases ≈ ±50–60 mV with the shallow depression between them. This hump structure in $G(V)$ possesses the overall change in $G(V)$ ~20% of the background. One finds the gap-like peaked structures beyond the central region that reveal superconducting-gap peculiarities and subtle features at -20 mV as discussed in the text concerning Figure 4.

The ±50–60 mV gap-like structures were also obtained for the different junction as is shown in curve B of Figure 6. The curve exhibits bends or kinks in this case, which exhibit a weaker change (≈5%) against the background $G(V)$ value, but their bias positions at ± ~50 mV are in

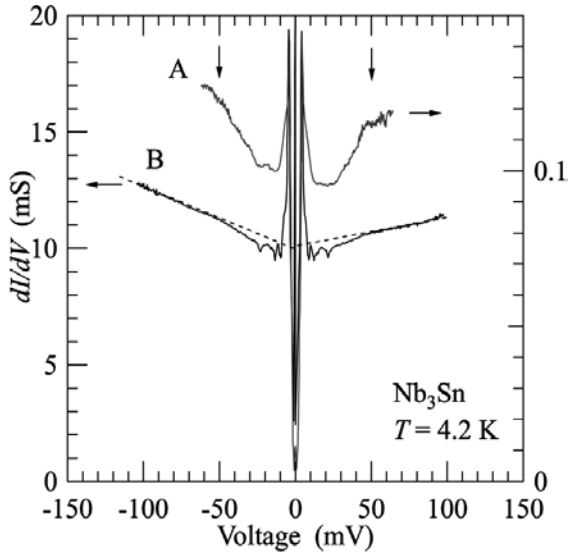

Figure 6. $G(V)$ for Nb_3Sn break junctions in the bias range up to ±150 mV.

accordance with each other. This fact testifies that the structures observed in this bias region have a common origin. Anyway, the subtle peak features at ±20 mV are well reproduced and most probably have the same origin as discussed in the context of Figure 4. In curve B, the ±5.5 mV superconducting-gap-edge peaks corresponding to the bulk $T_c \approx 18$ K are seen as well. All the features including the conventional superconducting gap of ±4.5 mV are reproduced in curve B regardless of the conductance $G(V)$ magnitude, which is ~10^2 times larger than that of curve A. From these patterns, the reproducible characteristic structures at ±5.5 mV, ±20 mV, ±50 mV inherent to Nb_3Sn are confirmed.

Further measurements above T_c were carried out in order to be sure that the above hump structures are not due to the superconductivity-induced spurious effects. Figure 7 shows the tunnelling spectra for different break junctions at temperatures 4.2 K (Figure 6, curve B) and above T_c. The mechanically supported break junctions go usually very unstable at high temperatures. Therefore, we could not ubiquitously obtain certain spectral features for all the junctions. Nevertheless, as shown in Figure 7, the tunnelling conductance spectra show reproducible gap-edge-like structures at characteristic biases around ±50 mV, which are in agreement with the hump structures appropriate to the conductance measured when the junction electrodes were at lower temperatures, deep in the superconducting state. The biases of the apparent gap-edge-like structures are distributed around the ±40–60 mV range. Similar scattered characteristic bias positions already appeared in the low-temperature superconducting data depicted in Figure 6. We should emphasize here that the very existence of the energy gap in the normal state above T_c is remarkable for Nb_3Sn.

Comparison of the substantially suppressed sub-gap conductance features for the normal-state data of Figure 7 with the extrapolated zero-bias conductance values of curve A in Figure 6 indicates that a sufficient quality of the junction interface should be realized to notice the partial

http://dx.doi.org/10.5772/59338

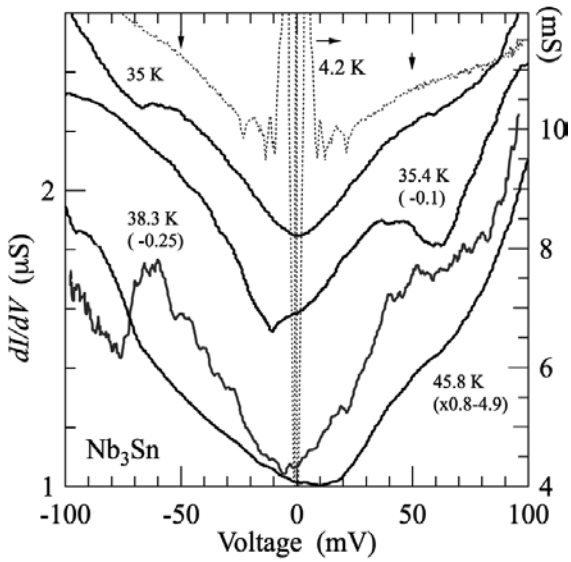

Figure 7. $G(V)$ for different Nb_3Sn break junctions well above T_c up to 45.8 K.

density-of-states gapping in the quasi-particle tunnelling studies. The zero-bias conductance depression values are noted to constitute about 30% of the normal state conductance. Therefore, assuming the SIS geometry of the break junction, one can estimate that about 17% of the density of states $N(E_F)$ at the Fermi energy E_F was removed due to formation of the normal-state gap with the position at about ±50–60 mV. The gap structures in $G(V)$ above 35 K depicted in Figure 7 exist well above the bulk $T_c \approx 18$ K. Each $G(V)$ curve corresponds to its own break junction. One observes reproducible gap-edge-peak positions ±40–60 mV in the conductance spectra. Such characteristic values are kept almost constant together with the inner gap structures. The asymmetric gap structures obtained for the symmetric break-junction configuration testify that the single-crystalline samples were cracked along defects or grain boundaries, resulting in the conspicuously asymmetric junction properties. Although the highest temperature of measurements was 45.8 K, it is remarkable that the gap locations at 50 mV are almost the same as the hump positions found at 4 K in the superconducting state.

Since the smaller features at ±20 mV of Figure 4 displayed in the superconducting state are approximately reproduced, the peculiarities found at this bias range and reported previously for Nb_3Sn [25–30], which have been attributed to the electron–phonon interaction manifestations in the spectra for this compound, should be rather considered as the gap-edge structures of a non-superconducting nature. Since the present observations seem to be important in order to interpret the Nb_3Sn tunnelling characteristics found previously, we collected various tunnel spectra in Figure 8. As shown, the ±20 mV structures manifest themselves regularly at temperatures from 4.2 K up to 35 K, well above T_c.

The significant conductance asymmetry with respect to the bias as is demonstrated in Figures 7 and 8 was observed in the majority of the tunnelling experiments dealing with the normal-

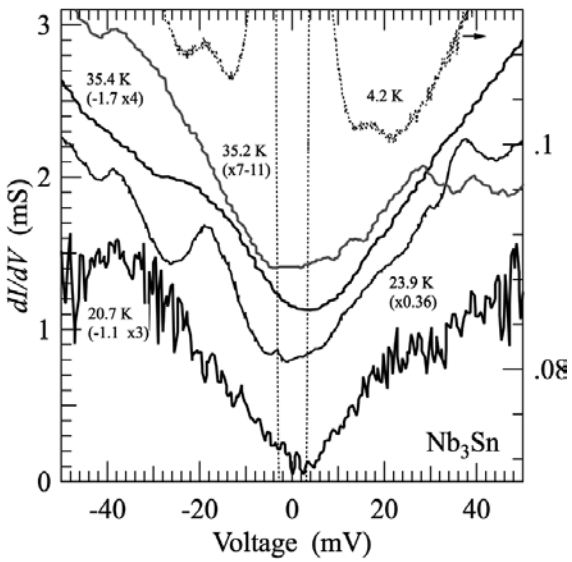

Figure 8. $G(V)$ for different Nb_3Sn break junctions showing mainly the smaller ±20–30 mV gap structures.

state gap or the dip-hump structures in high-T_c cuprate superconductors [33]. Such asymmetries can be naturally understood by considering the phase of the CDW order parameter. This phase may enter and substantially distort the quasi-particle tunnelling characteristics in the partially CDW-gapped and at the same time partially normal-metal state formed in the symmetric set-up of the break junction between CDW conductors if the symmetry is somehow violated. In particular, her hand, appearance of this asymmetry, together with the manifestations of double-gap features at both inner biases of ±20–30 mV and almost twice larger values ±50 mV, indicates that the gap structures possessing the smaller values ±20 mV are probably due to the asymmetric junction formation with the CDW gap Σ and the conductance featured at $V = \pm \Sigma/e$. The dissimilarity between $G(V)$ branches in apparently symmetric junctions may be a consequence of the broken symmetry phenomenon [15, 33]. In this case, both electrodes are in the same CDW-gapped state but with Σ_{left} and Σ_{right} having different signs! Alternatively, an asymmetric junction might be formed after cracking the sample with one of the electrodes being in a CDW-free metallic state. Then $G(V)$ is also asymmetric [15, 33].

Possible emergence of extra gapping due to the CDW influence on the Nb_3Sn tunnel spectra makes ambiguous the routine interpretation of extra $G(V)$ structures as the result of strong-coupling features induced by the electron–phonon interaction, although such an identification is familiar and often quite correct for more conventional superconductors [40]. Once such structures are recognized as the intrinsic gaps, like in our case, the difficulties of interpretation should be resolved taking into account the gapping by instabilities in the electron–hole channel. The weak hump structure depicted in Figure 4 is now understood as the $\pm \Sigma/e$ singularity emerging due to the partial Fermi surface CDW-driven gapping in the junction, its asymmetric form being induced by the broken symmetry in the CDW state with the opposite signs of CDW order parameters in the electrodes. On the other hand, as we have indicated

http://dx.doi.org/10.5772/59338

above, the asymmetric $G(V)$ shape of the apparently symmetric junction may emerge due to the actual formation of the asymmetric (one-side normal-metal) junction. In this case, the CDW-driven current-voltage characteristics are asymmetric for any phase of Σ except $\pi/2$ [15, 33]. The realization of the actually asymmetric configuration in the nominally symmetric junctions was observed in the break-junction measurements of both CDW conductors [41] and superconductors [42].

We attribute the normal-state gap features to the (martensitic) structural phase transition observed in the A-15 compound Nb_3Sn [1, 2, 13–15, 20, 24, 31, 34, 43], on the basis of the evidence given in the Introduction. Below the corresponding transition temperature, the cubic crystallographic symmetry is deformed and the tetragonal periodic lattice distortions appear driven by the Peierls-type instability due to the displacement of Nb atoms. The concomitant CDW leads to the quasi-particle gap formation in the parent electronic density of states $N(E)$. Since in Nb_3Sn the CDW transition hardly affects the transport properties [12], the dielectric energy gap Σ should distort only a small section of the Fermi surface. Its electronic signature is very weak and hence there were previously not so many discussions about the peculiarities of the tunnel conductance spectra characterizing Nb_3Sn junctions. Moreover, CDW distortions in Nb_3Sn seem to be spatially inhomogeneous similarly to what is inherent to cuprate layered structures [16, 33]. This would make the manifestations of the CDW peculiarity in the electron spectrum much smoother than in conventional cases of sharp second-kind phase transitions. Therefore, the CDW gapping reveals itself in the tunnelling $G(V)$ as a weak pseudo-gap-like feature well known for other objects [16, 17, 33, 44]. Actually, the average depth of the CDW-related gap-like structure constitutes less than half of the background. This is readily understood taking into account the inhomogeneity effects and the gapping of only a small Fermi surface section.

High-T measurements revealed the existence of the gap-like structure at 46 K, which is above the reported martensitic transition $T_m = T_{CDW} \approx 43$ K, and the gap-edge value does not decrease even at this temperature as compared with the low temperature data. This is in contrast to the apparent decrease of the normal-state gap energy above T_c reported by Escudero and Morales [31], although we agree with those authors that the gap feature survives above 45–50 K. Generally speaking, the inhomogeneity of the CDW structures should result in the scattered T_{CDW} values. The broad singularities at ±50–60 mV can be attributed to the CDW gap edges with $\pm 2\Sigma/e$ corresponding to the martensitic transition, which normally occurs at T_{CDW} [1, 2]. According to our data, T_{CDW} is in the range ≈46–50 K, so that the gap ratio $2\Sigma/k_B T_{CDW}$ can be estimated as ≈14±2. This value is significantly larger than the mean-field s-wave BCS ratio 3.53 describing the isotropic Cooper pairing. However, such values are typical for CDW phase transitions although their *reduced* gaps $\Sigma(T)/\Sigma(0)$ are well described by the BCS-like mean-field equations. For instance, $2\Sigma/k_B T_{CDW}$ is about 15 for the normal CDW transition in the low-dimensional conductor $NbSe_3$ [45].

Finally, it should be noted that the theoretical approach to the interplay between superconductivity and CDW phenomena, which started in connection to A-15 compounds [13], was recently successfully applied to treat the pseudo-gap manifestations in copper oxides [15–17,

33]. The presented observations strongly support the idea that certain phenomena in A-15 and high-T superconductors, in particular the dip-hump structures, are of the similar origin.

4. Summary

From the break-junction tunnelling measurements of the Nb_3Sn single crystals, the representative superconducting gaps were found to be 2Δ = 4–4.5 meV ($2\Delta/k_BT_c \approx 2.8$) and 5.5–6meV ($2\Delta/k_BT_c \approx 3.7$). The smaller gap is probably due to the proximity effect involving the Sn-deficient phase, while the larger one is naturally attributed to the bulk value. Hence, the two-gap superconductivity in Nb_3Sn confirmed here and found elsewhere is not an intrinsic two-gap superconductivity driven by two interacting distinct electron bands.

The high-bias tunnelling conductance exhibits gap-like structures with the characteristic values 2Σ = 50–60 meV, which are observed up to at least ~50 K. These gaps can be due to the CDW pairing associated with the martensitic structural phase transition observed at $T_m \equiv T_{CDW}$. The gap ratio $2\Sigma/k_BT_{CDW}$ is estimated to be 14±2, which is typical for the known CDW conductors. Further measurements, with the emphasis on the higher temperature evolution of Σ, should be necessary to clarify the nature of the CDW-related phenomena in this A-15 compound.

Acknowledgements

This work was supported by a Grant-in-Aid for Scientific Research (24540377) of the Japan Society for the Promotion of Science (JSPS). The work was partially supported by the Project N 24 of the 2015–2017 Scientific Cooperation Agreement between Poland and Ukraine.

Author details

Toshikazu Ekino[1*], Alexander M. Gabovich[2], Akira Sugimoto[1], Yuta Sakai[1] and Jun Akimitsu[3]

*Address all correspondence to: ekino@hiroshima-u.ac.jp

1 Hiroshima University, Graduate school of Integrated Arts and Sciences, Higashihiroshima, Japan

2 Institute of Physics, National Academy of Science, Kiev, Ukraine

3 Aoyama-Gakuin University, Department of Physics, Sagamihara, Japan

http://dx.doi.org/10.5772/59338

References

[1] Testardi L RStructural instability and superconductivity in A-15 compounds :Rev. Mod. Phys.1975:47:(3637-648.

[2] Müller J;Al5-type superconductors Rep. Prog.Phys.1980:43:(5) 643-687.

[3] Cava R J: Oxide superconductors J. Am. Ceram. Soc.2000:83(1):5-28.

[4] Scanlan R M, Malozemoff A P, Larbalestier D C:Superconducting materials for large scale applications Proc. IEEE. 2004:92(10):1639- 1654.

[5] Gurevich A:To use or not to use cool superconductors? Nature Mater.2011:10(4): 255-259.

[6] Canfield P C:Still alluring and hard to predict at 100 Nature Mater. 2011:10(4): 259-261.

[7] Tarantini C, Gurevich A:High-field properties of pure and doped MgB2 and Fe-based superconductor MRS Bull. 2011:36(8):626-630.

[8] Kumakura H:Development and prospects for the future of superconducting wires Jpn. J. Appl. Phys. 2012:51(1):010003.

[9] Tanabe K,Hosono H: Frontiers of research on iron-based superconductors toward their application Jpn. J. Appl. Phys.2012:51(1):010005.

[10] Godeke A:A review of the properties of Nb3Sn and their variation with A15 composition,morphology and strain state Supercond. Sci. Technol. 2006:19(8):R68.

[11] Godeke A, tenHaken B,tenKate H H J,Larbalestier D C: A general scaling relation for the critical current density in Nb3SnSupercond. Sci. Technol. 2006:19(10):R100.

[12] Gorkov L PProperties of A15 compounds and one-dimensionality : In: Progress in Low Temperature Physics, Vol.VIIB.ed.Brewer D F: North Holland, Amsterdam: 1978.518-589 p.

[13] Bilbro G,McMillan W L:Theoretical model of superconductivity and the martensitic transformation in A15 compounds Phys. Rev. B1976:14(5):1887-1892.

[14] Nakayama J: {Structural transformations and superconductivity in A15 compounds J. Phys. Soc. Jpn.1977:43(5):1533- 1538.

[15] Gabovich A M, Voitenko A I,Ausloos M: Charge-density waves and spin-density waves in existing superconductors: competition between Cooper pairing and Peierls or excitonic instabilities Phys. Rep.2002:367(6):583- 709.

[16] Ekino T,Gabovich A M, LiMai Suan, Pękała M,Szymczak H, VoitenkoAI;Analysis of the pseudogap-related structure in tunneling spectra of superconducting Bi2Sr2Ca-Cu2O8+δ revealed by the break-junction technique Phys. Rev. B. 2007:76(18):180503.

[17] Ekino T, Gabovich A M, LiMai Suan,Pękała M,Szymczak H, Voitenko A I: The phase diagram for coexisting d-wave superconductivity and charge-density waves: cuprates and beyond J. Phys. Condens. Matter. 2011:23(38):385701.

[18] Ekino T,Gabovich A M, LiMai Suan, Takasaki T, Voitenko A I, Akimitsu J, Fujii H, Muranaka T, Pękała M P, Szymczak H:Spatially heterogeneous character of superconductivity in MgB2 as revealed by local probe and bulk measurements Phys. C. 2005:426-431:230-233.

[19] Ekino T, Sugimoto A, GabovichA M: Scanning-tunneling microscopy/spectroscopy and break-junction tunneling spectroscopy of FeSe1–xTex Fiz. Nizkikh Temp. 2013:39(3):343-353.

[20] Zehetmayer M: A review of two-band superconductivity: materials and effects on the thermodynamic and reversible mixed-state propertiesSupercond. Sci. Technol. 2013:16(4):043001.

[21] Vieland L J, Wicklund A W: Specific heat of niobium-tin Phys. Rev. 1968:166(2): 424-431.

[22] Guritanu V, Goldacker W, Bouquet F, Wang Y, Lortz R, Goll G, Junod A: Specific heat of Nb3Sn: The case for a second energy gap Phys.Rev. B. 2004:70(18):184526.

[23] Marz M, Goll G, Goldacker W, Lortz R: Second superconducting energy gap of Nb3Sn observed by breakjunction point-contact spectroscopy Phys.Rev. B. 2010:82(2):024507.

[24] Escudero R, Morales F, Bernès S: Specific heat studies of pure Nb3Sn single crystals at low temperature J. Phys. Condens. Matter.2009:21(32):325701.

[25] Shen L Y L: Tunneling into a high-*Tc* superconductor - Nb3Sn Phys. Rev. Lett. 1972:29(16):1082-1086.

[26] Vedeneev S I, GolovashkinA I, Levchenko I S, Motulevich G P: Investigation of tunnel characteristics of sputtered superconducting Nb3Sn films ZhurnÉksp. Teor. Fiz. 1972:63(3):1010-1019 [Sov. Phys. JETP. 1973:36(3):531-535].

[27] Wolf E L, Zasadzinski J, Arnold G B, More D F, Rowell J M, Beasley M R: Tunneling and the electron-phonon-coupled superconductivity of *Nb*3Sn Phys.Rev.B. 1980:22(3):1214-1217.

[28] Rudman D A, Hellman F, Hammond R H, Beasley M R: A15 NbSn tunnel junction fabrication and properties J. Appl. Phys. 1984:55(10):3544-3553.

[29] Geerk J, Kaufmann U, Bangert W, Rietschel H: Electron tunneling into *Nb*3Sn, *Nb*3Ge, and *Nb*3Al Phys. Rev. B. 1986:33(3):1621-1626.

[30] Moreland J, Ekin J W: Electron tunneling experiments using NbSn ''break'' junctions J. Appl. Phys. 1985:58(10):3888-3895.

[31] Escudero R, Morales F: Point contact spectroscopy of Nb3Sn crystals: Evidence of a CDW gap related to the martensitic transitionSolid State Commun. 2010:150(15-16): 715-719.

[32] Kopaev Yu V: About the interplay theory between electron and structural transformations and superconductivity Trudy FIAN.1975:86:3-100.

[33] Gabovich A M, Voitenko A I, Ekino T,Li M S,Szymczak H, Pekala M: Competition of superconductivity and charge density waves in cuprates: Recent evidence and interpretation Adv. Condens. Matter Phys. 2010:2010:681070.

[34] Bhatt R N: Microscopic theory of the martensitic transition in *A*−15 compounds based on a three-dimensional band structure Phys. Rev. B. 1977:16(5):1915-1932.

[35] Tütüncü H M, Srivastava G P, Bağci S, Duman S: Theoretical examination of whether phonon dispersion in Nb3Sn is anomalous Phys. Rev. B. 2006:74(21):212506.

[36] Barone A, Paterno G: The Physics and Applications of the Josephson Effect: Johney and Sons, New York: 1982, 529pp.

[37] Coleman R V, Giambattista B, Hansma P K, Johnson A, Mcnairy W W,Slough C G: Scanning tunnelling microscopy of charge-density waves in transition metal chalcogenides Adv. Phys. 1988:37(6):559-644.

[38] Ekino T, Takabatake T, Tanaka H, Fujii H: Tunneling evidence for the quasiparticle gap in Kondo semiconductors CeNiSn and CeRhSb Phys. Rev. Lett. 1995:75(23): 4262-4265.

[39] Dynes R C, Narayanamurti V, Garno J P: Direct measurement of quasiparticle-lifetime broadening in a strong-coupled superconductor Phys. Rev. Lett. 1978:41(21): 1509-1512.

[40] Geerk J, Lohneysen H v: Convolution effects in superconductive tunneling Phys. Rev. Lett. 2007:99(25):257005.

[41] Jung M H, Ekino T, Kwon Y S, Takabatake T: Tunneling spectroscopy of RTe2 (R = La, Ce) and possible coexistence between charge-density waves and magnetic order-Phys. Rev. B. 2001:63(3):035101.

[42] Ekino T, Fujii H, Kosugi M, Zenitani Y, Akimitsu J: Tunneling spectroscopy of the superconducting energy gap in *R*Ni2B2C (*R* = Y and Lu) Phys. Rev. B. 1996:53(9): 5640-5649.

[43] Ekino T, Sugimoto A, Sakai Y, GabovichA M, Akimitsu J:Fiz. Tunneling spectra of break junctions involving Nb3Sn Nizkikh Temp. (2014):40(10):1182-1186.

[44] Monceau P: Electronic crystals: an experimental overview Adv. Phys. 2012:61(4): 325-581.

[45] Ekino T, Akimitsu J: Electron tunneling study of NbSe3 Jpn. J. Appl. Phys. Suppl. 1987:26(Supplement 26-3):625-626.

Chapter 5

New Prospective Applications of Heterostructures with $YBa_2Cu_3O_{7-x}$

M. I. Faley, O. M. Faley, U. Poppe, U. Klemradt and
R. E. Dunin-Borkowski

Additional information is available at the end of the chapter

http://dx.doi.org/10.5772/59364

1. Introduction

Among high-T_c superconductors with $T_c > 77$ K, $YBa_2Cu_3O_{7-x}$ (YBCO) is the most elaborated material for electric power applications and low noise electronics. Discovered in 1987 [1], YBCO is now included in the most advanced high-T_c superconducting epitaxial oxide thin-film heterostructures with other metal-oxide materials. Cables for electric power transportation, motors, generators and others large scale applications are using 2nd generation flexible superconducting tapes comprising epitaxial YBCO films with critical current about 2 MA/cm^2 at 77 K [2]. Electronic applications of high-T_c superconductors have lower economic impact and received up to now less publicity but they are also becoming competitive. Low noise high-T_c superconducting quantum interference devices (SQUIDs) are made from high quality epitaxial YBCO films and grain boundary Josephson junctions. With a help of a 16-mm multilayer superconducting flux transformer the best magnetic field resolution of high-T_c SQUIDs about 4 fT/√Hz at 77 K was achieved [3]: all-oxide heterostructures based on high-quality epitaxial YBCO thin films with other metal-oxide layers are indispensable for construction of high-T_c SQUIDs with ultimate sensitivity [4]. High-T_c SQUIDs serve as sensors of magnetic field in the LANDTEM geophysical survey system that has located mineral deposits worth Australian $6bn [5]. Metallic contaminant detection systems are integrated in the food production lines and important for manufacturers of lithium-ion batteries. These systems are gaining sensitivity with high-T_c SQUID sensors [6]. Scanning high-T_c SQUID biosusceptometry is used to track noninvasively labelled colorectal tumors by conducting different preoperative and intraoperative in vivo examinations [7]. In this chapter the prospective applications of epitaxial thin film heterostructures based on YBCO in information technology, electron microscopy and magnetoencephalography are described.

INTECH
open science | open minds

© 2015 The Author(s). Licensee InTech. This chapter is distributed under the terms of the Creative Commons Attribution License (http://creativecommons.org/licenses/by/3.0), which permits unrestricted use, distribution, and reproduction in any medium, provided the original work is properly cited.

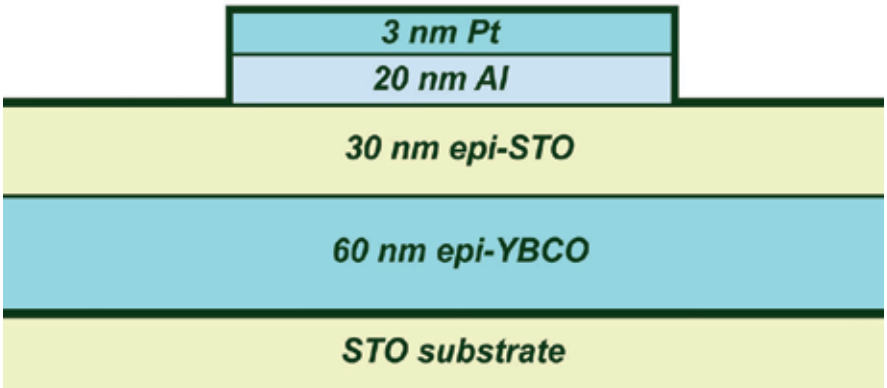

Figure 1. Sketch of YBCO-STO-Al-Pt heterostructure used for the investigation of the resistive switching effect in the present work.

2. Information technology

Storage of information is essential in computers and communication devices which are now indispensable in our everyday life. Resistive switching and the related oxygen motion in $SrTiO_3$ may take place in regions as small as 3 nm [8], [9] which corresponds to a hypothetically possible size of future non-volatile resistive random-access memory (RRAM) memories of about 1 TB/cm^2. Important attributes of resistive switching elements are the presence of a rectification effect due to a Schottky barrier at one of the interfaces of the insulator with electrodes and the presence of a conducting channel for oxygen vacancies and electrons within the insulator [10], [11]. A large difference between the work functions (WF) of the insulator and the WF of one of the electrodes is required for a pronounced Schottky effect at the interface and a large amplitude of the resistive switching. An advantage of using of YBCO for RRAMs is the high value of its WF ~ 6.1 eV [12], [13]. This value of WF is significantly larger than WFs of Pt or Au electrodes (WF~ 5 eV) and TiO_2 and $SrTiO_3$ (STO) insulators (WF~ 4.3 eV).

Resistive switching memory elements were made using epitaxial thin film heterostructures YBCO-STO-Pt [14]. These elements can operate at room temperature and improve their On/Off resistance switching ratio at lower temperatures. The rectification effect at the interface with YBCO is increasing when YBCO is in the superconducting state [15] giving a hope for further increasing of the On/Off resistance switching ratio. We have produced YBCO-STO-Al-Pt heterostructures (see sketch in Fig.1) and studied their resistive switching and microstructural properties. With YBCO as the bottom electrode a Schottky-like bottom interface is formed whereas the contact between the STO and Al is ohmic: WF of Al is ~ 4.1 eV. A 3 nm thick Pt film served for passivation of Al film.

The YBCO and STO films of the YBCO-STO-Al-Pt heterostructure were prepared by high oxygen pressure DC magnetron sputtering technique [16], [17]. The YBCO electrode was grounded using ohmic contact with a silver pad and a piece of indium. 20-μm-square top

http://dx.doi.org/10.5772/59364

electrodes consisting from Al and Pt films were deposited on STO by DC magnetron sputtering in pure argon and patterned by deep-UV photolithography and ion beam etching. The patterning was finished by removing of the residuals by chemical etching of aluminium film with developer for AZ photoresist AZ326MIF. Electrical contact to the top electrode was performed by a flexible Pt wire using a micromanipulator and an optical microscope. The electrical measurements were performed at room temperature in ambient atmosphere.

Pristine contacts have a resistance of about 100 GOhm. Activation of the memory cells was performed by the process of electrodegradation (electroforming) of the STO insulator at a negative voltage of −6 V and a compliance current of 6 mA. Opposite polarity did not activate the cells but irreversibly destroyed them by formation of oxygen bubbles at the STO-Al interface. Only one conducting channel appeared at each contact pad as the result of electroforming and the position of this channel was beyond traces of Pt wire in the top electrode. The I(V) and R(V) characteristics of the YBCO-STO-Al-Pt heterostructure are shown in Fig. 2 and Fig. 3 respectively. All contacts have demonstrated similar characteristics.

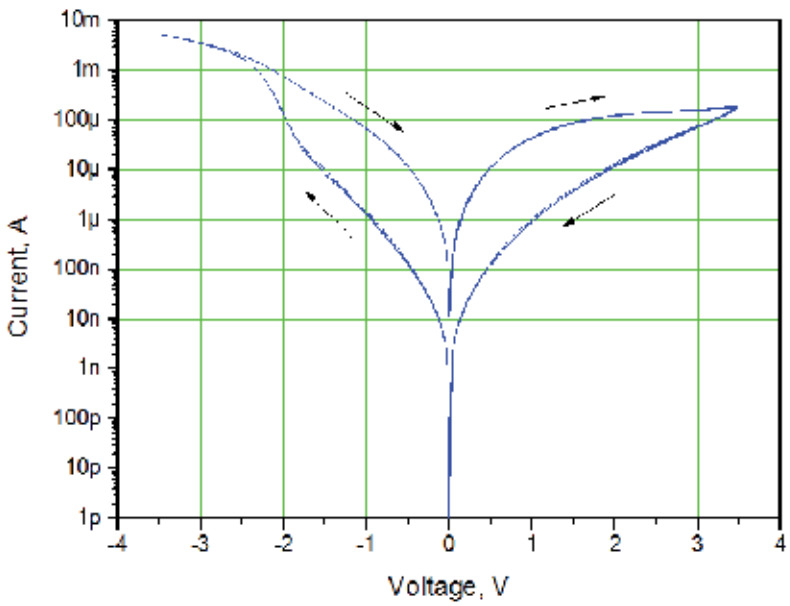

Figure 2. I(V)-characteristics of YBCO-STO-Al-Pt heterostructure demonstrating five continuous resistive switching cycles.

Scanning electron microscopy of the electroformed area was performed in the lower secondary electron image (LEI) mode (see Fig. 4). A conducting channel with diameter ~400 nm through STO film and a trace of overheated area near this channel were observed. Investigation of the conducting channel and its interfaces with electrodes by cross-sectional high resolution transmission electron microscopy will give more information about the microstructure and physical nature of operation of the resistive switching effect in these contacts.

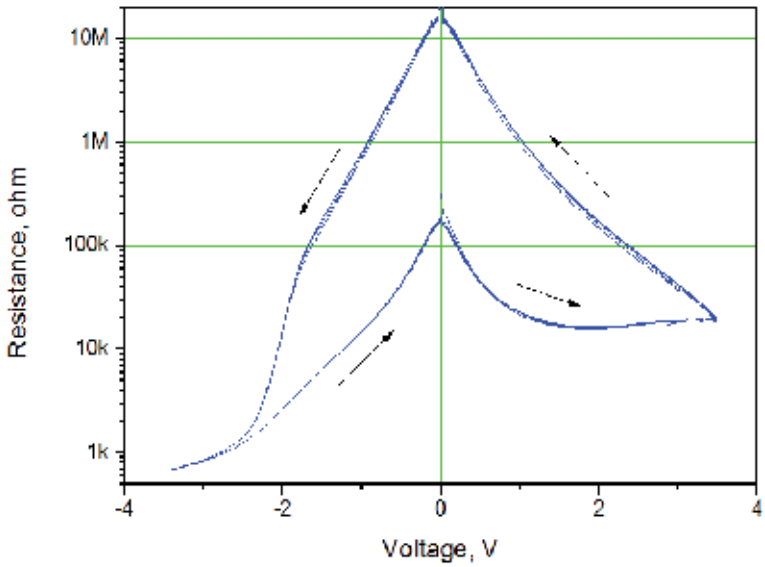

Figure 3. R(V)-characteristics of YBCO-STO-Al-Pt heterostructure demonstrating five continuous resistive switching cycles.

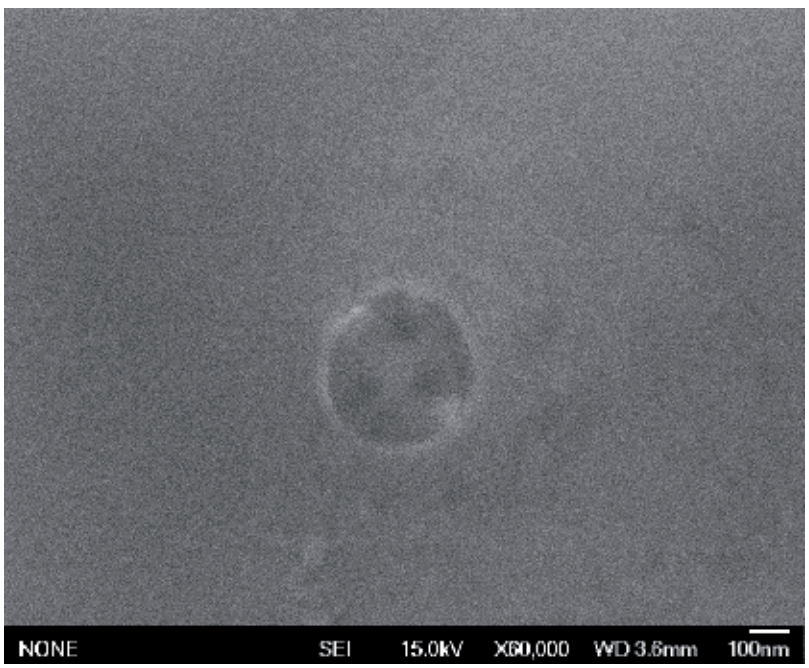

Figure 4. SEM image of the electroformed area of YBCO-STO-Al-Pt heterostructure performed in the LEI mode.

http://dx.doi.org/10.5772/59364

A possible mechanism of the observed resistive switching effect in the YBCO-STO-Al-Pt heterostructure can be the following. During the process of electrodegradation, a conducting channel through the STO film separated by a highly ohmic Schottky barrier from the bottom electrode is formed. The nature of the conducting channel is described elsewhere [11]. The conducting channel serves for a transport of electrons and oxygen ions by the switching electric fields. The reactions of creation (at negative bias) and dissociation (at positive bias) of oxygen vacancies near the bottom interface probably lead to the greatest contribution to the On/Off resistance switching ratio of the described contacts. A part of oxygen atoms can migrate through the bottom interface while the other part can be accommodated inside STO leading to local strain and elastic deformation of STO lattice near the bottom interface. Serving as a reservoir of oxygen atoms, the high value of the work function and the mechanical strength of YBCO are favourable for the superior operation, reproducibility and long term stability of the resistive switching elements described above.

3. Electron microscopy

Modern fifth-order aberration-corrected high resolution transmission electron microscopy (TEM) is able to resolve a crystal spacing less than 50 pm [18]. Especially correction of chromatic aberrations is considered as extremely challenging technological task. The complicated electron optics, extreme machining precision and stability for the power supplies are in the sub 0.1 ppm range are required. One possibility for the further improvement of the resolution of TEM will depend on ability to suppress fluctuations of magnetic fields along the optic axis and especially in magnetic lenses [19]. Some of the magnetic fluctuations are related to thermal fluctuations (Johnson-Nyquist noise) and can be reduced by cooling of the microscope column and lenses to cryogenic temperatures [19].

The temporal stability of magnetic fields in magnetic lenses is limited by several sources of interference, including fluctuations of the current in their coils and the fact that a ferromagnetic yoke can act as an antenna, which couples external electromagnetic interference or magnetic fields generated by movable magnetic objects to the electron beam. Both the movement of magnetic domains (Barkhausen noise) and thermal current fluctuations (Johnson-Nyquist noise) inside the yoke can lead to statistical fluctuations of the magnetic flux that propagates through it. In addition, since the permeability of the yoke is temperature-dependent, fluctuations in temperature can result in variations in the magnetic field in the lens.

We investigate a new approach for improving the performance of magnetic lenses for electron microscopy and other applications where highly stable magnetic fields are required. We have proposed using superconducting rings around the ends of the pole piece to stabilize magnetic fields in the ferromagnetic yokes of magnetic lenses for electron microscopy [20]. Our proposal involves introducing a superconducting ring around a ferromagnetic yoke, in which the magnetic flux should remain constant to a much greater precision than the stability of conventional power supplies allows. Fluctuations of the magnetic field in the yoke induce a current in the superconducting ring, which results in an oppositely directed magnetic flux in

the yoke that exactly compensates these fluctuations. Because the superconductor has no resistance, the induced current can flow indefinitely and the magnetic field in the ferromagnetic yoke can be maintained indefinitely. In this way, the current induced in the superconducting ring compensates fluctuations in the magnetic field, while the required DC value of the magnetic field is provided by the coils. By positioning the superconducting ring outside the magnetic field of the lens, dissipation of the induced currents due to creep of Abrikosov vortices can be avoided.

This new concept originates from the phase coherence of Cooper pairs in superconductors and dependence of Berry's phase of charged particles on magnetic vector potential. As a consequence, magnetic flux through closed ring of superconductor is automatically kept constant due to exact compensation of changes in external magnetic field by persistent superconducting current induced in the superconducting ring (see Fig. 5) [21].

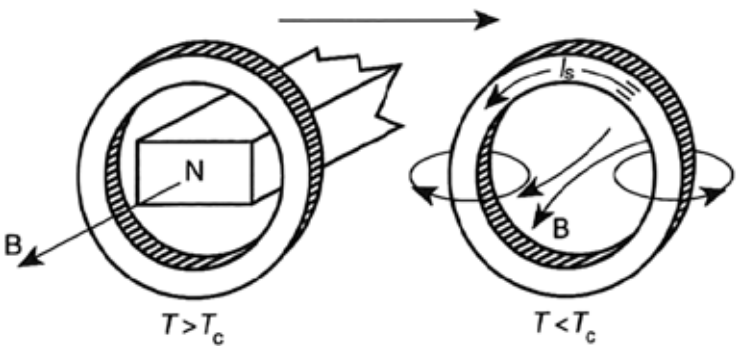

Figure 5. Excitation of persistent current in a superconducting ring [21].

This ability of a superconductor to keep magnetic flux constant can be visualised by a demonstrative experiment shown in Fig. 6. The magnetic field induced by the persistent current in YBCO forces the substrate to maintain its position relative to the magnet constant in spite of the counteracting influence of gravitation.

A simple computer simulation of magnetic field of source of fluctuating magnetic fields (1) and ferromagnetic core (2) depending on the presence of superconducting stabilizer (3) was performed (see Fig. 7). This simulation qualitatively shows that superconducting rings practically eliminate fluctuating magnetic fields in the gap (4). Due to high permeability of ferromagnet (~10000) the major part of the magnetic flux through superconducting ring is concentrated inside the ferromagnetic yoke. Induced superconducting currents keep magnetic flux penetrating through the rings constant and this eliminates fluctuations in the gap (4).

A "proof-of-principle" demonstration of the proposed approach was achieved by using the experimental setup shown in the form of a schematic diagram and a photograph in Figures 8a and 8b, respectively. A high-T_c DC SQUID [3] operating at a temperature of 77 K was placed in the vicinity of a gap in a nanocrystalline VITROPERM core VAC W867-01 and used for sensitive non-invasive characterisation of the magnetic field in the stabilized region. Two

http://dx.doi.org/10.5772/59364

Figure 6. Levitation of 1 cm^2 substrate with 100 nm YBCO film under $SmCo_5$ permanent magnet.

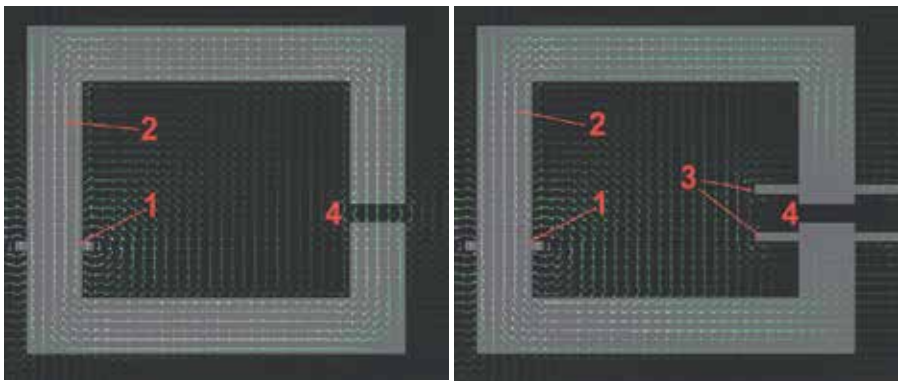

Figure 7. Computer simulation of magnetic fields of source of fluctuating magnetic fields (1) with a ferromagnetic core (2) without superconducting stabilizer (left picture) and with superconducting stabilizer (3) (right picture).

serially connected platinum thermometers PT-100 were used as local heating elements. The heating element was glued on superconducting ring and thermally insulated from liquid nitrogen by silicone glue.

Figure 9 demonstrates the operation of the superconducting magnetic field stabilizer. Magnetic field fluctuations were simulated by adding an alternating current (AC) field (~100 Hz) to the

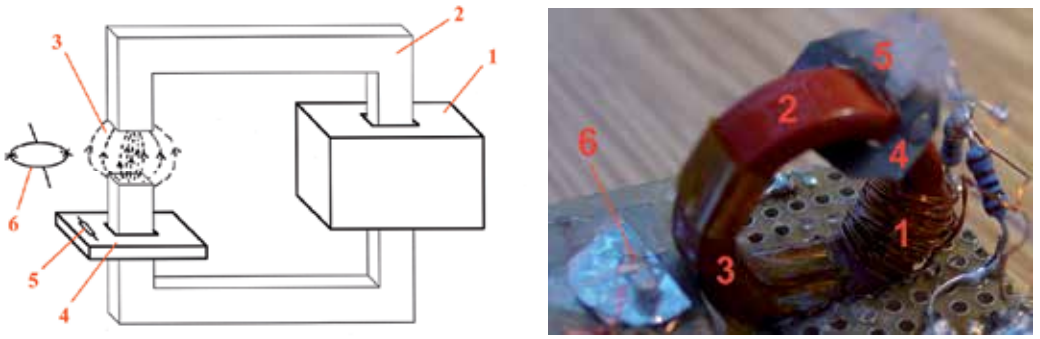

(a) (b)

Figure 8. a) Sketch of experimental setup with main field coil (1), soft magnetic yoke (2), stabilized magnetic field region (3), superconducting ring (4), local heating element to allow flux entrance into the superconducting ring for a change of flux (5) and SQUID detector (6) to monitor the flux in the stabilized region. (b) Photograph of experimental setup, which was placed in liquid nitrogen for the measurement.

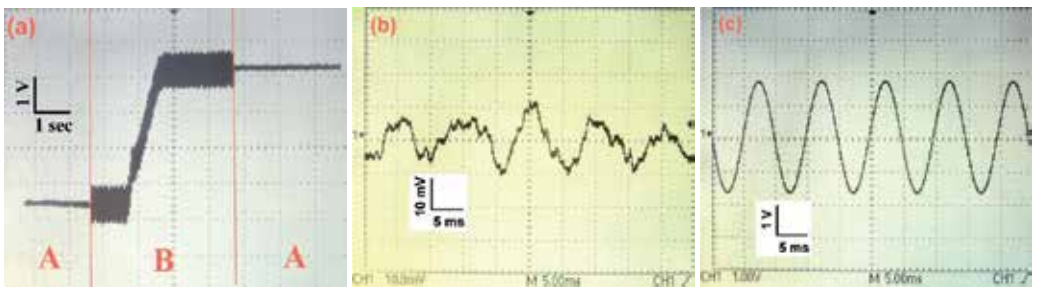

Figure 9. a) Oscillogram showing measured magnetic field in stabilized (A) and adjusted (B) modes in the test setup. During timespan B, the additional interference, which was simulated by adding an AC field to the main (DC) field of the coil, appears. The measured DC field was then also changed to a different value during heating of the superconducting ring. (b) Test signals with SC stabilizer ON and (c) with SC stabilizer OFF.

main DC field of the coil. The superconducting ring was made from an $YBa_2Cu_3O_7$ high-T_c thin film tape that was cooled to 77 K in stabilizing mode A. Even in the non-optimized demonstrator shown in figure 8b, more than 99 % of the magnetic field fluctuations were removed by the stabilizer when compared to mode B, in which the superconducting ring was switched to its normal state by heating above the superconducting transition temperature. In mode B, adjustment to a new magnetic field value was possible, as shown in figure 9a. Figure 9b shows the magnetic field in mode A and figure 9c shows the magnetic field in mode B measured with 5 ms time scale.

Schematic representation of commercially available 2nd generation flexible $YBa_2Cu_3O_7$ high-T_c thin film tape which was used for preparation of superconducting (SC) rings in the present study is shown in figure 10 [22]. The 100 mm wide and 100 μm thick stainless steel Hastelloy substrate is covered by a solution deposition planarization (SDP) layer to reduce surface

roughness on to nanometer level. Buffer layer of 200 nm MgO film is prepared by ion beam assisted deposition (IBAD) method followed by epitaxial growth. Epitaxial 3 μm thick YBCO film is deposited on MgO by reactive co-evaporation process and covered by 1μm silver film. The tape is able to transport persistent superconducting current over 500 A/cm at 77 K. We have patterned superconducting rings from such tape by laser cutter machine and/or by a diamond file.

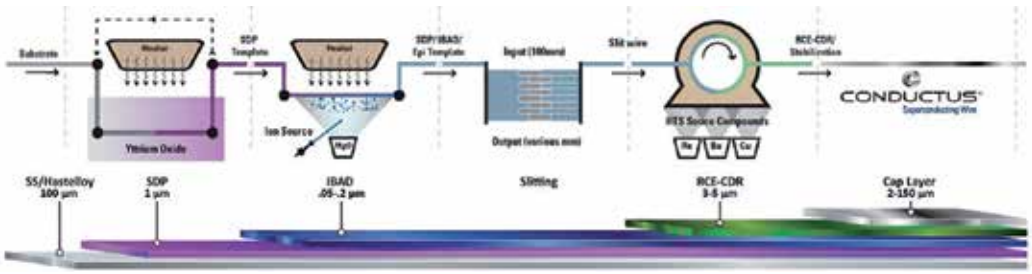

Figure 10. Schematic representation of the Conductus® superconducting wire manufacturing process for commercially available $YBa_2Cu_3O_7$ high-T_c thin film tapes [22].

Advantage of application of superconducting tapes for magnetic field stabilizer is their low costs (~100$/m), flexibility, high critical current and possibility of patterning by a simple mechanical machining. Currently, up to 12 mm wide tapes are commercially available. Up to 10 cm wide tapes with complete heterostructure including YBCO are expected to appear soon on market. Single crystal wafers with epitaxial YBCO films can be also used but they are much more expensive, thicker and brittle.

The superconducting magnetic field stabilizer can be applied to several types of scanning electron microscope or transmission electron microscope (TEM) lenses. Sketches of prospective setups for objective lens are shown in figures 11 – 15 [20].

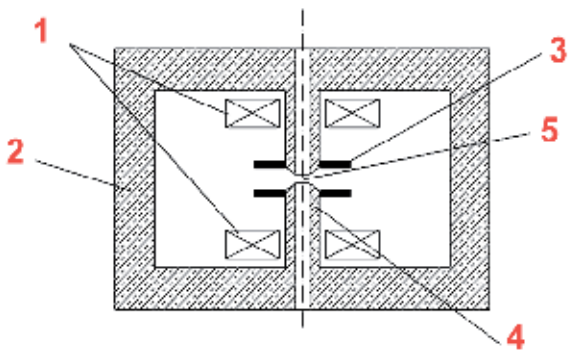

Figure 11. Sketch of prospective setup for a TEM objective lens [20]. Coils (1) provide magnetic flux through the yoke (2). Two stabilizing SC rings (3) are placed near the pole piece ends (4) to stabilize magnetic field in the sample area (5).

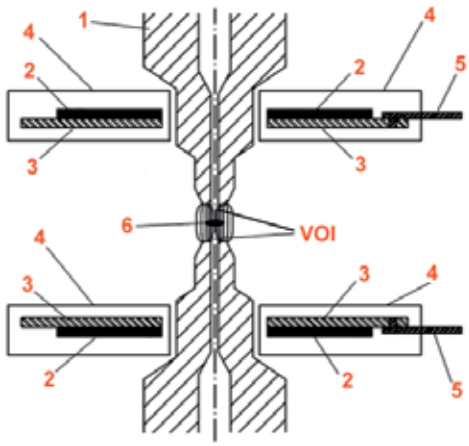

Figure 12. Sketch of prospective setup for a TEM objective lens [20]. The coils (not shown) providing the main magnetic flux through the yoke (1). The poles are surrounded by SC rings (2), which are placed on heat conducting substrates (3) inside thermal insulations (4) and cooled through cold leads (5). Magnetic field is stabilized in volume of interest (VOI) near the sample (6).

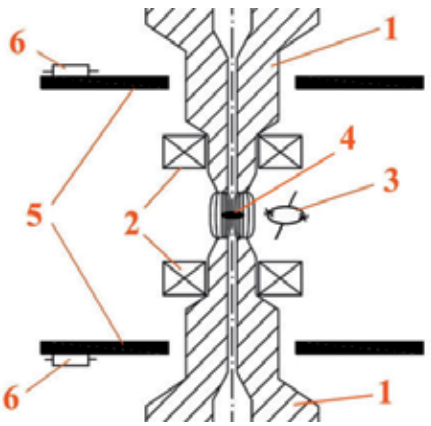

Figure 13. Sketch of prospective setup for a TEM objective lens [20]. Apart from the coils (not shown) providing the main magnetic flux through the yoke (1), two additional coils (2) can be used together with a SQUID detector (3) in feedback mode for fine adjustment of the magnetic lens field near the sample (4). Two stabilizing SC rings (5) with local resistive heaters (6) are placed near the pole piece ends.

There is still a long way to actual implementation of superconductivity for electron microscopy. The superconducting magnetic field stabilizer and cooling elements should fit into modern complicated array of electron lenses and realized with the same extreme machining precision as other parts of the electron microscopes. But the requirement of further improving of resolution of electron microscopes may prevail and, sooner or later, make this way beneficial.

http://dx.doi.org/10.5772/59364

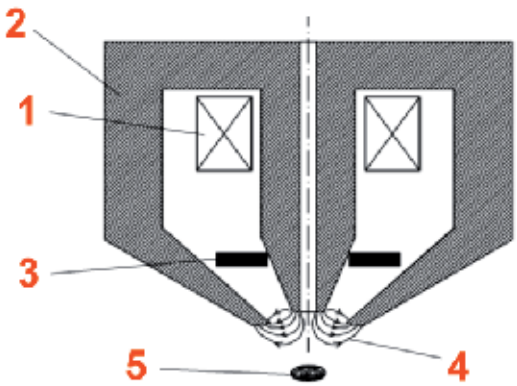

Figure 14. Sketch of prospective setup for an SEM conical objective lens [20]. Coil (1) provides magnetic flux through a yoke (2). A stabilizing SC ring (3) is placed near the pole piece end to stabilize the magnetic field in the area of the strong magnetic field gradient (4), which focuses the electron beam onto the sample.

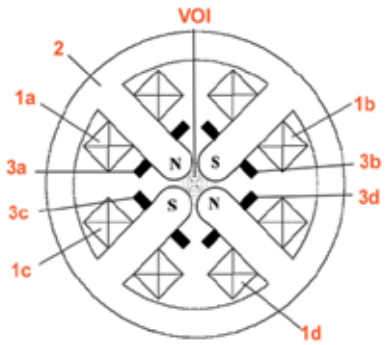

Figure 15. Sketch of prospective setup for a quadrupole lens [20]. Coils (1a-d) provide magnetic flux through the yoke (2). Stabilizing SC rings (3a-d) are placed near the pole piece ends (S, N) to stabilize the magnetic fields and their gradients in the volume of interest (VOI).

4. Magnetoencephalography (MEG)

The importance of developing a new generation of non-invasive imaging techniques that can be used to understand human brain function is reflected, for example, in the "Human Brain Project" (EU) and the "BRAIN Initiative" (USA). Multichannel MEG systems that are based on low temperature SQUIDs are well developed and routinely used for the non-invasive investigation of multiple time-dependent sources of weak magnetic field generated by the human brain. MEG systems that are based on sensitive high-T_c SQUIDs promise to improve signal-to-noise ratio and to provide better source characterization by reducing the SQUID-to-scalp separation [23]. In a high-T_c system, one can achieve significant savings in energy and operational cost, in particular by avoiding problems with the supply of liquid helium [24, 25]. A single-channel MEG system based on high-T_c DC SQUID flip-chip magnetometers with a

16 mm x 16 mm multilayer flux transformer has achieved a magnetic field resolution of ~ 4 fT/√Hz at 77.4 K [26, 3], which is similar to the magnetic field resolution of individual channels in commercial MEG systems based on 28 mm x 28 mm low-T_c SQUIDs [27].

The magnetic signals that are detected by MEG originate from neocortical columns, each of which consists of ~50,000 pyramidal cells with a net current ~10 nA. The magnetic fields measured by MEG are ~ 100 fT in the frequency range 1 Hz to 1 kHz. A spatial resolution of the MEG system of a few mm for such sources is usually sufficient. These values result in mutually dependent restrictions on the sensitivity, size and positioning of the SQUIDs: a reduction in the size of the sensors and in their proximity to the neural sources in the brain can partially compensate for a loss in sensitivity. On the other hand, more sensitive sensors allow for greater flexibility in the construction of the system. High-T_c SQUIDs can be cooled in cryostats that have fewer radiation shields and can be placed much closer to the outer wall than low-T_c SQUIDs. Assuming a similar field resolution and similar sizes of the sensors, the signal-to-noise ratio obtained during the detection of superficial and/or shallower sources of neuromagnetic signals by a high-T_c MEG system can be higher than for a low-T_c MEG system. At least 40% more information can be obtained using a high-T_c MEG system when compared to the state-of-the-art in low-T_c MEG systems [28].

The first source localization of brain activity using a single channel high-T_c system for MEG was demonstrated recently [29]. Taking into consideration possible systematic temporal drifts in the physiological and functional condition of the investigated brain area during the measurements, at least ten simultaneously operating channels are required for better diagnosis in practical applications of high-T_c MEG systems: for example, 7 signal channels and 3 reference channels. The construction of high-T_c MEG systems with more than 100 channels would be the next step in this development. However, multichannel high-T_c MEG systems have not yet been realized because of a number of issues associated with the integration of high-T_c SQUID magnetometers into the dense arrays of sensors that are required for MEG systems. Here, we describe these problems and suggest some solutions. First, we describe the properties of high-T_c SQUIDs that are essential for the construction of multichannel systems. Several issues, including crosstalk between the sensors, vibration-free cooling of sensors, minimization of the sensor-to-object distance, as well as optimization of the sensor positions and gantry design, are discussed.

In a sufficiently magnetically well shielded room, it is preferably to use magnetometers instead of gradiometers for improved sensitivity to deep and/or distant sources. The magnetometers can be made fully with thin film technology, avoiding the use of superconducting wires. This results in comparable capabilities for high-T_c and low-T_c SQUIDs.

Multichannel high-T_c MEG systems comprise many high-T_c SQUIDs, some of which may require replacement over time. Although the technology required for producing low noise high-T_c SQUID magnetometers for MEG has been developed (see [3] and [30] and references therein), it is still not a mass production technology. Scaling to a higher production rate can be achieved by using parallel processing and/or larger single crystal MgO wafers, which are available in sizes of up to ~10 cm. High oxygen pressure sputtering allows deposition of large homogeneous areas of high-quality stoichiometric epitaxial heterostructures of superconduct-

http://dx.doi.org/10.5772/59364

ing cuprates with a mirror-like surface and superior electron transport properties [16]. The typical superconducting transition temperatures and critical current densities of $YBa_2Cu_3O_{7-x}$ (YBCO) films obtained by this method are ~93 K and ~6 10^6 A/cm^2 at 77.4 K, respectively.

The most suitable high-T_c SQUID magnetometers for multichannel systems from a price and quality point of view were recently developed [3]. These SQUIDs are based on high-T_c step-edge Josephson junctions, which are fabricated from specially oriented YBCO films grown on graphoepitaxially buffered steps on MgO substrates [30], [31]. The predecessors of such junctions were developed in the CSIRO group (see [32] and references therein). The cross-sectional areas of the graphoepitaxial junctions used in the SQUIDs are ~ 0.1 μm^2, which is about two orders of magnitude smaller than the cross-sectional area of typical Nb-based low-T_c junctions. Step edge junctions are also characterized by a larger normal state resistance R_n ~20 Ohm, a higher I_cR_n of ~ 0.6 mV at 77.4 K and a lower capacitance C of ~10 fF, when compared to bicrystal high-T_c Josephson junctions [30]. The high resistance of these junctions leads to large voltage swings of the SQUIDs (by ~ 50 μV), but it promotes coupling to radio-frequency (RF) electromagnetic interference and results in the need for measures to achieve better RF filtering and shielding. The low capacitance of the Josephson junctions is advantageous for lowering the intrinsic flux noise of DC SQUIDs [33], [34]:

$$S_\Phi \approx 32 k_B T L \left(LC / \beta_C \right)^{1/2}, \tag{1}$$

where $\beta_C = 2\pi I_C R_n^2 / \Phi_0 \approx 0.4$ is the McCumber parameter and Φ_0=2.07 10^{-15} T m^2 is the magnetic flux quantum. The lower operating temperatures of low-T_c SQUIDs are almost compensated by the typically much higher capacitance of their Josephson junctions (~1 pF). This property can explain the comparably high sensitivities of high-T_c and low-T_c SQUIDs in spite of the much higher operating temperature of high-T_c SQUIDs.

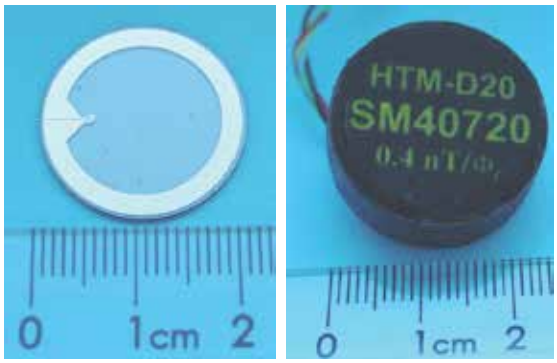

Figure 16. A multilayer high-Tc superconducting flux transformer with a 20 mm pick-up loop and a 14-turn input coil (left photograph) and an encapsulated DC SQUID magnetometer containing such a flux transformer (right photograph).

In MEG systems, near-optimal sensitivity of SQUIDs to magnetic fields can be provided by a superconducting flux transformer with a 14-turn input coil and a pick-up loop with an outer diameter of 20 mm. Figure 16 shows a photograph of such a flux transformer and a vacuum-tight encapsulated high-T_c magnetometer (type HTM-D20) intended for assembly into a multichannel MEG system. The capsule has an outer diameter of ~24 mm, which is smaller than the 27-mm capsule for 16-mm magnetometers of type HTM-16 [35]. It encloses a flip-chip magnetometer, a feedback coil and a heater. The magnetometer consists of a 20 mm flux transformer that is inductively coupled to the high-T_c SQUID, as described in [3].

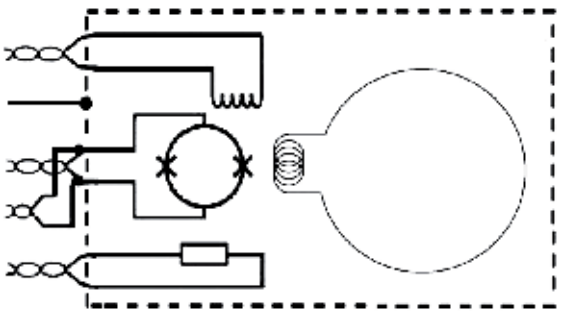

Figure 17. Schematic diagram of a vacuum-tight encapsulated SQUID with a superconducting flux transformer, a feedback coil, a heater and a grounded RF shield.

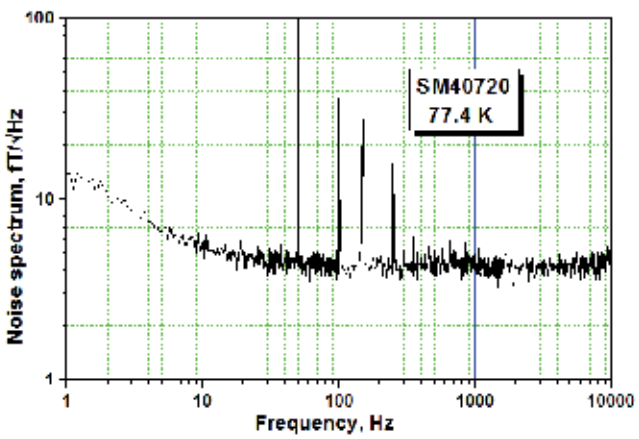

Figure 18. Noise spectrum of an encapsulated HTM-D20 magnetometer in a superconducting shield.

A schematic diagram of an encapsulated SQUID flip-chip magnetometer is shown in Figure 17. The 10-turn modulation and feedback coil has a diameter of 3 mm and is coupled directly to the SQUID. The magnetometer has a magnetic field sensitivity of ~0.4 nT/Φ_0 and a magnetic field resolution of ~4 fT/√Hz at 77.4 K (see 18). The measurement of the noise spectrum was performed inside a 3-layer μ-metal shield and an YBCO superconducting shield.

http://dx.doi.org/10.5772/59364

In multi-channel SQUID systems, an important requirement is to prevent crosstalk between channels. Linearization of the output signal of each SQUID in a multichannel system is provided by modulation and feedback signals to each SQUID from its feedback coils. Parasitic inductive coupling between the feedback coil and the pick-up of the neighboring sensors should be minimized. Such coupling can be expressed in terms of crosstalk between the SQUID sensors in terms of the ratio between the flux induced by the feedback coil in a test sensor Φ_1 by a nearby inducing sensor and the flux read by the inducing sensor Φ_2:

$$\frac{\Phi_1}{\Phi_2} = \frac{M_{1,2}}{M_{1,1}} \approx \frac{\Phi_1^{pu}}{\Phi_2^{pu}}, \tag{2}$$

where Φ_1^{pu} and Φ_2^{pu} are the fluxes in the pick-up loops of these two sensors, $M_{1,1}$ is the mutual inductance between the feedback coil and the sensing coil of the inducing SQUID and $M_{1,2}$ is the mutual inductance between the feedback coil of the inducing SQUID and the sensing coil of the test sensor (see Figure 19).

Low crosstalk operation of SQUID arrays requires low values of $M_{1,2}$ and at the same time high values of $M_{1,1}$. The highest value of $M_{1,1}$ is generally provided by coupling the relatively large feedback coil to a pick-up loop that has a similar size, but in this case the value of $M_{1,2}$ is unacceptably high. With a fixed size of feedback coil, any increase in $M_{1,1}$ results in an increase in $M_{1,2}$. In this work, we propose a 3-mm multi-turn feedback coil that is inductively coupled to a 3-mm direct coupled pick-up loop of the SQUID [3].

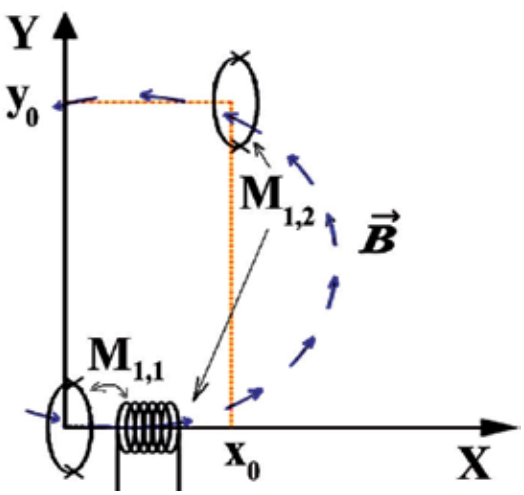

Figure 19. Schematic diagram of the setup for measuring crosstalk.

The feedback coil can be described as a magnetic dipole with a magnetic moment. $|\vec{m}|=IN\pi r^2$ and a magnetic field

$$\vec{B}=\frac{\mu_0}{4\pi}\left[\frac{3(\vec{m}\vec{L})\vec{L}}{L^5}-\frac{\vec{m}}{L^3}\right], \tag{3}$$

where $\vec{L}$ is the distance from the dipole to the point of measurement, $\mu_0=4\pi\ 10^{-7}$ H/m, N=10 is the number of turns in modulation coil, and r=1.5 mm is the radius of the feedback coil and the pick-up loop of the SQUID. The crosstalk is:

$$\frac{\Phi_1^{pu}}{\Phi_2^{pu}}\approx\frac{\mu_0 m}{4\pi\Phi_2^{pu}}\int_{y_0-R}^{y_0+R}\int_{-\sqrt{R^2-(y-y_0)^2}}^{\sqrt{R^2-(y-y_0)^2}}\frac{2x_0^2-y^2-z^2}{\left(x_0^2+y^2+z^2\right)^{5/2}}dzdy, \tag{4}$$

where R=1 cm is the radius of the pick-up loop of the neighboring magnetometer. The flux Φ_2 induced by the feedback coil in the pick-up loop of the inducing SQUID is:

$$\Phi_2^{pu}\approx\frac{\mu_0 m r^2}{2\left(r^2+x_0^2\right)^{3/2}}. \tag{5}$$

The result of the calculation of Eqs. (4) and (5) is shown in Figure 20, while experimentally measured data for Φ_1/Φ_2 are shown in Figure 21.

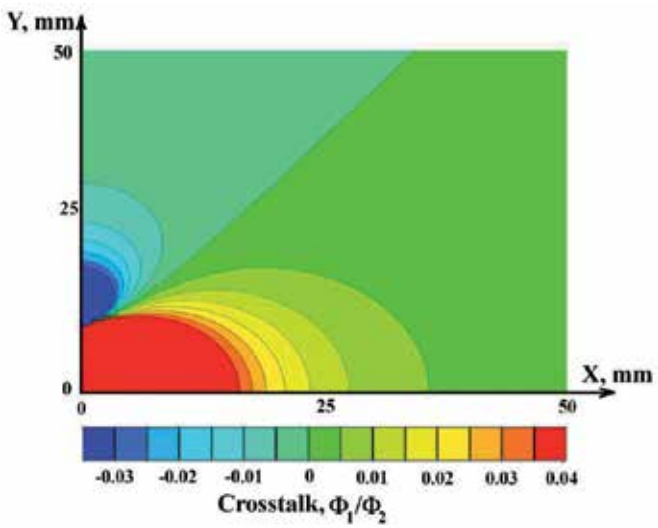

Figure 20. Crosstalk calculation according to Eqs. (4) and (5).

http://dx.doi.org/10.5772/59364

A crosstalk of below 1 % was achieved at distances of more than 30 mm in both orientations. This measurement confirms the possibility to build close-packed arrays of high-T_c SQUID magnetometers with the proposed configuration of feedback coil.

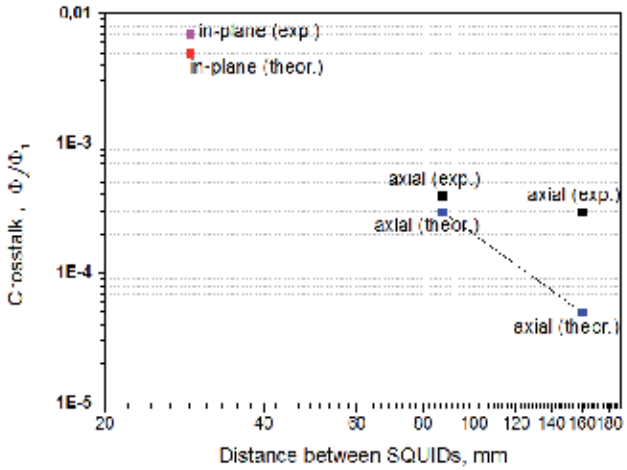

Figure 21. Experimentally measured crosstalk for different positions of neighbouring sensors and corresponding estimations: 1.) (■, ■) for a coplanar orientation (along the Y-axis in Figure 19) and 2.) (■, ■) for an axial orientation (along the X-axis).

In order to take full advantage of high-T_c SQUIDs, they should be placed in a dense array as close as possible to the scalp and to neighboring sensors. More than 100 encapsulated HTM-D20 magnetometers can be arranged around the head of an adult human (see Figure 22). The problem is the variety of individual sizes of heads that should be accommodated in a mechanically adjustable MEG system to maintain close proximity of the sensors to the scalp.

Figure 22. Example of positioning more than 100 encapsulated HTM-D20 magnetometers around a 3D model of the head of an adult human.

In principle, each channel can be placed in an individual cryostat with a small area at its lower end and individually adjusted to the scalp [36]. The advantage of such a segmented helmet construction is the possibility to realize a SQUID-to-scalp separation down to ~3 mm by using a very thin wall at the bottom end of a small cryostat. The main disadvantage is the increased tangential separation between the channels due to the sidewalls of the cryostat, leading to the attenuation of high spatial frequencies in the MEG signals. Multiple cryogen transfers and cryostat costs are less critical for high-T_c systems when compared to the low-T_c systems suggested in [36]. One can use, for example, a single central reservoir with a solid and liquid nitrogen mixture at a triple point temperature of 63.15 K and flexible leads for controlled temperature transfer to the sensors of the individual channels. This approach would solve the problem of vibration-free cooling of the sensors, which is especially important for MEG systems.

Another approach is to use several multi-channel systems with individual cryostats with near-flat bottom ends. Each cryostat can then enclose, for example, 7 signal channels, as achieved in a dual seven-channel low-T_c MEG system from Biomagnetic Technologies, Inc. (see Figure 2 in [37]). Such a configuration can be used for small region recording by high-T_c MEG system and can have advantages in spatial resolution when compared to a low-T_c MEG system and a high resolution EEG system [38].

The high-T_c sensors may be placed very close to the scalp by locating them in the vacuum space of the cryostat, as shown schematically in Figure 23. In this case, the sensors are fixed inside thermal conducting sockets and cooled sidewards. The thermal radiation shields between the sensors and the warm wall are not shown here. Alternatively, the sensors can be placed inside individual dimples on the other side of the cold wall, preferably immersed in liquid nitrogen.

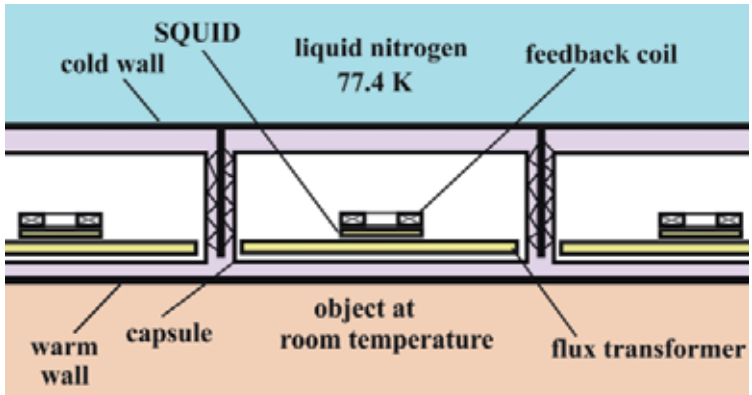

Figure 23. Schematic view of an array of HTM-D20 magnetometers cooled sidewards in the vacuum space of a liquid nitrogen cryostat.

When constructing the cryostat holder or gantry for a multichannel high-T_c MEG system, one should take into account that the density of liquid nitrogen (~0.8 kg/liter) is much higher than that of liquid helium (~0.128 kg/liter). A typical 50 liter cryostat for MEG would be ~33 kg

http://dx.doi.org/10.5772/59364

heavier if it would be filled with liquid nitrogen. This may require modifications of contemporary gantries for low-T_c MEG systems.

Acknowledgements

The authors gratefully acknowledge D. Meertens and R. Speen for technical assistance and the German IB-BMBF project 01DJ13014 for partial financial support.

Author details

M. I. Faley[1,4], O. M. Faley[2,4], U. Poppe[3], U. Klemradt[2,4] and R. E. Dunin-Borkowski[1,4]

*Address all correspondence to: m.faley@fz-juelich.de

1 Forschungszentrum Jülich GmbH, Jülich, Germany

2 RWTH Aachen University, Aachen, Germany

3 CEOS GmbH, Heidelberg, Germany

4 Jülich-Aachen Research Alliance in Future Information Technologies (JARA-FIT), Germany

References

[1] Wu, M. K. et al. Superconductivity at 93 K in a new mixed-phase Y-Ba-Cu-O compound system at ambient pressure. Phys. Rev. Lett. 1987;58 908–912.

[2] Li Y., Reeves J., Xiong X., Qiao Y., Xie Y., Hou P., Knoll A., Lenseth K., and Selvamanickam V., Fast growth process of long-length YBCO coated conductor with high critical current density. IEEE Trans. Appl. Supercond. 2005;15(2) 2771-2774.

[3] Faley M. I., Poppe U., Dunin-Borkowski R. E., Schiek M., Boers F., Chocholacs H., Dammers J., Eich E., Shah N. J., Ermakov A. B., Slobodchikov V. Yu., Maslennikov Yu. V., and Koshelets V. P. High-T_c DC SQUIDs for magnetoencephalography, IEEE Trans. Appl. Supercond., 2013;23(3) 1600705(5).

[4] Faley M. I. Epitaxial oxide heterostructures for ultimate high-T_c quantum interferometers. In Adir Luiz A. (ed.) Applications of High-T_c Superconductivity. Rijeka: InTech; 2011 p.147-176. http://www.intechopen.com/books/show/title/applications-of-high-tc-superconductivity. (accessed 12 September 2014).

[5] Commonwealth Scientific and Industrial Research Organisation. CSIRO: LANDTEM: helping to unearth A$6bn dollars in mineral deposits. http://www.csiro.au/Organisation-Structure/Divisions/CMSE/Our-stories/Landtem.aspx. (accessed 12 September 2014).

[6] Tanaka S., Fujita H., Hatsukade Y., Nagaishi T., Nishi K., Ota H., Otani T., and Suzuki S. High Tc SQUID Based Metallic Contaminant Detection System for Beverage or Ground Meat, IEEE Trans. Appl. Supercond. 2007;17(2) 756-759.

[7] Huang K.-W., Chieh J.-J., Lin I.-T., Horng H.-E., Yang H.-C. and Hong C.-Y., Anti-CEA-functionalized superparamagnetic iron oxide nanoparticles for examining colorectal tumors in vivo. Nanoscale Research Letters. 2013;8 413(8).

[8] Szot K., Dittmann R., Speier W., and Waser R. Nanoscale resistive switching in $SrTiO_3$ thin films. Phys. Stat. Sol. 2007;1(2) R86–R88.

[9] Cen C., Thiel S., Hammerl G., Schneider C. W., Andersen K. E., Hellberg C. S., Mannhart J. and Levy J. Nanoscale control of an interfacial metal–insulator transition at room temperature. Nature Materials. 2008;7 298-302.

[10] Sawa A. (2008). Resistive switching in transition metal oxides, Materials Today, Vol. 12, N.6, pp.28-36.

[11] Szot K., Bihlmayer G., Speier W., Chapter 4-Nature of the resistive switching phenomena in TiO_2 and $SrTiO_3$: Origin of the Reversible Insulator–Metal Transition. Solid State Physics. 2014(65) 353-559.

[12] Shkuratov S. I., Mesyatz V. G., Ivanov S. N. and Yumaghuzin Yu.M., Field emission electron spectroscopy of high temperature superconductors. Superconductivity: Physics, Chemistry, Technique. 1990;3(6) 1145-1221 (in Russian).

[13] Hirano T., Ueda M., Matsui K.-i., Fujii T., Sakuta K., and Kobayashi T., Dielectric properties of $SrTiO_3$ epitaxial film and their application to measurement of work function of $YBa_2Cu_3O_y$ epitaxial film. Jpn. J. Appl. Phys. 1992;31 1345.

[14] Li K., Wen Z., Wu D., Zhai H. and Li A., Bipolar resistive switching based on $SrTiO_3/YBa_2Cu_3O_7$ epi-layers, J. Phys. D: Appl. Phys. 2013(46) 035308.

[15] Yang Q., Zhang H., Dai Q., Nie R. and Wang F. The abnormal temperature-dependent rectification effect in $BiFeO_3/YBa_2Cu_3O_x$ heterostructures. Journal of Physics: Conference Series. 2014;507 012052(5).

[16] Poppe, U., Klein, N., Dähne, U., Soltner, H., Jia, C. L., Kabius, B., Urban. K., Lubig, A., Schmidt, K., Hensen, S., Orbach, S., Müller, G., & Piel, H. Low resistivity epitaxial $YBa_2Cu_3O_7$ thin films with improved microstructure and reduced microwave losses, J. Appl. Phys., 1992;71 5572-5578.

[17] Faley M. I., and Poppe U. Sputtering sources for high-pressure sputtering with large targets and sputtering method. Patent WO2012051980 (26.04.2012),

US20130199924A1 (08.08.2013), CN 103168338 A (19.06.2013). Priority date 22.10. 2010.

[18] Erni R., Rossell M. D., Kisielowski C., and Dahmen U. Atomic-Resolution Imaging with a Sub-50-pm Electron Probe, Phys. Rev. Lett. 2009;102 096101.

[19] Uhlemann S., Müller H., Hartel P., Zach J., and Haider Max. Thermal Magnetic Field Noise Limits Resolution in Transmission Electron Microscopy, Phys Rev. Lett. 2013;111 046101.

[20] Faley M. I. and Poppe U. Supraleitender Magnetfeldstabilisator, Patent pending DE102014003536. (2014).

[21] Buckel W. and Kleiner R. Supraleitung. (2013). ISBN 978-3-527-41139-9.

[22] The Conductus® Superconducting Wire Manufacturing Process: http:// www.suptech.com/the_conductus_process_n.php. (accessed 12 September 2014).

[23] Oisjoen F., Schneiderman J. F., Figueras G. A., Chukharkin M. L., Kalabukhov A., Hedstrom A., Elam M., Winkler D. High-T_c superconducting quantum interference device recordings of spontaneous brain activity: Towards high-Tc magnetoencephalography. Applied Physics Letters. 2012;100 132601.

[24] Peplow M. US bill would keep helium store afloat. Nature. 2013;497 168–9.

[25] Good J. Comment: Solving the liquid helium problem. Materials Today. 2014;17(1) 2-3.

[26] Faley M.I., Poppe U., Urban K., Paulson D.N., and Fagaly R.L. A new generation of the HTS multilayer DC-SQUID magnetometers and gradiometers. Journal of Physics: Conference Series. 2006;43 1199-1202.

[27] "Elekta Neuromag® System Hardware", Technical manual, Revision F (2005).

[28] Schneiderman J.F. Information content with low-vs. high-Tc SQUID arrays in MEG recordings: The case for high-Tc SQUID-based MEG. Journal of Neuroscience Methods. 2014;222 42– 46.

[29] Dammers J., Chocholacs H., Eich E., Boers F., Faley M., Dunin-Borkowski R. E. and Shah N. J. Source localization of brain activity using helium-free interferometer. Appl. Phys. Lett. 2014;104 213705.

[30] Faley M.I., Meertens D., Poppe U., Dunin-Borkowski R.E. Graphoepitaxial Josephson junctions and DC SQUIDs. 14th International Superconductive Electronics Conference (ISEC) 7-11 July 2013, IEEE Xplore Digital Library. 2013 1-3. doi: 10.1109/ISEC. 2013.6604264.

[31] Faley M. I. Reproduzierbarer Stufen-Josephson-Kontakt. Patent DE 102012006825 A1 (10.10.2013).

[32] Mitchell E. E. and Foley C. P. YBCO step-edge junctions with high I_cR_n. Supercond. Sci. Technol. 2010;23 065007.

[33] Clarke J., "SQUID Fundamentals", in: H. Weinstock (Ed.), SQUID Sensors: Fundamentals, Fabrication and Applications (NATO ASI Series E: Applied. Science. 329), Kluwer Academic, Dordrecht, 1996 p.1–62.

[34] Schmelz M., Stolz R., Zakosarenko V., Anders S., Fritzsch L., Roth H., Meyer H.-G. Highly sensitive miniature SQUID magnetometer fabricated with cross-type Josephson tunnel junctions. Physica C. 2012;478 77–80.

[35] Faley M. I., Poppe U., Urban K., Paulson D. N., Starr T., and Fagaly R. L. Low noise HTS dc-SQUID flip-chip magnetometers and gradiometers. IEEE Transactions on Appl. Supercond. 2001;11(1) 1383-1386.

[36] Matlashov A., Bakharev A., Zhuravlev Y., and Slobodchikov V. Biomagnetic multichannel system consisting of several self-contained autonomous small-size units. In: Koch H. and Lübbig H. (ed.) Superconducting Devices and Their Applications. Berlin: Springer-Verlag; 1992;64 511-516.

[37] Fagaly R. L. Neuromagnetic instrumentation. In: Sato S. (ed.) Advances in Neurology. New York: Raven Press; 1990;54: Magnetoencephalography 11-32.

[38] Malmivuo J. Comparison of the Properties of EEG and MEG in Detecting the Electric Activity of the Brain. Brain Topography. 2012;25 1–19.

Chapter 6

High Critical Current Density MgB_2

Wenxian Li and Shi-Xue Dou

Additional information is available at the end of the chapter

http://dx.doi.org/10.5772/59492

1. Introduction

The highest critical transition temperature (T_c) among all the intermetallic superconductors in that was discovered MgB_2 has changed the previous approaches to the theory of superconductivity because the T_c limit in metallic superconductors had been believed to be ~ 30 K, which is predicted by the Bardeen-Cooper-Schrieffer (BCS) theory [1]. In the BCS theory of superconductivity [2, 3], the expression for T_c is derived as $T_c = \theta e^{(-1/\lambda_{eff})}$, where θ is always equal to the MgB_2 Debye temperature, θ_D. λ_{eff} is defined as the electron and phonon coupling constant $\lambda = N(E_F) \times V$. $N(E_F)$ is the normal state electron number density the Fermi surface, and V is the average electron interaction matrix element corresponding to the attraction. A weak coupling, $\lambda << 1$, is assumed to exist between the electrons and phonons in the initial BCS theory. In this case, the value of T_c is limited to $T_c \approx 30$ K. According to the BCS theory, an element or compound with larger $N(E_F)$, V, and θ_D has high T_c value. However, θ_D of MgB_2 is comparable to those of other diborides and other light materials. Furthermore, the $N(E_F)$ is relatively low because of the absence of d-electrons. Thus, the unusually high T_c in MgB_2 has confused researchers with respect to the origin of its superconductivity. Considerable theoretical and experimental work has been conducted to explore the superconducting mechanism in MgB_2.

MgB_2 is the first superconductor to be proved to have two distinct superconducting gaps in its superconducting state [4]. Initially, an unconventional exotic superconducting mechanism was suggested for the material [5, 6]. Then, other researchers proposed hole superconductivity, which is similar to what occurs in high temperature superconductors (HTS), based on the fact that holes are the dominant charge carriers in the normal state [7, 8]. MgB_2 has now been accepted as a phonon-mediated BCS type superconductor. The superconductivity is attributed to selective coupling between specific electronic states and specific phonons, such as the E_{2g} mode. The unusually high T_c value arises from the strong phonon anharmonicity.

INTECH
open science | open minds

© 2015 The Author(s). Licensee InTech. This chapter is distributed under the terms of the Creative Commons Attribution License (http://creativecommons.org/licenses/by/3.0), which permits unrestricted use, distribution, and reproduction in any medium, provided the original work is properly cited.

Choi *et al.* have calculated the phonon frequencies and electron-phonon interactions from frozen phonon calculations at all the symmetry points of the Brillouin zone [9]. Six non-acoustic modes at the Brillouin zone centre Γ are divided into four distinct phonon modes based on the point symmetry of the lattice. The two vibrations along the *c*-axis are singly degenerate modes of A_{2u} and B_{1g}. For the A_{2u} mode, both Mg and B move in opposite directions along *c*. For B_{1g}, the B atoms move in opposite directions, while the Mg is stationary. The other two modes along the *x* or *y* directions involving only in-plane motions are doubly degenerate. The vibration of Mg and B planes in opposite directions along the *x* or *y* directions is E_{1u} mode. Mg atoms are stationary in the E_{2g} mode, while B atoms exhibit a breathing vibration in the *x* or *y* directions. This mode is highly anharmonic. The theoretical vibration energy of the E_{2g} mode is around 75 meV [10, 11], which is in agreement with the results from Raman measurements [12, 13].

MgB_2 is easy to make into bulk, wire, tape, and thin film forms. However, the critical current density (J_c) of pristine MgB_2 drops rapidly in high magnetic field due to the weak pinning forces and low upper critical field (H_{c2}). Many techniques have been employed to improve the application potential of MgB_2, such as chemical doping, irradiation, thermo-mechanical processing, and magnetic shielding. Although the critical current density, upper critical field, and irreversibility field (H_{irr}) have been greatly increased [14], many difficulties need to be overcome for further application. The origin of the flux pinning force and relevant fabrication techniques will be discussed in this work. Lattice distortion is found to be one of the most effective sources of flux pinning centers in pure MgB_2. Then, the combined effects of connectivity and lattice disorder on the flux pinning force are investigated based on nanosize SiC doped MgB_2.

The depairing current density, J_d, can be estimated from the Ginzburg-Landau (GL) formula:

$$J_d = \Phi_0 / \left[3 / \left(\sqrt{3} \right) \pi \mu_0 \lambda^2 (T) \xi (T) \right], \tag{1}$$

where Φ_0 is the flux quantum, μ_0 the permeability of vacuum, λ the penetration depth, and ξ the coherence length [15]. However, it is not the theoretical maximum [16]. With the help of optimized pinning, about 15% of J_d can be obtained at low magnetic fields in superconductors [17, 18]. The high field values for pure MgB_2 are λ = 80 nm and ξ = 12 nm, respectively. J_d at zero K is estimated as ~1.3×10^8 A.cm^{-2}. The contribution from π-band charge carriers to the depairing current density is quite low, only about 10% [16], and the interaction energy induces the difference from the high field value. The depairing current is reduced in samples with defects because of the increased λ values [18].

The grain boundaries in MgB_2 do not show the weak link effect, and clean grain boundaries are not obstacle to supercurrents [19, 20]. On the other hand, dirty grain boundaries do potentially reduce the critical current [21]. Insulating phases on the grain boundaries, such as MgO, boron oxides [22] or boron carbide [23], normal conducting phases [24], porosity, and cracks [25], can further reduce the cross-section effective of supercurrents. The high porosity in *in-situ* prepared MgB_2 is responsible for its low density, only about half (or less) of its theoretical value [26].

http://dx.doi.org/10.5772/59492

The concept of connectivity, A_{con}, has been introduced to quantify the effective cross-section (σ_{eff}) for supercurrents [21, 27]: $A_{con} = \sigma_{eff} / \sigma_0$, where σ_0 is the geometrical cross-section. The connectivity is estimated from the phonon contribution to the normal state resistivity through $A_{con} \approx \Delta\rho_{theo}/\Delta\rho_{exp}$, with $\Delta\rho_{theo} \approx 9\ \mu\Omega$ cm. This estimate is based on the assumption that σ_{eff} is reduced equivalently in the normal and superconducting state [18]. The supercurrents are limited by the smallest effective cross-section along the conductor. A single large transverse crack can reduce strongly J_c, while only slightly increases the resistivity of a long sample. Unreacted magnesium decreases $\Delta\rho_{exp}$ [28] and the effective paths for supercurrents. The thin insulating layers located on grain boundaries can decrease the effective connectivity A_{con}, inducing high $\Delta\rho_{exp}$, although this kind of defect is transparent to supercurrents. The $\Delta\rho_{theo}$ values within the grains depend on the defects and strain in the grains. Sharma observed negative $\Delta\rho_{exp}$ in highly resistive samples [29]. Despite these objections, A_{con} is very useful for estimating the connectivity of samples if the resistivity is not too high. A clear correlation between the resistivity and the critical current was found in thin films [27]. It should be noted that this procedure is not always reliable, although it offers a possibility for understanding the influences of the connectivity on the supercurrent [18].

The *in-situ* route is a practical technique to improve the H_{c2} and J_c performance of MgB_2 using magnesium or MgH_2 as the precursor material [30-39], which reacts with boron after mixing and compacting. Low annealing temperature generates MgB_2 samples with small grains [25, 40-52] due to the poor crystallinity, and the great amount of grain boundaries result in strong pinning and high H_{c2}. Magnesium deficient samples can be fabricated by adjusting the stoichiometry of the precursor materials. This method can generate strong lattice strain in MgB_2, which decreases T_c, and increases H_{c2} [44, 53-56]. On the other hand, an excess magnesium ratio in the raw materials can compensate for the evaporation loss of Mg due to its low melting temperature and the reaction loss due to the reaction with oxygen or the sheath material. The morphology and particle size of the precursor magnesium powders are crucial for the superconductivity and superconducting performance of the final MgB_2 [57]. The grain size of the initial boron powder also has a significant influence on the MgB_2 samples. Some researchers have employed ball milling and mechanical alloying of the magnesium and boron mixture, reducing the grain size and enhancing the critical supercurrent [55, 58-65].

The reaction kinetics between magnesium and boron can be modified by chemical or compound dopants [66], which influence the grain shape and size [67, 68], the secondary phases [69], MgB_2 density [70], and the element stoichiometry [71]. Carbon doping is one of the most promising methods to improve the superconducting performance of MgB_2. The carbon sources include B_4C [72, 73], carbon [52, 66, 67, 74], carbon nanotubes [75-78], nanodiamonds [78, 79], NbC [80], SiC [41, 51, 57, 66, 72, 81-89], and organic compounds [39, 47, 90]. SiC is one of the most promising dopants because it can react with magnesium and boron to form C doped MgB_2 at quite low temperatures (600 °C), based on the dual reaction model [66]. Higher processing temperatures are necessary for most of the other carbon sources, leading to grain growth and worse pinning. Comparable results to those with SiC have also obtained, however, with nanoscale carbon powder [91], stearic acid [92], and carbon nanotubes [76].

The *in-situ* technique also suffers from its disadvantage of low mass density, which is originates from the annealing process, because the precursor powder has a lower density than MgB_2. High pressure synthesis increases the density [93, 94]. On the other hand, the density of *ex-situ* materials is usually close to the real density of MgB_2 [94] and can be further improved by hot isostatic pressing (HIP) [91, 95, 96]. However, the grain size of *ex-situ* produced materials is comparatively large and inhomogeneous due to the post annealing [97, 98]. Small grains (~ 100–200 nm) have also been reported [99]. A high temperature heat treatment is necessary for the *ex-situ* process to improve the connectivity [99-102]. This heat treatment leads to recrystallization and H_{c2} reduction [25]. It is concluded that disorder induced by the low temperature processing is insufficient for high superconducting performance of the *ex-situ* MgB_2. Furthermore, thermally stable defects, such as dopants, are necessary for enhancing the high field performance [18].

2. Thermal-strain-induced high J_c in high density SiC-MgB_2 bulk

The connectivity is considered to be a critical issue for improving the J_c of MgB_2 based superconductors. Furthermore, an efficient flux pinning force is crucial for high magnetic field application. Here, we employed an *in-situ* diffusion process to make high density MgB_2 bulks and investigate the efficiency of the high flux pinning force induced by lattice thermal strain [103]. Microstructural analysis and Raman scattering measurements were employed to investigate the origins of the huge flux pinning force. Doping nano-SiC particles into MgB_2 has been proven to be particularly effective in significantly enhancing J_c, H_{irr}, and H_{c2} [14, 104, 105]. In contrast to chemical doping effects, tensile stress is believed to act as a source of strong flux pinning centers when there is no reaction between SiC and MgB_2. Both the J_c and T_c are improved by thermal strain on the interface between SiC and MgB_2 during the diffusion process [106] and hybrid physical-chemical vapor deposition (HPCVD) [107]. The influences of the stress field on the flux pinning force and the electron-phonon coupling constant are discussed to clarify the superconducting performance of high density SiC-MgB_2 composite fabricated through the diffusion method.

Crystalline B with 99.999% purity was pressed into pellets or mixed with 10wt% SiC particles and then pressed into pellets. The pellets were sealed in iron tubes and padded with 99.8% Mg powder. The Mg to B atomic ratio was 1.15:2.0. The diffusion process is time dependente. The sintering condition were 1123 K for 10 h under a flow of high purity argon gas to achieve fully reacted MgB_2 bulks. Then the samples were cooled down to room temperature. X-ray diffraction (XRD) was employed to characterize the phases, and the results were refined to determine the *a*-axis and *c*-axis lattice parameters and the lattice distortion. Microstructure observations were performed with a transmission electron microscope (TEM). The magnetic J_c was derived from the height of the magnetization loop ΔM using the Bean model: $J_c = 15\Delta M/[\pi a^3 h)]$, where a and h are the radius and height of a cylindrical sample. The T_c value could be deduced from the temperature dependence curve of the magnetic susceptibility $M(T)$. To observe the temperature effects of lattice strain, Raman spectra were collected using a confocal laser Raman spectrometer (Renishaw inVia plus) under a 100× microscope. The excitation laser is Ar^+ 514.5 nm.

The density of the pure MgB_2 sample is about 1.86 g/cm^3, which is about 80% of the theoretical density. This value is much higher than those of the samples made by the *in-situ* process, which were less than 50%. The SiC-MgB_2 composite shows an even higher density of 1.91 g/cm^3 due to the SiC addition. Figure 1 shows the Rietveld refinement XRD patterns of the pure MgB_2 and the 10wt% SiC doped MgB_2 samples. In this case, SiC did not react with magnesium and boron to form C doped MgB_2 and Mg_2Si. The product is a SiC-MgB_2 composite. The Rietveld refinement analysis indicates that the unreacted SiC content was about 9.3wt%, similar to the SiC content in the precursor. This is consistent with the absence of Mg_2Si in the XRD pattern as shown in Figure 1. The result is different when the SiC-doped MgB_2 prepared by the *in-situ* technique [14, 41, 84], in which only a very small amount of SiC remaines, while Mg_2Si is always present due to the reaction of Mg with SiC. The *a*- and *c*-axis lattice parameters were 3.0850 Å and 3.5230 Å for pure MgB_2, and 3.0840 Å and 3.5282 Å for SiC doped MgB_2, respectively. The *a*-axis parameters are virtually equivalent for the two samples, whereas the *c*-axis one is slightly stretched in the SiC-MgB_2 composite. The phenomenon is different from the shortening of the *a*-axis parameter in *in-situ* processed SiC doped MgB_2, while the *c*-axis parameter remains unchanged [14, 89].

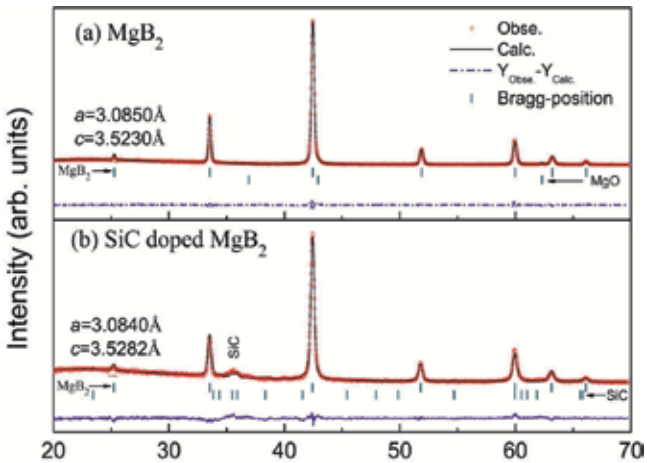

Figure 1. Rietveld refined XRD patterns of pure MgB_2 and 10wt% SiC doped MgB_2 samples made by the diffusion process at 850 °C for 10 h. The *a*-axis parameters are virtually the same for the two samples, whereas the *c*-axis parametar is stretched in the SiC-MgB_2 composite.

To explain the abnormal *c*-axis enlargement of the SiC-MgB_2 composite, the thermal expansion coefficients, α, of MgB_2 and SiC are considered. It is reasonable to assume that both the MgB_2 and the SiC are in a stress-free state at the sintering temperature of 1123 K due to the relatively high sintering temperature over a long period of time. However, the lattice parameters are determined by the thermal strain during the cooling process. The temperature dependences of the α values for MgB_2 and SiC are especially different. Figure 2(a) plots the $\alpha(T)$ for MgB_2 and SiC along the *a*- and *c*-axes, based on the data of References [108-111]. It clearly shows the weak temperature dependence of$\alpha(T)$ for SiC in both directions, whereas the changes are great for MgB_2 and are characterized by high anisotropy. The averaged $\alpha(T)$ is also huge in MgB_2 as

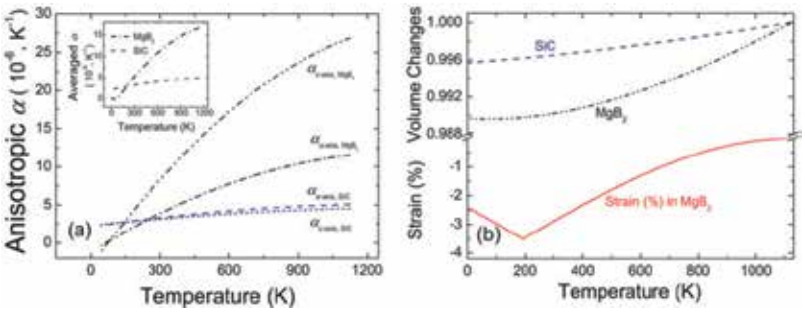

Figure 2. (a) Thermal expansion coefficients (α) along the a-axis and c-axis for MgB_2 and SiC as a function of temperature. The averaged α(T) values for MgB_2 and SiC are plotted in the inset. (b) Plots of the normalized lattice changes for MgB_2 and SiC, and the thermal strain in the matrix during cooling from 1123 K to 0 K.

shown in the inset of Figure 2(a). The α_{SiC} decreases slightly from 5×10^{-6}/K at 1123 K to 2.5×10^{-6}/K at 0 K, whereas the α_{MgB_2} drops quickly from 1.7×10^{-5}/K at 1123 K to zero at 0 K. Based on $\alpha(T)$, the normalized lattice change and lattice strain in the MgB_2 matrix of SiC-MgB_2 composite during cooling from 1123 K to 0 K can be derived, as shown in Figure 2(b). An assumption of Figure 2(b) is that the two phases are strongly connected and the volume shrinkage of MgB_2 is confined by the relatively stable SiC. The normalized lattice strain is estimated to be -0.55% in SiC-MgB_2 along the *c*-axis at room temperature. The negative value corresponds to tensile strain in the MgB_2. The large *c*-axis strain in the doped MgB_2 results in an enlargement in the *c*-axis by 0.15 % in comparison with pure MgB_2. As estimated from the Williamson-Hall model [112], the lattice strain is 0.208 and 0.306 along the *a*-axis, and 0.292 and 1.13 along the *c*-axis for pure and SiC-MgB_2, respectively. The lattice strain along the *c*-axis in the SiC-MgB_2 has increased from that of pure MgB_2 by a factor of 4, which is attributed to the high anisotropy in the thermal expansion coefficient of MgB_2.

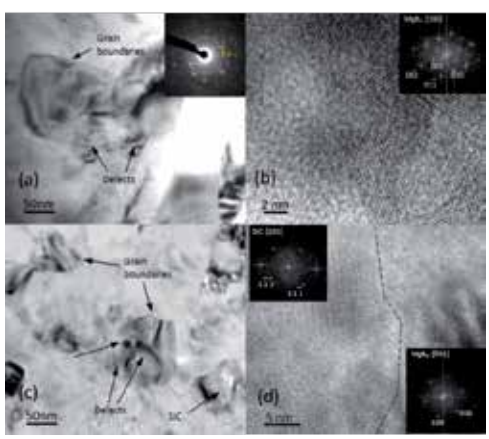

Figure 3. (a) Bright field TEM image of the pure MgB_2 with indexed SAD pattern (inset). (b) High resolution electron microscope (HREM) image of interface in pure MgB_2 with FFT pattern along the [100] axis (inset). (c) Bright field TEM image of SiC-MgB_2. (d) HREM image of interface in SiC-MgB_2 and FFT patterns of SiC and MgB_2 from each side of the interface. The dashed line shows the interface of SiC and MgB_2.

http://dx.doi.org/10.5772/59492

The unreacted SiC buried in the MgB_2 matrix is believed to be one of the most effective sources of strain, and the strongly connected interfaces of SiC and MgB_2 are the most effective flux pinning centers. The micro morphologies can be detected using TEM to explore the defects and grain boundaries both in the pure MgB_2 and in the SiC-MgB_2. Figures 3(a) shows a bright field image of pure MgB_2. A high density of defects, such as dislocations and lattice distortion, is observed in the MgB_2 phase, and the grain size is about 100 nm,as estimated from the grain boundaries. In contrast to with the highly porous structure in the MgB_2 samples [91], the samples made by the diffusion process are well connected with high density. The indexed selected area diffraction (SAD) image shows very pure polycrystalline MgB_2. A high resolution grain boundary image is shown in Figure 3(b). The interface is very clean and well connected. The indexed fast Fourier transform (FFT) pattern indicates that the right part parallels the (1 1 0) plane. The micro structure of SiC-MgB_2 is similar with that of pure MgB_2 with high density of defects. Furthermore, nanosize SiC particle are detected in the MgB_2 matrix as indicated in Figure 3(c). Figure 3(d) shows the interface of SiC and MgB_2. Based on the FFT analysis, the interface is marked with a dashed line on the image. The left side is a SiC grain paralleling the (1 0 1) plane and the right side is a MgB_2 grain paralleling the (0 0 1) plane. This kind of interface will impose tensile stress along the *c*-axis in MgB_2 because the thermal expansion coefficient for MgB_2 is highly anisotropic in the [001] direction, while that for SiC is nearly isotropic, which is responsible for the enlarged *c*-axis of MgB_2.

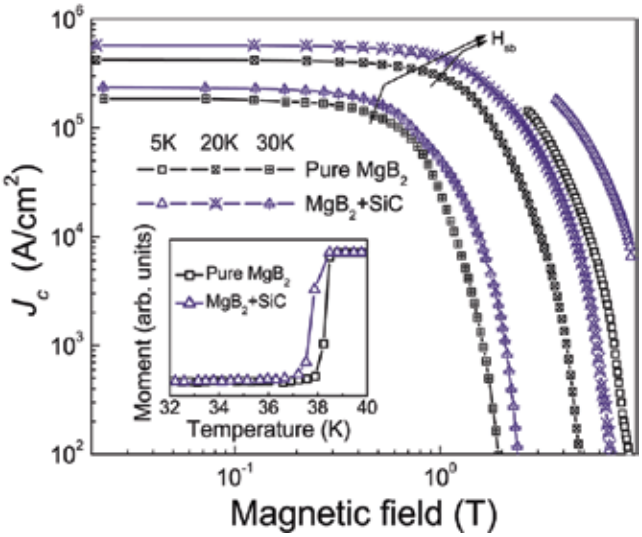

Figure 4. The magnetic J_c versus field at 5 K, 20 K, and 30 K for pure and nano-SiC doped samples. The inset shows the superconducting transitions of the two samples [103].

Based on the collective pinning model, [113], J_c is independent of the applied field in the single-vortex pinning regime (low magnetic field region: $H < H_{sb}$), where H_{sb} is the crossover field from single-vortex to small-bundle pinning. The J_c decreases exponentially in the small-bundle regime (high magnetic field: $H_{sb} < H < H_{irr}$). According to the dual model [14], the significant

effect of SiC doping on J_c comes from the high level of C substitution on the B planes, which is responsible for the reduction of the self-field J_c[104, 105]. However, the SiC-MgB_2 composite sample shows not only an improved in-field J_c, but also no degradation in self-field J_c, as indicated in Figure 4. The approximate H_{sb} values are also indicated on the J_c curves for 20 K and 30 K, although H_{sb} has not been detected at 5 K due to the relatively high supercurrents. The *in-situ* processed SiC doped MgB_2 normally shows a decrease in T_c of 1.5 to 2 K, [14, 104, 105], but this present SiC-MgB_2 composite sample features a small drop of 0.6 K, as shown in the inset of Figure 4. This phenomenon is attributed to the absence of any reaction between Mg and SiC, as well as the stretched MgB_2 lattice, as indicated by the XRD pattern [107].

To investigate whether the lattice strain is significant in SiC-MgB_2 during low temperature measurements to obtain $M(H)$ and $M(T)$ curves, Raman spectra were collected before and after the measurements. The Raman spectra for the pure MgB_2 are shown in Figure 5(a) and (b) to compare the cooling effects on the matrix. Both the spectra have been fitted with three peaks: ω_1, ω_2, and ω_3 [114-116]. Based on the previous results, ω_2 is the reflection of the E_{2g} mode at the Γ point of the Brillouin zone in the simple hexagonal MgB_2 structure (space group: *P6/mmm*), while ω_1 and ω_3 come from the lattice distortion. The effects of ω_1 are not discussed in the following analysis because of its small influence on the spectra. As indicated by the fitting parameters that are shown in Figure 5, both the peak centers and the full width at half maximum (FWHM) values show negligible differences before and after the low temperature measurements because of synchronic volume fluctuation. The weak temperature dependence of the Raman spectra for pure MgB_2 is in agreement with the results of Shi *et al* [117]. The ω_2 peak of the Raman spectrum of SiC-MgB_2 before the low temperature measurement has shifted to the low frequency of 585 cm^{-1}, as shown in Figure 6(a). The FWHM of the ω_2 peak increases from ~200 cm^{-1} to 210 cm^{-1}. Furthermore, the FWHM of the ω_3 peak increases from ~93 cm^{-1} to 125 cm^{-1}. The variations in both the Raman shift and the FWHM indicate strong lattice strain in the SiC-MgB_2 composite. Figure 6(b) shows the cooling effect on the Raman spectrum of SiC-MgB_2. The FWHM of the ω_2 peak further increases to 228 cm^{-1}, and the frequency of the ω_3 peak shifts to 770 cm^{-1}. These results suggest that the stress field is very strong during the low temperature measurements in the SiC-MgB_2 composite. Considering the stable defect structures in the sample at room temperature and the measurement temperatures, the high J_c performance is attributed to the thermal strain. Although the interface or grain boundaries themselves are effective flux pinning centers, the thermal strain provides more efficient flux pinning force, based on the comparison of the J_c values in pure the MgB_2 and the SiC-MgB_2 composite.

It should be noted that the broadened ω_2 peak in SiC-MgB_2 is a signal of strong electron-E_{2g} coupling, which is responsible for the high T_c in MgB_2. The electron-E_{2g} coupling constant is estimated from the Allen equation [118]: $\Gamma_2 = 2\pi\lambda_{E_{2g}} N(0)\omega^2_{E_{2g}}$, where Γ_2 is the ω_2 linewidth, $\lambda_{E_{2g}}$ is the strength of the electron-E_{2g} coupling, and $N(0)$ is the density of states on the Fermi surface. The experimental phonon frequency and linewidth are simply and directly related to the electron-phonon coupling constant (EPC), $\lambda_{E_{2g}}$. The total density of states (DOS) at the Fermi energy, E_F, of pure MgB_2 is taken as 0.354 states/eV/cell/spin. The σ band contribution is 0.15 and the π band is 0.204 [119]. $N(0)$ is assumed to be constant for the small changes of electrons

http://dx.doi.org/10.5772/59492

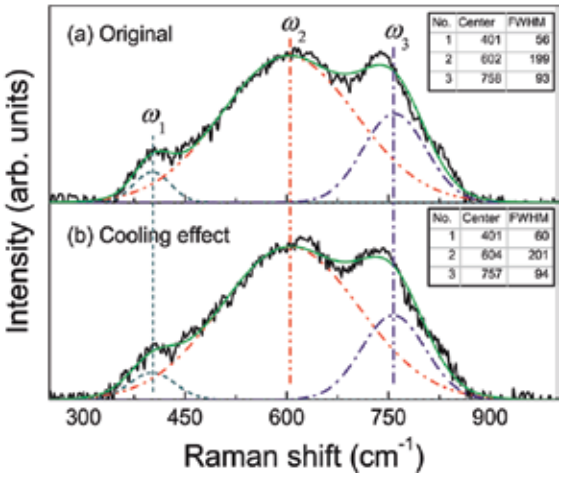

Figure 5. Fitting and experimental results for the normalized ambient Raman spectrum of MgB_2 sintered at 850 °C for 10 h (a), and the cooling effect on the Raman spectrum (b) [103].

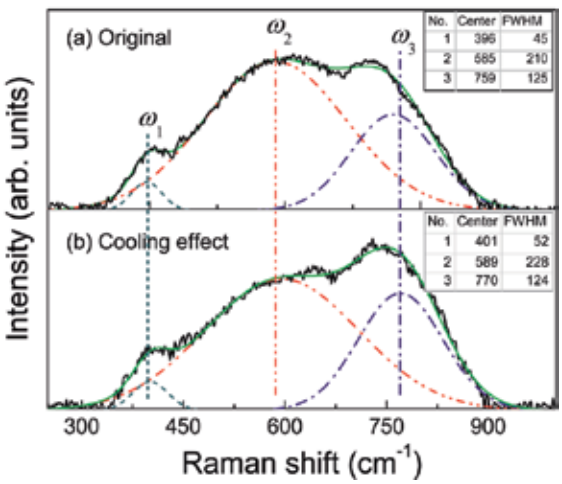

Figure 6. Fitting and experimental results for the normalized ambient Raman spectrum of SiC-MgB_2 sintered at 850 °C for 10 h (a), and the cooling effect on the Raman spectrum (b) [103].

and holes in MgB_2 and SiC-MgB_2. Taking the fitting values of the ω_2 peaks with cooling effects, the $\lambda_{E_{2g}}$ values for the pure MgB_2 and SiC-MgB_2 are 2.327 and 2.706, respectively. The $\lambda_{E_{2g}}$ of SiC-MgB_2 is just slightly higher than that of the pure MgB_2. However, the T_c of SiC-MgB_2 is slightly decreased compared to that of the pure MgB_2. The total EPC constants are degraded by the scattering effects of SiC impurities in the MgB_2 matrix, which can be estimated with the McMillan formula [120], as modified by Allen and Dynes:[121] $T_c = \frac{\langle \omega_{\log} \rangle}{1.2} \exp\left(\frac{-1.04(1+\lambda)}{\lambda - \mu^*(1+0.62\lambda)} \right)$, where $\langle \omega_{\log} \rangle = \left(390 \times \omega_{E_{2g}}^2 \times 690 \right)$ is the averaged phonon frequency [122], with 390 and 690 cm^{-1}

being the phonon frequencies of the other modes in the MgB_2 system [123], μ^* is the Coulomb pseudopotential, taken as equal to 0.13 [124], and λ is the total EPC constant. Taking these values, λ is calculated as 0.888 in pure MgB_2 and 0.886 in SiC-MgB_2, respectively. Although the values are very similar, the λ of MgB_2 is a little higher because of its low impurity scattering effects. It should be noted that the λ values were overestimated using the McMillan formula for the two-gap nature of MgB_2. However, the overestimations do not change the dependence of λ on the strain effect due to the main contribution of the σ-band. The residual resistivity of SiC-MgB_2 is 16 $\mu\Omega$ cm, but it is just 12 $\mu\Omega$ cm for pure MgB_2, due to the weak impurity scattering effects.

In summary, the thermal strain originating from the interface of SiC and MgB_2 is one of the most effective sources of flux pinning centers to improve the supercurrent critical density. The weak temperature dependence of the thermal expansion coefficient of SiC stretches the MgB_2 lattice as the temperature decreases. The thermal strain supplies much more effective flux pinning force than the interfaces and grain boundaries themselves. The low temperature effects on Raman spectra include very strong lattice stretching at the application temperature of MgB_2, which has benefits from both the J_c and the T_c behaviors.

3. High connectivity MgB_2 wires fabricated by combined *in-situ*/*ex-situ* process

The self-field critical current density, $J_c(0)$, of MgB_2 is much higher than for pure or doped samples processed with *in-situ* annealing [75, 81, 125-128]. $J_c(0)$ values have been reported as high as 3.5×10^7 A/cm^2 at 4.2 K and 1.6×10^8 A/cm^2 at 2 K in highly connected thin films made by HPCVD [129, 130]. The connectivity is much lower than the theoretical value in *in-situ* MgB_2 because the technique involves a liquid-solid phase reaction process with considerable shrinkage due to the high density of MgB_2 compared to the powder mixture of Mg and B [104, 115]. Although the diffusion process could increase the J_c of bulk samples, the $J_c(0)$ and disorder of wires and tapes cannot be improved using similar methods. Several research groups have reported possible techniques to increase the connectivity of *in-situ* filamentary tapes. High pressure sintering and cold high pressure densification (CHPD) can make it possible to fabricate high density wire and tape samples [96, 131, 132]. Nevertheless, neither HIP nor CHPD are suitable for long MgB_2 wires and tapes, and the J_c values are still lower than needed for practical application. Kováč et al. reported a mixed *in-situ*/*ex-situ* process to make MgB_2 wires, and it was found that the J_c was increased when the *ex-situ* powder ratio were 23% and 50% [133]. They used commercial MgB_2 powder from Alfa Aesar in this process with a very wide grain size distribution ranging from submicrometer size up to 100 μm. In this work, high quality home-made *ex-situ* powder was used to repeat the mixed *in-situ*/*ex-situ* process to develop MgB_2/Fe wires with high connectivity and strong disorder to increase both the low and high field J_c properties [134]. The home-made powder was fabricated through low temperature annealing, and the particle size was homogeneous and as small as ~200 nm. The J_c dependence on microstruc-

ture, connectivity, and disorder in MgB_2 wires was analyzed based on the microstructure observations.

MgB_2 wires were fabricated by the powder-in-tube (PIT) process using a ball-milled mixture of Mg (99%) and amorphous B (99%). The *in-situ* wires were sintered at 750, 850, 950, and 1050 °C for 30 min in high purity Ar and marked as 750in, 850in, 950in, and 1050in, respectively. The *in-situ* MgB_2 powder was sintered at 650 °C for 30 min in high purity Ar flow and then ball-milled. Then the PIT method was employed to fabricate *in-situ/ex-situ* combined MgB_2/Fe wires using 1:3 ratio of precursor powders to form a mixture of Mg and B powders. All the green wires were annealed at 750, 850, 950, and 1050 °C for 30 min in high purity Ar and marked as 750inex, 850inex, 950inex, and 1050inex, respectively.

The phases and microstructure were characterized by XRD (D/max-2200) and field emission gun scanning electron microscopy (FEG-SEM: JSM-6700F) at room temperature. The superconducting properties were detected from 5 K to 305 K using a Physical Properties Measurement System (PPMS: Quantum Design). The critical superconducting transition temperature, T_c, is defined as the onset point on the magnetic moment *vs.* temperature curve, $M(T)$, measured in a magnetic field of 25 Oe. The magnetic J_c was derived from the Bean model. The resistivity dependence on applied magnetic field and temperature, $\rho(H, T)$, was measured using the four-probe method with H from 0 T to 13 T applied perpendicularly to the current direction, from 5 K to 305 K. H_{c2} and H_{irr} were defined as the magnetic field values at 90% and 10% on the superconducting transition on the $\rho(H, T)$ curve, respectively. The active connectivity factor, A_F, was calculated based on the $\rho(H, T)$ behavior.

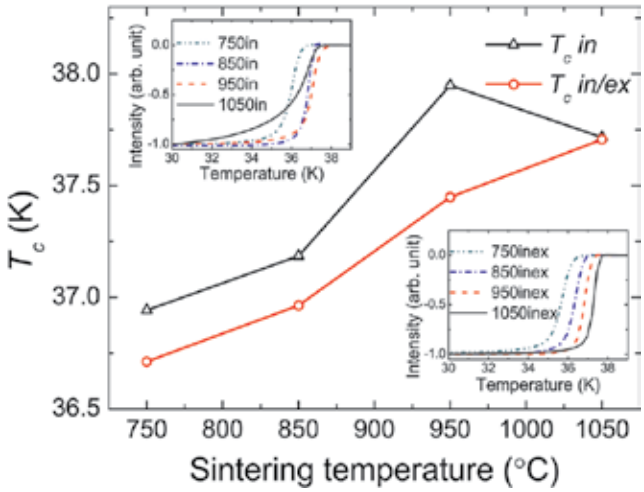

Figure 7. T_c dependence on sintering temperatures. The insets display the normalized magnetic moment dependence on measurement temperature for *in-situ* samples (upper) and for combined *in-situ/ex-situ* samples (lower) [134].

According to the indexed XRD patterns, the samples contain a small amount of MgO. The MgO contents are high in 950in, 1050in, and 1050exin compared with the other samples. The broad

transition widths from the normal state to the superconducting state of these samples confirm the high impurity contents, as shown in the insets of Figure 7. The 1050in transition width is ~7 K compared with the width of ~2 K for the other samples, which is attributed to the degraded connectivity of the magnetic flux due to the high MgO content. The *in-situ* sintered samples show higher T_c values by 0.5 – 1 K compared with the *in-situ/ex-situ* ones. The T_c of 1050in is similar to that of 1050inex because of the high amount of impurity phase. Ball milling of the raw materials induces a great amount of defects in the *in-situ/ex-situ* samples, which display lower T_c compared with the *in-situ* samples [135, 136]. The connectivity of the *in-situ/ex-situ* samples is worse than those of the *in-situ* samples judging from their big transition widths. The low amount of Mg evaporation may be responsible for the narrow transition width of 1050inex compared with that of 1050in because the stable precursor MgB_2 and low quantity of Mg in the raw materials reduce the magnesium loss during the sintering at 1050 °C.

Typical SEM images of the *in-situ* samples are shown in Figure 8. The grain size of 750in is about 300 nm, and the grains show an isolated distribution due to independent growth. 850in, 950in, and 1050in have big clusters of grains because the increasing sintering temperatures have extended the crystal growth time. Some clusters are as big as 1 μm in 1050in. The crystallinity is enhanced at higher sintering temperatures. A high sintering temperature induces raw magnesium evaporation and MgO formation, which can be observed as small white particles without contrast under SEM in 1050in.

The crystal shapes for the *in-situ/ex-situ* samples are irregular with a dispersed distribution of grain sizea, as shown in Figure 9. The grain size of 750inex is small because of the low sintering temperature. The recrystallization effect is triggered for 850inex, 950inex, and 1050inex, and big grains as large as 1 μm are observed. 1050in and 1050inex show similar microstructures because the high sintering temperature provides enough energy and a long time for the crystal growth.

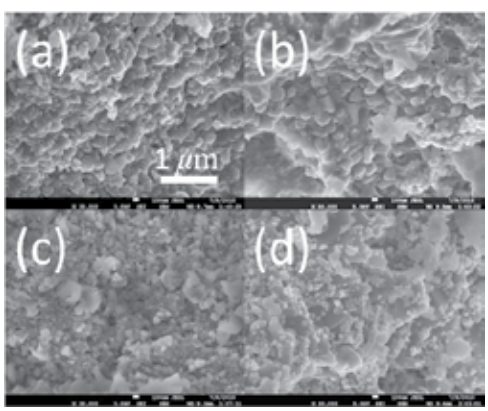

Figure 8. SEM images for the *in-situ* samples sintered at (a) 750 °C, (b) 850 °C, (c) 950 °C, and (d) 1050 °C. The crystal growth was improved gradually with increasing sintering temperature.

Figure 10 compares the J_c dependence on applied magnetic field measured at 5 K and 20 K. The J_c value of 1050in is the worst because of the high MgO content. The J_c performances of

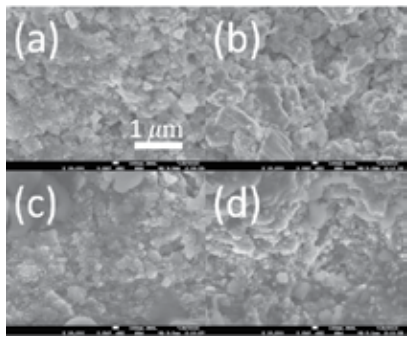

Figure 9. SEM images for the combined *in-situ/ex-situ* samples sintered at (a) 750 °C, (b) 850 °C, (c) 950 °C, and (d) 1050 °C. The grains are inhomogeneous due to the ball milled MgB_2 precursor and the recrystallization effects.

750in, 850in, 750inex, and 1050inex are quite similar over the whole field range. While the J_c deteriorated in 950in and 1050in under higher magnetic fields. 850inex and 950inex show amazingly high J_c properties. The J_c values at 5 K under 8 T magnetic field are around five times higher than those of the best *in-situ* samples. The inset of Figure 10 compares the low field performances measured at 20 K. The *in-situ* samples, except for 1050in, show competitive low field J_c. The high crystal quality of 950in is of benefit for its high self-field J_c performance. 750inex and 850inex show low self-field J_c values. While 950inex and 1050inex display improved J_c, the values are lower than the self-field J_c of 950in due to the high MgO contents.

The J_c performance depends on the flux pinning mechanism under different magnetic field intensities. The collective pinning model classifies the disorder-induced spatial fluctuations in the vortex lattice into three regimes based on the strength the magnetic field: e.g. single-vortex, small-bundle, large-bundle, and charge-density-wave type relaxation of the vortex lattice [113]. The practicable J_c of MgB_2 falls into the single-vortex pinning region and the small-bundle pinning region in the phase diagram. The connectivity determines the J_c performance in the single-vortex pinning regime because the effective charge carrier density is responsible for the self-field J_c, while H_{c2} and H_{irr} are responsible for the J_c performance in the small-bundle regime based on the disorder or defects.

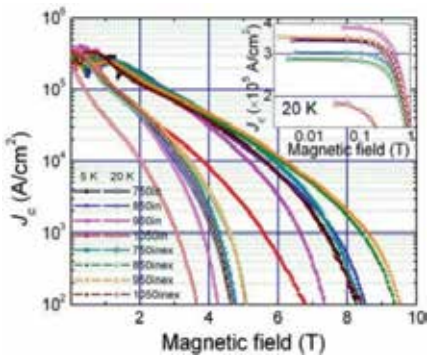

Figure 10. J_c dependence on applied magnetic field at 5 K and 20 K. The inset compares the self-field J_c behavior at 20 K [134].

A practical quantity to evaluate the connectivity is the active area fraction, A_F [21],

$$A_F = \frac{\Delta\rho_{\text{ideal}}}{\Delta\rho(300\text{K})}, \tag{2}$$

where,

$$\Delta\rho_{\text{ideal}} = \rho_{\text{ideal}}(300\text{K}) - \rho_{\text{ideal}}(40\text{K}) \approx 9\,\mu\Omega\,\text{cm}, \tag{3}$$

is the resistivity of fully connected MgB_2 without any disorder [18], and

$$\Delta\rho(300) = \rho(300K) - \rho(T_c). \tag{4}$$

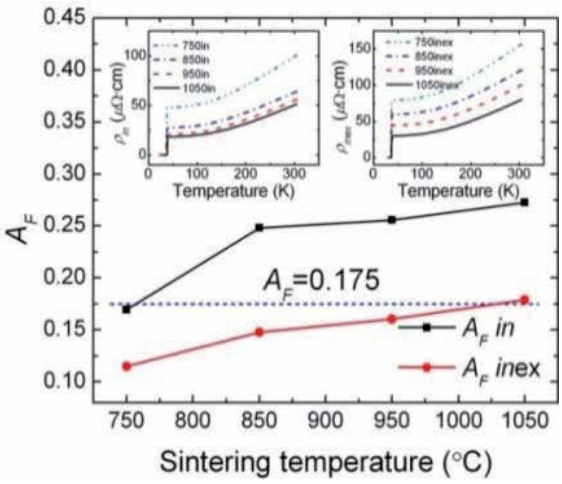

Figure 11. A_F dependence on sintering temperature. The short dashed line indicates A_F = 0.175. The upper left inset compares the resistivity of the *in-situ* samples. The upper right inset compares the resistivity of the combined *in-situ/ex-situ* samples [134].

Figure 11 compares the A_F of all the samples. All the samples show lower connectivity compared with those of ideal crystals, as indicated by the low A_F values. The A_F value of 750in is just 0.169, and high sintering temperature enhances the connectivity. It is ~ 0.26 for 850in. Higher sintering temperatures than 850 °C can improve the A_F slightly, which indicates that the connectivity is easy to improve for *in-situ* samples. Although the MgO content is high in 1050in, its high A_F value is attributed to sufficient crystallization. However, its low magnetic field J_c was degraded by MgO. The combined *in-situ/ex-situ* samples show rather low A_F values compared with the *in-situ* samples. The phenomenon is consistent with the high resistivity of the *in-situ/ex-situ* samples, as shown in the insets of Figure 11. The gradually improved

connectivity improves the A_F values for the *in-situ/ex-situ* samples due to the improved solid state reaction. The self-field J_c performances are also improved for 950inex and 1050inex.

The J_c performance in the small-bundle region depends on a strong flux pinning force. The flux pinning centers could be lattice distortion, most types of defects, and grain boundaries [110, 137]. The temperature dependences of H_{c2} and H_{irr} determine the strength of the pinning force, as shown in Figure 12. The high field J_c performance is in agreement with the H_{c2} and H_{irr} behavior. The 1050in sample shows the lowest H_{c2} and H_{irr} among all the samples. 850inex and 950inex show the highest H_{c2} and H_{irr}, which are consistent with their high J_c values in the small-bundle region. The *ex-situ* powder induces strong disorder and proper crystallization, which are responsible for the high H_{c2} and H_{irr} values.

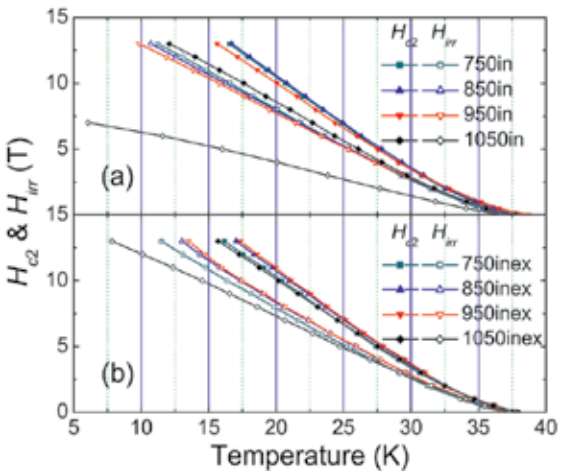

Figure 12. H_{c2} and H_{irr} of (a) the *in-situ* samples and (b) the combined *in-situ/ex-situ* samples [134].

In summary, both connectivity and disorder show strong influences on the J_c properties of MgB_2. The connectivity is responsible for the high effective charge carrier density, which determines the self-field J_c performance. The strong flux pinning force induced by defects and disorder is responsible for the promising J_c in high magnetic field. The enhanced J_c performances of 850inex and 950inex are attributed to the optimized connectivity and disorder. The J_c values obtained in this work are still far below the J_d value, ~8.7×10^8 A/cm^2 for pure MgB_2. The J_c improvement in MgB_2 should be explored based on the chemical doping effects and combined *in-situ/ex-situ* process.

4. Nano-SiC doped MgB_2 wires made by combined *In-Situ/Ex-Situ* process

The combined *in-situ/ex-situ* process has proved to be a promising technique for the fabrication of practical MgB_2 wires. The J_c of MgB_2 superconductors has been enhanced through many different kinds of dopants or additives [125], especially different carbon sources [75, 81,

126-128, 138, 139]. In this work, a mixed *in-situ/ex-situ* technique was employed to develop nano-SiC doped MgB_2 wires with high connectivity and strong flux pinning force to increase both the low and high field J_c properties [140]. The SiC particle size is another critical issue for introducing strong flux pinning forces into MgB_2. The size of SiC used in this work is smaller than the sizes used in previous research, and the J_c dependence on sintering temperature also shows a very different trend [81, 104, 141, 142].

The powder-in-tube (PIT) process was employed to make practical MgB_2 wires from a ball-milled mixture of Mg (99%), B (99%, amorphous), and SiC (< 15 nm).]The sample fabrication and characterization are similar to the techniques mentioned for the pure samples in the last section.

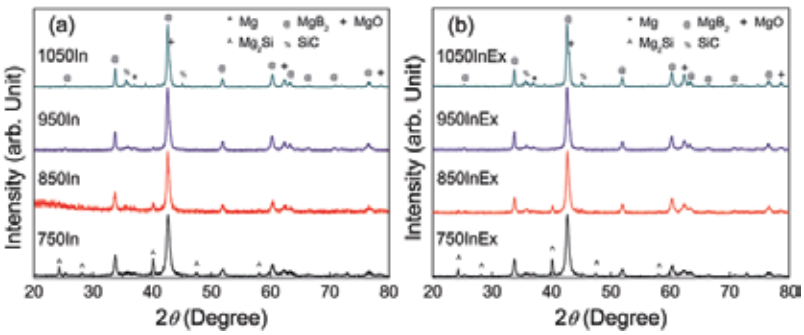

Figure 13. XRD patterns of nano-SiC doped MgB_2/Fe wires fabricated by (a) the *in-situ* technique and (b) the *in-situ/ex-situ* technique, with sintering at 750, 850, 950, and 1050 °C, respectively. All patterns were indexed with MgB_2, MgO, Mg_2Si, SiC, and Mg [140].

Figure13 shows the XRD patterns of the two batches of samples. According to the indexed XRD patterns, all samples show quite high purity of MgB_2, with only small amounts of MgO and un-reacted Mg and SiC. The un-reacted Mg can be detected because of the high content of SiC in the raw materials [104, 115, 143]. The most interesting phase change relates to the change in the Mg_2Si content with sintering temperature. 750in shows very high Mg_2Si content, which decreases with increasing sintering temperature and becomes a trace peak in 1050in. However, more than a trace of Mg_2Si can only be found in samples sintered at lower temperature using the combined *in-situ/ex-situ* method, 750inex and 850inex. The variation of Mg_2Si content is an important signal of the C and Si distributions in the MgB_2 matrix. Figure 14 shows SEM images of 850in and 850inex. The 850in sample contains large slits between MgB_2 clusters due to the volume contraction during the *in-situ* sintering of Mg and B powders. The 850inex sample shows hard-packed MgB_2 clusters because the *ex-situ* precursor is a course of nucleating centers and releases the strain of the *in-situ* MgB_2.

The critical transition temperatures (T_c) of the two batches of samples are compared in Figure 15. It is found that the T_c values of the *in-situ* sintered samples are always slightly lower than those for the samples from the other batch, except for 1050in, and the T_c dependence on sintering temperature of the two batches of samples is exactly the same, which means that the

T_c depends greatly on the sintering temperature, but not on the different techniques. However, the transition widths from the normal state to the superconducting state are quite different for the two batches of samples, as shown in the inset of Figure 15. The transition widths of the *in-situ* sintered samples are quite broad compared with those fabricated by the combined technique. The transition width is about 4 K for 750in and becomes 3 K for the 850in and 950in samples sintered at higher temperature due to the high crystallinity. It should be noted that the transition of 1050in shows a two-step behaviour, which may be attributed to the inhomogeneous carbon substitution effect or the inhomogeneous SiC distribution in the raw materials. The transition widths of all the samples made by the *in-situ/ex-situ* combined technique are 2.5 K, showing behaviour that is independent of the sintering temperature. This means that the crystallinity is increased through the *in-situ/ex-situ* combined technique because the precursor MgB_2 powder is a source of high quality nucleating centres for the newly formed MgB_2 during the solid-liquid reaction between the magnesium and the boron.

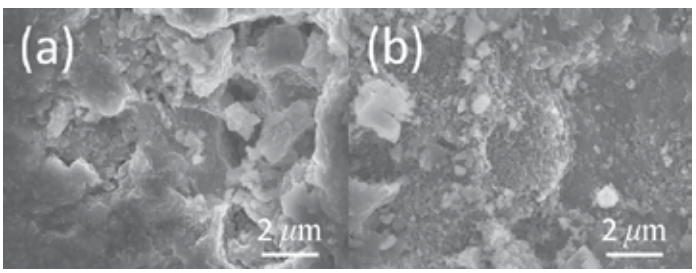

Figure 14. SEM photos of (a) 850in and (b) 850inex [140].

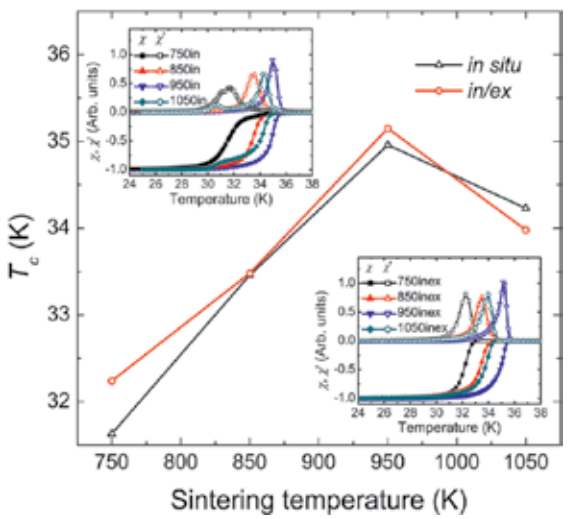

Figure 15. T_c dependence on sintering temperature. The insets show the normalized magnetic moment dependence on the measuring temperature for the *in-situ* samples (upper) and for the *in-situ/ex-situ* samples (lower) [140].

The J_c dependence on the applied field is shown in Figure 16 for typical samples, which were measured at 5 K and 20 K, respectively. It should be noted that the J_c dependence on sintering temperature in this work is totally different from previously reported results, because the solid-liquid reaction dynamics is different due to the small SiC particle size, less than 15 nm, which is much smaller than the particle sizes used before. The J_c benefits from the high sintering temperature. 750in, 850in, and 750inex display non-competitive performance over the whole field range. 1050inex has very high low field J_c values but its J_c deteriorates with increasing magnetic field. The J_c properties of 950in, 850inex, and 950inex show outstandingly high J_c performances among all the samples. It is concluded that the *in-situ/ex-situ* combined technique only requires a lower sintering temperature to achieve high quality MgB_2 wires, which is very important for industrial application in terms of energy saving and equipment simplification. The J_c values of 750inex are double those of 750in at 5 K and 20 K over the measured magnetic field range. The inset of Figure 16 displays the low field performances at 20 K to avoid the influence of the flux jumping effect. 750in and 750inex show quite low J_c values in lower magnetic field. 1050in and 850inex show competitive self-field J_c. The ball-milling process used to produce the *ex-situ* MgB_2 powder destroyes the porous structure and enhances the density of MgB_2 fabricated by the *in-situ/ex-situ* combined process. This is because of the small particle size of SiC used in this work, which induces different reaction dynamics during the *in-situ* or *in-situ/ex-situ* processing [81, 104, 141, 142], so that the present J_c dependence on sintering temperature is quite different from what has been previously reported. It is proposed that the liquid Mg reacts with SiC first to form Mg_2Si and releases free C at low sintering temperature. Then the Mg_2Si reacts with B to form MgB_2 and releases free Si at high sintering temperatures. Both C and Si have very small sizes and cannot be detected by XRD. The coherence length, ξ, of MgB_2 is anisotropic. $\xi_{ab}(0) = 3.7 – 12$ nm, and $\xi_c(0) = 1.6 - 3.6$ nm [110], which is shorter than the particle size of Mg_2Si. The Mg_2Si particles cannot be effective flux pinning centers, but are rather useless impurities in the MgB_2 matrix, which decrease the density of current carriers. However, the free C and Si can be very strong flux pinning centers because of their small sizes, which are responsible for the high J_c performance in high magnetic fields. According to the collective pinning model [113], the J_c performance in the low magnetic field region depends on the density of current carriers due to its weak field dependence, while the high magnetic field J_c performance depends on the flux pinning force due to the increased high H_{c2} and H_{irr}. The approximate H_{sb} values are also indicated on the J_c curves estimated at 20 K, as shown in the inset of Figure 16, where H_{sb} is the crossover field from single-vortex to small-bundle pinning based on the collective pinning model. However, H_{sb} has not been detected at 5 K due to the relatively high supercurrents [103].

The strength of the pinning force can be reflected by the dependence of H_{c2} and H_{irr} on the normalized temperature, as shown in Figure 17. Carbon substitution is one of the most effective methods to improve the H_{c2} and H_{irr} because of the increased scattering by C doping, and the increased scattering can also contribute to decreased T_c and merging of the two gaps [144]. It should be noted that the H_{c2} and H_{irr} for 750in, 850in, and 750inex have their highest values at low temperature, which means a strong flux pinning force. The poor J_c is of these samples attributed to the lower density of current carriers. Both 1050in and 1050inex show the lowest H_{c2} and the lowest H_{irr} among all the samples. 850in, 950in, 850inex, and 950inex show competitive H_{c2} and H_{irr} performances, which are responsible for their high J_c values under high magnetic field.

http://dx.doi.org/10.5772/59492

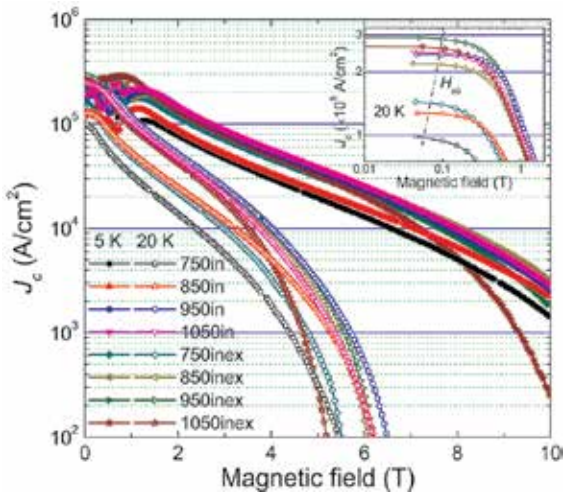

Figure 16. J_c at 5 K and 20 K. The inset indicates the J_c behavior in low magnetic field at 20 K. H_{sb}, the crossover field from single-vortex to small-bundle pinning, is indicated by the dashed-dotted line at its probable position on the J_c curves [140].

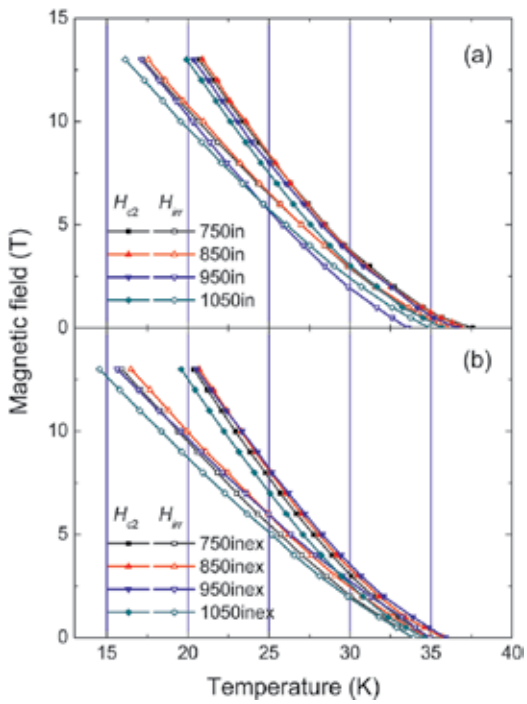

Figure 17. Comparison of H_{c2} (solid symbols) and H_{irr} (open symbols) for (a) MgB_2/Fe wires doped with nano-SiC and (b) MgB_2/Fe wires doped with nano-SiC, with sintering at 750, 850, 950, and 1050 °C, respectively [140].

In conclusion, high sintering temperature can improve the critical current density of small-particle-size SiC doped MgB_2. The two-step reactions between Mg, SiC, and B release free C and Si to form strong flux pinning centers. The current carrier density and flux pinning force are important factors in the improvement of the J_c performance of nano-SiC doped MgB_2. The current carrier density determines the J_c behavior in the single-vortex regime, where J_c is independent of applied magnetic field. The flux pinning force determines the J_c performance in the small-bundle pinning regime, where the doping induced defects are believed to act as flux pinning centers. Nano-SiC doped MgB_2/Fe wires fabricated by the combined process are worth ongoing research to develop optimized processing parameters for practical purposes.

5. Conclusions

The diffusion method can greatly improve the critical current density compared with the normal technique, which indicates that the critical current density greatly depends on the connectivity of MgB_2 grains. The combined process improves the connectivity of MgB_2 grains and the compactness of the superconducting core in wires, which induces high critical current density in zero field. The flux pinning force can also be improved by dopants for magnetic field application. Further research could focus on parameter optimization of the combined process to fabricate high quality MgB_2 wires.

Acknowledgements

The authors thank Dr. T. Silver for her useful discussions. This work is supported by the Program for Professor of Special Appointment (Eastern Scholar) at Shanghai Institutions of Higher Learning, the Australian Research Council (project ID: DP0770205), and Hyper Tech Research Inc.

Author details

Wenxian Li[1,2,3*] and Shi-Xue Dou[2]

*Address all correspondence to: shuliwx@shu.edu.cn

1 School of Materials Science & Engineering, Shanghai University, Shanghai, China

2 Institute for Superconducting & Electronic Materials, University of Wollongong, Wollongong, Australia

3 School of Computing, Engineering & Mathematics, University of Western Sydney, Sydney, Australia

http://dx.doi.org/10.5772/59492

References

[1] Nagamatsu J, Nakagawa N, Muranaka T, Zenitani Y, and Akimitsu J, Superconductivity at 39 K in magnesium diboride, Nature 2001; 410(6824) 63-64.

[2] Ginzburg VL, Nobel Lecture: On superconductivity and superfluidity (what I have and have not managed to do) as well as on the "physical minimum" at the beginning of the XXI century, Rev. Mod. Phys. 2004; 76(3) 981-998.

[3] Bardeen J, Cooper LN, and Schrieffer JR, Theory of Superconductivity, Phys. Rev. 1957; 108(5) 1175-1204.

[4] Canfield PC and Crabtree G, Magnesium diboride: Better late than never, Phys. Today 2003; 56(3) 34-40.

[5] Ivanov VA, van den Broek M, and Peeters FM, Strongly interacting sigma-electrons and MgB_2 superconductivity, Solid State Commun. 2001; 120(2-3) 53-57.

[6] Baskaran G, Resonating-valence-bond contribution to superconductivity in MgB_2, Phys. Rev. B 2002; 65(21) 212505.

[7] Hirsch JE, Hole superconductivity in MgB_2: a high T_c cuprate without Cu, Phys. Lett. A 2001; 282(6) 392-398.

[8] Hirsch JE and Marsiglio F, Electron-phonon or hole superconductivity in (MgB_2), Phys. Rev. B 2001; 64(14) 144532.

[9] Choi HJ, Cohen ML, and Louie SG, Anisotropic Eliashberg theory of MgB_2: T_c, isotope effects, superconducting energy gaps, quasiparticles, and specific heat, Physica C 2003; 385(1-2) 66-74.

[10] Yildirim T, Gulseren O, Lynn JW, Brown CM, Udovic TJ, Huang Q, Rogado N, Regan KA, Hayward MA, Slusky JS, He T, Haas MK, Khalifah P, Inumaru K, and Cava RJ, Giant anharmonicity and nonlinear electron-phonon coupling in MgB_2: A combined first-principles calculation and neutron scattering study, Phys. Rev. Lett. 2001; 87(3) 037001.

[11] Liu AY, Mazin II, and Kortus J, Beyond Eliashberg superconductivity in MgB_2: Anharmonicity, two-phonon scattering, and multiple gaps, Phys. Rev. Lett. 2001; 87(8) 087005.

[12] Hlinka J, Gregora I, Pokorny J, Plecenik A, Kus P, Satrapinsky L, and Benacka S, Phonons in MgB_2 by polarized Raman scattering on single crystals, Phys. Rev. B 2001; 64(14) 140503.

[13] Goncharov AF, Struzhkin VV, Gregoryanz E, Hu JZ, Hemley RJ, Mao HK, Lapertot G, Bud'ko SL, and Canfield PC, Raman spectrum and lattice parameters of MgB_2 as a function of pressure, Phys. Rev. B 2001; 64(10) 100509.

[14] Dou SX, Shcherbakova O, Yeoh WK, Kim JH, Soltanian S, Wang XL, Senatore C, Flukiger R, Dhalle M, Husnjak O, and Babic E, Mechanism of enhancement in electromagnetic properties of MgB_2 by nano SiC doping, Phys. Rev. Lett. 2007; 98(9) 097002.

[15] Tinkham M, Introduction to Superconductivity, 2nd ed., New York: McGraw-Hill,, 1996; 123.

[16] Nicol EJ and Carbotte JP, Theory of the critical current in two-band superconductors with application to MgB_2, Phys. Rev. B 2005; 72(1) 014520.

[17] Arcos DH and Kunchur MN, Suppressed flux motion in magnesium diboride films, Phys. Rev. B 2005; 71(18) 184516.

[18] Eisterer M, Magnetic properties and critical currents of MgB_2, Supercond. Sci. Technol. 2007; 20(12) R47-R73.

[19] Finnemore DK, Ostenson JE, Bud'ko SL, Lapertot G, and Canfield PC, Thermodynamic and transport properties of superconducting $Mg^{10}B_2$, Phys. Rev. Lett. 2001; 86(11) 2420-2422.

[20] Kawano K, Abell JS, Kambara M, Babu NH, and Cardwell DA, Evidence for high intergranular current flow in a single-phase polycrystalline MgB_2 superconductor, Appl. Phys. Lett. 2001; 79(14) 2216-2218.

[21] Rowell JM, The widely variable resistivity of MgB_2 samples, Supercond. Sci. Technol. 2003; 16(6) R17-R27.

[22] Klie RF, Idrobo JC, Browning ND, Regan KA, Rogado NS, and Cava RJ, Direct observation of nanometer-scale Mg- and B-oxide phases at grain boundaries in MgB_2, Appl. Phys. Lett. 2001; 79(12) 1837-1839.

[23] Pogrebnyakov AV, Xi XX, Redwing JM, Vaithyanathan V, Schlom DG, Soukiassian A, Mi SB, Jia CL, Giencke JE, Eom CB, Chen J, Hu YF, Cui Y, and Li Q, Properties of MgB_2 thin films with carbon doping, Appl. Phys. Lett. 2004; 85(11) 2017-2019.

[24] Hassler W, Birajdar B, Gruner W, Herrmann M, Perner O, Rodig C, Schubert M, Holzapfel B, Eibl O, and Schultz L, MgB_2 bulk and tapes prepared by mechanical alloying: influence of the boron precursor powder, Supercond. Sci. Technol. 2006; 19(6) 512-520.

[25] Fischer C, Hassler W, Rodig C, Perner O, Behr G, Schubert M, Nenkov K, Eckert J, Holzapfel B, and Schultz L, Critical current densities of superconducting MgB_2 tapes prepared on the base of mechanically alloyed precursors, Physica C 2004; 406(1-2) 121-130.

[26] Yeoh WK, Kim JH, Horvat J, Dou SX, and Munroe P, Improving flux pinning of MgB_2 by carbon nanotube doping and ultrasonication, Supercond. Sci. Technol. 2006; 19(2) L5-L8.

[27] Rowell JM, Xu SY, Zeng H, Pogrebnyakov AV, Li Q, Xi XX, Redwing JM, Tian W, and Pan XQ, Critical current density and resistivity of MgB_2 films, Appl. Phys. Lett. 2003; 83(1) 102-104.

[28] Kim KH, Betts JB, Jaime M, Lacerda AH, Boebinger GS, Jung CU, Kim HJ, Park MS, and Lee SI, Mg as a main source for the diverse magnetotransport properties of MgB_2, Phys. Rev. B 2002; 66(2) 020506.

[29] Sharma PA, Hur N, Horibe Y, Chen CH, Kim BG, Guha S, Cieplak MZ, and Cheong SW, Percolative superconductivity in $Mg_{1-x}B_2$, Phys. Rev. Lett. 2002; 89(16) 167003.

[30] Kumakura H, Kitaguchi H, Matsumoto A, and Yamada H, Upper critical field, irreversibility field, and critical current density of powder-in-tube-processed MgB_2/Fe tapes, Supercond. Sci. Technol. 2005; 18(8) 1042-1046.

[31] Nakane T, Jiang CH, Mochiku T, Fujii H, Kuroda T, and Kumakura H, Effect of SiC nanoparticle addition on the critical current density of MgB_2 tapes fabricated from MgH_2, B and MgB_2 powder mixtures, Supercond. Sci. Technol. 2005; 18(10) 1337-1341.

[32] Hata S, Yoshidome T, Sosiati H, Tomokiyo Y, Kuwano N, Matsumoto A, Kitaguchi H, and Kumakura H, Microstructures of MgB_2/Fe tapes fabricated by an powder-in-tube method using MgH_2 as a precursor powder, Supercond. Sci. Technol. 2006; 19(2) 161-168.

[33] Jiang CH, Hatakeyama H, and Kumakura H, Preparation of MgB_2/Fe tapes with improved J_c property using MgH_2 powder and a short pre-annealing and intermediate rolling process, Supercond. Sci. Technol. 2005; 18(5) L17-L22.

[34] Fujii H, Togano K, and Kumakura H, Enhancement of critical current densities of powder-in-tube processed MgB_2 tapes by using MgH_2 as a precursor powder, Supercond. Sci. Technol. 2002; 15(11) 1571-1576.

[35] Jiang CH, Nakane T, Hatakeyama H, and Kumakura H, Enhanced J_c property in nano-SiC doped thin MgB_2/Fe wires by a modified PIT process, Physica C 2005; 422(3-4) 127-131.

[36] Jiang CH, Hatakeyama H, and Kumakura H, Effect of nanometer MgO addition on the PIT processed MgB_2/Fe tapes, Physica C 2005; 423(1-2) 45-50.

[37] Matsumoto A, Kumakura H, Kitaguchi H, and Hatakeyama H, Effect of SiO_2 and SiC doping on the powder-in-tube processed MgB_2 tapes, Supercond. Sci. Technol. 2003; 16(8) 926-930.

[38] Pachla W, Morawski A, Kovac P, Husek I, Mazur A, Lada T, Diduszko R, Melisek T, Strbik V, and Kulczyk M, Properties of hydrostatically extruded *in situ* MgB_2 wires doped with SiC, Supercond. Sci. Technol. 2006; 19(1) 1-8.

[39] Yamada H, Hirakawa M, Kumakura H, and Kitaguchi H, Effect of aromatic hydrocarbon addition on *in situ* powder-in-tube processed MgB_2 tapes, Supercond. Sci. Technol. 2006; 19(2) 175-177.

[40] Goldacker W, Schlachter SI, Obst B, Liu B, Reiner J, and Zimmer S, Development and performance of thin steel reinforced MgB_2 wires and low-temperature processing for further improvements, Supercond. Sci. Technol. 2004; 17(5) S363-S368.

[41] Matsumoto A, Kumakura H, Kitaguchi H, Senkowicz BJ, Jewell MC, Hellstrom EE, Zhu Y, Voyles PM, and Larbalestier DC, Evaluation of connectivity, flux pinning, and upper critical field contributions to the critical current density of bulk pure and SiC-alloyed MgB_2, Appl. Phys. Lett. 2006; 89(13) 132508.

[42] Yamamoto A, Shimoyama J, Ueda S, Iwayama I, Horii S, and Kishio K, Effects of B_4C doping on critical current properties of MgB_2 superconductor, Supercond. Sci. Technol. 2005; 18(10) 1323-1328.

[43] Perner O, Habler W, Eckert R, Fischer C, Mickel C, Fuchs G, Holzapfel B, and Schultz L, Effects of oxide particle addition on superconductivity in nanocrystalline MgB_2 bulk samples, Physica C 2005; 432(1-2) 15-24.

[44] Jiang CH, Nakane T, and Kumakura H, Superior high-field current density in slightly Mg-deficient MgB_2 tapes, Appl. Phys. Lett. 2005; 87(25) 252505.

[45] Wu YF, Lu YF, Yan G, Li JS, Feng Y, Tang HP, Chen SK, Xu HL, Li CS, and Zhang PX, Improved superconducting properties in bulk MgB_2 prepared by high-energy milling of Mg and B powders, Supercond. Sci. Technol. 2006; 19(11) 1215-1218.

[46] Kim JH, Yeoh WK, Qin MJ, Xu X, and Dou SX, The doping effect of multiwall carbon nanotube on MgB_2/Fe superconductor wire, J. Appl. Phys. 2006; 100(1) 013908.

[47] Kim JH, Zhou S, Hossain MSA, Pan AV, and Dou SX, Carbohydrate doping to enhance electromagnetic properties of MgB_2 superconductors, Appl. Phys. Lett. 2006; 89(14) 142505.

[48] Chen SK, Lockman Z, Wei M, Glowacki BA, and MacManus-Driscoll JL, Improved current densities in MgB_2 by liquid-assisted sintering, Appl. Phys. Lett. 2005; 86(24) 242501.

[49] Ueda S, Shimoyama J, Iwayama I, Yamamoto A, Katsura Y, Horii S, and Kishio K, High critical current properties of MgB_2 bulks prepared by a diffusion method, Appl. Phys. Lett. 2005; 86(22) 222502.

[50] Zhang XP, Gao ZS, Wang DL, Yu ZG, Ma YW, Awaji S, and Watanabe K, Improved critical current densities in MgB_2 tapes with ZrB_2 doping, Appl. Phys. Lett. 2006; 89(13) 132510.

[51] Shcherbakova O, Dou SX, Soltanian S, Wexler D, Bhatia M, Sumption M, and Collings EW, The effect of doping level and sintering temperature on $J_c(H)$ performance in nano-SiC doped and pure MgB_2 wires, J. Appl. Phys. 2006; 99(8) 08M510.

[52] Ma YW, Zhang XP, Nishijima G, Watanabe K, Awaji S, and Bai XD, Significantly enhanced critical current densities in MgB_2 tapes made by a scaleable nanocarbon addition route, Appl. Phys. Lett. 2006; 88(7) 072502.

[53] Ribeiro RA, Bud'ko SL, Petrovic C, and Canfield PC, Effects of boron purity, Mg stoichiometry and carbon substitution on properties of polycrystalline MgB_2, Physica C 2003; 385(1-2) 16-23.

[54] Liao XZ, Serquis A, Zhu YT, Peterson DE, Mueller FM, and Xu HF, Strain effect on the critical superconducting temperature of MgB_2, Supercond. Sci. Technol. 2004; 17(8) 1026-1030.

[55] Perner O, Eckert J, Hassler W, Fischer C, Acker J, Gemming T, Fuchs G, Holzapfel B, and Schultz L, Stoichiometry dependence of superconductivity and microstructure in mechanically alloyed MgB_2, J. Appl. Phys. 2005; 97(5) 056105.

[56] Serquis A, Zhu YT, Peterson EJ, Coulter JY, Peterson DE, and Mueller FM, Effect of lattice strain and defects on the superconductivity of MgB_2, Appl. Phys. Lett. 2001; 79(26) 4399-4401.

[57] Yamada H, Hirakawa M, Kumakura H, Matsumoto A, and Kitaguchi H, Critical current densities of powder-in-tube MgB_2 tapes fabricated with nanometer-size Mg powder, Appl. Phys. Lett. 2004; 84(10) 1728-1730.

[58] Fang H, Padmanabhan S, Zhou YX, and Salama K, High critical current density in iron-clad MgB_2 tapes, Appl. Phys. Lett. 2003; 82(23) 4113-4115.

[59] Fischer C, Rodig C, Hassler W, Perner O, Eckert J, Nenkov K, Fuchs G, Wendrock H, Holzapfel B, and Schultz L, Preparation of MgB_2 tapes using a nanocrystalline partially reacted precursor, Appl. Phys. Lett. 2003; 83(9) 1803-1805.

[60] Strickland NM, Buckley RG, and Otto A, High critical current densities in Cu-sheathed MgB_2 formed from a mechanically-alloyed precursor, Appl. Phys. Lett. 2003; 83(2) 326-328.

[61] Flukiger R, Suo HL, Musolino N, Beneduce C, Toulemonde P, and Lezza P, Superconducting properties of MgB_2 tapes and wires, Physica C 2003; 385(1-2) 286-305.

[62] Goldacker W, Schlachter SI, Liu B, Obst B, and Klimenko E, Considerations on critical currents and stability of MgB_2 wires made by different preparation routes, Physica C 2004; 401(1-4) 80-86.

[63] Flukiger R, Lezza P, Beneduce C, Musolino N, and Suo HL, Improved transport critical current and irreversibility fields in mono- and multifilamentary Fe/MgB_2 tapes and wires using fine powders, Supercond. Sci. Technol. 2003; 16(2) 264-270.

[64] Grovenor CRM, Goodsir L, Salter CJ, Kovac P, and Husek I, Interfacial reactions and oxygen distribution in MgB_2 wires in Fe, stainless steel and Nb sheaths, Supercond. Sci. Technol. 2004; 17(3) 479-484.

[65] Senkowicz BJ, Giencke JE, Patnaik S, Eom CB, Hellstrom EE, and Larbalestier DC, Improved upper critical field in bulk-form magnesium diboride by mechanical alloying with carbon, Appl. Phys. Lett. 2005; 86(20) 202502.

[66] Dou SX, Shcherbakova O, Yoeh WK, Kim JH, Soltanian S, Wang XL, Senatore C, Flukiger R, Dhalle M, Husnjak O, and Babic E, Mechanism of enhancement in electromagnetic properties of MgB_2 by nano SiC doping, Phys. Rev. Lett. 2007; 98(9) 097002.

[67] Zhao Y, Feng Y, Shen TM, Li G, Yang Y, and Cheng CH, Cooperative doping effects of Ti and C on critical current density and irreversibility field of MgB_2, J. Appl. Phys. 2006; 100(12) 123902.

[68] Xu X, Kim JH, Yeoh WK, Zhang Y, and Dou SX, Improved J_c of MgB_2 superconductor by ball milling using different media, Supercond. Sci. Technol. 2006; 19(11) L47-L50.

[69] Haigh S, Kovac P, Prikhna TA, Savchuk YM, Kilburn MR, Salter C, Hutchison J, and Grovenor C, Chemical interactions in Ti doped MgB_2 superconducting bulk samples and wires, Supercond. Sci. Technol. 2005; 18(9) 1190-1196.

[70] Ma YW, Kumakura H, Matsumoto A, Hatakeyama H, and Togano K, Improvement of critical current density in Fe-sheathed MgB_2 tapes by $ZrSi_2$, ZrB_2 and WSi_2 doping, Supercond. Sci. Technol. 2003; 16(8) 852-856.

[71] Kumar D, Pennycook SJ, Narayan J, Wang H, and Tiwari A, Role of silver addition in the synthesis of high critical current density MgB_2 bulk superconductors, Supercond. Sci. Technol. 2003; 16(4) 455-458.

[72] Yamamoto A, Shimoyama J, Ueda S, Katsura Y, Iwayama I, Horii S, and Kishio K, Universal relationship between crystallinity and irreversibility field of MgB_2, Appl. Phys. Lett. 2005; 86(21) 212502.

[73] Lezza P, Senatore C, and Flukiger R, Improved critical current densities in B_4C doped MgB_2 based wires, Supercond. Sci. Technol. 2006; 19(10) 1030-1033.

[74] Yeoh WK, Kim JH, Horvat J, Xu X, Qin MJ, Dou SX, Jiang CH, Nakane T, Kumakura H, and Munroe P, Control of nano carbon substitution for enhancing the critical current density in MgB_2, Supercond. Sci. Technol. 2006; 19(6) 596-599.

[75] Dou SX, Yeoh WK, Horvat J, and Ionescu M, Effect of carbon nanotube doping on critical current density of MgB_2 superconductor, Appl. Phys. Lett. 2003; 83(24) 4996-4998.

[76] Kim JH, Yeoh WK, Qin MJ, Xu X, Dou SX, Munroe P, Kumakura H, Nakane T, and Jiang CH, Enhancement of in-field J_c in MgB_2/Fe wire using single- and multiwalled carbon nanotubes, Appl. Phys. Lett. 2006; 89(12) 122510.

[77] Kovac P, Husek I, Skakalova V, Meyer J, Dobrocka E, Hirscher M, and Roth S, Transport current improvements of *in situ* MgB_2 tapes by the addition of carbon nanotubes, silicon carbide or graphite, Supercond. Sci. Technol. 2007; 20(1) 105-111.

[78] Cheng CH, Yang Y, Munroe P, and Zhao Y, Comparison between nano-diamond and carbon nanotube doping effects on critical current density and flux pinning in MgB_2, Supercond. Sci. Technol. 2007; 20(3) 296-301.

[79] Cheng CH, Zhang H, Zhao Y, Feng Y, Rui XF, Munroe P, Zeng HM, Koshizuka N, and Murakami M, Doping effect of nano-diamond on superconductivity and flux pinning in MgB_2, Supercond. Sci. Technol. 2003; 16(10) 1182-1186.

[80] Gao ZS, Zhang XP, Wang DL, Liu X, Li XH, Ma YW, and Mossang E, Effects of NbC addition on the critical current density of MgB_2 tapes, Supercond. Sci. Technol. 2007; 20(1) 57-61.

[81] Dou SX, Soltanian S, Horvat J, Wang XL, Zhou SH, Ionescu M, Liu HK, Munroe P, and Tomsic M, Enhancement of the critical current density and flux pinning of MgB_2 superconductor by nanoparticle SiC doping, Appl. Phys. Lett. 2002; 81(18) 3419-3421.

[82] Soltanian S, Wang XL, Horvat J, Dou SX, Sumption MD, Bhatia M, Collings EW, Munroe P, and Tomsic M, High transport critical current density and large H_{c2} and H_{irr} in nanoscale SiC doped MgB_2 wires sintered at low temperature, Supercond. Sci. Technol. 2005; 18(5) 658-666.

[83] Chen SK, Tan KS, Glowacki BA, Yeoh WK, Soltanian S, Horvat J, and Dou SX, Effect of heating rates on superconducting properties of pure MgB_2, carbon nanotube- and nano-SiC-doped MgB_2/Fe wires, Appl. Phys. Lett. 2005; 87(18) 182504.

[84] Dou SX, Braccini V, Soltanian S, Klie R, Zhu Y, Li S, Wang XL, and Larbalestier D, Nanoscale-SiC doping for enhancing J_c and H_{c2} in superconducting MgB_2, J. Appl. Phys. 2004; 96(12) 7549-7555.

[85] Ma YW, Zhang XP, Xu AX, Li XH, Xiao LY, Nishijima G, Awaji S, Watanabe K, Jiao YL, Xiao L, Bai XD, Wu KH, and Wen HH, The effect of $ZrSi_2$ and SiC doping on the microstructure and J_c-B properties of PIT processed MgB_2 tapes, Supercond. Sci. Technol. 2006; 19(1) 133-137.

[86] Sumption MD, Bhatia M, Rindfleisch M, Tomsic M, and Collings EW, Transport and magnetic J_c of MgB_2 strands and small helical coils, Appl. Phys. Lett. 2005; 86(10) 102501.

[87] Kumakura H, Kitaguchi H, Matsumoto A, and Hatakeyama H, Upper critical fields of powder-in-tube-processed MgB_2/Fe tape conductors, Appl. Phys. Lett. 2004; 84(18) 3669-3671.

[88] Li S, White T, Laursen K, Tan TT, Sun CQ, Dong ZL, Li Y, Zho SH, Horvat J, and Dou SX, Intense vortex pinning enhanced by semicrystalline defect traps in self-aligned nanostructured MgB_2, Appl. Phys. Lett. 2003; 83(2) 314-316.

[89] Sumption MD, Bhatia M, Rindfleisch M, Tomsic M, Soltanian S, Dou SX, and Collings EW, Large upper critical field and irreversibility field in MgB_2 wires with SiC additions, Appl. Phys. Lett. 2005; 86(9) 092507.

[90] Hossain MSA, Kim JH, Wang XL, Xu X, Peleckis G, and Dou SX, Enhancement of flux pinning in a MgB_2 superconductor doped with tartaric acid, Supercond. Sci. Technol. 2007; 20(1) 112-116.

[91] Liao XZ, Serquis A, Zhu YT, Civale L, Hammon DL, Peterson DE, Mueller FM, Nesterenko VF, and Gu Y, Defect structures in MgB_2 wires introduced by hot isostatic pressing, Supercond. Sci. Technol. 2003; 16(7) 799-803.

[92] Gao ZS, Ma YW, Zhang XP, Wang DL, Yu ZG, Watanabe K, Yang HA, and Wen HH, Strongly enhanced critical current density in MgB_2/Fe tapes by stearic acid and stearate doping, Supercond. Sci. Technol. 2007; 20(5) 485-489.

[93] Wen HH, Li SL, Zhao ZW, Jin H, Ni YM, Ren ZA, Che GC, and Zhao ZX, Magnetic relaxation and critical current density of the new superconductor MgB_2, Supercond. Sci. Technol. 2002; 15(3) 315-319.

[94] Prikhna TA, Gawalek W, Savchuk YM, Moshchil VE, Sergienko NV, Habisreuther T, Wendt M, Hergt R, Schmidt C, Dellith J, Melnikov VS, Assmann A, Litzkendorf D, and Nagorny PA, High-pressure synthesis of MgB_2 with addition of Ti, Physica C 2004; 402(3) 223-233.

[95] Serquis A, Liao XZ, Zhu YT, Coulter JY, Huang JY, Willis JO, Peterson DE, Mueller FM, Moreno NO, Thompson JD, Nesterenko VF, and Indrakanti SS, Influence of microstructures and crystalline defects on the superconductivity of MgB_2, J. Appl. Phys. 2002; 92(1) 351-356.

[96] Serquis A, Civale L, Hammon DL, Liao XZ, Coulter JY, Zhu YT, Jaime M, Peterson DE, Mueller FM, Nesterenko VF, and Gu Y, Hot isostatic pressing of powder in tube MgB_2 wires, Appl. Phys. Lett. 2003; 82(17) 2847-2849.

[97] Eyidi D, Eibl O, Wenzel T, Nickel KG, Schlachter SI, and Goldacker W, Superconducting properties, microstructure and chemical composition of MgB_2 sheathed materials, Supercond. Sci. Technol. 2003; 16(7) 778-788.

[98] Pan AV, Zhou SH, Liu HK, and Don SX, Properties of superconducting MgB_2 wires: versus reaction technique, Supercond. Sci. Technol. 2003; 16(5) 639-644.

[99] Serquis A, Civale L, Hammon DL, Coulter JY, Liao XZ, Zhu YT, Peterson DE, and Mueller FM, Microstructure and high critical current of powder-in-tube MgB_2, Appl. Phys. Lett. 2003; 82(11) 1754-1756.

[100] Serquis A, Civale L, Hammon DL, Liao XZ, Coulter JY, Zhu YT, Peterson DE, and Mueller FM, Role of excess Mg and heat treatments on microstructure and critical current of MgB_2 wires, J. Appl. Phys. 2003; 94(6) 4024-4031.

[101] Suo HL, Beneduce C, Dhalle M, Musolino N, Genoud JY, and Flukiger R, Large transport critical currents in dense Fe- and Ni-clad MgB_2 superconducting tapes, Appl. Phys. Lett. 2001; 79(19) 3116-3118.

[102] Grasso G, Malagoli A, Ferdeghini C, Roncallo S, Braccini V, Siri AS, and Cimberle MR, Large transport critical currents in unsintered MgB_2 superconducting tapes, Appl. Phys. Lett. 2001; 79(2) 230-232.

[103] Li WX, Zeng R, Lu L, and Dou SX, Effect of thermal strain on J_c and T_c in high density nano-SiC doped MgB_2, J. Appl. Phys. 2011; 109(7) 07E108.

[104] Li WX, Zeng R, Lu L, Li Y, and Dou SX, The combined influence of connectivity and disorder on J_c and T_c performances in Mg_xB_2+10 wt % SiC, J. Appl. Phys. 2009; 106(9) 093906.

[105] Li WX, Zeng R, Lu L, Zhang Y, Dou SX, Li Y, Chen RH, and Zhu MY, Improved superconducting properties of powder-in-tube processed $Mg_{1.15}B_2$/Fe wires with nano-size SiC addition, Physica C 2009; 469(15-20) 1519-1522.

[106] Zeng R, Dou SX, Lu L, Li WX, Kim JH, Munroe P, Zheng RK, and Ringer SP, Thermal-strain-induced enhancement of electromagnetic properties of SiC-MgB_2 composites, Appl. Phys. Lett. 2009; 94(4) 042510.

[107] Pogrebnyakov AV, Redwing JM, Raghavan S, Vaithyanathan V, Schlom DG, Xu SY, Li Q, Tenne DA, Soukiassian A, Xi XX, Johannes MD, Kasinathan D, Pickett WE, Wu JS, and Spence JCH, Enhancement of the superconducting transition temperature of MgB_2 by a strain-induced bond-stretching mode softening, Phys. Rev. Lett. 2004; 93(14) 147006.

[108] Neumeier JJ, Tomita T, Debessai M, Schilling JS, Barnes PW, Hinks DG, and Jorgensen JD, Negative thermal expansion of MgB_2 in the superconducting state and anomalous behavior of the bulk Gruneisen function, Phys. Rev. B 2005; 72(22) 220505.

[109] Li Z and Bradt RC, Thermal expansion of the hexagonal (4H) polytype of SiC, J. Appl. Phys. 1986; 60(2) 612-614.

[110] Buzea C and Yamashita T, Review of the superconducting properties of MgB_2, Supercond. Sci. Technol. 2001; 14(11) R115-R146.

[111] Jorgensen JD, Hinks DG, and Short S, Lattice properties of MgB_2 versus temperature and pressure, Phys. Rev. B 2001; 6322(22) 224522.

[112] Williamson GK and Hall WH, X-ray line broadening from filed aluminium and wolfram, Acta Metall. Mater. 1953; 1)22-31.

[113] Blatter G, Feigelman MV, Geshkenbein VB, Larkin AI, and Vinokur VM, Vortices in high-temperature superconductors, Rev. Mod. Phys. 1994; 66(4) 1125-1388.

[114] Li WX, Li Y, Chen RH, Zeng R, Zhu MY, Jin HM, and Dou SX, Electron-phonon coupling properties in MgB_2 observed by Raman scattering, J. Phys.-Condens. Matter 2008; 20(25) 255235.

[115] Li WX, Li Y, Chen RH, Zeng R, Dou SX, Zhu MY, and Jin HM, Raman study of element doping effects on the superconductivity of MgB_2, Phys. Rev. B 2008; 77(9) 094517.

[116] Li WX, Zeng R, Poh CK, Li Y, and Dou SX, Magnetic scattering effects in two-band superconductor: the ferromagnetic dopants in MgB_2, J. Phys.-Condens. Matter 2010; 22(13) 135701.

[117] Shi L, Zhang HR, Chen L, and Feng Y, The Raman spectrum and lattice parameters of MgB_2 as a function of temperature, J. Phys.-Condens. Matter 2004; 16(36) 6541-6550.

[118] Allen PB, Neutron spectroscopy of superconductors, Phys. Rev. B 1972; 6(7) 2577-2579.

[119] Kortus J, Dolgov OV, Kremer RK, and Golubov AA, Band filling and interband scattering effects in MgB_2: Carbon versus aluminum doping, Phys. Rev. Lett. 2005; 94(2) 027002.

[120] McMillan WL, Transition temperature of strong-coupled superconductors, Phys. Rev. 1968; 167(2) 331-334.

[121] Allen PB and Dynes RC, Transition-temperature of strong-coupled superconductors reanalyzed, Phys. Rev. B 1975; 12(3) 905-922.

[122] Kortus J, Mazin II, Belashchenko KD, Antropov VP, and Boyer LL, Superconductivity of metallic boron in MgB_2, Phys. Rev. Lett. 2001; 86(20) 4656-4659.

[123] Osborn R, Goremychkin EA, Kolesnikov AI, and Hinks DG, Phonon density of states in MgB_2, Phys. Rev. Lett. 2001; 87(1) 017005.

[124] Brinkman A, Golubov AA, Rogalla H, Dolgov OV, Kortus J, Kong Y, Jepsen O, and Andersen OK, Multiband model for tunneling in MgB_2 junctions, Phys. Rev. B 2002; 65(18) 180517.

[125] Collings EW, Sumption MD, Bhatia M, Susner MA, and Bohnenstiehl SD, Prospects for improving the intrinsic and extrinsic properties of magnesium diboride superconducting strands, Supercond. Sci. Technol. 2008; 21(10) 103001.

[126] Li WX, Li Y, Chen RH, Yeoh WK, and Dou SX, Effect of magnetic field processing on the microstructure of carbon nanotubes doped MgB_2, Physica C 2007; 4601)570-571.

[127] Yeoh WK, Horvat J, Dou SX, and Munroe P, Effect of carbon nanotube size on superconductivity properties of MgB_2, IEEE Trans. Appl. Supercond. 2005; 15(2) 3284-3287.

[128] Li WX, Li Y, Zhu MY, Chen RH, Xu X, Yeoh WK, Kim JH, and Dou SX, Benzoic acid doping to enhance electromagnetic properties of MgB_2 superconductors, IEEE Trans. Appl. Supercond. 2007; 17(2) 2778-2781.

[129] Zhuang CG, Meng S, Zhang CY, Feng QR, Gan ZZ, Yang H, Jia Y, Wen HH, and Xi XX, Ultrahigh current-carrying capability in clean MgB_2 films, J. Appl. Phys. 2008; 104(1) 013924.

[130] Zeng XH, Pogrebnyakov AV, Zhu MH, Jones JE, Xi XX, Xu SY, Wertz E, Li Q, Redwing JM, Lettieri J, Vaithyanathan V, Schlom DG, Liu ZK, Trithaveesak O, and Schubert J, Superconducting MgB_2 thin films on silicon carbide substrates by hybrid physical-chemical vapor deposition, Appl. Phys. Lett. 2003; 82(13) 2097-2099.

[131] Flukiger R, Hossain MSA, and Senatore C, Strong enhancement of J_c and B_{irr} in binary MgB_2 wires after cold high pressure densification, Supercond. Sci. Technol. 2009; 22(8) 085002.

[132] Hossain MSA, Senatore C, Flukiger R, Rindfleisch MA, Tomsic MJ, Kim JH, and Dou SX, The enhanced J_c and B_{irr} of MgB_2 wires and tapes alloyed with $C_4H_6O_5$ (malic acid) after cold high pressure densification, Supercond. Sci. Technol. 2009; 22(9) 095004.

[133] Kovac P, Reissner M, Melisek T, Husek I, and Mohammad S, Current densities of MgB_2 wires by combined ex process, J. Appl. Phys. 2009; 106(1) 013910.

[134] Li WX, Zeng R, Zhang Y, Xu X, Li Y, and Dou SX, Evolution of electromagnetic properties and microstructure with sintering temperature for MgB_2/Fe wires made by combined *In-Situ*/*Ex-Situ* process, IEEE Trans. Appl. Supercond. 2011; 21(3) 2635-2638.

[135] Xu X, Kim JH, Dou SX, Choi S, Lee JH, Park HW, Rindfleish M, and Tomsic M, A correlation between transport current density and grain connectivity in MgB_2/Fe wire made from ball-milled boron, J. Appl. Phys. 2009; 105(10) 103913.

[136] Romano G, Vignolo M, Braccini V, Malagoli A, Bernini C, Tropeano M, Fanciulli C, Putti M, and Ferdeghini C, High-energy ball milling and synthesis temperature study to improve superconducting properties of MgB_2 *ex-situ* tapes and wires, IEEE Trans. Appl. Supercond. 2009; 19(3) 2706-2709.

[137] Li WX, Chen RH, Li Y, Zhu MY, Jin HM, Zeng R, Dou SX, and Lu B, Raman study on the effects of sintering temperature on the $J_c(H)$ performance of MgB_2 superconductor, J. Appl. Phys. 2008; 103(1) 013511.

[138] Chen RH, Zhu MY, Li Y, Li WX, Jin HM, and Dou SX, Effect of pulsed magnetic field on critical current in carbon-nanotube-doped MgB_2 wires, Acta Physica Sinica 2006; 55(9) 4878-4882.

[139] Zhang XP, Ma YW, Gao ZS, Yu ZG, Watanabe K, and Wen HH, Effect of nanoscale C and SiC doping on the superconducting properties of MgB_2 tapes, Acta Physica Sinica 2006; 55(9) 4873-4877.

[140] Li WX, Zeng R, Wang JL, Li Y, and Dou SX, Dependence of magnetoelectric properties on sintering temperature for nano-SiC-doped MgB_2/Fe wires made by combined *in situ*/*ex situ* process, J. Appl. Phys. 2012; 111(7) E7135-E7135.

[141] Dou SX, Pan AV, Zhou S, Ionescu M, Wang XL, Horvat J, Liu HK, and Munroe PR, Superconductivity, critical current density, and flux pinning in $MgB_{2-x}(SiC)_{x/2}$ superconductor after SiC nanoparticle doping, J. Appl. Phys. 2003; 94(3) 1850-1856.

[142] Dou SX, Pan AV, Zhou S, Ionescu M, Liu HK, and Munroe PR, Substitution-induced pinning in MgB_2 superconductor doped with SiC nano-particles, Supercond. Sci. Technol. 2002; 15(11) 1587-1591.

[143] Zhang Y, Dou SX, Lu C, Zhou H, and Li WX, Effect of Mg/B ratio on the superconductivity of MgB_2 bulk with SiC addition, Phys. Rev. B 2010; 81(9) 094501.

[144] Angst M, Bud'ko SL, Wilke RHT, and Canfield PC, Difference between Al and C doping in anisotropic upper critical field development in MgB_2, Phys. Rev. B 2005; 71(14) 144512.

Chapter 7

Spintronics Driven by Superconducting Proximity Effect

Guoxing Miao

Additional information is available at the end of the chapter

http://dx.doi.org/10.5772/59942

1. Introduction

In this chapter, we will discuss a few selected topics on the applications of superconducting proximity effect, and the related inverse proximity effect, in the field of spintronics. Superconducting proximity effect occurs when Cooper pairs from a superconductor propagate into the adjacent metallic systems and induce superconducting correlations in the otherwise non-superconducting materials. Due to the limited coherence length of Cooper pairs, this effect is confined to the very interface between the two materials and can be used as a method to trigger supercurrent flow, or to create particle-hole symmetry, in a wide range of devices. The inverse proximity effect can be viewed as the counteraction of the above-mentioned effect. Superconductivity in the original superconductor material inevitably weakens when it drives superconductivity into its neighbours; in addition, back flow of unpaired electrons and sometimes spin polarized electrons, will create more pair breaking within the superconductor and weaken it further. These effects can, however, be used as effective ways to control superconductivity through spin manipulations.

This chapter is organized in the following way. After a brief introduction on superconducting proximity effect and inverse proximity effects, we will continue our discussions from a few device points of view. 1. Proximity induced superconductivity in low dimensional electron systems, such as in the surface states of a 3D topological insulator and in the Rashba-split bands of a heavy metal/semiconductor nanowire. These form the most promising platforms that can host the elusive Majorana fermions for quantum computing applications. 2. Inverse proximity from multiple ferromagnetic neighbours can controllably turn superconductivity On and Off. The change in superconductivity states also leads to a large change in the device resistance, known as the superconducting spin valve effect.

i. Superconducting proximity effect — the example of Majorana fermion creation

ii. Inverse proximity on superconductors — the example of superconducting spin valves

INTECH
open science | open minds

© 2015 The Author(s). Licensee InTech. This chapter is distributed under the terms of the Creative Commons Attribution License (http://creativecommons.org/licenses/by/3.0), which permits unrestricted use, distribution, and reproduction in any medium, provided the original work is properly cited.

2. Superconducting proximity effect — the example of Majorana fermion creation

The term superconducting proximity effect [1, 2], by default, refers to the leak-out of a superconductor's Cooper pair wave function into an otherwise non-superconducting material, and the generation of induced superconductivity in that material. This is a spontaneous process that occurs whenever the superconductor makes clean enough contact with a metallic system. Fig.1 illustrates the distribution of superconductor pairing potential Δ across the interface between a superconductor and a normal metal. Far away from the interface, Δ simply sits at the respective bulk values, being Δ_0 on the superconductor side and vanishing on the normal metal side. The proximity effect shows up clearly near the interface: Δ is weakened on the superconductor side but gradually emerges in the normal metal towards the interface. Naturally, the two systems have to be in atomic contact for such wave function overlap to happen effectively. The interface transparency is critical for the strength of the proximity, and is often characterized with an impedance parameter γ_B such that the interfacial transparency $T = \frac{1}{1+\gamma_B}$. The transparency captures the interfacial quality as well as the wave function matching between the materials. In Fig.1, a clear discontinuity is seen across the interface which indicates a less-than-perfect interfacial transparency. A cleaner interface means stronger proximity, which adds some quite stringent requirements to the materials' development.

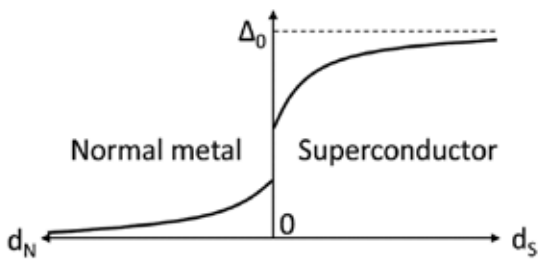

Figure 1. Evolution of the superconductor pairing potential Δ near an S/N interface. Δ_0 is the bulk pairing potential of the superconductor.

Such superconducting proximity effect is of particular interest to the spintronics community because it not only allows for spontaneously driving a non-superconducting material into superconductivity, but also enables actively pumping supercurrents over a prolonged distance across a non-superconducting material. Their fundamental principles are the same: extension of the superconductor wave function into the non-superconducting material. Naturally, the proximity effect can propagate into a material as long as there are available electronic states near the Fermi level: i.e., a metallic material. There have been some quite important reports in the field demonstrating superconductor coupling through unconventional media: for example, the manifestation in 2D semiconductor electron gases [3, 4, 5] and topological insulator surface states [6, 7, 8]; the two-valley nature with

http://dx.doi.org/10.5772/59942

relativistic Dirac electrons of graphene [9]; the gate tunability when coupled to 1D carbon nanotubes [10, 11], as well as with 0D C_{60} molecules [12] and InAs quantum dots [13]; the flow of supercurrents through double-stranded DNA molecules [14]; and the conversion into spin triplet supercurrents in half-metals [15, 16].

Whereas the superconducting proximity effect can essentially drive any electron system into superconducting, we focus our attention on a very specific topic: generation of the long-sought-after Majorana fermions on superconductor platforms and application of these particles to topological quantum information processing [17]. A Majorana fermion, by definition, is a spin-1/2 particle identical to its own antiparticle, as opposed to a conventional Dirac fermion. Being its own antiparticle suggests that the particle has to be charge neutral as well. A superconductor's wavefunction has perfect electron-hole symmetry, making it an ideal platform for creating objects with similar properties. Other than being electrically charged, the quasiparticle excitations in a superconductor come really close to the Majorana fermions. Naturally, many of the proposals for creating Majorana fermions in solid-state systems involve superconductivity as one of the core ingredients. There are a number of ingenious device concepts for realizing Majorana fermions in a superconductor platform. The most practical route of synthesizing a localized Majorana fermion is to build on the platform of p-wave superconductors [18, 19] such as strontium ruthenate (Sr_2RuO_4): a spinless p_x+ip_y superconductor [20]. A p-wave superconductor's wavefunction is two-fold degenerate and has chirality on the angular momentum; it is therefore often termed the chiral p-wave state. It differs from the more conventional s-wave BCS superconductors and d-wave high-temperature superconductors in the sense that the electrons prefer to pair into spin-triplet configurations. Since ferromagnetism is observed in many closely related strontium ruthenate compounds (such as $SrRuO_3$), it is natural to consider the possibility of triplet pairing on these superconducting species. There has been compelling evidence confirming that Sr_2RuO_4 is indeed a p-wave superconductor [21]. This spontaneous time-reversal symmetry breaking ensures that the system is stable against magnetic impurity scattering, but not so much against normal elastic impurity scatterings, such as from non-magnetic defects, grain boundaries, or surfaces. As a result, it is very hard to obtain materials with a high enough quality for device purposes. With Sr_2RuO_4 as an example, while its T_C can reach as much as 1.5 K in the best-quality single crystals, it is practically non-superconducting in any of the thin films deposited so far [21], which is a significant obstacle for its potential application in the topological quantum computer architectures.

The superconductor proximity effect comes in as an experimentally feasible route to "simulate" a p-wave superconductor that can subsequently host Majorana modes on the resulting 2D platforms [22, 23]. Now that the particle-hole symmetry has already been guaranteed on the given platforms by the superconductivity induced from the superconducting proximity effect, what about the spinless nature of the p-wave superconductors? The signature we need to look for is the so-called helical Dirac spin state, as illustrated in Fig.2, which readily shows up on the surface of a 3D topological insulator [24]. A 3D topological insulator is a quantum spin Hall insulator with an inside that is insulating and a surface that is conducting [25]. Due

to the nontrivial topology of the material, its interface with a topologically trivial insulator, such as a normal insulator or vacuum, always has the conducting surface states present, which are strictly protected by the topological orders. We will not go into too much detail about topological insulator itself as it is not the focus of this article, except to point out that: a) the electron dispersion relation shows a helical spin texture — the electrons' spin orientation and momentum direction are tightly locked due to strong spin-orbit coupling; b) the dispersion is linear for the energy range we are interested in — known as the relativistic Dirac dispersion; and c) there is no energy gap and no spin degeneracy — a single band structure, different from a zero-gap semimetal or the spin and valley degenerate graphene. As the ingenious proposal from Fu and Kane [22] demonstrates, by coupling the helical surface states of a topological insulator with a conventional s-wave BCS superconductor through proximity effect, one can essentially simulate the properties of a p-wave superconductor and perform any subsequent operations with the composite states. Due to the two-dimensional nature of the topological surface states, the resultant "p-wave superconductor" is also two-dimensional. When a vortex nucleates on such a surface, it defines a non-superconducting region which essentially creates an "edge" on the surface localized to a tiny circle. A closed contour around this circle has a Berry phase shift of π due to the rotation of spin orientation around this circle. A Majorana zero mode is trapped within this vortex core, and can therefore be moved coherently when one physically moves this vortex around, as if it is a standalone physical particle. Once these localized, non-Abelian Majorana bound states are established, one can then perform the necessary braiding operation on them which covers all the quantum gates required for quantum information processing [17].

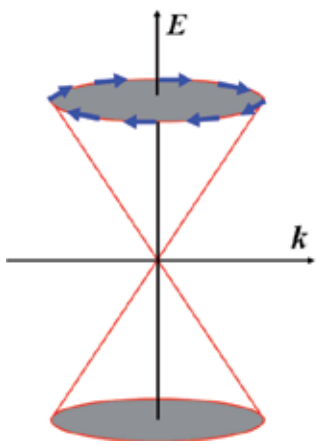

Figure 2. Electron energy dispersion with a helical spin texture similar to the surface states of a topological insulator. Blue arrows indicate the directions of the spins, and red cones indicate the linear dispersion near the Dirac point.

Though a topological insulator makes a convenient platform for creating a p-wave superconductor and the subsequent Majorana fermions, the above proposal remains an experimental challenge mainly due to the difficulties associated with perfecting the topological materials

http://dx.doi.org/10.5772/59942

themselves, which requires significantly more effort along the road [24, 26, 27, 28]. Experimentalists have progressed remarkably further on a much more mature material platform: the surface of a semiconductor with strong Rashba spin-orbit coupling. Evidence of Majorana bound states has already been reported in this direction [29, 30, 31]. The basic idea here is to also look for an electronic state that resembles the helical spin states as described above, and the Rashba spin-orbit coupling, resulting from structural change at interfaces; this idea can become a convenient solution to the problem. Fig.3 illustrates the effect of Rashba spin-orbit coupling on a "free" electron band. Due to the relativistic effect, electrons moving in the interfacial electric fields also experience effective magnetic fields on their rest frame. Forward-moving electrons and backward-moving electrons see opposite in-plane effective magnetic fields. In the forward-moving direction, the spin-"inward" electrons are lifted higher in energy than the spin-"outward" electrons, and vice versa in the opposite-moving direction. Here the inward and outward spin orientations are with respect to the paper of drawing, and which spin configuration has lower energy is also determined by the Rashba field direction of that interface. Note that the spins are still degenerate at the k=0 point where the spin-orbit coupling vanishes, and it creates a crossing between the two bands. The dispersion relation is nearly linear in k close to this crossing point. Fig.3 only depicts the situation of one-dimensional electron motions (x-direction). Imagine that we are actually dealing with a two-dimensional surface, and the k space extends in both x and y directions. This will revolve the spin-split bands around the centre axis of k=0, and the crossing point evolves into a Dirac point under the electrons' two-dimensional motion. Because the Rashba field is normal to the xy-plane electron motion, the resulting effective magnetic fields — and therefore the principle spin quantum axes —always lie within the xy-plane and transverse to the direction of motion. This leads to a helical spin texture as depicted in Fig.3. Note that two helical spin-textured Fermi surfaces exist in this structure and a perpendicular Zeeman field along z-direction is necessary to open a gap at the Dirac point and remove the spin degeneracy from this system, eventually rendering it spinless. With this construction of a helical spin state through Rashba spin-orbit coupling, we can again proceed with superconducting proximity effect to simulate the properties of a p-wave superconductor.

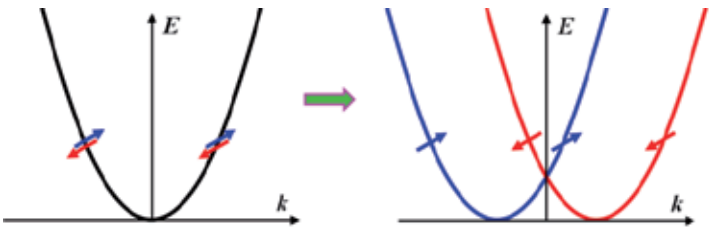

Figure 3. Illustration of a Rashba type spin-orbit splitting. Left: a typical parabolic "free" electron band with two-fold spin degeneracy. Right: In the presence of Rashba spin-orbit coupling, moving electrons feel an effective magnetic field on their rest frame, and the two spin channels are therefore split in energy. The effect is linear with respect to the wave vector *k*, and opposite for the two types of spins. Therefore, the Rashba spin-orbit coupling adds a linear component to the quadratic function, creating a uniform shift of the parabolas from the origin but in opposite directions for the opposite spin channels.

The proposal from Das Sarma et al. [23] is based on a 2D semiconductor electron system governed by the following equation of motion,

$$H_0 = \frac{\hbar^2 p^2}{2m^*} - \mu + V_z \sigma_z + \alpha\left(\vec{\sigma} \times \vec{p}\right) \cdot \hat{z} \tag{1}$$

Here, m^*, μ, V_z, α, are the electrons' effective mass, the chemical potential, the out-of-plane Zeeman splitting, and the Rashba spin-orbit coupling strength, respectively. Without the Zeeman term, the band structure would look just like that in Fig.3: revolving around the centre axis, as described above. We can easily see that the Zeeman term has a negligible influence on the total wavefunction when $\vec{p}$ is large, but becomes dominant close to $\vec{p}$ =0 and opens up an energy gap right at the Dirac point, with the gap size $2V_z$ determined by the electrons' g-factor and the applied Zeeman field strength. This perpendicular Zeeman field is critical in this proposal for removing the spin degeneracy from the structure, leaving only one band present within the Zeeman gap. One does need to carefully tune the Fermi level of the system to within this gap to take advantage of this feature. The next ingredient is the superconducting proximity effect, which will induce superconductivity into the semiconductor's Rashba-split surface states. In order for the proximity effect to be effective, the semiconductor needs to be sufficiently conducting, in addition to possessing strong Rashba spin-orbit coupling. These requirements readily identify some of the heavy-element, low-gap semiconductors as the most promising choices, such as InSb or InAs. They tend to also have very large conduction electron g-factors, dozens of times larger than 2, making them even more ideal in applied magnetic fields. The superconductors, on the other hand, tend to have lower critical magnetic fields if the field direction is pointing out of the film plane, and in many cases the superconductivity will be completely destroyed by a field of a few Tesla. In order to induce appreciable Zeeman splitting, hopefully a few meV or higher, without suppressing the superconductivity, magnetic insulators are often used in these proposals to induce the necessary perpendicular Zeeman field. These materials are known to produce large exchange Zeeman fields onto adjacent free electrons, and are most effective on low-dimensional 2D or 1D electron systems [32]. The induced effective field can reach hundreds of Tesla with this approach. With exchange fields being short ranged, they have negligible influence on the superconductivity because the superconductor and the magnetic insulator are not in direct contact. Later, Alicea et al. [33] offered a clever twist on the above proposals by combining the Dresselhaus spin-orbit coupling, intrinsic to III-V semiconductors because of their crystallographic inversion asymmetry, and the Rashba spin-orbit coupling, due to the structural inversion asymmetry at interfaces, in a semiconductor quantum well structure with selected crystalline orientations. Now that the principle spin quantum axis no longer lies within the electrons' motion plane, a magnetic field with reasonable strength applied parallel to the plane surface, coupled with the relatively large g-factors in these semiconductors, can also open up an appreciable energy gap at the centre point, removing the spin degeneracy found there. Once the spinless platform is constructed, the next important practice is to tune the chemical potential of the system right to the middle of this gap through chemical doping or electric field gating. One can then place

http://dx.doi.org/10.5772/59942

a conventional s-wave superconductor on top, which induces superconductivity into the system through proximity effect. The induced superconducting correlation opens up another energy gap on the conduction electrons and the system becomes fully gapped. With all these ingredients in place, the system can be described with exactly the same Bogoliubov-de Gennes (BdG) equations as the topological p-wave superconductors, and Majorana bound states are expected to exist at vortex cores on this special platform.

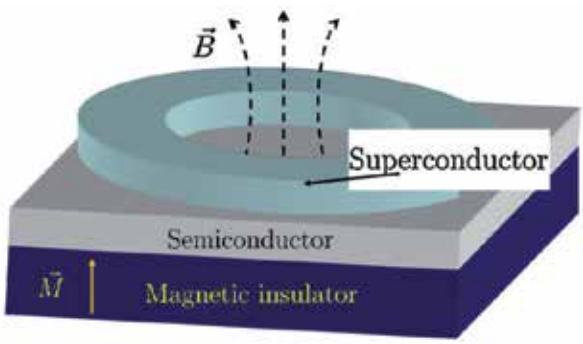

Figure 4. Majorana state bound to a vortex core on a heterostructure of a Rashba semiconductor platform, with both superconducting and magnetic proximity effects [23].

Another route of synthesizing Majorana fermions is to perform superconducting proximity on top of a heavy metal surface with strong Rashba spin-orbit coupling [34, 35]. The Rashba splitting tends to be much larger than in the semiconductor systems. Under the strong Rashba spin-orbit coupling, the metal's surface states also show two spin-split parabolas, with a crossing at k=0 similar to those shown in Fig.3. A perpendicular external magnetic field, or a perpendicular exchange field from magnetic insulators, will open up a Zeeman gap at the cross point, and an s-wave superconductor will induce superconductivity into the system through superconducting proximity effect. While the superconducting gap stays with the chemical potential of the system, one still needs to match the chemical potential to the middle of the Zeeman gap. Due to the abundance of carriers in the metallic systems, however, it is extremely difficult to move the chemical potential through electric field gating. Therefore, one has to carefully select a suitable electron system to begin with, with the crossing point of the surface states not too far from the metal's Fermi level. Fig.5 shows one such set-up. Tunnelling spectrum to the interface can reveal the existence of the desired, gapped Rashba surface states. Once the superconducting proximity effect kicks in, appearance of Majorana zero-energy modes can mediate resonant Andreev reflection between two leads, with perfect conductance of $2e^2/h$ independent on the coupling strength. As a comparison, conventional resonant Andreev reflection only shows the maximum conductance when the two coupling amplitudes are identical.

The construction of the p-wave-superconductor-like electron systems makes the search for Majorana fermions much more tangible for experimentalists. It is now possible to revisit Kitaev's initial concept of 1D wires hosting Majorana end modes [36], which has been subse-

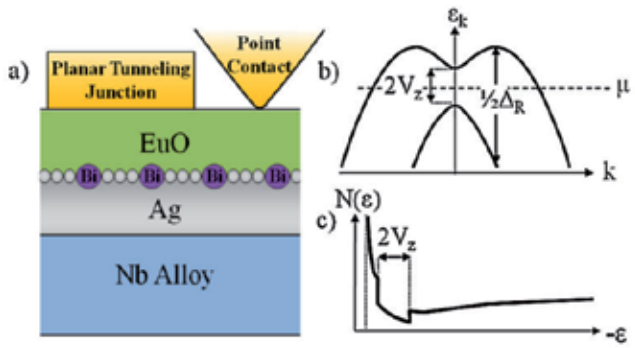

Figure 5. The proposed sample layout for the heavy-metal-based Majorana fermion creation [34]. (a) Ag(111) surface with 1/3 monolayer of Bi coverage in the $(\sqrt{3}\times\sqrt{3})$ R30° reconstruction. Superconducting proximity from an s-wave superconductor (Nb alloy), and magnetic proximity from a magnetic insulator (EuO), together create a topological superconductor channel on the system. (b) Electrons confined on the metal surface experience strong Rashba spin-orbit coupling and form two parabolas crossing at k=0. The gap of $2V_Z$ comes from the exchange fields from EuO, and the chemical potential μ of the system needs to be tuned to the mid-gap. (c) Potential verification of the surface states through tunnelling spectrum, where one should see a dip corresponding to the opening of the exchange gap and a van Hove singularity corresponding to the very top of the Rashba bands.

quently extended onto semiconductor nanowire platforms coupled with strong superconducting proximity effect [37, 38, 39]. The two ends of a 1D wire form a protected pair of Majorana fermions. This is analogous to a vortex on a 2D topological superconductor, which is also a boundary of the 2D platform but a physically moveable entity. To create a 1D p-wave superconductor wire, one can start with a 1D semiconductor wire and drive it into superconductivity with superconducting proximity effect. The regions surrounding the nanowire are just topologically trivial superconductors/insulators, leaving the enclosed topological superconductor nanowire intact. One can also start with the constructed 2D p-wave superconductor platforms as described earlier, and use selected electric and magnetic manipulation to suppress or flip the polarity of the topological superconductivity in order to define the desired 1D nanowire region with a distinct topology. Specifically, magnetic insulators can exert very strong interfacial exchange fields onto the desired 2D platforms, and can therefore be used as a local control to open and close the Zeeman gap of the system without much adverse influence on the superconductor system. Electric field manipulation from gate electrodes allows for local and active tuning of chemical potentials in the system. The topologically nontrivial superconductor state is enabled when the chemical potential is tuned into the mid gap, and will be destroyed when it is too far off. Therefore, we see that we can conveniently perform the fusion and braiding operations on the Majorana end modes with controlled gating on the 1D wire networks [39]. Similar manipulations can also be achieved on 2D platforms by controllably moving the vortices. Quantum information is stored non-locally on these non-Abelian systems and therefore is largely immune to any local perturbations, as long as the topology of the above systems remains protected by the superconducting and exchange gaps. These properties ensure that topological quantum computing on these solid-state platforms is inherently error-tolerant. We will not discuss in this article the details of braiding operations for topological quantum information processing, except to point out that quantum braids cover all the

http://dx.doi.org/10.5772/59942

necessary quantum gates required for quantum computing. One can refer to the original article by Kitaev et al. [17] for an accurate account for topological quantum computation with non-Abelian anyons.

There have been a number of reports about successfully observing the signatures of Majorana fermions along the route of the proposed proximity-driven platforms [29,30,31, 40, 41, 42]. Semiconductors offer the most opportunities so far because of their maturity in technology. The first convincing report [29] was based on InSb nanowires with strong spin-orbit coupling and a very large g-factor ($g \approx 50$), and the device layout is shown in Fig.6. The nanowire portion under the superconductor is the region of interest, where the superconducting proximity effect drives this nanowire region into superconducting. Note that the superconductor only covers half of the wire in order that the electric fields coming from the buried gate electrodes are not completely screened. This practice is very important to ensure that the chemical potential of this portion of wire can be tuned into the middle of the Zeeman-split gap with controlled gating. The semiconductor nanowire with strong Rashba spin-orbit coupling can be treated as a quasi-1D electron system, and its dispersion relation is essentially the same as that illustrated in Fig.3's right-hand panel, with two Rashba-spin-split parabolas in zero magnetic fields. In the nanowire geometry, one can find that when the applied magnetic field is along the wire direction, a Zeeman energy gap opens up at the Dirac point of the dispersion curve. The above actions ensure that Majorana bound states will emerge at the ends of the wire when the topological superconductor phase disappears and the normal gapped semiconductor/superconductor phase emerges. A quantum mechanical tunnelling measurement on this Majorana mode confirmed that it is bound strictly at zero energy throughout the field range in which it is supported. It emerges when the field applied along the wire opens up the Zeeman gap, and disappears when the field becomes too strong and destroys the topological superconductor phase. The behaviour is distinctly different from other phenomena such as Andreev reflection and Kondo effect, and is therefore widely accepted as the first observation of Majorana bound states in solid-state systems. The bound state vanishes under elevated temperatures, because thermal excitations start to overcome the gap protections. Strictly speaking, a semiconductor nanowire is not exactly a 1D electron system, and there are multiple transverse subbands due to the finite width. The above 1D wire theory was expanded to the more general multichannel situations [34, 43], and the protected Majorana modes exist in the quasi-1D wires as long as there are only an odd number of bands crossing the Fermi level and the wire is not substantially wider than the superconducting coherence length. These conditions are both satisfied in this experiment. The magnetic field was applied along the wire direction in this experiment, and a magnetic field perpendicular to the device plane (out-of-the-page) is no longer a suitable choice. The circular geometry of the nanowires leads to a circular distribution of the Rashba electric fields, and for some parts of the wire surface the applied magnetic field would be aligned parallel to the wire surface and perpendicular to the wire direction. Magnetic field in such a configuration is only able to shift the Dirac point a little bit in energy and momentum, but is not able to open up the desired exchange gap. Therefore, some parts of the wire would remain gapless if a perpendicular-to-the-device-plane magnetic field is chosen.

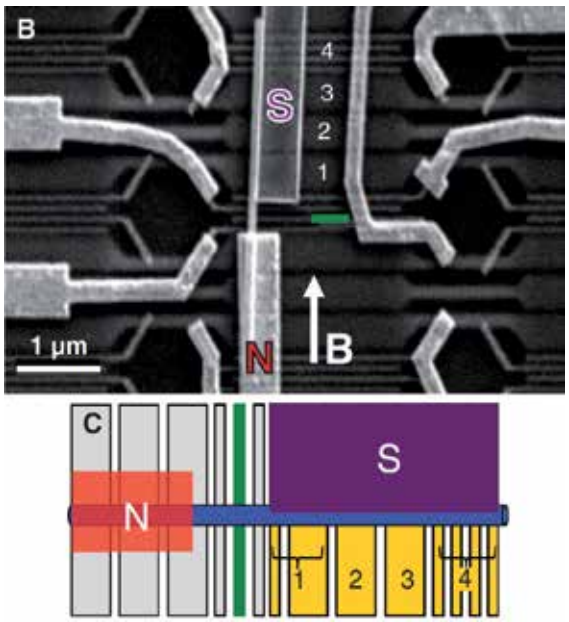

Figure 6. Device layout for the experimental evidence of Majorana fermion in a solid-state system [29]. The electrodes seen on the background, numbered 1, 2, 3, 4, etc., are the gate electrodes, separated from the nanowire and top electrodes by Si_3N_4 dielectrics. The nanowire is in contact with a normal metal (N) on one end, and a superconductor (S) on the other. The gate electrode labelled in dark green is the one used to create a tunnel barrier between the two sides of the nanowire. This effectively forms a S-NW-N tunnel junction for spectroscopy measurement. The nanowire region covered under the superconductor would have proximity-induced superconductivity in it, and a Majorana bound state is therefore trapped at the very edge of the superconductor region when the topology changes. It shows up as a zero-bias peak on the tunnel spectroscopy when a suitable magnetic field is applied along the wire direction.

3. Inverse proximity on superconductors — The example of superconducting spin valves

As we have described above, the superconducting proximity effect describes the superconductor's wavefunction propagating into non-superconducting materials and inducing superconducting paring in there. Because of the leak-out of paired electrons, and the influx of unpaired electrons, the proximity effect would naturally generate a counter effect that weakens the superconductor itself. This is known as the inverse proximity effect. We will only focus our attention on a specific aspect of it — inverse proximity from ferromagnetic materials. The presence of spin information in the ferromagnets allows for spintronic manipulation on the superconductor system. For a detailed review on superconducting proximity with ferromagnets, please see the thorough review articles by Buzdin and Bergeret et al. [44, 45]. Here we proceed to demonstrate the inverse proximity effect from ferromagnets by illustrating with superconducting spin valve devices that can essentially turn the superconductivity On and Off through spin manipulations.

http://dx.doi.org/10.5772/59942

The propagation of superconductor wavefunction in a ferromagnetic metal is qualitatively different from that in a normal metal. This originates from the mutual incompatibility between a BCS superconductor, in which opposite spins pair up into Cooper pairs, and a ferromagnet, in which spins prefer to align parallel to each other to minimize the exchange energy. The presence of magnetic species in or near a superconductor material could be a drag if one wants to maximize the performance of the superconductor, because magnetic interactions break time reversal symmetry and become a strong source of Cooper pair breaking. We can, however, achieve desired controllability on the superconductor devices through manipulating the proximity-coupled magnetic systems. Fig.7 illustrates the propagation of superconducting wavefunction into a ferromagnetic metal. We note that instead of a simple exponential decay as in the normal metal/superconductor situation (Fig.1), the superconducting order parameter picks up a fast oscillatory behaviour. This can be qualitatively understood by considering the two electrons of a Cooper pair with opposite spins sitting inside an exchange field. One of the electrons, with its spin aligned along the exchange field direction, has its kinetic energy lowered by δE, while the opposite electron sees an increase in its kinetic energy by δE in the exchange field. Therefore, they start to propagate with different wavevector k, and the Cooper pair as a whole no longer has zero net momentum as it used to when it was inside the superconductor. For an electron near the Fermi level of a parabolic band, the kinetic energy is quadratic to the wavevector k and an increase (or decrease) in the kinetic energy by δE leads to a change in the wavevector by $\delta E/\hbar v_{\mathrm{F}}$, where v_{F} is the Fermi velocity. The Cooper pair now gains a centre-of-mass momentum of $2\delta E/v_{\mathrm{F}}$, and therefore the order parameter of the Cooper pairs will oscillate in space with a period of $\hbar v_F/2\delta E$. This roughly describes the system in the clean limit. For the dirty limit of a diffusive system, the Cooper pair motion can be described well with the Usadel equation [46]. Under the assumption that the exchange energy is much larger than the pairing energy, which is true for most ferromagnets relative to superconductors, the pair wave function can be solved and has a form of $\Delta \exp\left(-\frac{x}{\xi_f}\right)\cos(\frac{x}{\xi_f})$ [44], i.e., an oscillatory function with exponential damping. In this special situation, the decay length and the oscillation period coincide (but they do not have to in more general situations). Here, $\xi_f = \sqrt{D_f / \delta E}$, $D_f = \frac{1}{3} v_F l$ is the diffusion coefficient and l is the electrons' mean-free-path in the ferromagnet. The oscillatory behaviour of the pair wave function adds an oscillatory dependence to the structure's overall critical temperature [47] when the ferromagnet layer thickness is comparable or longer than the pair oscillating period ξ_{F}. This has been verified in various superconductor-ferromagnet bilayer structures [48, 49, 50, 51]. One can readily see that when the ferromagnet layer thickness is equal to $\pi\xi_{\mathrm{F}}$, the wavefunction has a phase shift of π across the ferromagnet layer, and the superconductivity is therefore weakened. As the ferromagnet increases in thickness, the phase oscillates back and forth and the system shows an oscillatory, non-monotonic behaviour in the critical temperature. The parameter ξ_{F} can be approximately read out from the oscillation period of T_C. The oscillatory behaviour of the pair wavefunction shows up not only in the phases, but also in the electron density of states inside the ferromagnets. At certain distance away from the interface, the density of states can even become larger than the normal value in the absence of superconducting proximity [52].

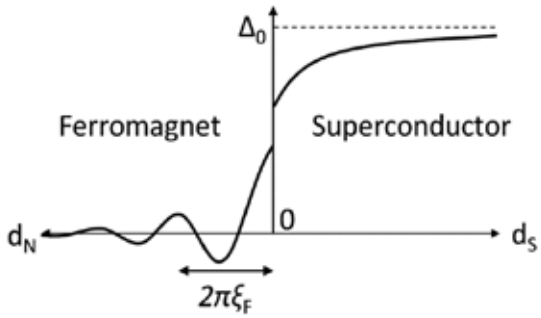

Figure 7. Evolution of the superconductor pairing potential near a S/F interface. The pairing potential inside the ferromagnet shows a strong oscillatory and damping behaviour due to the large internal exchange field. ξ_F characterizes the superconducting correlation oscillation length as well as the correlation decay length within a strong ferromagnet, where the exchange energy δE far exceeds the pairing potential Δ.

Though it is not immediately clear, the above discussions already imply that superconductivity within the superconductor itself will also be significantly weakened in the presence of a strong ferromagnet. A critical difference of the proximity with a strong ferromagnet, compared to that with a normal metal, is the extremely short decay length of the pairing potential. By connecting the superconducting wavefunction across the interface, one can already see that the steep slope of the pairing potential on the ferromagnet side influences that on the superconductor side and pulls the whole pairing potential profile downward. The exact boundary condition matching is subject to the interfacial transparency and the respective diffusion coefficients. A stronger ferromagnet creates stronger exchange interaction and shorter ξ_F: therefore, stronger suppression to the superconductivity. Now we can consider constructing a sandwich of ferromagnet/superconductor/ferromagnet: i.e., a superconducting spin valve structure [53, 54]. Although the two ferromagnet layers will both strongly suppress superconductivity in the sandwiched middle layer, we can try to cancel out their influence through spin manipulation. Recall that when one of the ferromagnet layers is placed on top of the superconductor, strong suppression of superconductivity is present. If we place the second ferromagnet layer with the same spin polarity, the inverse proximity effects coming from both ferromagnets strengthen each other and suppress superconductivity even more. This spin-parallel configuration ensures that the wavefunction over the whole structure is symmetric with respect to the film centre (mid-plane of the superconductor). We can conceptually fold the wavefunction in the middle and it becomes identical to that of a bilayer situation. Because the equivalent thickness of the superconductor layer is only half of its actual thickness, the layer suffers even stronger suppression from the inverse proximity effect. If we instead place the second ferromagnet with an opposite spin polarity relative to the first one, i.e., configuring the system into a spin-antiparallel state, the proximity effects from the two ferromagnets differ precisely by a phase of π and will largely cancel each other out. Superconductivity is therefore restored in this configuration.

We now use an epitaxial pristine structure of Fe/V/Fe as an example to illustrate the above mentioned superconducting spin valve effect [51]. The structure was deposited with molecular

http://dx.doi.org/10.5772/59942

beam epitaxy (MBE) onto MgO-buffered Si(100) substrates. X-ray diffraction verified the epitaxy of the films showing clear four-fold symmetry in the off-axis diffraction patterns. The quality of the films and interfaces can be verified with the critical temperature T_C and upper critical field H_{C2} measurements on V single layer films and Fe/V bilayer films. Fig.8 (a) shows that T_C varies linearly with respect to the inverse film thickness. Such dependence indicates clearly that there exists a superconducting "dead" layer on the film surface due to the lowering of electron density and weakening of phonon coupling there [55]. This surface layer is superconductingly inactive, and amounts to about 1 atomic layer (0.18 nm) on the pure V films (interfaced with MgO on both sides), confirming the superior quality of these films. On the other hand, the series of bilayer samples of V with proximity to 6 nm Fe show a significantly steeper slope, corresponding to a much thicker inactive layer of 13.5 nm. For V of the same thickness, presence of Fe pulls T_C much lower than MgO does in pure V films. This is a clear manifestation of the above-described inverse superconducting proximity effect: the presence of a ferromagnet strongly suppresses superconductivity in the adjacent superconductor. Fig. 8 (b) shows the upper critical fields of the set of films with 30 nm V. The addition of proximity from Fe again significantly suppresses superconductivity. The linear dependence of H_{C2} square with respect to temperature is an indication of two-dimensional superconductivity behaviour, which follows $H_{C2}(T)=H_{C2}(0)(1-\frac{T}{T_C})^{1/2}$ [56]. From the determined slope of the plot, we can identify the superconducting coherence length ξ_S, being about 8.2 nm for the 30 nm V films. It is interesting to note that the slope does not change when the proximity effect from Fe kicks in, indicating that no change happens to the Cooper pair correlations. This is quite expected because the proximity effect and inverse proximity effect do not modify the pairing mechanisms within the superconductor, and the addition of a few nm metals has little influence on the electrons' mean-free-paths either. Fig.8 (c) shows the most important aspects of the inverse superconducting proximity effect: the quick oscillation and damping of T_C with thickness. As we have described earlier, T_C oscillates with the ferromagnetic layer thickness because of the Cooper pairs' phase oscillation inside an exchange field. We can roughly estimate the superconducting correlation length inside the ferromagnet ξ_F to be about 1 nm. We can also clearly see that the superconductivity suppression from inverse proximity effect is quite dramatic: with a few monolayers of Fe overlayer, the critical temperature already drops from the original value of over 5K to only slightly above 3K. The oscillation quickly damps out after several ξ_F, when the Cooper pair wavefunction is almost fully suppressed. After the first few nm, further increase of the ferromagnetic layer thickness does not continue to influence the overall wavefunction. On the other hand, we notice that T_C does not really drop to zero before recovering, as we have depicted before. This actually is also a consequence of the fast damping behaviour which significantly limits the transparency of the Cooper pairs into the ferromagnet. Beyond the first few nm, the remaining portion of the ferromagnet has no significant further contribution to the T_C suppression. In addition, because the measurement of T_C is over the whole structure, the region of the superconductor far away from the interface essentially retains the original superconductivity strength, and renders the whole structure superconducting under conventional DC measurements. Detailed calculations on T_C of such ferromagnet/superconductor bilayer structures confirm that the oscillation indeed quickly reaches a saturation value after the ferromagnet thickness increases beyond the first few oscillations [57].

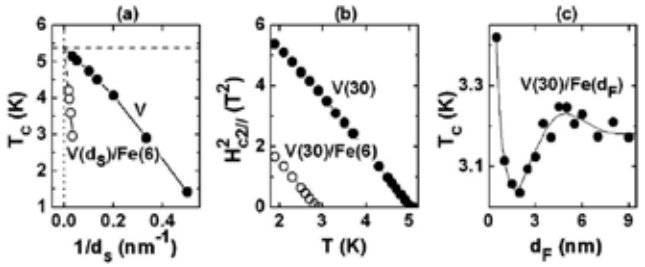

Figure 8. Critical temperature T_C and upper critical field H_{C2} for epitaxial V and Fe/V films [51]. (a) T_C as a function of inverse V layer thickness; (b) H_{C2} square as a function of temperature; (c) T_C damping and oscillation with respect to the Fe layer thickness, the solid line is provided as a guide for the eye. ξ_F can be estimated to be about 1 nm.

Next, we consider the magnetoresistance of these superconducting spin valves. The structure is fully epitaxial, with high interfacial quality. In order to magnetically separate the two Fe layers, a CoO antiferromagnetic layer was introduced above the top Fe layer, which exerts exchange bias [58] on the top Fe layer and essentially pins the magnetization of this layer to a chosen direction. When the applied magnetic field only sweeps in a range not exceeding the exchange bias pinning strength, one can only observe magnetic switching of the "free" layer, which is the bottom Fe layer in this structure. Fig.9 (a) shows the magnetoresistance results across temperatures close to T_C. When the magnetic field varies, clear resistance high and low states are observed, indicating that the structure toggles between the non-superconducting and superconducting states. In the spin-parallel configuration, the inverse proximity effects from both ferromagnet layers strengthen each other and strongly suppress superconductivity of the sandwiched V layer, leading to the high-resistance, non-superconducting state; in the spin-antiparallel configuration, the inverse proximity effects largely cancel each other out and the system returns to the low resistance, superconducting state. For certain temperatures the ratio between the normal resistance and the superconducting resistance is essentially infinite, making the magnetoresistance ratio essentially infinite. The effect is only pronounced in a very narrow temperature window close to T_C, because this is when the superconductivity is already quite weakened by thermal energy, and slight perturbations from the environment (such as from the inverse proximity effects) can readily drive the system in and out of its superconducting state.

Fig.9 (b) shows T_C determined for the two spin configurations. Clearly, spin-parallel state has weaker superconductivity and lower T_C, while spin-antiparallel state has stronger superconductivity and higher T_C. In the temperature range between these two T_C, a large resistance difference exists between the two states leading to the large magnetoresistance described above. The superconducting spin valve effect relies on the fact that the two ferromagnet layers are effectively coupled to each other through the superconductor. Therefore, the effect decreases as the superconductor layer thickness increases, and essentially drops to zero when the superconductor layer is much thicker than the superconducting coherence length ξ_S of about 8 nm in this system. On the other hand, if the superconductor layer is too thin, its superconductivity would be fully suppressed by the Fe layers and the superconducting spin

http://dx.doi.org/10.5772/59942

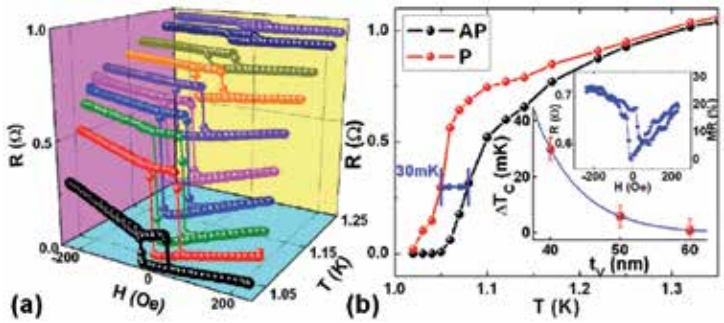

Figure 9. Measured superconducting spin valve effect in the epitaxial Fe/V/Fe structure [51]. (a) Device resistance as a function of applied magnetic field H and temperature T. A large magnetoresistance is associated with the switching of the free Fe layer in the temperature range close to T_C. (b) Resistance as a function of temperature for the structure in its spin-parallel (P) and spin-antiparallel (AP) configurations. There is a clear offset of 30mK between their corresponding T_C's. Inset: T_C offset as a function of the V layer thickness, and an example of a magnetoresistance curve for the sample with 50 nm V.

valve effect is also no longer achievable. The T_C shift as seen in Fig.9 (b) is clear indication of the operation temperature range of this effect, which is, however, limited to only tens of mK across many different systems [59, 60, 61, 62,51]. Improving interfacial transparency is the key for further improving the performance of these devices. Fig.10 shows the calculated variation of the P and AP T_C's with the change of the interfacial transparency [53]. The curves with the highest transparency (solid lines, T_F=25) clearly show a region with very large T_C shift. For example, around d_F/ξ_F=0.4, T_C of the AP state is around half the bulk value while that of the P state is fully suppressed. For samples of this structure, infinite magnetoresistance would show up for any temperatures below half the bulk T_C, making it a practically usable device for turning the superconductivity On and Off. As a comparison, for the curves corresponding to the lowest interfacial transparency, T_F = 1, the T_C difference between P and AP states is very small throughout all the d_F choices. This is easy to understand because poor interface transparency breaks up the correlation between the superconductor and the ferromagnets: therefore, the correlation between the two ferromagnets also vanishes. The two ferromagnets do not feel much influence from each other and the P and AP configurations make little difference. Although a weak superconducting spin valve effect is still present, the resultant magnetoresistance is very small and there is no truly On and Off tuning of superconductivity, making it less useful in practice.

We next examine a special type of superconducting spin valve, where the ferromagnet layers are not metallic but insulating [63]. The above described inverse superconducting proximity mechanism does not apply because the Cooper pair wavefunction cannot penetrate into the insulators. The inverse proximity happens due to the interfacial exchange interactions from the localized moments of the magnetic insulator, which exert a large effective Zeeman field onto the superconductor and can also suppress the superconductivity [32]. The interaction between the magnetic insulator and the carriers in the superconductor is through indirect exchange interaction, where the free electrons communicate with multiple localized magnetic moments of the magnetic insulator, and become spin-polarized in the process. This behaves

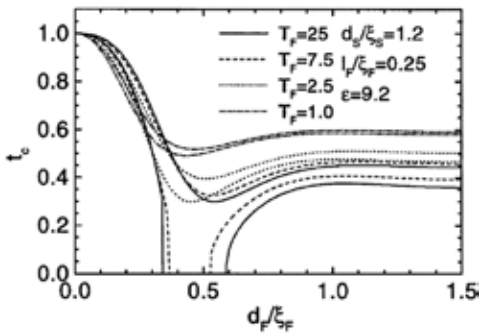

Figure 10. Expected T_C shift in superconducting spin valves when the interface transparency is varied [53]. Here d_S and d_F are the superconductor and ferromagnet layer thicknesses, l_F is the electron mean-free-path in the ferromagnet, ξ_S and ξ_F are the superconducting correlation lengths in the superconductor and ferromagnet, and ε is a parameter depending on the properties of both the superconductor and the ferromagnet, getting smaller with stronger ferromagnets. Two curves are shown for each choice of interfacial transparency, with the upper curve corresponding to the AP state and the lower one to the P state.

as an effective Zeeman field on the electron system and favours one type of spins over the other, therefore counteracts the tendency of Cooper pairing and suppresses superconductivity. Now that the magnetism-superconductivity interaction is established, it is again possible to use spin manipulations to control superconductivity in a sandwich structure [64]. The magnetic insulator material used in this study was EuS, which has been shown to generate exchange fields as large as a few Tesla on thin superconducting Al films [65, 66]. Under this effective Zeeman field on the conduction electrons, Cooper paring in the superconductor becomes less stable and superconductivity is thus weakened accordingly. A second magnetic insulator layer, when configured with its magnetic orientation opposite to the first one, will serve to cancel the exchange fields from the first one, provided that the electrons' mean-free-paths are long enough relative to the superconductor layer thickness such that the Zeeman fields from one side can propagate across the whole superconductor layer and influence the other side. As a result, we again recover a spin valve performance: when the two magnetic insulators are aligned parallel to each other, their exchange fields stack up and destroy the superconductivity in the system; when they are aligned antiparallel to each other, their effects cancel and the system goes back to the superconducting state. Experimentally, toggling the superconductivity On and Off leads to a very large magnetoresistance response, as shown in Fig.11. Here the system is in the spin-parallel state (finite resistance, non-superconducting state) when the external field is large and both EuS layers are saturated in the same direction; and in the spin-antiparallel state (zero resistance, superconducting state) when the external field is tuned between the magnetic switching fields of the two EuS layers, such that one of the layers flips while the other does not. Similar to the superconducting spin valves with magnetic metals, this effect only shows up in a very narrow temperature window close to T_C, when the superconductivity is already very weak to begin with. Though this effect appears very similar to the previously described superconducting spin valve effect, there is one critical difference: in this structure, there are negligible superconducting proximity and inverse proximity effects because of the insulating nature of the ferromagnets. The observed magnetic

http://dx.doi.org/10.5772/59942

tuning of superconductivity is in fact a result of the propagation of magnetic exchange interaction into the superconductor — the magnetic proximity effect, which is especially pronounced with magnetic insulators [32]. As a result, the system is described with the Cooper pairs feeling the average exchange fields *inside the superconductor* rather than with Cooper pairs feeling the exchange fields *inside the ferromagnets*.

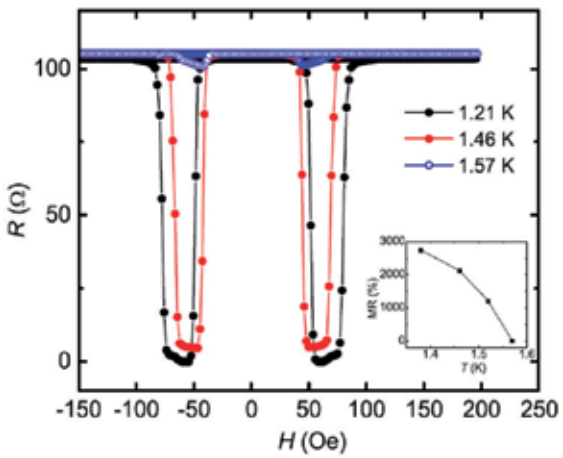

Figure 11. Superconducting spin valve effect in a magnetic insulator/superconductor/magnetic insulator sandwich structure (EuS/Al/EuS) [64]. Inset shows the variation of magnetoresistance ratio over the temperatures close to T_C.

4. Summary

In summary, we have used a few very specific examples (the creation of Majorana fermions on 2D surface states and the superconducting spin valves with ferromagnets) to illustrate the application of superconducting proximity and inverse proximity effects in spintronics. These examples can be viewed as passive devices of superconducting proximity/inverse proximity. One can also use active pumping of Cooper pairs to drive supercurrents into non-superconducting materials, which is yet another manifestation of the superconducting proximity effect and can induce superconducting Josephson coupling on many spintronics platforms, such as graphene and topological insulators. The Josephson effect will be covered in other chapters of this book and we will not discuss it in this chapter. Overall, we see that the superconducting proximity and inverse proximity effects are convenient approaches to couple superconductivity with many other types of spin systems, and allow us to create hybrid devices that can benefit from these very distinct spin states: superconductivity, magnetism, and topological quantum spin Hall state. Such manipulation of superconductivity offers important new routes for information storage and processing, and rapid advances are expected to happen in these directions taking information processing to the quantum level. We, as well as many other groups in the world, are actively working toward such goals.

Acknowledgements

The author wish to thank the Natural Sciences and Engineering Research Council of Canada (NSERC) for support on this work.

Author details

Guoxing Miao*

Address all correspondence to: guo-xing.miao@uwaterloo.ca

Institute for Quantum Computing and Electrical and Computer Engineering, University of Waterloo, Waterloo ON, Canada

References

[1] Meissner H, Superconductivity of Contacts with Interposed Barriers, Phys. Rev. 1960; 117: 672.

[2] de Gennes P G, Boundary Effects in Superconductors, Rev. Mod. Phys. 1964; 36: 225.

[3] Takayanagi H, Kawakami T, Superconducting Proximity Effect in the Native Inversion Layer on InAs, Phys. Rev. Lett. 1985; 54: 2449.

[4] Nitta J, Akazaki T, Takayanagi H, Arai K, Transport Properties in an InAs-inserted-channel In0.52Al0.48As / In0.53Ga0.47As Heterostructure Coupled Superconducting Junction, Phys. Rev. B 1992; 46: 14286(R).

[5] Nguyen C, Kroemer H, Hu E L, Anomalous Andreev Conductance in InAs-AlSb Quantum Well Structures with Nb Electrodes, Phys. Rev. Lett. 1992; 69: 2847.

[6] Zhang D, Wang J, DaSilva A M, Lee J S, Gutierrez H R, Chan M H W, Jain J, Samarth N, Superconducting Proximity Effect and Possible Evidence for Pearl Vortices in a Candidate Topological Insulator, Phys. Rev. B 2011; 84: 165120.

[7] Williams J R, Bestwick A J, Gallagher P, Hong S S, Cui Y, Bleich A S, Analytis J G, Fisher I R, Goldhaber-Gordon D, Unconventional Josephson Effect in Hybrid Superconductor-Topological Insulator Devices, Phys. Rev. Lett. 2012; 109: 056803.

[8] Qu F, Yang F, Shen J, Ding Y, Chen J, Ji Z, Liu G, Fan J, Jing X, Yang C, Lua L, Strong Superconducting Proximity Effect in Pb-Bi2Te3 Hybrid Structures, Sci Rep. 2012; 2: 339.

[9] Heersche H B, Jarillo-Herrero P, Oostinga J B, Vandersypen L M K, Morpurgo A F, Bipolar Supercurrent in Graphene, Nature 2007; 446: 56–59.

[10] Morpurgo A F, Kong J, Marcus C M, Dai H, Gate-Controlled Superconducting Proximity Effect in Carbon Nanotubes, Science 1999; 286 (5438): 263–265.

[11] Jarillo-Herrero P, van Dam J A, Kouwenhoven L P, Quantum Supercurrent Transistors in Carbon Nanotubes, Nature 2006; 439: 953–956.

[12] Winkelmann C B, Roch N, Wernsdorfer W, Bouchiat V, Balestro F, Superconductivity in a Single-C60 Transistor, Nature Physics 2009; 5: 876–879.

[13] van Dam J A, Nazarov Y V, Bakkers E P A M, De Franceschi S, Kouwenhoven L P, Supercurrent Reversal in Quantum Dots, Nature 2006; 442: 667–670.

[14] Kasumov A Y, Kociak M, Guéron S, Reulet B, Volkov V T, Klinov D V, Bouchiat H, Proximity-Induced Superconductivity in DNA, Science 2001; 291 (5502): 280–282.

[15] Peña V, Sefrioui Z, Arias D, Leon C, Santamaria J, Varela M, Pennycook S J, Martinez J L, Coupling of Superconductors Through a Half-Metallic Ferromagnet: Evidence for a Long-Range Proximity Effect, Phys. Rev. B 2004; 69: 224502.

[16] Keizer R S, Goennenwein S T B, Klapwijk T M, Miao G X, Xiao G, Gupta A, A Spin Triplet Supercurrent Through the Half-Metallic Ferromagnet CrO2, Nature 2006; 439(7078): 825.

[17] Kitaev A Yu, Fault-Tolerant Quantum Computation by Anyons, Annals. Phys. 2003; 303(1): 2–30.

[18] Read N, Green D, Paired States of Fermions in Two Dimensions with Breaking of Parity and Time-Reversal Symmetries and the Fractional Quantum Hall Effect, Phys. Rev. B 2000; 61: 10267.

[19] Ivanov D A, Non-Abelian Statistics of Half-Quantum Vortices in p-Wave Superconductors, Phys. Rev. Lett. 2001; 86: 268.

[20] Das Sarma S, Nayak C, Tewari S, Proposal to Stabilize and Detect Half-Quantum Vortices in Strontium Ruthenate Thin Films: Non-Abelian Braiding Statistics of Vortices in a px+ipy Superconductor, Phys. Rev. B 2006; 73: 220502(R).

[21] Mackenzie A P, Maeno Y, The Superconductivity of Sr2RuO4 and the Physics of Spin-Triplet Pairing, Rev. Mod. Phys. 2003; 75: 657.

[22] Fu L, Kane C L, Superconducting Proximity Effect and Majorana Fermions at the Surface of a Topological Insulator, Phys. Rev. Lett. 2008; 10 (9): 096407.

[23] Sau J D, Lutchyn R M, Tewari S, Das Sarma S, Generic New Platform for Topological Quantum Computation Using Semiconductor Heterostructures, Phys. Rev. Lett. 2010; 104(4): 040502.

[24] Hasan M Z, Kane C L, Colloquium: Topological Insulators, Rev. Mod. Phys. 2010; 82: 3045.

[25] Fu L, Kane C L, Mele E J, Topological Insulators in Three Dimensions, Phys. Rev. Lett. 2007; 98: 106803.

[26] He L, Kou X, Wang K L, Review of 3D Topological Insulator Thin-Film Growth by Molecular Beam Epitaxy and Potential Applications, phys. stat. sol. - Rap. Res. Lett. 2013; 7: 50–63.

[27] Sasaki S, Kriener M, Segawa K, Yada K, Tanaka Y, Sato M, Ando Y, Topological Superconductivity in CuxBi2Se3

[28] Wang M X, Liu C, Xu J P, Yang F, Miao L, Yao M Y, Gao C L, Shen C, Ma X, Chen X, Xu Z A, Liu Y, Zhang S H, Qian D, Jia J F, Xue Q K, The Coexistence of Superconductivity and Topological Order in the Bi2Se3 Thin Films, Science 6 April 2012; 336: 52–55.

[29] Mourik V, Zuo K, Frolov S M, Plissard S R, Bakkers E P A M, Kouwenhoven L P, Signatures of Majorana Fermions in Hybrid Superconductor-Semiconductor Nanowire Devices, Science 2012; 336 (6084): 1003–1007.

[30] Deng M T, Yu C L, Huang G Y, Larsson M, Caroff P, Xu H Q, Anomalous Zero-Bias Conductance Peak in a Nb–InSb Nanowire–Nb Hybrid Device, Nano Lett. 2012; 12, 6414–6419.

[31] Das A, Ronen Y, Most Y, Oreg Y, Heiblum M, Shtrikman H, Zero-bias Peaks and Splitting in an Al-InAs Nanowire Topological Superconductor as a Signature of Majorana Fermions, Nature Physics 2012; 8: 887–895.

[32] Miao G X, Moodera J S, Spin Manipulation with Magnetic Semiconductor Barriers, Phys. Chem. Chem. Phys. 2014; DOI: 10.1039/c4cp04599h, in print.

[33] Alicea J, Majorana Fermions in a Tunable Semiconductor Device, Phys. Rev. B 2010; 81: 125318.

[34] Potter A C, Lee P A, Multichannel Generalization of Kitaev's Majorana End States and a Practical Route to Realize Them in Thin Films, Phys. Rev. Lett. 2010; 105: 227003.

[35] Law K T, Lee P A, Ng T K, Majorana Fermion Induced Resonant Andreev Reflection, Phys. Rev. Lett. 2009; 103: 237001.

[36] Kitaev A Y, Unpaired Majorana Fermions in Quantum Wires, Physics-Uspekhi 2001; 44: 131.

[37] Lutchyn R M, Sau J D, Das Sarma S Majorana Fermions and a Topological Phase Transition in Semiconductor-Superconductor Heterostructures. Phys. Rev. Lett. 2010; 105 (7): 077001.

[38] Oreg Y, Refael G, von Oppen F, Helical Liquids and Majorana Bound States in Quantum Wires, Phys. Rev. Lett. 2010; 105: 177002.

[39] Alicea J, Oreg Y, Refael G, von Oppen F, Fisher M P A, Non-Abelian Statistics and Topological Quantum Information Processing in 1D Wire Networks, Nature Physics 2011; 7: 412–417.

[40] Nadj-Perge S, Drozdov I K, Li J, Chen H, Jeon S, Seo J, MacDonald A H, Bernevig B A, Yazdani A, Observation of Majorana Fermions in Ferromagnetic Atomic Chains on a Superconductor, Science 2014; 346(6209): 602–607.

[41] Stanescu T D, Tewari S, Majorana Fermions in SemiconductorNanowires: Fundamentals, Modeling, and Experiment, J. Phys.: Condens. Matter 2013; 25: 233201.

[42] Beenakker C W J, Search for Majorana Fermions in Superconductors. Annu. Rev. Condens. Matter Phys. 2013; 4: 113.

[43] Lutchyn R M, Stanescu T D, Das Sarma S, Search for Majorana Fermions in Multiband Semiconducting Nanowires, Phys. Rev. Lett. 2011; 106: 127001.

[44] Buzdin A I, Proximity Effects in Superconductor-Ferromagnet Heterostructures, Rev. Mod. Phys. 2005; 77: 935–976.

[45] Bergeret F S, Volkov A F, Efetov K B, Odd Triplet Superconductivity and Related Phenomena in Superconductor-Ferromagnet Structures, Rev. Mod. Phys. 2005; 77: 1321–1373.

[46] Usadel K D, Generalized Diffusion Equation for Superconducting Alloys, Phys. Rev. Lett. 1970; 25: 507.

[47] Buzdin A I, Kuprianov M Y, Transition Temperature of a Superconductor-Ferromagnet Superlattice, Pis'ma Zh. Eksp. Teor. Fiz. 1990; 52, 1089–1091.

[48] Jiang J S, Davidović D, Reich D H, Chien C L, Oscillatory Superconducting Transition Temperature in Nb/Gd Multilayers, Phys. Rev. Lett. 1995; 74: 314.

[49] Mercaldo L V, Attanasio C, Coccorese C, Maritato L, Prischepa S L, Salvato M, Superconducting-Critical-Temperature Oscillations in Nb/CuMn Multilayers, Phys. Rev. B 1996; 53: 14040.

[50] Sidorenko A S, Zdravkov V I, Prepelitsa A A, Helbig C, Luo Y, Gsell S, Schreck M, Klimm S, Horn S, Tagirov L R, Tidecks R, Oscillations of the Critical Temperature in Superconducting Nb/Ni bilayers, Annalen der Physik 2003; 12: 37–50.

[51] Miao G X, Ramos A V, Moodera J S, Infinite Magnetoresistance from the Spin Dependent Proximity Effect in Symmetry Driven bcc-Fe/V/Fe Heteroepitaxial Superconducting Spin Valves,Phys. Rev. Lett. 2008; 101: 137001.

[52] Kontos T, Aprili M, Lesueur J, Grison X, Inhomogeneous Superconductivity Induced in a Ferromagnet by Proximity Effect, Phys. Rev. Lett. 2001; 86: 304.

[53] Tagirov L R, Low-Field Superconducting Spin Switch Based on a Superconductor/Ferromagnet Multilayer, Phys. Rev. Lett. 1999; 83: 2058.

[54] Buzdin A I, Vedyayev A V, Ryzhanova N V, Spin-Orientation-Dependent Superconductivity in F/S/F Structures, Europhys. Lett. 1999; 48: 686.

[55] Wolf S A, Kennedy J J, Nisenoff M, Properties of Superconducting rf Sputtered Ultrathin Films of Nb,J. Vac. Sci. Technol. 1976; 13: 145.

[56] Tinkham M, Introduction to Superconductivity, McGraw-Hill, New York, 1978.

[57] Demler E A, Arnold G B, Beasley M R, Superconducting Proximity Effects in Magnetic Metals, Phys. Rev. B 1997; 55: 15174.

[58] Berkowitz A E, Takano K, Exchange Anisotropy — A Review, J. Magn. Magn. Mater. 1999; 200: 552–570.

[59] Gu J Y, You C Y, Jiang J S, Pearson J, Bazaliy Ya B, Bader S D, Magnetization-Orientation Dependence of the Superconducting Transition Temperature in the Ferromagnet-Superconductor-Ferromagnet System: CuNi/Nb/CuNi, Phys. Rev. Lett. 2002; 89: 267001.

[60] Potenza A, Marrows C H, Superconductor-Ferromagnet CuNi/Nb/CuNi Trilayers as Superconducting Spin-Valve Core Structures, Phys. Rev. B 2005; 71: 180503(R).

[61] Moraru I C, Pratt W P, Birge N O, Magnetization-Dependent Tc Shift in Ferromagnet/Superconductor/Ferromagnet Trilayers with a Strong Ferromagnet, Phys. Rev. Lett. 2006; 96: 037004.

[62] Nowak G, Zabel H, Westerholt K, Garifullin I, Marcellini M, Liebig A, Hjörvarsson B, Superconducting Spin Valves Based on Epitaxial Fe/V Superlattices, Phys. Rev. B 2008; 78: 134520.

[63] de Gennes P G, Coupling Between Ferromagnets Through a Superconducting Layer, Phys. Lett. 1966; 23: 10–11.

[64] Li B, Roschewsky N, Assaf B A, Eich M, Epstein-Martin M, Heiman D, Munzenberg M, Moodera J S, Superconducting Spin Switch with Infinite Magnetoresistance Induced by an Internal Exchange Field, Phys. Rev. Lett. 2013; 110: 097001.

[65] Moodera J S, Hao X, Gibson G A, Meservey R, Electron-Spin Polarization in Tunnel Junctions in Zero Applied Field with Ferromagnetic EuS Barriers, Phys. Rev. Lett. 1988; 61: 637.

[66] Hao X, Moodera J S, Meservey R, Spin-Filter Effect of Ferromagnetic Europium Sulfide Tunnel Barriers, Phys. Rev. B 1990; 42: 8235.

Chapter 8

The Superconducting Order Parameter in High-Tc Superconductors – A Point-Contact Spectroscopy Viewpoint

M. Tortello and D. Daghero

Additional information is available at the end of the chapter

http://dx.doi.org/10.5772/59587

1. Introduction

Superconductivity can be regarded as a macroscopic quantum phenomenon. In quantum mechanics, particles can be described as wavefunctions with an amplitude and a phase. The striking effect occurring in the superconducting state is that electrons couple together forming Cooper pairs which can all be described by the same wavefunction, the order parameter (OP). In some cases, a superconductor can feature multiple order parameters but still preserving its macroscopic quantum nature.

High-temperature superconductivity (HTSC) was discovered in 1986 in copper-based compounds (cuprates) by J.G. Bednorz and K.A. Müller [1], who were awarded the Nobel prize the following year. Cuprates have now been extensively studied, but a definitive answer concerning the fundamental mechanism responsible for the occurrence of their superconducting state has not been given yet [2].

A report in February 2008 of superconductivity in the Fe-based compound $LaFeAsO_{1-x}F_x$ with a critical temperature $T_c = 26$ K [3], soon increased up to 55 K in similar compounds [4], raised exceptional interest in the whole solid-state-physics community. One of the reasons for this excitement was that a new class of high-temperature superconductors based on Fe instead of Cu was discovered. It is hoped that the study of this new class might clarify the other and, ideally, HTSC in general.

This discovery is certainly the most important in the field in the past 26 years. Many papers have been published on this topic: in October 2010, about 2000 experimental and 500 theoretical papers were already published and/or posted on the arXiv, an online repository for electronic preprints of scientific papers. Considerable progress has been achieved in a relatively short

INTECH
open science | open minds

© 2015 The Author(s). Licensee InTech. This chapter is distributed under the terms of the Creative Commons Attribution License (http://creativecommons.org/licenses/by/3.0), which permits unrestricted use, distribution, and reproduction in any medium, provided the original work is properly cited.

time, but several crucial points are still awaiting definitive proof, and some apparently contradicting results still have to be reconciled.

In this regard, the knowledge of the number, amplitude and symmetry of the order parameters in a superconductor is a fundamental building block of any microscopic theory of superconductivity and therefore is mandatory in order to fully understand the physics of high- T_c superconductors. Moreover in the most complete theories of superconductivity, like the Eliashberg theory, the order parameter can be dependent on energy giving the possibility, in some cases, to experimentally resolve features related to the electron-boson interaction that is the fundamental glue producing the electron pairing and the emergence of superconductivity. This is very important as the knowledge of the microscopic mechanism responsible for the occurrence of superconductivity can help searching for new superconductors with higher T_c and better properties, in view of their application.

In this chapter we will briefly summarize (with no claim of exhaustiveness) the most relevant aspects of high-temperature superconductors that have been investigated by point-contact spectroscopy, mainly (but not only) in the regime of Andreev reflection. In section 2 we will introduce the very basic concept of order parameter, and provide an overview of the symmetries that have been proposed for various high-temperature superconductors. Section 3 will describe the technique of point-contact spectroscopy, the conditions that must be fulfilled in order to obtain reliable spectra, and the mechanism of Andreev reflection. The models used to describe this mechanism and to fit the experimental spectra (in order to extract information about the number, the amplitude and symmetry of the gap(s)) will be discussed as well.

Section 4 will finally provide a quick overview of the main results of point-contact spectroscopy in the two major classes of high-temperature superconductors, namely the cuprates and the iron-based compounds. It will be shown how the capabilities of point-contact spectroscopy have been extended and the relevant models have been refined in order to face the challenge represented by these very complex materials.

2. The Superconducting Order Parameter (OP)

The first successful (semi-)microscopic [5] theory of superconductivity was the Bardeen-Cooper-Schrieffer (BCS) theory [6, 7]. In the BCS picture, an attractive interaction between electrons (no matter how weak) can generate an instability of the Fermi sea towards the formation of pairs of electrons (Cooper pairs). The coupling is strongly favored for electrons with opposite spin and momentum. In conventional superconductors this interaction is rationalized as being due to the exchange of a virtual phonon between two electrons. However, the theory itself does not require specifying what is the origin of the attractive interaction and can thus be generalized to describe any kind of pairing glue other than that caused by phonons. Since the BCS ground state turns out to be favorable in energy with respect to the Fermi sea ground state, at $T=0$ all electrons are paired and, as already noted, they are described by a single wavefunction, the order parameter. In order to create single quasi-particle states, Cooper pairs have to be "broken apart" by giving to the system an energy equal to 2Δ, where Δ is the

http://dx.doi.org/10.5772/59587

energy gap that separates the BCS ground state from the lowest-lying single-particle excitations. Δcorresponds to the amplitude of the order parameter. The meaning of its name is clear because it indicates that there are no allowed quasi-particle states at energies between $E_F - \Delta$ and $E_F + \Delta$.

In the original BCS paper [6] the theory is formulated in a weak electron-phonon coupling approximation. Therefore, it is assumed that the energy gap is much smaller than the typical phonon energy, $\Delta \ll k_B\theta_D$(θ_D being the Debye temperature).

In this way, the electron-phonon pairing V, which would in general be dependent on the wavevector $\boldsymbol{k}$, can be approximated as $V_{\boldsymbol{k},\boldsymbol{k}'} = -V$ (BCS approximation) for energies below $k_B\theta_D$ and zero elsewhere. The minus sign indicates that the potential is attractive. Within this approximation the expression for the temperature-dependent energy gap is

$$\Delta(T) = 2NV\int_0^{k_B\theta_D} d\epsilon \frac{\Delta(T)}{2\sqrt{\epsilon^2 + \Delta(T)^2}} \tanh\left[\frac{\sqrt{\epsilon^2 + \Delta(T)^2}}{2k_BT}\right] \quad (1)$$

where N is the electronic density of states at the Fermi level for a definite spin and NV is the BCS coupling parameter. The equation can be solved numerically. The gap is therefore constant and isotropic over the whole Fermi surface and it is usually said that in this case the symmetry of the order parameter is of the isotropic s -wave type, i.e. $\Delta(\boldsymbol{k})=\Delta_0$(see Figure 1).

2.1. The anisotropy of the OP, multiple OPs and some important symmetries

If the pairing potential $V_{\boldsymbol{k},\boldsymbol{k}'}$ is no longer assumed to be constant over the Fermi surface (FS), the original BCS formulation can be generalized[1] and the expression for the gap becomes [8]

$$\Delta(\mathbf{k},T) = \int V(\mathbf{k},\mathbf{k}')\Delta(\mathbf{k}',T)\left[\int_0^{k_B\theta_D} \frac{d\epsilon}{\sqrt{\epsilon^2 + \Delta(\mathbf{k}',T)^2}} \tanh\left(\frac{\sqrt{\epsilon^2 + \Delta(\mathbf{k}',T)^2}}{2k_BT}\right)\right] dN' \quad (2)$$

where $dN' = dS'/4\pi^3\hbar v_F'$ is the element of the density of states associated with the area dS' of the Fermi surface and where the summation over $\boldsymbol{k}'$ implies also summation over all bands crossing the Fermi level. As a consequence of the momentum-dependent pairing, the energy gap will in general be anisotropic on the Fermi surface. In conventional superconductors the pairing potential is usually always attractive and, as a consequence, the gap function is positive and its phase is zero.

A particular anisotropic gap structure, called anisotropic s -wave, is shown (for simplicity in the 2D form) in Figure 1.

Since the electrons involved in the pairing are those in the vicinity of the Fermi surface, the " angular momentum representation" [9] will be used from now on. In this way, different OP

1 Here we still use the acronym " BCS" meaning that the basic assumption of a weak electron-boson coupling is still valid; nevertheless, the addition of a -dependence in the gap is not accounted for by the original BCS paper.

symmetries can be easily expressed through the variable ϕ, so that $\boldsymbol{k} = k_F(\cos\phi, \sin\phi)$. Within this representation, the anisotropic s -wave pairing can be expressed as

$$\Delta(\phi) = \Delta_0\left[(1-\epsilon) + \epsilon\cos(2\phi)^4\right] \tag{3}$$

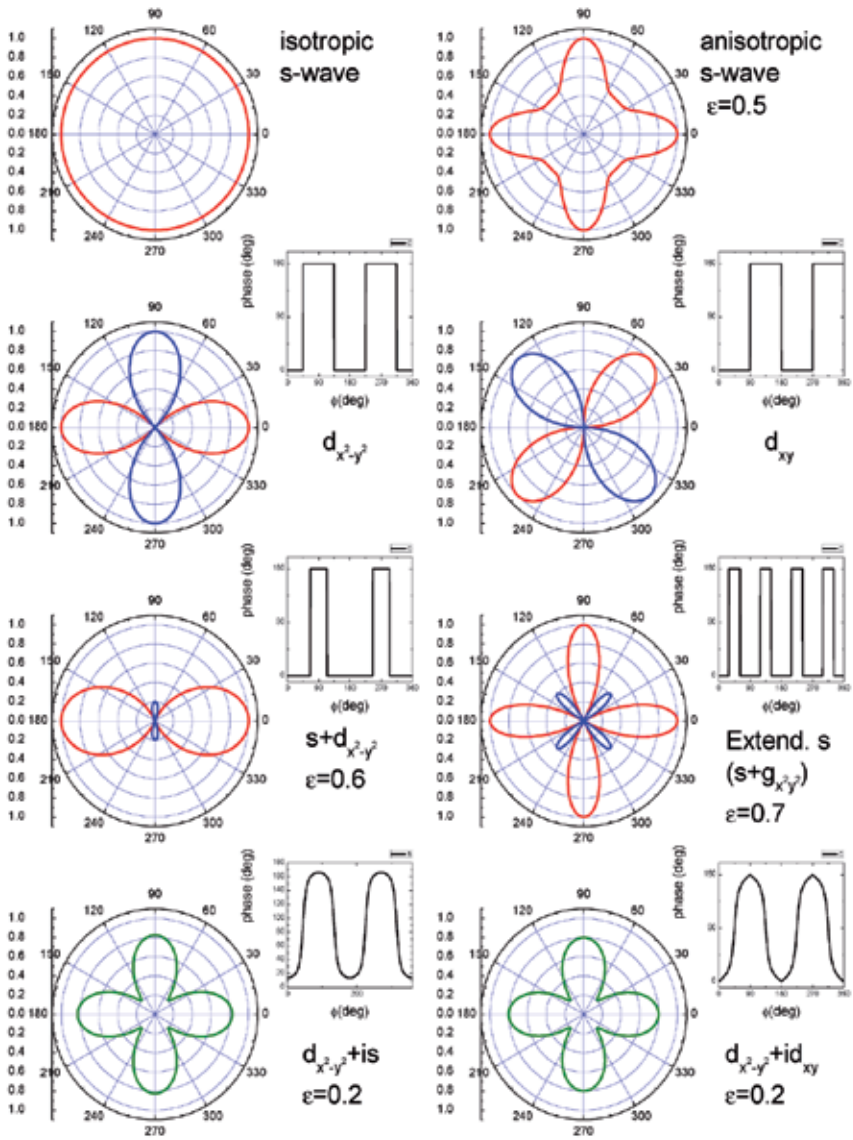

Figure 1. Polar plots of the amplitude of the order parameter for different symmetries and plot of the phase as a function of the angle ϕ. In the case of s -wave symmetry and anisotropic s -wave symmetry the phase is constant and equal to 0 and thus has not been plotted. Red: positive amplitude. Blue: negative amplitude. Green: absolute value of the order parameter for mixed symmetries with imaginary component.

http://dx.doi.org/10.5772/59587

Figure 1 reports the function for =0.5.

After the discovery of the cuprate superconductors more exotic symmetries were investigated in which the gap function can vary in phase and even change sign. The locus of points in the reciprocal space where the gap function changes sign is called nodal line and when nodal lines intersect the Fermi surface the OP is said to be nodal, as it occurs, for example, in some cuprate superconductors (see section 4.1). Another interesting situation can take place when the material features multiple FS sheets that, however, do not intersect the nodal lines. In this case the gaps can feature opposite sign on different FS sheets. As it will be shown in a short while and in section 4.2, this particular gap structure has been theoretically predicted for several Fe-based superconductors (FeBS).

$\Delta(\boldsymbol{k})$ can be expanded in a series of spherical functions, which are often labeled as atomic orbitals (s, p, d, f, $g$etc.). Not every symmetry is allowed in a certain compound. First of all, if the pairs are spin singlets only s -, d -, g -wave symmetries and so on are allowed. Then, depending on the symmetry of the lattice under consideration, only some of them (and their admixture) are possible [10]. The situation in which the symmetry of the order parameter is lower than that of the crystal is usually referred to as unconventional pairing. From now on we will consider only spin-singlet types of pairing as this will be the case for cuprates and FeBS, discussed later on.

The d -wave symmetry can either be of the $d_{x^2-y^2}$ or d_{xy} type. In the first case, the gap function can be written as $\Delta(\phi)=\Delta_0\cos(2\phi)=\Delta_0[\cos(\phi)^2-\sin(\phi)^2]$. The function is real and features line nodes at $\phi=45+n\pi/2$ where it changes sign from positive (red in Figure 1) to negative (blue). On the other hand, the d_{xy} -wave symmetry is expressed in angular coordinates as $\Delta(\phi)=\Delta_0\sin(2\phi 2\Delta_0(\cos\phi\sin\phi)$ and has node lines at $\phi=n\pi/2$. It is easy to see that it corresponds to the previous one but rotated by 45° in the plane, as shown in Figure 1.

Mixed symmetries have also been proposed. For example, an $s+d_{x^2-y^2}$-wave symmetry, where $\Delta(\phi)=\Delta_0[(1-)+\cos(2\phi)]$ or complex admixtures like $d+is$ or $d+id$ have been considered while interpreting PCARS data in cuprates (section 4.1). Some of them are shown in Figure 1.

If the Fermi surface is made up of multiple sheets the gap can be different on each of them and, generally, also be $\boldsymbol{k}$ -dependent on the single sheets. This situation is called multi-band or multi-gap superconductivity which can therefore be regarded as a particular case of anisotropic superconductivity. The BCS weak-coupling formulation was generalized to the multi-band case at the end of the '50s [11, 12]. Assuming the potential to be different on two bands, 1 and 2, but constant on each of them, the disjoint representation can be used and from equation 2 the two gap parameters, in turn constant on each band, can be obtained [13]:

$$\begin{aligned}\Delta_1 &= \Lambda_{11}\Delta_1\int_0^{k_B\theta_D} d\epsilon \frac{\tanh\left(\sqrt{\epsilon^2+\Delta_1^2}\,/2k_BT\right)}{\sqrt{\epsilon^2+\Delta_1^2}} + \Lambda_{12}\Delta_2\int_0^{k_B\theta_D} d\epsilon \frac{\tanh\left(\sqrt{\epsilon^2+\Delta_2^2}\,/2k_BT\right)}{\sqrt{\epsilon^2+\Delta_2^2}} \\ \Delta_2 &= \Lambda_{22}\Delta_2\int_0^{k_B\theta_D} d\epsilon \frac{\tanh\left(\sqrt{\epsilon^2+\Delta_2^2}\,/2k_BT\right)}{\sqrt{\epsilon^2+\Delta_2^2}} + \Lambda_{21}\Delta_1\int_0^{k_B\theta_D} d\epsilon \frac{\tanh\left(\sqrt{\epsilon^2+\Delta_1^2}\,/2k_BT\right)}{\sqrt{\epsilon^2+\Delta_1^2}}\end{aligned} \tag{4}$$

assuming that the cut-off phonon frequency is the same for the two bands. Here, $\Lambda_{ij}=V_{ij}N_j$ where the averaged pairing potential V_{ij} is called intraband if $i=j$ and interband if $i\neq j$.

In order to better understand multi-gap superconductivity and the many different situations that may stem out of equations 4 let us briefly take into consideration two examples of multi-band superconductors, MgB_2 and FeBS. MgB_2 is certainly the clearest example of two-band, two-gap superconductor. It features two (groups of) bands, $\sigma$and π. The σ band would be superconducting on its own, thanks to a considerable electron-phonon intraband pairing, $NV_{\sigma\sigma}$, while the π band would not. However, a small amount of *interband* coupling, $NV_{\sigma\pi}$ couples the σ band to the π one which is made superconduct by the first.

Completely different is one of the most popular scenario invoked to explain superconductivity in FeBS [14]. The intraband electron-phonon coupling is thought to be too small to set superconductivity in [15], but a predominant *repulsive* interband coupling (likely of magnetic origin) can drive the hole-like and electron-like FS sheets into the superconducting state, giving rise to a gap function of opposite sign on the two types of bands. It is worth noticing that this situation occurs in the framework of the s -wave symmetry, but, because of this sign-changing gap, is referred to as$s_{\pm}$. Within this symmetry, the occurrence of " accidental nodes" has been predicted and experimentally observed in particular situations, depending on fine details of the pairing interaction and on the specific electronic structure. Therefore, i) a multi-band model can give rise to extremely diverse situations as far as the OPs are concerned and, in particular, ii) even within the same symmetry, s-wave for instance, the OPs can feature very different *structures* [16]. As we will see for FeBS in 4.2, different gap structures could imply very dissimilar pairing mechanisms of superconductivity.

2.2. The energy-dependent OP in the Eliashberg theory

In 1960 Eliashberg built [17, 18, 19] a strong-coupling generalization of the BCS theory. The Eliashberg theory is still based on the electron-phonon interaction, but relaxes the requirement that this interaction is weak. As a result, the theory accounts for the renormalization of the electron mass arising from the electron-phonon interaction. The Eliashberg theory takes into account the exact electron-phonon spectral function, $\alpha^2F(\boldsymbol{k},\boldsymbol{k}',E)$ and the energy dependence of the gap function, $\Delta(\boldsymbol{k},E)$.

By introducing the Gor'kov F function and working simultaneously with the Green function G and F, Eliashberg could apply the standard perturbation theory to the superconducting state and obtain a 2×2 matrix self-energy correction. The diagonal terms are called $\Sigma(\boldsymbol{k},E)$ and the off-diagonal ones are $\Delta(\boldsymbol{k},E)$. The poles of the Green functions are located at $\pm((E_{\boldsymbol{k}}+\Sigma_{\boldsymbol{k}})^2+\Delta_{\boldsymbol{k}}^2)^1$ and correspond to the single particle excitations (hole-like and electron-like). $\Sigma_{\boldsymbol{k}}$is interpreted as a shift in the generalized BCS excitation energy due to interactions between electrons and $\Delta_{\boldsymbol{k}}$ as the energy-dependent gap function [7]. The complete expression of the Eliashberg equations goes beyond the scope of this chapter but what is important to retain here is that now the order parameter is a complex function of the energy. For example, after averaging over the Fermi surface (in the case of an isotropic OP), we obtain

http://dx.doi.org/10.5772/59587

$$\Delta(E) = Re\left[\Delta\left(E\right)\right] + i\,\mathrm{Im}\left[\Delta\left(E\right)\right] \tag{5}$$

The imaginary part of Δ increases with the increase of the electron-boson coupling and takes into account the finite lifetime of the Cooper pairs. Another interesting quantity is the electron-phonon coupling constant, λ defined, in the isotropic case, as $\int_0^\infty [2\alpha^2 F(E)/E]dE$. λ gives an estimation of the electron-boson coupling and can be related to the original BCS pairing parameter by $NV \equiv (\lambda - \mu^* 1 + \lambda)$, where μ^* is a purely electronic quantity referring to the average Coulomb potential on the Fermi surface. As it will be shown later, in case of strong-coupling superconductors, the energy-dependence of the order parameter can manifest itself in the tunneling or point-contact spectra, possibly giving important hints about the pairing mechanism.

It is also possible to account for the gap anisotropy within the Eliashberg theory even though this can be very demanding from the computational point of view [20]. In this regard, it is worth recalling a method developed by P.B. Allen, that adopts a particular set of functions, called Fermi-surface harmonics, that can considerably simplify the solution of the Eliashberg equations in this case [21, 22].

3. Point-Contact Andreev Reflection Spectroscopy (PCARS)

Point-contact spectroscopy (PCS) was developed in the '70s [23], especially for studying the electron-phonon interaction in metals. It was found out later though, that it could be used to study many kinds of quasi-particle excitation and scattering mechanism, like the electron-magnon interaction, crystal-field excitations, scattering with magnetic impurities and so on [24]. Then, especially after the theoretical work of Blonder, Tinkham and Klapwijk in 1982 [25], it also turned out to be a very powerful and unique method for studying the order parameter in superconducting materials.

There already exist some very comprehensive reviews or books on point-contact spectroscopy in the literature where very detailed and exhaustive information about the technique and its achievements can be found [24, 26 - 29]. The reader who wants to study PCS in greater detail can refer to those. Below we will only report some basic information that will help to better follow the issues addressed in section 4.

3.1. Point-contact spectroscopy: Ballistic, thermal and diffusive regime

There are several different ways of fabricating point contacts [24] but one of the most popular is the so-called needle-anvil or " hard" PCS technique. It consists of gently pressing a very sharp metallic tip against the material under study so as to create a " small" (point-like) contact, and in measuring the $I-V$ characteristics across the junction thus formed. However, it is also worth mentioning here another technique, called " soft" PCS technique [30]. The soft PCS consists in making the point contact by using a small drop of silver paint put on the sample surface instead of the metallic tip. This method can be used even on brittle samples or very

thin films because no pressure is applied (hence the name " soft"). Moreover, it ensures a higher thermal and mechanical stability and, by applying short voltage or current pulses (fritting), the properties of the contact can often be tuned.

The principle of PCS (in normal metals) is that the quasi-particle that enters the material under study through the contact can be scattered by elementary excitations. This process leaves its fingerprints in the $I-V$ characteristics of the contact, that allow determining the energy spectrum of the excitations. Of course, for the whole process to be meaningful, the energy of the injected quasi-particles must be well known and this is true only if they do not lose energy through scattering in the contact region. In this regard, the situation when they don't scatter inside the contact region is called *ballistic regime* and is the ideal condition for getting good spectroscopic data. The *diffusive regime* occurs when they instead undergo elastic scattering in the contact. In this case it is still possible to observe energy-resolved quasi-particle scattering but the signal will likely be lower. Finally, when electrons scatter inelastically inside the contact region information regarding their energy is lost, the contact can get considerably heated and spectroscopy is definitely hampered: it is the *thermal regime*. If we model the contact area by a circular orifice of radius a, the ballistic regime is defined by the condition $a \ll \ell_e$, the diffusive by $a \ll \Lambda$ and the thermal one by $a \gg \ell_i$. ℓ_e and ℓ_i are the elastic and inelastic electronic mean free paths, respectively and Λ is the diffusion length, $\Lambda=\sqrt{\ell_i \ell_e}$.

In the ballistic regime the resistance of the contact can be described by the Sharvin resistance $4\rho\ell 3\pi a^2$), where ρ is the resistivity and, in case of contacts between different materials (heterocontacts), the product $\rho\ell$ is that of the bank with the smaller Fermi energy [26]. From this formula it is possible to determine if a contact fulfills the ballistic condition, $a \ll \ell$, by comparing the experimental resistance across the contact R_N with the condition $R_N \ll 4\rho 3\pi\ell$). It is worth noticing though, that if the contact does not fulfill the above condition, it does not necessarily mean that the regime is not ballistic. Indeed, the actual contact can likely be the parallel of several nano-contacts so that the condition here reported can be regarded as an upper limit. When it is not fulfilled, one has to look at other experimental features that could allow to conclude that the contact is ballistic. For instance, heating effects should be absent. In particular, if the differential resistance of the contact as a function of the voltage drop across the contact has the same functional form of the resistivity as a function of the temperature, then the contact is most probably in the thermal regime.

When point contact measurements are carried out in the superconducting state, the process that allows determining the energy of the superconducting gap is either Andreev reflection or quasi-particle tunneling, depending on the height of the potential barrier at the interface. In any case, the spectroscopic information is energy-resolved only if the contact (in the normal state) is in the ballistic or at most diffusive regime. In the Andreev reflection regime, another condition is generally to be fulfilled, i.e. $a \ll \xi$, where ξ is the superconducting coherence length. This is necessary to avoid that superconductivity in the vicinity of the contact is destroyed by the injected current, which in that region may become overcritical [28].

3.2. PCS in superconductors: The BTK model and beyond

Point-contact spectroscopy can be a very powerful technique to probe the order parameter in superconductors mainly thanks to the existence of the Andreev reflection [31], a quantum

http://dx.doi.org/10.5772/59587

process that occurs at the interface between a normal metal N and a superconductor S. To explain the Andreev reflection in a nutshell, let us consider an electron incoming from N with an energy $eV < \Delta$. When it reaches the $N-S$ interface (that we now suppose perfectly ideal, i.e. with no potential barrier) it cannot be transmitted into S as a quasi-particle, as there are no allowed energy states in that energy range. It is then reflected as a hole (Andreev reflection) and, to conserve the charge balance, a Cooper pair is transmitted in S. This fact is equivalent to a doubling of the conductance at voltages $V < \Delta/e$. If the energy of the incoming electron is instead $eV > \Delta$ it can be transmitted as a quasi-particle and the conductance is that of an $N-N$ junction. It is clear then that the " change of slope" in the conductance occurs at energies corresponding to the energy gap whose amplitude can thus be estimated.

In 1982, Blonder, Tinkham and Klapwijk (BTK) gave the first satisfactory theoretical description of the Andreev reflection occurring in $N-S$ microconstrictions [25] that can be compared to experimental point-contact data. By solving the Bogoliubov-de Gennes (BdG) equations, BTK were able to calculate the probability coefficients of the transmission and reflection of the quasi-particles at the $N-S$ interface. In particular, the Andreev reflection is one of the processes that come out from the solution of the BdG equations. Noticeably, they also took into account the effect of a potential barrier at the interface, so that the complete transition from the ideal Andreev reflection (metallic contact, with no barrier) to the tunneling regime (thick barrier) was modeled. Also, two more processes can occur at the interface in the presence of a barrier which are called normal and " anomalous" reflection. In the BTK model, the potential barrier is taken into account by a dimensionless parameter $Z = U_0/(\hbar v_F)$, where U_0 is the height of the potential barrier, represented by the repulsive potential $U_0\delta(x)$ localized at the interface [25]. Note that although Z can be defined in this (rather abstract) way, BTK themselves underline that it should rather be thought of as a phenomenological parameter when comparing the predictions of their model to experimental data. Z can thus account for any source of elastic scattering in the neck, irrespective of its microscopic origin [32]. Besides considering both the N and S Fermi surface to be spherical, and the gap to have an isotropic s-wave symmetry, the model also assumes the momentum of incoming electrons to be perpendicular to the interface. We will thus refer to this result as the 1D BTK model. The effect of the temperature can be accounted for by a proper convolution of the conductance with the Fermi distribution function [26]. The mismatch of the Fermi velocities between the two sides of the contact can be included in the model by substituting the parameter Z with an effective barrier parameter, $Z_{eff} = \sqrt{Z^2 + [(1-r)^2 4r}$, where $r = v_{F1}/v_{F2}$ is the ratio of the Fermi velocities in the superconducting and in the normal side [32]. Despite its simplicity, the 1D BTK model allowed comparison to experimental data with a fairly good agreement.

Since the BTK model predicted conductance curves with sharper structures and less spread in energy than the actual experiments, a further parameter, Γ, was introduced to represent the reduced quasi-particles lifetime mainly due to i) the presence of an imaginary part in the self-energy (see 2.2 and ref. [33]) and ii) any kind of inelastic scattering at the interface caused by non-ideal conditions (dead layers etc.) [34]. Γ, called the broadening parameter, can easily be introduced into the model by the simple substitution $E \rightarrow E + i\Gamma$.

The unidirectional electron incidence assumed in the 1D BTK model is an oversimplification whenever the system is not perfectly isotropic. In these cases, one has to account for the fact that electrons can approach the interface along any direction. However, if we restrict for the

time being to a plane perpendicular to the interface and call θ_N the angle between the incident electron and the normal to the interface, $\boldsymbol{n}$, the expression for the normalized conductance at $T=0$ is

$$G_{2D}(E)=\frac{\int_{-\frac{\pi}{2}}^{+\frac{\pi}{2}}\sigma(E,\theta_N)\cos\theta_N d\theta_N}{\int_{-\frac{\pi}{2}}^{+\frac{\pi}{2}}\tau_N(\theta_N)\cos\theta_N d\theta_N} \tag{6}$$

where $\sigma(E,\theta_N)$ is the BTK conductance expressed by

$$\sigma\left(E,\theta_N\right)=\tau_N\cdot\frac{1+\tau_N\left|\gamma_+(E)\right|^2+\left(\tau_N-1\right)\left|\gamma_+\left(E\right)\gamma_-\left(E\right)\right|^2}{\left|1+\left(\tau_N-1\right)\gamma_+\left(E\right)\gamma_-\left(E\right)\exp\left(i\varphi_d\right)\right|^2}. \tag{7}$$

$\tau_N(\theta_N)$ is the barrier transparency, defined as

$$\tau_N\left(\theta_N\right)=\frac{\cos\left(\theta_N\right)^2}{\cos\left(\theta_N\right)^2+Z^2}. \tag{8}$$

and

$$\gamma_\pm\left(E\right)=\frac{E-\sqrt{E^2-\left|\Delta_\pm\right|^2}}{\left|\Delta_\pm\right|} \tag{9}$$

Moreover, $\varphi_d=(\varphi_- -\varphi_+)$and $\varphi_\pm$ are the phases of $\Delta_\pm$, which in turn represent the pairing potential experienced by electron-like and hole-like quasi-particles (ELQs and HLQs) [35]. The formulation of the BTK conductance reported here [35], which is different from that of the original BTK paper and that we will call 2D BTK model, assumes also that the effective masses in N and S are equal. This formulation is apt to describe Andreev reflection in superconductors with all the symmetries of the OP that can be expressed in polar coordinates in the reciprocal plane (k_x,k_y). For example, the anisotropic s -wave OP would be expressed as

$$\Delta_\pm=\Delta_{is}+\Delta_{an}\cos^4\left[2\left(\pm\theta_N-\alpha\right)\right] \tag{10}$$

and the $d_{x^2-y^2}$ -wave one as

$$\Delta_\pm=\Delta_0\cos\left[2\left(\pm\theta_N-\alpha\right)\right] \tag{11}$$

α being the angle between the normal to the interface and the crystallographic axis a, that we assume to be zero in the configurations shown in Figure 1.

http://dx.doi.org/10.5772/59587

Figure 2a shows the temperature dependence of the 2D BTK conductance for an isotropic s -wave gap while panels c and d report the case for a $d_{x^2-y^2}$-wave gap with incident angle $\alpha=\pi/4$ and $\alpha=\pi/8$, respectively.

It is important to notice here that when tunneling (in the ab -plane) along the nodal direction in case of nodal symmetries (like $\pi/4$ for a $d_{x^2-y^2}$-wave OP), the shape of the spectra is very different from the s -wave case reported in panel a. The conductance curves feature a zero-bias conductance peak (ZBCP) that can be, at high Z values, higher than 2 (not allowed for the s -wave case) and that decreases when moving away from the nodal direction. At $\pi/8$ (panel d) it is lower, while other structures appear at finite energy. At the antinodal direction ($\alpha=0$, not shown) the spectra are more similar, when Z>0, to those for an s -wave OP but with a slightly V-shaped dip at zero bias [26].

The ZBCP can be a very important signature of the presence of nodes in the OP and is caused by the formation of zero-energy Andreev bound states (ABS) at the interface, due to the fact that along the nodal direction HLQs and ELQs experience pair potentials $\Delta_{\pm}$ with a phase difference equal to π [35] (see eq. 11).

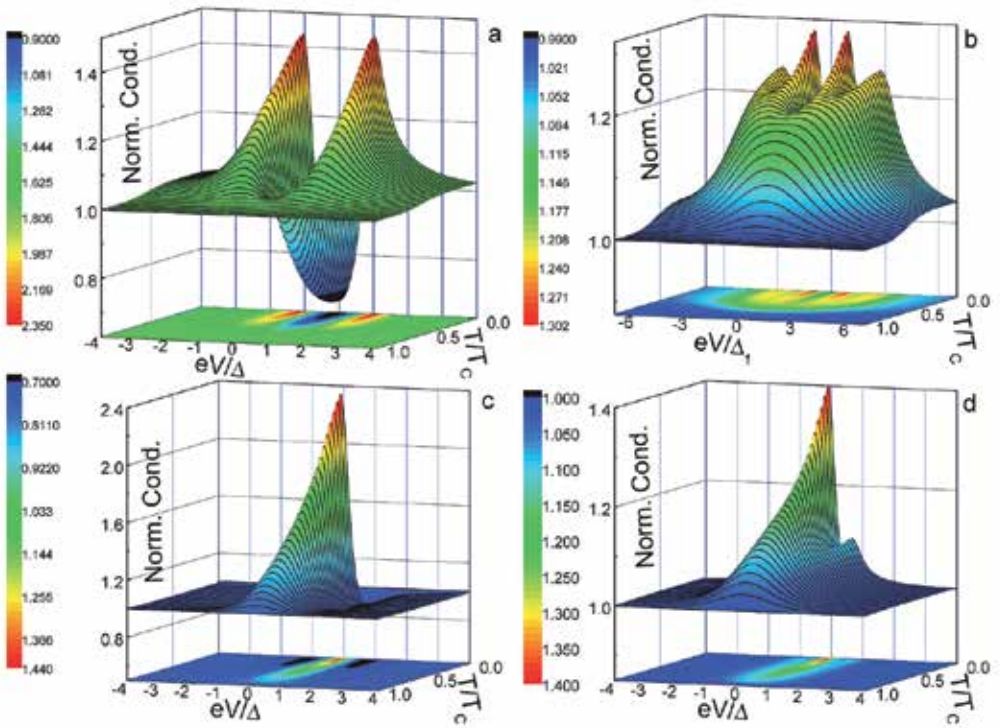

Figure 2. Temperature dependence of the normalized conductance curves calculated within the 2D BTK model for different symmetries of the order parameter. The parameters of the model have been chosen to mimic realistic experimental conditions. (a): isotropic s -wave gap, $\Gamma=\Delta/5$,$Z=0.8$. (b): two isotropic s -wave gaps with the sameT_c, $\Delta_2=3\Delta_1$, $\Gamma_i=\Delta_i/5$, $Z_i=0.4$, $w_1=0.5$. (c) $d_{x^2-y^2}$-wave gap, $\Gamma=\Delta/5$, $Z=1.2$, $\alpha=\pi/4$. (d): same as in c but now $Z=1.0$ and $\alpha=\pi/8$.

In some cases (for example when Z is low, or broadening effects are taking place) the ZBCP can be smeared out and look like a maximum rather than a peak. In these conditions, the Andreev spectra for the d -wave symmetry become very similar to those expected, for example, in the case of anisotropic s -wave gap with zeroes on the Fermi surface [27]. Moreover, as we will better see below, symmetries like the d -wave and the fully anisotropic s -wave can also appear similar when injecting the current along the c axis.

There may also be situations when, even though the OP features nodal lines, ABS don't occur because the line is, for instance, away from the Γ point in the first Brillouin zone and HLQs and ELQs always see the same sign of the OP. This is the case, for example, of $CaFe_2A_2$ under pressure [36], discussed in section 4.2.

Finally, panel b of Figure 2 shows the temperature dependence of the conductance calculated within a two-band, 2D BTK model with two isotropic s -wave gaps with the same T_c. In this case the total conductance is simply the weighed sum of the contribution of the two bands, $G_{Tot} = w_1 G_1 + (1 - w_1) G_2$, where w_1 is the weight of band 1 and $G_{1,2}$ are expressed by eq. (6).

The 2D BTK model has been commonly used to fit the PCARS spectra of various unconventional superconductors, namely cuprates, with a d -wave or a mixed symmetry of the OP. Cuprates being essentially 2D materials, with a cylindrical Fermi surface, this approach is justified. In other materials, however, like FeBS, the assumption of spherical or cylindrical FS is untenable and the 2D BTK approach, even if generalized to the multiband case, is necessarily approximated. It is actually possible to take into account arbitrary incident directions by adding an integration over the inclination angle ϕ. Following refs [37, 38], the most general formula for the conductance in the 3D case at $T = 0$ can be expressed as [26]:

$$\left\langle G(E) \right\rangle_{I\mathbf{Pn}} = \frac{\sum_i \left\langle \sigma_{i\mathbf{k}n}(E) \tau_{i\mathbf{k},n} \frac{v_{i\mathbf{k},n}}{v_{i\mathbf{k}}} \right\rangle_{FS_i}}{\sum_i \left\langle \tau_{i\mathbf{k},n} \frac{v_{i\mathbf{k},n}}{v_{i\mathbf{k}}} \right\rangle_{FS_i}} \tag{12}$$

where

$$\tau_{i\mathbf{k},n} = \frac{4 v_{i\mathbf{k},n} v_{N,n}}{\left(v_{i\mathbf{k},n} + v_{N,n} \right)^2 + 4 Z^2 v_N^2} \tag{13}$$

Here i indicates different FS sheets and the brackets an average over the i -th sheet. $\boldsymbol{n}$is the direction of current injection, $v_{i\boldsymbol{k},n} = \boldsymbol{v}_{i\boldsymbol{k}} \cdot \boldsymbol{n}$ is the projection, along $\boldsymbol{n}$, of the velocity on the i -th sheet. In the formula for $\tau_{i\boldsymbol{k},n}$, which is the normal-state barrier transparency, $v_{N,n} = \boldsymbol{v}_N \cdot \boldsymbol{n}$, $\boldsymbol{v}_N$ is the Fermi velocity of the normal material, assumed constant. $\sigma_{i\boldsymbol{k}n}(E)$is similar to eq. (7) but now τ_N is expressed as in eq. (13) and $\Delta = \Delta_{i\boldsymbol{k}}$. The calculation of the conductance in this case can be very demanding from the computational point of view and, in principle, requires the knowledge of the k -dependence of the order parameter on the whole FS. Therefore, we developed a method [27, 29] that under some assumptions and simplifications allows writing eq. (12) and (13) in the form of integrals over the angles θ and ϕ provided that: i) the different

http://dx.doi.org/10.5772/59587

FS are modeled by means of suitable 3D surfaces like hyperboloids, ellipsoids and so on, and ii) $\Delta(k)$admits a simple analytical expression in the same coordinates. It is in this way possible to perform the fitting procedure in an easier way. This model, in some cases, allows obtaining interesting information regarding the actual shape of the FS and the OP symmetry. For example, when the current is injected along the c -axis in superconductors with warped cylindrical FS sheets the conductance doesn't show ZBCPs for a d -wave OP because ELQs and HLQs feel the same sign of the OP. But neither the zero-bias maximum (that would be expected since the gap is zero in some regions of the FS) is observed. Instead, a zero-bias *minimum* occurs [27]. The same happens for OPs with full in-plane anisotropy, so that these two symmetries are almost impossible to distinguish by c -axis PCARS measurements. Only in-plane measurements can help discriminating between a d -wave and a fully-anisotropic s -wave, since only in the former ZBCPs due to Andreev bound states are expected at nodal directions.

Seen the other way around, if a superconductor has at least one FS sheet with line nodes in the OP and the conductance curves along the c axis feature zero-bias maxima, it means that the relevant FS sheet has a 3D character [27, 36]. As it will be shown in section 4.2, this is the case of $CaFe_2As_2$ under pressure and Co-doped $CaFe_2As_2$.

When tunneling along the c axis in cuprates, the situation is slightly different. Here, because of the perfectly 2D nature of the Fermi surface, the final states have only transverse wavevector [39] so that the conductance must be calculated by integration over the entire (k_x,k_y) plane. No ZBCP is thus expected to occur, and again – if some broadening is present or the barrier parameter is low – the d -wave symmetry might not be distinguishable from a symmetry with zeroes. Also in this case, measurements in the ab plane could be necessary to detect the possible presence of ABS and thus of gap nodes.

We have seen in section 2.2 that the actual order parameter is energy-dependent and that when the electron-boson coupling is strong enough the PCARS conductance can feature typical structures that arise from the spectrum of the bosonic excitations that may serve as a pairing glue. Indeed these features appear at the relevant boson energy, $\Omega_b$in the density of states that can be directly measured in tunneling experiments. Since the BTK model can also describe tunneling experiments when the barrier is large enough, it is possible to introduce the energy-dependent expression of the OP in equation 9. The electron-boson interaction (EBI) features in the conductance persist with decreasing values of Z (Andreev reflection regime) and appear at energies of about $\Delta + \Omega_b$ in single-band superconductors [26], while the situation can be more complex in multi-band ones [27]. However, as it will be shown in section 4.2.1, they can be nevertheless interpreted and convey important information regarding the pairing mechanism also in case of (strong-coupling) multi-band superconductors.

4. PCARS in High-Tc superconductors

4.1. PCARS in Cuprates

In cuprate superconductors, point contact spectroscopy has been used to address various fundamental issues concerning the superconducting order parameter, i.e. its amplitude, its

symmetry (and its possible change as a function of doping) and its relationship with the pseudogap (PG). As far as the latter point is concerned, the sensitivity of Andreev reflection to the phase coherence has provided complementary information to tunneling and STM experiments that probe instead the unpaired quasi-particles. As a result, the (superconducting) gap probed by PCARS and that closes at T_c differs significantly from the (pseudo)gap measured by tunnel spectroscopy at low temperature, and that can persist well above T_c (in hole-doped cuprates). While the former scales with the critical temperature (thus showing a maximum at optimal doping, OPT) the second decreases monotonically with increasing doping until they merge or become comparable at a critical doping (that in most cases is slightly above the optimal one), as shown in Fig. 3 f. Actually, the gap vs. pseudogap issue is very complicated, especially as for whether the pseudogap is associated to pre-formed pairs with no phase coherence (that however determine a suppression in the quasi-particle density of states around the Fermi level) or is instead unrelated to superconductivity. For a discussion of this issue please see [40, 28] and references therein.

As noticed in ref. [28], the observation of Andreev reflection itself in cuprates leads to some interesting conclusions: i) the Bogoliubov-de Gennes equations hold for these materials, and thus a fermionic description is appropriate for them; ii) the large mismatch in Fermi velocities between the normal counterelectrode and the cuprates, that should suppress Andreev reflection [41], in reality does not, because the renormalization of the Fermi velocity in the point-contact experiments differs from the full quasi-particle normalization (by the way, the same happens in heavy fermion superconductors); iii) Andreev reflection occurs in cuprates even though they do not fulfill the BCS condition $\Delta \ll E_F$ (especially in the underdoped, UD, regime) and are rather close to a transition to a Bose-Einstein condensation. It is clearly impossible here to account for all the published results; for further more detailed information, we suggest the very good reviews by Deutscher (mainly focused on hole-doped cuprates [40, 28] and Armitage *et al.* [42](focused on electron-doped cuprates).

As for the symmetry of the OP, it seems now well established that hole-doped cuprates have a superconducting OP with dominant $d_{x^2-y^2}$ symmetry (with nodes along the (110) direction) and, sometimes, minor imaginary contributions like is of id_{xy} that break the time-reversal symmetry [10]. There has been a long debate about the intrinsic (bulk) or extrinsic (related to the surface) origin of this additional component, and about the doping range in which it exists, as will be briefly mentioned in the following.

In $YBa_2Cu_3O_{7-}$ (YBCO), one of the most studied cuprates, early directional PCARS measurements in single crystals gave evidence of a ZBCP along the nodal direction (110) and of two Andreev maxima along the antinodal direction (100) [39], results confirmed by STM measurements in the same configurations (see fig.3a). The PCARS spectra were successfully fitted with the 2D BTK model by Tanaka and Kashiwaya for the case of a pure d -wave symmetry, which gave an energy gap of amplitude $\Delta \simeq 28$ meV and also set an upper limit of 5% for the weight of any possible isotropic OP component (s or is). In general, PCARS measurements away from the nodal direction are in very good agreement with a pure d -wave symmetry. However, later PCARS measurements along (100) in $Y_{1-x}Ca_xBa_2Cu_3O_{7-}$ crystals were shown to require (even for $x=0$) a $d+is$ fit [43] in which the relative amplitude of the s (d) component increased (decreased) with decreasing the barrier parameter Z (see fig.3b and c) independent

http://dx.doi.org/10.5772/59587

of the critical temperature or of the Ca content of the sample. In other words, an almost pure *d* -wave symmetry was found approaching the tunneling regime, while a substantial isotropic component was found in high-transparency contacts. This puzzling result was explained in terms of an unusual proximity effect that induces an *s* -wave OP in the normal metal, and on the S side depresses the *d* -wave component and enhances the (presumably preexisting) subdominant *is* -wave OP component [43, 28]. The emergence of the subdominant *is* component in the OP at the surface of YBCO was indeed predicted theoretically [44], unrelated to proximity effects and thus intrinsic to this material. Its most striking effect is to break the time-reversal symmetry, leading to spontaneous supercurrents that flow on the surface of the crystal, and that result in a Doppler shift of the Andreev bound states to finite energy. Thus, the ZBCP (that would be seen along the nodal direction for a pure *d* symmetry) spontaneously splits. This splitting has indeed been observed in some measurements [45] (see fig. 3d), but not in others [46]. In various cases a splitting was seen only in the presence of magnetic fields (and, moreover, in conditions where the surface screening supercurrents were presumably negligible, which would indicate that the subdominant imaginary component in the OP is not due to the Doppler shift of the ABS but is induced by the field itself) [47, 28]. STM measurements in Ca-YBCO films with (110) orientation at different doping levels finally showed that the spontaneous splitting occurs only in the overdoped (OD) regime, suggesting a doping-induced transition from pure *d* wave to a mixed $d + is$ or $d + id$ symmetry (with the imaginary component being no more than 10% of the main real component) [46]). Incidentally, this points towards a bulk nature of the subdominant component; its emergence could be due to an actual change in the pairing interaction within a quantum critical point scenario [28].

In $La_{2-x}Sr_xCuO_4$ (LSCO) the anisotropy of the OP is suggested by several experimental techniques such as specific heat, ARPES, Raman scattering, magnetoresistance. Strictly speaking, however, these do not prove that the gap has nodes. On the other hand, evidence *against* gap nodes in LSCO near optimal doping ($x = 0.15$) was given by early tunneling measurements in single-crystal break junctions. PCARS measurements in LSCO single crystals near optimal doping along the (110) direction did not show the expected ZBCP but rather two symmetric conductance maxima at 3-5 meV and a general shape that is incompatible with both the pure *s* -wave and the pure *d* -wave symmetry [48], and excludes any symmetry with nodes. A good fit of the spectra was obtained with an $s + d$ symmetry or an *extended s* -wave (with no zeros). A similar conclusion was later drawn for the *whole* doping range, from underdoped to overdoped – even though some PCARS measurements in underdoped crystals provided evidence of a ZBCP disappearing at a temperature T_c^* much lower than the bulk T_c, and which was well fitted to a pure *d* -wave symmetry of amplitude $\Delta = 5\,\text{meV}$ assuming $I \parallel (110)$ [28]. Stimulated by these results, we performed PCARS measurements in polycrystalline samples of LSCO with six different compositions, from underdoped to overdoped, by using a sharp Au tip pressed against the sample. The spectra gave no evidence of ZBCP and instead suggested, again, the absence of nodes in the whole superconducting dome. As a matter of fact, the shape of 100% of the spectra is absolutely incompatible with a pure *d* -wave symmetry (see fig.3e); they all show symmetric conductance maxima and some of them are very similar to those obtained in [48]. It is clear, even from the position of the maxima, that the gap amplitude has a maximum at optimal doping. The curves are best fitted by using either a $s + d$ symmetry [49] with a dominant *isotropic* component, or a $d + id$ symmetry [50] (even though a

pure s -wave fit is not too bad at least in some cases). In the latter case (preferable, since the compatibility of $s+d$ symmetry with the low-temperature lattice structure of LSCO is questionable) the d_{xy} component follows the trend of T_c as a function of Sr concentration and has thus a maximum at optimal doping, while the $d_{x^2-y^2}$ component tends to saturate to a constant value on increasing x [50] as shown in fig.3f. A strong suppression of both the $d_{x^2-y^2}$ component and of the gap magnitude $|\Delta|$ occurs at $x1$, where also T_c is reduced, further indicating a close relationship between the Andreev gap and the critical temperature.

The $d_{x^2-y^2}+id_{xy}$ symmetry that allows fitting our data is thus the same proposed for YBCO above optimal doping, and also invoked to explain the field-induced splitting of the ZBCP in YBCO and BSCCO. The conditions leading to the quantum phase transition from a pure $d_{x^2-y^2}$ to a mixed $d_{x^2-y^2}+id_{xy}$ one (with a smaller d_{xy} component) were indeed find to occur in LSCO in a small doping range from $x=0.19$ up to $x=0.24$, thus slightly shifted in the overdoped regime. Our results seem instead to indicate that the mixed symmetry is robust against doping, and persists in the whole superconducting dome (which also contrasts with the findings in YBCO). Since our junctions are all in the low- Z regime, an anomalous proximity effect (already discussed above for YBCO) cannot be excluded as the origin of the subdominant imaginary OP component [43]. This could be the case since more recent PCS measurements in underdoped LSCO in the tunneling (high Z) regime [51] have given spectra with symmetric conductance maxima in the (100) direction and a clear ZBCP in the (110) direction, as expected for a pure d -wave symmetry. It is worth noting that, in any case, these findings confirm that the gap measured by PCARS is different from that measured by tunnel or ARPES measurements, which decreases monotonically with doping (see fig.3f and g).

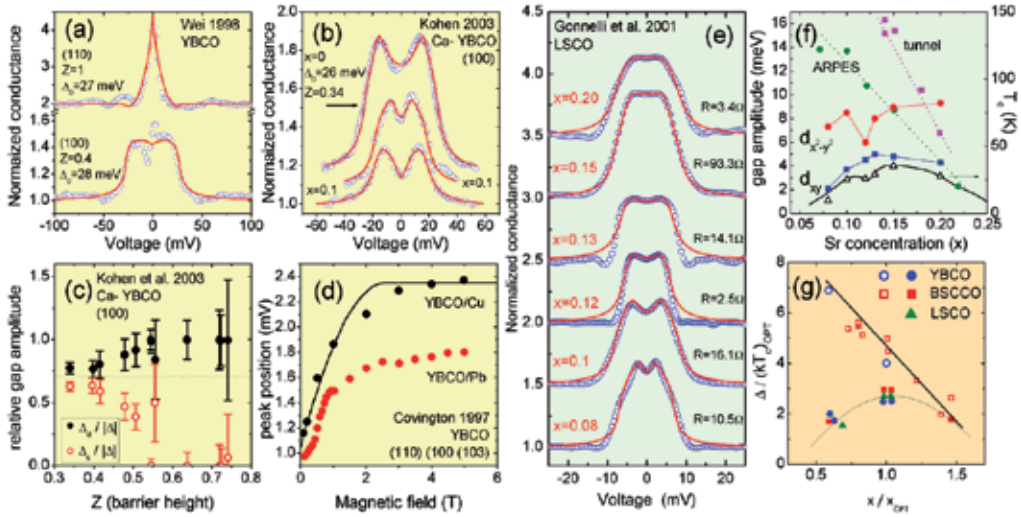

Figure 3. (a) Examples of PCARS spectra in YBCO along the nodal (110) and the antinodal (100) direction, with the relevant fit to a 2D BTK model with a pure d -wave symmetry (from [39]). (b) PCARS spectra in $Y_{1-x}Ca_xBa_2Cu_3O_{7-}$ crystals along the (100) direction with the relevant fit to a $d+is$ symmetry (from [43]). (c) Amplitude of the s and of the d -wave components as a function of the barrier parameter Z (from [43]), suggesting that the subdominant imaginary

http://dx.doi.org/10.5772/59587

component may be originated by an anomalous proximity effect. (d) Position of the peak observed in (110) tunneling spectra in YBCO as a function of the magnetic field. Notice that even in zero field the peak does not occur at zero bias (from [45]). (e) PCARS spectra in LSCO at various doping levels, and the relevant fit with a $d_{x^2+y^2} + id_{xy}$ symmetry (from [49, 50]). (f) Doping dependence of the $d_{x^2+y^2}$ and d_{xy} gap amplitudes compared to that of T_c and of the gap measured by tunnel and ARPES (from [49, 50]). (g) Normalized amplitude of the phase-coherence gap from Andreev reflection (solid symbols) and of the single-particle excitation gap (open symbols) for different cuprates (from [48, 28]).

Electron-doped cuprates (in which carriers are predominantly electrons) have general formula $R_{2-x}M_xCuO_4$ where R is a rare earth (Pr, Nd, Sm, Eu) and M is Ce or Th. The most studied are $Nd_{2-x}Ce_xCuO_4$ (NCCO) and $Pr_{2-x}Ce_xCuO_4$ (PCCO). These materials differ from hole-doped cuprates in many respects, among which: i) the lattice structure; ii) the maximum critical temperature (much lower in n-doped ones); iii) the phase diagram (e.g. the antiferromagnetic phase typical of the parent compounds persists upon much higher doping and even crosses the superconducting dome). Because of these and other differences, a straightforward generalization of the results obtained on hole-doped cuprates to the electron-doped cuprates is not reasonable. A careful investigation of the OP symmetry became possible only with the synthesis of high-quality samples. The most direct and convincing evidence of d -wave symmetry in PCCO came from tricrystal grain-boundary junction and ARPES measurements, but conflicting results indicating an s -wave symmetry were collected as well, for example by penetration depth measurements. In-plane PCARS measurements were carried out in c -axis oriented films of PCCO at different doping by Biswas *et al.* [52]. The precise direction of current injection in the *ab* plane was unknown. In the whole doping range, from UD to OD, high- Z contacts gave tunnel-like spectra with a zero-bias conductance minimum, coherence peaks at finite energy, and no ZBCP. Low- Z spectra were instead doping-dependent. In UD films they showed a single ZBCP (whose width was of the order of the gap amplitude) that was suppressed, but did not split, in a magnetic field parallel to (001). In OPT and OD samples, they displayed Andreev-reflection features in the form of symmetric maxima typically associated to a nodeless gap. This behavior was interpreted as suggesting a doping-induced transition between $d_{x^2-y^2}$ and s -wave (or a nodeless $d + is$) symmetry, despite a number of unexplained anomalies. Shan *et al.* carried out PCS measurements (with a metallic tip) in the tunneling regime in NCCO single crystals at optimal doping [51]. They unexpectedly obtained very similar spectra along the (110) and the (100) direction, characterized by: i) clear coherence peaks at the gap edges; ii) a shape typical of SIN junctions, with no Andreev-reflection conductance enhancement even at low contact resistance; iii) no zero-bias conductance peak. The spectra along (110) are thus absolutely incompatible with a pure d -wave symmetry that would give a ZBCP and no (or suppressed) coherence peaks. Instead, all the spectra admit an s -wave fit. The resulting gap amplitude turns out to follow the BCS weak-coupling predictions both for its amplitude and its temperature dependence. These results would prove that the OP of NCCO is certainly not pure d -wave; on the other hand, it is very unlikely that it is pure s -wave. Indeed, the fit itself works also with an anisotropic s symmetry or, for instance, by assuming a two-band picture (suggested by ARPES measurements) where one band (crossing the Fermi level at $\pi/2, \pi/2$) has an OP with pure d -wave symmetry and the other (at $(\pm\pi,0)$ and $(0, \pm\pi)$) an OP with a s -wave symmetry [51]. Tunneling spectra in SIS c -axis junctions in PCCO carried out by Dagan *et al.* [53] were later shown to be compatible with a non-monotonic d -

wave symmetry (with gap maxima displaced away from the (100) direction, as suggested by Raman spectroscopy and ARPES experiments) in the whole doping range. This symmetry is consistent with the observation of phase-sensitive experiments, even though, exactly as the pure d -wave, it would give a ZBCP due to the presence of ABS along the nodal direction and a marked in-plane anisotropy of the spectra. The lack of both these features in the tunneling experiments was then ascribed to the materials being in the dirty limit ($\xi > \ell$). Interestingly, the gap determined by the fit follows a BCS-like temperature dependence and scales with T_c, with a BCS gap ratio $2\Delta / k_B T_c \simeq 3.5$, thus similar to the one predicted by the BCS theory. According to the authors, this would indicate that PCCO and NCCO are characterized by a weak electron-boson coupling.

4.2. PCARS in Fe-based superconductors

PCARS experiments started being performed on FeBS [54] soon after their discovery and, initially, they were carried out on polycrystalline samples. Indeed the advantage of PCARS with respect to other spectroscopic techniques (namely ARPES and STM) is that it does not require an atomically flat surface. However, early measurements were often contradictory and some authors reported different results regarding the number and symmetry of the OP(s), i.e. single-gap, multi-gap, nodal or nodeless superconductivity. After a while though, also thanks to the availability of higher-quality samples, the multi-band nature of the FeBS became clear even if, in a few cases, it may be difficult to single out more than one gap in the PCARS spectra. Moreover, most of the results seem now in favor of an s -wave type of symmetry that could either feature an s_{++} or $s_{\pm}$ gap structure (characterized by isotropic OPs with different sign on the hole-like and electron-like FS), with possible zeroes or nodes occurring in particular situations.

As for the pairing, since a phonon-mediated mechanism seems to have been ruled out soon [15], the two main possible scenarios are at present a magnetic one (either with itinerant or localized electrons) or a charge/orbital one [66]. In the first case the OP is expected to change sign on different FS sheets, i.e. to have an $s\pm$ structure (even though in some cases it may preserve the same sign on different bands [67]) while in the second the main candidate is the s_{++} wave, with no sign change. Despite great progress has been achieved in a considerably short time, the symmetry and, in particular, the structure of the OP in these compounds appear still rather elusive, maybe even more than it seemed a few years ago. This statement certainly regards PCARS as well, which has been mainly applied up to now to the investigation of the compounds that belong to the 1111 and 122 family, mostly to the latter.

PCARS on 1111 FeBS has been performed mainly on polycrystalline samples or thin films (Figure 4a-c and i) as it is still rather difficult to grow large crystals. To the best of our knowledge, only one PCARS result has been published on single crystals of the 1111 family, namely on F-doped Sm-1111 [68]. There, Karpinski *et al.* reported AR spectra, measured by injecting the current along the *ab* -plane, that were fitted by two nodeless gaps, in good agreement with other results obtained on polycrystals by Daghero *et al.* [56] (panel b). On the other hand, early measurements by Chen *et al.* [55] were interpreted in terms of a single BCS gap (panel a), i.e. isotropic, independent of energy and with a $2\Delta / k_B T_c$ ratio of about 3.5 and temperature behavior

http://dx.doi.org/10.5772/59587

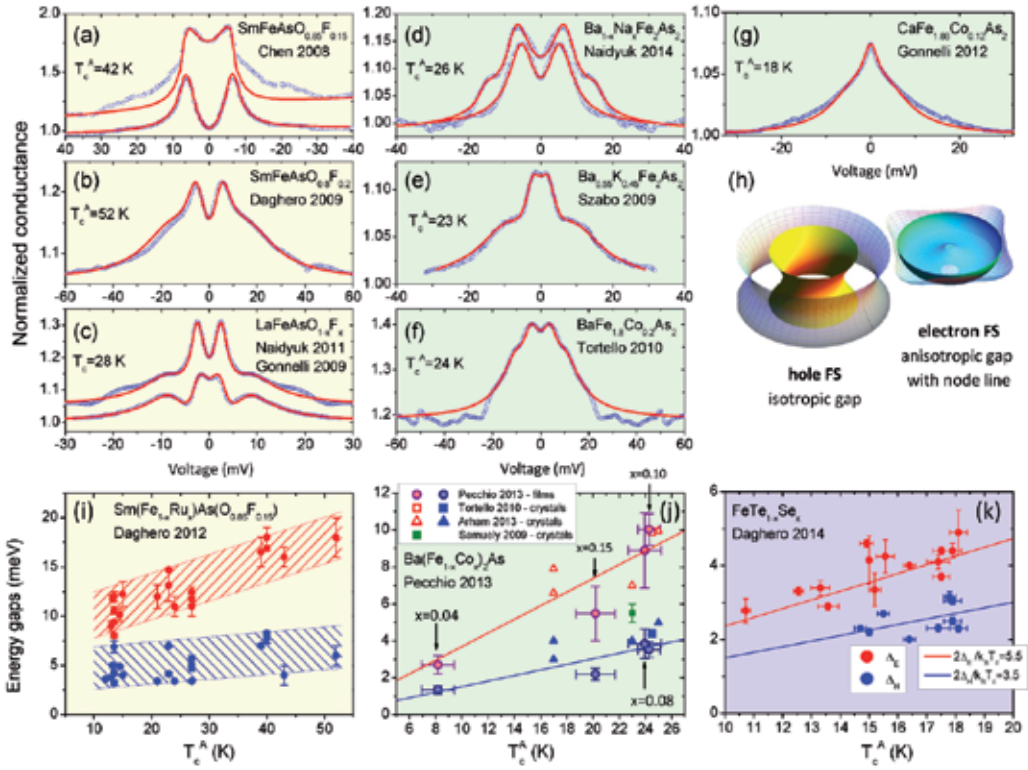

Figure 4. (a,b) Symbols: examples of PCARS spectra in polycrystalline Sm-1111 (from refs. [55] and [56]) with the relevant fit (lines), with a single isotropic gap (a) and two isotropic gaps (b). (c) PCARS spectra in La-1111 polycrystals (from [57]) and films (from [58]) with the relevant fit with two isotropic gaps as suggested in [27]. (d) PCARS spectra in $Ba_{1-x}Na_xFe_2As_2$ single crystals [59] fitted with either two (upper curves) or one (lower curve) isotropic gap. Whether the shoulders at $\simeq 15$ meV are due to a second gap is actually doubtful. (e,f) PCARS spectra in K-doped (from [60]) and Co-doped Ba-122 (from [61]) single crystals with the fit with two isotropic gaps. (g) An in-plane example of PCARS spectra in Co-doped Ca-122 crystals that prove the presence of nodes in the gap, with the relevant 3D-BTK fit with two gaps, of which one has a horizontal line of nodes. The model FS and the gap structure used in the 3D BTK model are shown in (h) as matt and gridded surfaces. (i) Effect of isovalent substitution (Ru in the Fe site) on the gaps of Sm-1111. The gaps are reported as a function of T_c^A (from [62]). (j) T_c^Adependence of the gaps in $Ba(Fe_{1-x}Co_x)_2As_2$ films with different x (indicated by labels) compared to other PCARS results [61, 63, 64]. In the UD regime $(x \leq 10)$ the gap ratios $2\Delta_i / k_B T_c$ are 3.52 and 9 (lines), in the OD regime they decrease. (k) Gaps of $FeTe_{1-x}Se_x$ films with $x = 0.3$, 0.4 and 0.5 as a function of T_c^A (from [65]). The gap ratios $2\Delta_i / k_B T_c$ are constant (solid lines). In (i, j, k) the gaps were obtained by fitting the PCARS spectra with two isotropic gaps.

as in the original BCS paper [6]. Daghero *et al.* [56] reported a rather large scattering of the values for the large OP, which is also one of the arguments invoked to argue that the large gap is actually not a gap. However, there can be other explanations. First, the features associated to the larger gap are often less defined in energy [58] and may not give rise to double maxima but show up rather as " shoulders" in the conductance. Second, it is actually possible that more than two gaps are present in these compounds, and that PCARS is unable to discriminate between the (multiple) large ones. It turns indeed out that the minimal theoretical model to reproduce the

experimental gaps, within the Eliashberg-like theory assuming a spin-fluctuations-mediated mechanism, has to take into account at least three bands [69]. On the other hand, a fit of the experimental spectra with a three-gap model could easily be meaningless because of the much too high number of free parameters. Therefore, a two-gap model is generally used and the noticeable scattering of the large gap values in, for instance, ref. [56] has most probably to be ascribed to the fact that more than two gaps are picked up, as a whole, by different PCARS spectra. PCARS was also performed on 1111 thin films [58] where the large gap was difficult to resolve. There, this fact was mainly explained by a possible large interband scattering that smears out the larger gap features, even though it has been shown that a two-gap model could indeed fit the data rather well [27], as reported in the upper curve of panel c.

The possibility to grow large single crystals of the 122 family made these materials the most studied ones among FeBS, also as far as PCARS is concerned (Figure 4d-h and j). Multi-gap, nodeless superconductivity was reported for K-, Co- and Ni-doped Ba 122 crystals [60, 61, 70] (see Figures 4e, f and 5a, respectively). On the other hand, only one gap has been clearly resolved, at least up to now, in $Ba_{1-x}Na_xFe_2As_2$ ($x=0.25$) [59] (Figure 4d, lower curve) and $SrFe_{1.74}Co_{0.26}As_2$ [71]. In particular, additional structures were observed in $Ba_{1-x}Na_xFe_2As_2$ at higher energies that, when fitted as a second gap, gave an unrealistically large $2\Delta/k_BT_c$ value, $\approx$15, (panel d, upper curve). By the way, similar features have recently been reported also for Fe(Te,Se) thin films and interpreted as electron-boson interaction features [65]. PCS results in Na-doped Sr 122 didn't show AR features but V-shaped spectra, that were interpreted in terms of possible electron scattering from magnetic order [72].

In some cases, depending on the details of the pairing interaction, the structure of the order parameter can become, within the s -wave symmetry, anisotropic and feature gap minima or line nodes where the OP changes sign on a FS sheet, either hole- or electron-like [73, 74, 16]. In these situations, the use of the 3D BTK model that takes into account the actual shape of the Fermi surface, even though approximated by a suitable parametric function, can be unavoidable in order to catch these finer details of the gap structure. Horizontal line nodes have indeed been observed by PCARS in the $CaFe_2As_2$ compound under pressure [36]. The point contact spectra were very well fitted by the 3D BTK model and results theoretically supported both by calculations of the electronic structure (within the Density Functional Theory) and of the gap structure (within a Random Phase Approximation approach in a ten-orbital model), thus giving a self-consistent experimental/theoretical picture of the OP in this compound. A similar gap structure (but more anisotropic) is inferred also by PCARS measurements on Co-doped $CaFe_2As_2$ where the spectra can be fitted by the 3D BTK model taking into account the FS topology, as shown in Figure 4g and h.

As for the 111 family, multiple nodeless gaps were reported for Co-doped NaFeAs [75] while only one nodeless gap was observed by PCARS measurements on LiFeAs [76].

Multiband superconductivity was also reported for Fe(Te,Se) films. In this case, the small gap was the most difficult to resolve [65]. Ref. [65] also reported the evolution of the two gaps as a function of T_c, which increases with increasing the Se content from $x=0.3$ to $x=0.5$. The two gaps have been found to decrease rather monotonically with the critical temperature of the PCARS junctions (see Figure 4k) and since their gap ratios remain constant, this means that

http://dx.doi.org/10.5772/59587

the amplitudes of the gaps perfectly scale with T_c, i.e. if plotted as a function of doping they would mimic the behavior of the critical temperature. The only caveat in this respect is that the values of the gap amplitudes in each point contact are related to the *local* T_c^A of the contact rather than to bulk properties (such as the average doping or the T_c measured by electrical transport).

There are not so many examples in the literature, up to now, of systematic PCARS studies of the evolution of the OPs as a function of doping or disorder. Panels i and j report other examples of energy gaps as a function of the critical temperature, when the latter is modulated by means of chemical substitutions, either isovalent (Ru for Fe) in optimally F-doped Sm-1111 polycrystals (i), or aliovalent (Co for Fe) in Ba-122 thin films (j). This kind of studies might be very important in the attempt of unraveling the symmetry and structure of the OPs since, in some cases, a change of symmetry has been theoretically predicted when changing some lattice parameters [77].

Interband interference effects and sub-gap bound states in the Andreev spectra have been theoretically predicted as a consequence of an $s_{\pm}$ gap structure [78]. These features though, have not been reported in any experimental PCARS study up to now. Possibly they may be washed out by broadening effects or may occur at particular conditions of the model that make them hardly distinguishable from a more stardard s_{++} BTK conductance. According to this model, these interference effects indeed depend on a free parameter, αwhose value has not been predicted theoretically and changes dramatically the shape of the spectra. However, interference effects on the BTK conductance due to a sign-changing s -wave OP in multi-band systems have also been recently calculated [79] by using the quantum waveguides theory. Simple analytical formulas were obtained that depend on the ratios of the Fermi velocities of the normal metal and the superconducting bands and could be easily compared to experimental spectra, possibly helping to catch signatures of a sign-changing OP.

4.2.1. Electron-boson interaction in FeBS

As already noticed in 2.2, in case of moderate- to strong-coupling regime, the energy dependence of the OP can give rise to EBI features in the conductance spectra that can be better singled out by taking the sign-changed second derivative of the I-V characteristic. These features can give important information regarding the pairing mechanism because they indicate that electrons are actually interacting with some fundamental excitation of the material under study. EBI characteristics were reported for Co- and Ni-doped (Figure 5a) Ba-122 single crystals [61, 70]. In both Co- and Ni- doping the main EBI feature showed up at $E_p \approx \Delta_{max} + \Omega_b$ (panel b). The characteristic bosonic energy, $\Omega_b$was very similar to the spin-resonance energy observed in neutron scattering experiments on the same compound [80].

Moreover, $\Omega_b$decreased as a function of temperature (panel c), a behavior incompatible with a phononic interaction whose energy is expected to be temperature-independent. As reported in section 3.2, it is possible to include the energy-dependent expression for the gap in the BTK model and compare the result with the experimental normalized conductance. Panel d reports

an example for an optimally F-doped Sm-1111 polycrystalline sample [27] where it is shown that, besides reproducing the two energy gaps, the theoretical conductance can reproduce very well the EBI feature at about 40 meV and the shape of the high-energy tails, but not the one at 25 meV. This might be due to finer details of the bosonic spectral function that was modeled by a Lorentzian function in the theoretical analysis. It is also worth reminding in this regard that, as shown in ref. [27], in multiband systems the EBI features don't necessarily occur at energies of the order of $\Delta_{max} + \Omega_b$, but a detailed calculation of the energy dependence of the gap is desirable. Similar results have also been recently reported for Fe(Te,Se) thin films [65]. The presence of EBI features at these energies and the fact that the experimental gaps can be reproduced within the Eliashberg-like model, by using a spectral function with Lorentzian shape whose characteristic energy is Ω_b [27, 61, 65], strongly support a spin-fluctuations-mediated mechanism of superconductivity in FeBS.

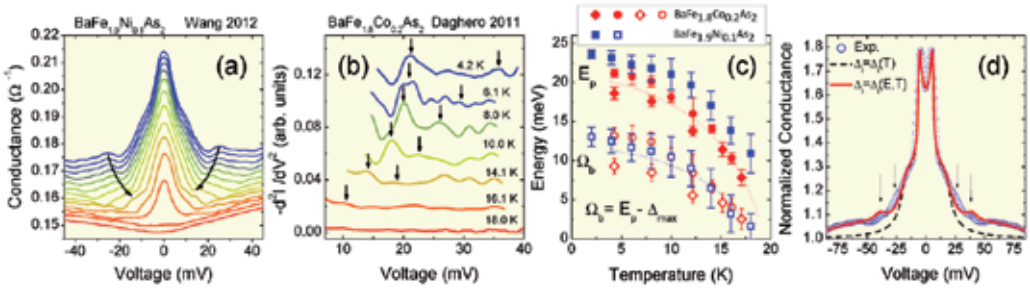

Figure 5. (a) Temperature dependence of the raw conductance curves (shifted downward for clarity) obtained from a *c* -axis Ag/$BaFe_{1.9}Ni_{0.1}As_2$ junction. Temperatures range from 2 K (upper one) to 20 K with a step of 2 K. The last curve is measured at 21 K. Arrows indicate the temperature evolution of the EBI features occurring at energies of about $E_p(T) \approx \Delta_{max}(T) + \Omega_b(T)$ where $\Omega_b(T)$ is the characteristic bosonic energy (from [70]). (b) Temperature dependence of the sign-changed second derivative of the $I-V$ characteristics in the $BaFe_{1.5}Co_{0.2}As_2$ point-contact junctions (from [27, 61]). (c) Temperature evolution of E_p and Ω_b in $BaFe_{1.9}Ni_{0.1}As_2$ (squares) and $BaFe_{1.8}Co_{0.2}As_2$ (diamonds and circles) single crystals as reported in refs. [70, 61]. (d) Normalized conductance curve (circles) measured from a Ag/$SmFeAsO_{0.8}F_{0.2}$ point-contact junction. The dashed line is a BTK fit to the experiment, obtained using energy-independent values for the gaps (Δ_1=6.0meV and Δ_2=19.5 meV). The solid line is a theoretical curve obtained by introducing in the BTK model the energy-dependent gap functions calculated within the three-band Eliashberg theory whose values are Δ_1=17.23 meV, Δ_2=6.03meV and Δ_3=−19.56 meV (from [27]).

EBI features have also been observed in the normal state of KFe_2As_2 [81]. The d^2V/dI^2 characteristics showed a peak at about 20 meV, while were featureless at higher and lower energies. The results were interpreted on the basis of charge excitations (excitonic-like), a non-phononic and non-magnetic type of interaction never observed before in PCS spectra. The authors argued that the manifestation of the EBI features in PCS spectra on these compounds has been possible thanks to an electron mass renormalization larger than in many metallic systems.

Finally, a conductance enhancement around zero bias has been reported in the PCS spectra in the normal state of several FeBS, and interpreted as being tied to interactions with orbital

http://dx.doi.org/10.5772/59587

fluctuations, thus providing indication of electronic nematicity [82]. It has also been argued that such excess density of states can be actually picked up by PCS thanks to the presence of non-negligible electronic correlations in the studied materials [83].

5. Conclusion

The BCS theory (and, when necessary, its generalizations to the anisotropic and multiband case) was able to give a satisfactory description of conventional superconductors in terms of electron-phonon coupling, and the Eliashberg theory can better describe them when the coupling is stronger. Both theories can, in principle, be generalized to any pairing glue. In electron-phonon superconductors, the OP parameter is generally single and isotropic but more complex anisotropies [84] or multi-band scenarios [30] have been observed as well.

However, superconductivity in unconventional HTSC cannot be explained by the same pairing mechanism. In this regard, the knowledge of the number, amplitude, symmetry and structure of their OP is essential in order to satisfactorily describe their superconducting state and pairing mechanism. As a matter of fact, this task turned out to be tremendously more complicated and challenging than for conventional superconductors.

Thanks to the Andreev reflection process, PCARS has been able to address this issue to a good extent. The complicated scenarios proposed for HTSC pushed the development of models of increasing complexity that certainly helped to achieve a more accurate analysis of the experimental data and to catch important details regarding the OP in HTSC. At the same time, as we have seen by mainly focusing on the results of PCS in the Andreev reflection regime, several issues are still open in this field.

There is a general consensus that several cuprates have a dominant d -wave symmetry. However, for many of them additional components of the OP (mixed symmetries) were reported, which sometimes appeared to set in only at certain doping levels. Their origin still needs to be clarified as well as the pairing mechanism and its relation to the OP. Moreover, sample- or surface-related issues may also play a role.

Often, PCARS results turned out to be different from those obtained by ARPES or STM. Although some of these discrepancies still have to be reconciled, on the other hand they sometimes gave complementary information because, for example, PCARS is sensitive to the phase-coherent pairs while STM probes the single-particle states. Contrasting results have been obtained for electron-doped cuprates as well, some of which also considerably differ from those observed in the hole-doped ones, even suggesting that some of them are weak-coupling BCS (one isotropic gap with $2\Delta/k_BT_c \approx 3.5$) superconductors. Therefore, a consistent generalization between the two types of cuprates is very far from being achieved.

Most FeBS certainly feature multiple superconducting bands and gaps and a more general picture of the present state of the art can be achieved. Nevertheless, a precise knowledge of

the main features of the OPs is still lacking. Even the knowledge of tiny differences in their structure might be important in order to unravel their pairing glue and, apparently, some new compounds seem to pose into question some of the most successful theoretical models. In particular, distinguishing between an $s_{\pm}$ - and s_{++} -wave structure of the OP is turning out to be a conundrum and unambiguous phase-sensitive experiments on single crystals have not been performed yet in FeBS. Several have been proposed though, and experiments making use of point contacts may also be very useful in this regard [85].

PCARS is not sensitive to the phase of the OP and, unlike in cuprates, interference effects (that would be expected only for the $s_{\pm}$ -wave structure) have not been clearly observed yet. Their (possible) observation is indeed complicated by the particular electronic structure and by the similarity between the two main OP structures proposed. However, theoretical models of increasing complexity are being developed that may be able to detect signatures of a possible sign change of the OP in FeBS. For the time being, the use of the 3D BTK model turned out to be very useful and helped to catch, even though somehow indirectly, finer details of the structure of the OPs, like gap anisotropies or line nodes, thus putting more stringent constraints on the present theoretical predictions. The study of the dependence of the OPs as a function of doping or disorder in FeBS might be very important also because the few PCARS results reported up to now do not show the puzzling behavior obtained in many PCARS studies on cuprates.

Moreover, the possibility to detect electron-boson interaction features in the point contact characteristics may be crucial in clarifying the pairing mechanism as not only EBI features indicate the presence of some fundamental excitation, but more specifically show their interaction with the electrons in the material.

FeBS feature many differences in comparison with cuprates and, as we have briefly mentioned, PCARS methods and models are evolving for better investigating the former class of compounds. Also, PCARS results obtained up to now, although far from being conclusive, seem less puzzling than for cuprates. Therefore, it is hoped that the progress achieved up to now and the new methods developed for investigating FeBS by PCARS may at least aid shedding light on cuprates as well. A more general and complete picture of HTSC and a clarification of their relevant pairing mechanism(s) is indeed a major objective of the present research in the field of solid state physics. The achievement of this goal would hopefully pave the way for the discovery of new materials with higher T_c and better properties, especially in view of the current applications of superconductivity and of the potentially revolutionary ones that may be realized with new high- T_c superconductors.

Acknowledgements

The authors would like to warmly thank R.S. Gonnelli and G.A. Ummarino for useful discussions and for perusing the manuscript. The results of our group shown in this chapter, were obtained also thanks to the contributions of V.A. Stepanov and P. Pecchio.

http://dx.doi.org/10.5772/59587

Author details

M. Tortello* and D. Daghero

*Address all correspondence to: mauro.tortello@polito.it

Dipartimento di Scienza Applicata e Tecnologia (DISAT), Politecnico di Torino, Torino, Italy

References

[1] J. G. Bednorz and K. A. Müller. Possible high T_c superconductivity in the Ba-La-Cu-O system. *Z. Physik, B*, 64:189, 1986.

[2] VV. AA. Celebratory issue on high T_c superconductors. *Nature Phys.*, 2, 2006.

[3] Y. Kamihara, T. Watanabe, M. Hirano, and H. Hosono. Iron-based layered superconductor $LaO_{1-x}F_xFeAs$ (x = 0.05-0.12) with T_c = 26 K. *J. Am. Chem. Soc.*, 130:3296, 2008.

[4] Z. A. Ren, J. Yang, W. Lu, W. Yi, X. L. Shen, Z. C. Li, G. C. Che, X. L. Dong, L. L. Sun, F. Zhou, and Z. X. Zhao. Superconductivity in the iron-based F-doped layered quaternary compound $NdO_{1-x}F_xFeAs$. *Europhys. Lett.*, 82:57002, 2008.

[5] A. M. Gabovich and V. I. Kuznetsov. What do we mean when using the acronym BCS? The Bardeen Cooper Schrieffer theory of superconductivity. *Eur. J. Phys.*, 34:371, 2013.

[6] J. Bardeen, L. N. Cooper, and J. R. Schrieffer. Theory of superconductivity. *Phys. Rev.*, 108:1175–204, 1957.

[7] J. R. Waldram. *Superconductivity of metals and cuprates*. Institute of Physics Publishing, 1996.

[8] I. I. Mazin and V. P. Antropov. Electronic structure, electron–phonon coupling, and multiband effects in MgB_2. *Physica C*, 385:49, 2003.

[9] R. A. Klemm, C. T. Rieck, and K. Scharnberg. Order-parameter symmetries in high-temperature superconductors. *Phys. Rev. B*, 61:5913, 2000.

[10] C. C. Tsuei and J. R. Kirtley. Pairing symmetry in cuprate superconductors. *Rev. Mod. Phys.*, 72:969, 2000.

[11] H. Suhl, B. T. Matthias, and L. R. Walker. Bardeen-Cooper-Schrieffer theory of superconductivity in the case of overlapping bands. *Phys. Rev. Lett.*, 3:552, 1959.

[12] V.A. Moskalenko. Superconductivity of metals with overlapping energy bands. *Fiz. Met. Metalloved. (Phys. Met. Metallogr. (URSS))*, 4:503, 1959.

[13] A. A. Golubov and I. I. Mazin. Sign reversal of the order parameter in *s*-wave superconductors. *Physica C*, 243:153, 1995.

[14] I. I. Mazin, D. J. Singh, M. D. Johannes, and M. H. Du. Unconventional superconductivity with a sign reversal in the order parameter of $LaFeAsO_{1-x}F_x$. *Phys. Rev. Lett.*, 101:057003, 2008.

[15] L. Boeri, O. V. Dolgov, and A. A. Golubov. Is $LaFeAsO_{1-x}F_x$ an electron-phonon superconductor? *Phys. Rev. Lett.*, 101:026403, 2008.

[16] P. J. Hirschfeld, M. M. Korshunov, and I. I. Mazin. Gap symmetry and structure of Fe-based superconductors. *Rep. Prog. Phys.*, 74:124508, 2011.

[17] G. M. Eliashberg. Interactions between electrons and lattice vibrations in a superconductor. *Sov. Phys. JETP*, 11:696, 1963.

[18] J.P. Carbotte. Properties of boson-exchange superconductors. *Rev. Mod. Phys.*, 62:1027, 1990.

[19] G. A. Ummarino. *Emergent Phenomena in Correlated Matter*, volume 3, chapter Eliashberg theory, pages 13.1–13.36. Forschungszentrum Julich Gmbh and Institute for Advanced Simulations, 2013.

[20] H. J. Choi, D. Roundy, H. Sun, M. L. Cohen, and S. G. Louie. The origin of the anomalous superconducting properties of MgB_2. *Nature*, 418:758–760, 2002.

[21] P.B. Allen. Fermi-surface harmonics: A general method for nonspherical problems. Application to Boltzmann and Eliashberg equations. *Phys. Rev. B*, 13:1416, 1976.

[22] P.B. Allen. New method for solving Boltzmann's equation for electrons in metals. *Phys. Rev. B*, 17:3725, 1978.

[23] I. K. Yanson. Nonlinear effects in the electric conductivity of point junctions and electron-phonon interaction in normal metals. *Sov. Phys. JETP*, 39:506–513, 1974.

[24] Yu. G. Naidyuk and I. K. Yanson. *Point-Contact Spectroscopy*, volume 145 of *Springer Series in Solid-State Sciences*. Springer, 2004.

[25] G. E. Blonder, M. Tinkham, and T. M. Klapwijk. Transition from metallic to tunneling regimes in superconducting microconstrictions: Excess current, charge imbalance, and supercurrent. *Phys. Rev. B*, 25:4515, 1982.

[26] D. Daghero and R.S. Gonnelli. Probing multiband superconductivity by point-contact spectroscopy. *Supercond. Sci. Technol.*, 23:043001, 2010.

[27] D. Daghero, M. Tortello, G.A. Ummarino, and R. S. Gonnelli. Directional point-contact Andreev-reflection spectroscopy of Fe-based superconductors: Fermi surface topology, gap symmetry, and electron-boson interaction. *Rep. Prog. Phys.*, 74:124509, 2011.

http://dx.doi.org/10.5772/59587

[28] G. Deutscher. Andreev-Saint-James reflections: A probe of cuprate superconductors. *Rev. Mod. Phys.*, 77:109–35, 2005.

[29] D. Daghero, M. Tortello, P. Pecchio, V. A. Stepanov, and R. S. Gonnelli. Point-contact Andreev-reflection spectroscopy in anisotropic superconductors: the importance of directionality. *Low Temp. Phys.*, 39:261, 2013.

[30] R. S. Gonnelli, D. Daghero, G. A. Ummarino, V. A. Stepanov, J. Jun, S. M. Kazakov, and J. Karpinski. Direct evidence for two-band superconductivity in MgB_2 single crystal from directional point-contact spectroscopy in magnetic field. *Phys. Rev. Lett.*, 89:247004, 2002.

[31] A. Andreev. Thermal conductivity of the intermediate state of superconductors. *Zh. Eksp. Teor. Fiz.*, 46:1823, 1964. Engl. Transl. Sov. Phys.-JETP 19, 1228 (1974).

[32] G.E. Blonder and M. Tinkham. Metallic to tunneling transition in Cu-Nb point contacts. *Phys. Rev. B*, 27:112, 1983.

[33] R. C. Dynes, V. Narayanamurti, and J. P. Garno. Direct measurement of quasiparticle-lifetime broadening in a strong-coupled superconductor. *Phys. Rev. Lett.*, 41:1509, 1978.

[34] A. Plecenik, M. Grajcar, Š. Beňaňka, P. Seidel, and A. Pfuch. Finite quasiparticle-lifetime effects in the differential condutance of $Bi_2Sr_2CaCu_2O_y$/Au junctions. *Phys. Rev. B*, 49:10016, 1994.

[35] S. Kashiwaya, Y. Tanaka, M. Koyanagi, and K. Kajimura. Theory for tunneling spectroscopy of anisotropic superconductors. *Phys. Rev. B*, 53:2667, 1996.

[36] R. S. Gonnelli, D. Daghero, M. Tortello, G. A. Ummarino, Z. Bukowski, J. Karpinski, P. G. Reuvekamp, R. K. Kremer, G. Profeta, K. Suzuki and K. Kuroki Fermi-surface topological phase transition and horizontal order parameter nodes in $CaFe_2As_2$ under pressure. Preprint at arXiv:1406.5623 [cond-mat.supr-con], 2014.

[37] A. Brinkman, A. A. Golubov, H. Rogalla, O. V. Dolgov, J. Kortus, Y. Kong, O. Jepsen, and O. K. Andersen. Multiband model for tunneling in MgB_2 junctions. *Phys. Rev. B*, 65:180517, 2002.

[38] I. I. Mazin. How to define and calculate the degree of spin polarization in ferromagnets. *Phys. Rev. Lett.*, 83:1427, 1999.

[39] J. Y. T. Wei, N.-C. Yeh, D. F. Garrigus, and M. Strasik. Directional Tunneling and Andreev Reflection on $YBa_2Cu_3O_{7-}$ Single Crystals: Predominance of d-Wave Pairing Symmetry Verified with the Generalized Blonder, Tinkham, and Klapwijk Theory. *Phys. Rev. Lett.*, 81:2542, 1998.

[40] G. Deutscher and R. Maynard. *The Gap Symmetry and Fluctuations in High-T_c Superconductors*, chapter From the Andreev reflection to the Sharvin contact conductance, pages 503–510. NATO Science Series: B. Kluwer Academic Publishers, 2002.

[41] S. Kashiwaya and Y. Tanaka. Tunnelling effects on surface bound states in unconventional superconductors. *Rep. Prog. Phys.*, 63:1641-1724, 2000.

[42] N. P. Armitage, P. Fournier, and R. L. Greene. Progress and perspectives on electron-doped cuprates. *Rev. Mod. Phys.*, 82:2421, 2010.

[43] A. Kohen, G. Leibovitch, and G. Deutscher. Andreev Reflections on $Y_{1-x}Cu_x$ Ba_2O_{7-}: Evidence for an Unusual Proximity Effect. *Phys. Rev. Lett.*, 90:207005, 2003.

[44] M. Fogelström, D. Rainer, and J. A. Sauls. Tunneling into Current-Carrying Surface States of High- Tc Superconductors. *Phys. Rev. Lett.*, 79:281, 1997.

[45] M. Covington, M. Aprili, E. Paraoanu, L. H. Greene, F. Xu, J. Zhu, and C. A. Mirkin. Observation of Surface-Induced Broken Time-Reversal Symmetry in $YBa_2Cu_3O_7$ Tunnel Junctions. *Phys. Rev. Lett.*, 79:277, 1997.

[46] A. Sharoni, G. Koren, and O. Millo. Correlation of tunneling spectra with surface nanomorphology and doping in thin $YBa_2Cu_3O_{7-}$ films. *Europhys. Lett.*, 54:675, 2001.

[47] R. Beck, Y. Dagan, A. Milner, A. Gerber, and G. Deutscher. Order-parameter-node removal in the d-wave superconductor $YBa_2Cu_3O_{7-x}$ in a magnetic field. *Phys. Rev. B*, 69:144506, 2004.

[48] G Deutscher, N. Achsaf, D. Goldschmidt, A. Revcolevschi, and A. Vietkine. Andreev reflections from $La_{2x}Sr_xCuO_4$ single crystals. *Physica C*, 282-287:140, 1997.

[49] R. S. Gonnelli, A. Calzolari, D. Daghero, L. Natale, G. A. Ummarino, V. A. Stepanov, and M. Ferretti. Evidence for pseudogap and phase-coherence gap separation by Andreev reflection experiments in $Au/La_{2-x}Sr_xCuO_4$ point-contact junctions. *Eur. Phys. J. B*, 22:411, 2001.

[50] D. Daghero, R. S. Gonnelli, G. A. Ummarino, and V. A. Stepanov. Possible *d+id* scenario in $La_{2-x}Sr_xCuO_4$ by point-contact measurements. *Int. J. Mod. Phys.*, 17:649, 2003.

[51] L. Shan, Y. Huang, H. Gao, Y. Wang, S. L. Li, P. C. Dai, F. Zhou, J. W. Xiong, W. X. Ti, and H. H. Wen. Distinct pairing symmetries in $Nd_{1.85}Ce_{0.15}CuO_{4-y}$ and $La_{1.89}Sr_{0.11}CuO_4$ single crystals: Evidence from comparative tunneling measurements. *Phys. Rev. B*, 72:144506, 2005.

[52] A. Biswas, P. Fournier, M. M. Qazilbash, V. N. Smolyaninova, H. Balci, and R. L. Greene. Evidence of a *d*- to *s*-Wave Pairing Symmetry Transition in the Electron-Doped Cuprate Superconductor $Pr_{2-x}Ce_xCuO_4$. *Phys. Rev. Lett.*, 88:207004, 2002.

[53] Y. Dagan, R. Beck, and R. L. Greene. Dirty Superconductivity in the Electron-Doped Cuprate $Pr_{2-x}Ce_xCuO_{4-}$: Tunneling Study. *Phys. Rev. Lett.*, 99:147004, 2007.

[54] J. Paglione and R. L. Greene. High-temperature superconductivity in iron-based materials. *Nature Phys.*, 6:645–58, 2010.

http://dx.doi.org/10.5772/59587

[55] T. Y. Chen, Z. Tesanovic, R. H. Liu, X. H. Chen, and C. L. Chien. A BSC-like gap in the superconductor $SmFeAsO_{0.85}F_{0.15}$. *Nature (London)*, 453:761, 2008.

[56] D. Daghero, M. Tortello, R. S. Gonnelli, V. A. Stepanov, N. D. Zhigadlo, and J. Karpinski. Evidence for two-gap nodeless superconductivity in $SmFeAsO_{1-x}F_x$ from point-contact Andreev-reflection spectroscopy. *Phys. Rev. B*, 80:060502(R), 2009.

[57] R. S. Gonnelli, D. Daghero, M. Tortello, G. A. Ummarino, V. A. Stepanov, J. S. Kim, and R. K. Kremer. Coexistence of two order parameters and a pseudogaplike feature in the iron-based superconductor $LaFeAsO_{1-x}F_x$. *Phys. Rev. B*, 79:184526, 2009.

[58] Yu. G. Naidyuk, O. E. Kvitnitskaya, I. K. Yanson, G. Fuchs, S. Haindl, M. Kidszun, L. Schultz, and B. Holzapfel. Point-contact study of $ReFeAs_{1-x}F_x$ (Re=La, Sm) superconducting films. *Supercond. Sci. Technol.*, 24:065010, 2011.

[59] Yu. G. Naidyuk, O. E. Kvitnitskaya, S. Aswartham, G. Fuchs, K. Nenkov, and S. Wurmehl. Exploring point-contact spectra of $Ba_{1-x}Na_xFe_2As_2$ in the normal and superconducting states. *Phys. Rev. B*, 84:094516, 2011.

[60] P. Szabó, Z. Pribulová, G. Pristáš, S. L. Bud'ko, P. C. Canfield, and P. Samuely. Evidence for two-gap superconductivity in $Ba_{0.55}K_{0.45}Fe_2As_2$ from directional point-contact Andreev-reflection spectroscopy. *Phys. Rev. B*, 79:012503, 2009.

[61] M. Tortello, D. Daghero, G. A. Ummarino, V. A. Stepanov, J. Jiang, J. D. Weiss, E. E. Hellstrom, and R. S. Gonnelli. Multigap Superconductivity and Strong Electron-Boson Coupling in Fe-Based Superconductors: A Point-Contact Andreev-Reflection Study of $Ba(Fe_{1-x}Co_x)_2As_2$ Single Crystals. *Phys. Rev. Lett.*, 105:237002, 2010.

[62] D. Daghero, M. Tortello, G.A. Ummarino, V. A. Stepanov, F. Bernardini, M. Tropeano, M. Putti, and R. S. Gonnelli. Effects of isoelectronic Ru substitution at the Fe site on the energy gaps of optimally F-doped SmFeAsO. *Supercond. Sci. Technol.*, 25:084012, 2012.

[63] H. Z. Arham, C. R. Hunt, J. Gillett, S. D. Das, S. E. Sebastian, D. Y. Chung, M. G. Kanatzidis, and L. H. Greene. Andreev reflection like enhancement above bulk T_c in electron underdoped iron arsenides. Preprint at arXiv:1307.1908 [cond-mat.supr-con], 2013.

[64] P. Samuely, Z. Pribulová, P. Szabó, G. Pristáš, S. L. Bud'ko, and P. C. Canfield. Point contact Andreev reflection spectroscopy of superconducting energy gaps in 122-type family of iron pnictides. *Physica C*, 469:507, 2009.

[65] D. Daghero, P. Pecchio, G.A. Ummarino, F. Nabeshima, Y. Imai, A. Maeda, I. Tsukada, Komiya S., and R. S. Gonnelli. Point-contact Andreev-reflection spectroscopy in Fe(Te,Se) films: multiband superconductivity and electron-boson coupling. *Supercond. Sci. Technol.*, 27:124014, 2014.

[66] R. M. Fernandes, A. V. Chubukov, and J. Schmalian. What drives nematic order in iron-based superconductors? *Nature Phys.*, 10:97–104, 2014.

[67] H Miao, P. Richard, Y. Tanaka, K. Nakayama, T. Qian, K. Umezawa, T. Sato, Y.-M. Xu, Y. B. Shi, N. Xu, X.-P. Wang, P. Zhang, H.-B. Yang, Z.-J. Xu, J. S. Wen, G.-D. Gu, X. Dai, J.-P. Hu, T. Takahashi, and H. Ding. Isotropic superconducting gaps with enhanced pairing on electron Fermi surfaces in $FeTe_{0.55}Se_{0.45}$. *Phys. Rev. B*, 85:094506, 2012.

[68] J. Karpinski, N. Zhigadlo, S. Katrych, Z. Bukowski, P. Moll, S. Weyeneth, H. Keller, R. Puzniak, M. Tortello, D. Daghero, R. S. Gonnelli, I. Maggio-Aprile, Y. Fasano, Ø. Fischer, K. Rogacki, and B. Batlogg. Single crystals of $LnFeAsO_{1-x}F_x$ (Ln = La, Pr, Nd, Sm, Gd) and $Ba_{1-x}Rb_xFe_2As_2$: Growth, structure and superconducting properties. *Physica C*, 469:370, 2009.

[69] G. A. Ummarino, M. Tortello, D. Daghero, and R. S. Gonnelli. Three-band *s*± Eliashberg theory and the superconducting gaps of iron pnictides. *Phys. Rev. B*, 80:172503–1–4, 2009.

[70] Z.-S. Wang, Z.-Yu Wang, H.-Q. Luo, X.-Ye Lu, J. Zhu, C.-H. Li, L. Shan, H. Yang, H.-H. Wen, and C. Ren. Electron-boson coupling and two superconducting gaps in optimally electron-doped $BaFe_{1.9}Ni_{0.1}As_2$ single crystals. *Phys. Rev. B*, 86:060508(R), 2012.

[71] X. Zhang, Y. S. Oh, Y. Liu, L. Yan, S.R. Saha, N. P. Butch, K. Kirshenbaum, K. H. Kim, J. Paglione, R. L. Greene, and I. Takeuchi. Evidence of a universal and isotropic $2\Delta/k_b T_c$ ratio in 122-type iron pnictide superconductors over a wide doping range. *Phys. Rev. B*, 82:020515(R), 2010.

[72] X. Lu, W. K. Park, H. Q. Yuan, G. F. Chen, G. L. Luo, N. L. Wang, A. S. Sefat, M. A. McGuire, R. Jin, B. C. Sales, D. Mandrus, J. Gillett, S. E. Sebastian, and L. H. Greene. Point-contact spectroscopic studies on normal and superconducting AFe_2As_2-type iron pnictide single crystals. *Supercond. Sci. Technol.*, 23:054009, 2010.

[73] I. I. Mazin, T. P. Devereaux, J. G. Analytis, Jiun-Haw Chu, I. R. Fisher, B. Muschler, and R. Hackl. Pinpointing gap minima in $Ba(Fe_{0.94}Co_{0.06})_2As_2$ via band-structure calculations and electronic raman scattering. *Phys. Rev. B*, 82:180502(R), 2010.

[74] K. Suzuki, H. Usui, and K. Kuroki. Possible three dimensional nodes in the *s*± superconducting gap of $BaFe_2(As_{1-x}P_2)_2$. *J. Phys. Soc. Jpn.*, 80:013710, 2011.

[75] H. Z. Arham, D. E. Bugaris, D. Y. Chung, M. G. Kanatzidis, and L. H. Greene. Point contact spectroscopy in the superconducting and normal state of $NaFe_{1-x}Co_xAs$. Preprint at arXiv:1406.0038v1 [cond-mat.supr-con], 2014.

[76] X. Zhang, B. Lee, S. Khim, K.H. Kim, R. L. Greene, and I. Takeuchi. Probing the order parameter of superconducting LiFeAs using Pb/LiFeAs and Au/LiFeAs point-contact spectroscopy. *Phys. Rev. B*, 85:094521, 2012.

[77] K. Kuroki, H. Usui, S. Onari, R. Arita, and H. Aoki. Pnictogen height as a possible switch between high- T_c nodeless and low-T_c nodal pairings in the iron-based superconductors. *Phys. Rev. B*, 79:224511, 2009.

http://dx.doi.org/10.5772/59587

[78] A. A. Golubov, A Brinkman, Y. Tanaka, I. I. Mazin, and O. V. Dolgov. Andreev spectra and subgap bound states in multiband superconductors. *Phys. Rev. Lett.*, 103:077003, 2009.

[79] F. Romeo and R. Citro. Minimal model of point contact Andreev reflection spectroscopy of multiband superconductors. Preprint at arXiv:1407.7397v1 [cond-mat.supr-con], 2014.

[80] D. S. Inosov, J. T. Park, P. Bourges, D. L. Sun, Y. Sidis, A. Schneidewind, K. Hradil, D. Haug, C. T. Lin, B: Keimer, and V. Hinkov. Normal-state spin dynamics and temperature-dependent spin-resonance energy in optimally doped $BaFe_{1.85}Co_{0.15}As_2$. *Nature Phys.*, 6:178–81, 2010.

[81] Yu. G. Naidyuk, O. E. Kvitnitskaya, N. V. Gamayunova, L. Boeri, S. Aswartham, S. Wurmehl, B. Büchner, D.V. Efremov, G. Fuchs, and S.-L. Drechsler. Single 20meV boson mode in Kfe_2As_2 detected by point-contact spectroscopy. Preprint at arXiv: 1408.1509v1 [cond-mat.supr-con], 2014.

[82] H. Z. Arham and L. H. Greene. Point contact spectroscopy of Fe pnictides and chalcogenides in the normal state. *Curr. Opin. Solid St. M.*, 17:81, 2013.

[83] W.-C. Lee, W. K. Park, H. Z. Arham, L. H. Greene, and P. W. Phillips. Theory of Point Contact Spectroscopy in Correlated Materials. Preprint at arXiv:1405.6357 [cond-mat.str-el], 2014.

[84] R. S. Gonnelli, D. Daghero, D. Delaude, M. Tortello, G. A. Ummarino, V. A. Stepanov, J. S. Kim, R. K. Kremer, A. Sanna, G. Profeta, and S. Massidda. Evidence for gap anisotropy in CaC_6 from directional point-contact spectroscopy. Phys. Rev. Lett., 100:207004, 2008.

[85] A. A. Golubov and I. I. Mazin. Designing phase-sensitive tests for Fe-based superconductors. Appl. Phys. Lett., 102:032601, 2013.

Theory

Chapter 9

How to Distinguish the Mixture of Two D-wave States from Pure D-wave State of HTSC

Peter Brusov and Tatiana Filatova

Additional information is available at the end of the chapter

http://dx.doi.org/10.5772/59180

1. Introduction

The chapter is devoted to the very important problem of the actual symmetry of the order parameter in cuprates, and, more generally, in unconventional superconductors. We adopt the concept of the mixed-order parameter. We calculated collective modes in the $d_{x2-y2} + id_{xy}$ case and found them to differ from those appropriate to the pure situation. The results are useful for both theoretical as well as experimental aspects of the discussed problem.

Several groups have worked in this direction and we can indicate the contributions of Tony Leggett, James Annett, David Pines, Doug Scalapino, and Sasha Balatsky et al. in the theory of the problem and of John Ketterson et al. in its experimental study.

In this chapter we look at collective excitations in unconventional superconductors (USC). This unusual topic was chosen for two reasons: 1) there is no superconductor for which unconventional pairing has been exactly established, while there is some evidence of nontrivial pairing in HFSC and HTSC; 2) the existence of collective excitations in superconductors is questionable.

Within the last couple of decades the situation has drastically changed, collective excitations becoming increasingly important in studies and experiments on USC.

An amplitude mode has been observed in ordinary superconductor films with frequency of order 2Δ. Furthermore, the type of pairing has been established for most superconductors. There is an s-pairing in electron-type HTSC and in ordinary superconductors, a p-pairing in pure ^3He; ^3He in aerogel, Sr_2RuO_4 (HTSC), UPt_3 (HFSC), and d-pairing in hole-type HTSC, organic superconductors, and some HFSC (UPd_2Al_3, $CePd_2Si_2$, $CeIn_3$, $CeNi_2Ge_2$, etc.).

In 2002 a microwave surface-impedance study of the HFSC UBe_{13} demonstrated an absorption peak [16]. The frequency-dependence as well as temperature-dependence of this peak scales

INTECH
open science | open minds

© 2015 The Author(s). Licensee InTech. This chapter is distributed under the terms of the Creative Commons Attribution License (http://creativecommons.org/licenses/by/3.0), which permits unrestricted use, distribution, and reproduction in any medium, provided the original work is properly cited.

with the BCS gap function Δ(T). This means that this was the first direct observation of the resonant absorption into a collective mode (CM). The CM energy turned out to be proportional to the superconducting gap. This was therefore a new page in the study of collective excitations in USC.

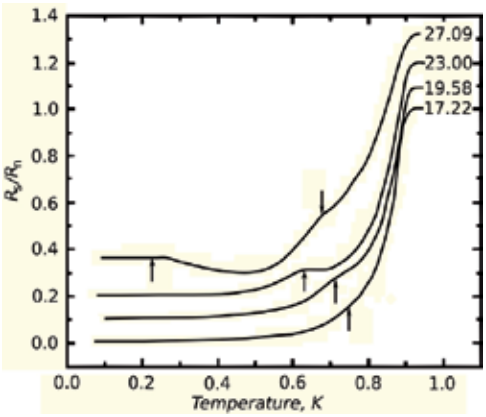

Figure 1. Temperature dependence of surface impedance in heavy-fermion superconductor UBe_{13} [Ref. 16].

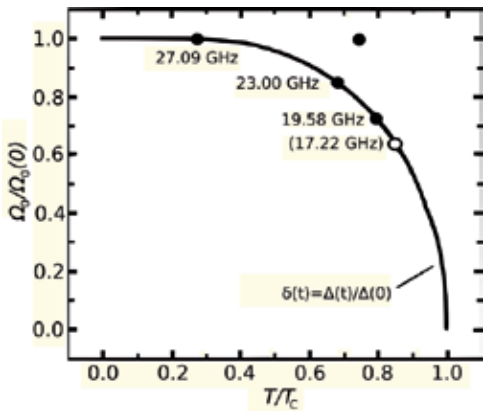

Figure 2. Normalized frequency of collective mode in heavy-fermion superconductor UBe_{13} [Ref. 16]

2. Two d-wave states mixture

As has been shown both experimentally [1] and theoretically, [2, 3] in HTSC a mixing of different d-wave states takes place. The collective-mode spectrum in a mixed $d_{x2-y2}+id_{xy}$ state of HTSC was calculated by Paul Brusov and Peter Brusov [4] for the first time. Within the d-pairing model for superconductive and superfluid Fermi-systems (HTSC, HFSC, etc.) earlier created by Brusov and Brusov within the path integration technique, [5-7] they showed that the spectrum in

http://dx.doi.org/10.5772/59180

mixture $d_{x2-y2}+id_{xy}$ state turns out to be quite different from spectra in both states d_{x2-y2} and d_{xy} in spite of the fact that both spectra are identical. [8, 10] Thus the ultrasound and/or microwave absorption experiments could be used as the probe of the CM spectrum, allowing the pure d-wave states to be distinguished from the mixture of the two d-wave states [18].

While most scientists believe that there is a *d*-wave pairing in HTSC, there is still an active debate over different ideas concerning mixture of *s*- and *d*-states, extended s-wave pairing, and mixture of different *d*-states [18]. The main cause of this is the absence of answers to the question of whether there is an exact-zero gap along some chosen lines in momentum space (as in the case of d_{x2-y2}) or an anisotropic gap that remains nonzero everywhere (except maybe at some points). There is no certain answer to this question that has been yielded by existing experiments (tunnelling, etc.) but the answer is quite principled. However, there are some experiments [1] which, suggesting realization in HTSC in a mixed state like $d_{x2-y2}+id_{xy,}$ could provide an explanation [3]. The possibility of a mixture of different d-wave states in HTSC has been considered by Annett et al., [2] who came to the conclusion that the most likely state is $d_{x2-y2}+id_{xy}$. [18]

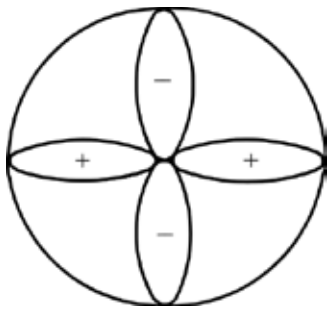

Figure 3. Gap symmetry in pure *d*-wave state (d_{xy} -state).

One possible way to distinguish pure *d*-states from mixture was suggested by Peter Brusov and Pavel Brusov[4], who considered the mixed $d_{x2-y2}+id_{xy}$ state and calculated the spectrum of collective modes in this state. The comparison of the spectrum of a pure d-wave state of HTSC with the spectrum of the mixed $d_{x2-y2}+id_{xy}$ state shows that they are significantly different. This means that they could be used as the probe of the symmetry of the order parameter in HTSC. [18]

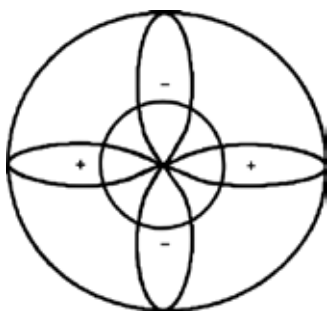

Figure 4. Gap symmetry in the mixed s-wave and d-wave states ($s+id_{xy}$).

3. Collective-Modes Spectrum Equations in a Mixed d-Wave State

3.1. Mixed d-wave-state model

Brusov et al.'s [4] study is generalized here for the case of arbitrary d_{xy}-state admixture. The mixed $(1-\gamma)d_{x^2-y^2} + i\gamma d_{xy}$ state in high-temperature superconductors is considered here and a full set of equations for the collective-modes spectrum in mixed d-wave state with arbitrary admixture of d_{xy}-state is derived.

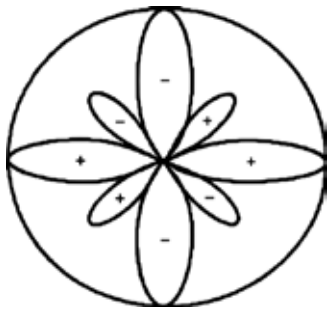

Figure 5. Gap symmetry in the mixed $(1-\gamma)d_{x^2-y^2}+ i\gamma d_{xy}$ state.

We have used the model of *d*-pairing in high-temperature superconductors and HFSC, created by Brusov et al.[5, 11]

It is described by the effective functional of action:

$$S_{\text{eff}} = g^{-1}\sum_{p,i,a} c_{ia}^{+}(p)c_{ia}(p) + \frac{1}{2}\ln\ \det\frac{\hat{M}\left(c_{ia}, c_{ia}^{+}\right)}{\hat{M}\left(c_{ia}^{(0)}, c_{ia}^{(0)+}\right)}, \tag{1}$$

where $c_{ia}^{(0)}$ is the condensate value of Bose-fields c_{ia} (symmetric traceless matrix) and $\hat{M}\left(c_{ia}, c_{ia}^{+}\right)$ is the 4×4 depending on Bose-fields and parameters of quasi-fermions matrix.

In the case of the *d*-pairing the number of degrees of freedom is equal to 10. This means that we have five complex canonical variables:

$$c_1 = c_{11} + c_{22}, c_2 = c_{11} - c_{22}, c_3 = c_{12} + c_{21},$$
$$c_4 = c_{13} + c_{31}, c_5 = c_{23} + c_{32}.$$

The effective action becomes equal to:

$$S_{\text{eff}} = (2g)^{-1}\sum_{p,j} c_j^{+}(p)c_j(p)\left(1+2\delta_{j1}\right) + \frac{1}{2}\ln\ \det\frac{\hat{M}\left(c_j^{+}, c_j\right)}{\hat{M}\left(c_j^{+(0)}, c_j^{(0)}\right)}, \tag{2}$$

http://dx.doi.org/10.5772/59180

where

$$
\begin{aligned}
&M_{11} = Z^{-1}\left[i\omega + \xi - \mu\left(\mathbf{H}\sigma\right)\right]\delta_{p_1 p_2},\\
&M_{22} = Z^{-1}\left[-i\omega + \xi + \mu\left(\mathbf{H}\sigma\right)\right]\delta_{p_1 p_2},\\
&M_{12} = M_{21}^{*} = \left(\beta V\right)^{-1/2}\left(\frac{15}{32\pi}\right)^{1/2}\left[c_1\left(1-3\cos^2\theta\right)+\right.\\
&+ c_2\sin^2\theta\cos 2\varphi + c_3\sin^2\theta\sin 2\varphi +\\
&\left.+ c_4\sin 2\theta\cos\varphi + c_5\sin 2\theta\sin\varphi\right]
\end{aligned}
\tag{3}
$$

here ***H***-magnetic field, $\sigma=(\sigma_1, \sigma_2, \sigma_3)$ – Pauli-matrices, $p=(\mathbf{k}, \omega)$; $\omega=(2n+1)\pi T$ are Fermi-frequencies and $x=(\mathbf{x}, \tau)$, ξ is the kinetic energy with respect to Fermi-level, μ-magnetic moment of quasi-fermion.

All the properties of the model superconducting Fermi-system with *d*-pairing are determined by functional (2).

Let us consider the mixed $(1-\gamma)d_{x^2-y^2} + i\gamma d_{xy}$ state of high-temperature superconductors. The order parameter in this state takes the following form:

$$
\Delta_0\left(T\right)\left[\left(1-\gamma\right)\begin{pmatrix}1 & 0 & 0\\ 0 & -1 & 0\\ 0 & 0 & 0\end{pmatrix} + i\gamma\begin{pmatrix}0 & 1 & 0\\ 1 & 0 & 0\\ 0 & 0 & 0\end{pmatrix}\right] \tag{4}
$$

or in canonical variables:

$$
\Delta_0\left(T\right)\left(0;\left(1-\gamma\right)\sin^2\theta\cos 2\varphi; i\gamma\sin^2\theta\sin 2\varphi; 0; 0\right) \tag{5}
$$

The gap equation has the following form:

$$
g^{-1} + \frac{\alpha^2 Z^2}{2\beta V}\sum_{p}\frac{\sin^4\Theta\left[\gamma^2+\cos^2 2\phi\left(1-2\gamma\right)\right]}{\omega^2+\xi^2+\Delta_0^2\sin^4\Theta\left[\gamma^2+\cos^2 2\phi\left(1-2\gamma\right)\right]} = 0, \tag{6}
$$

where

$\Delta_0=2cZ\alpha$, $\alpha=(15/32\pi)^{1/2}$ and gap

$$
\Delta^2\left(T\right) = \Delta_0^2\sin^4\Theta\left[\gamma^2+\cos^2 2\phi\left(1-2\gamma\right)\right]. \tag{7}
$$

For a limited case of γ=0, we obtain d_{x2-y2} state with order parameter $(0;\sin^2\theta\cos2\phi;0;0;0)$.

The gap equation in this case has the following form:

$$g^{-1}+\frac{\alpha^2Z^2}{2\beta V}\sum_p\frac{\sin^4\Theta\cos^2 2\phi}{\omega^2+\xi^2+\Delta_0^2\sin^4\Theta\cos^2 2\phi}=0 \tag{8}$$

and gap

$$\Delta^2(T)=\Delta_0^2\sin^4\Theta\cos^2 2\phi. \tag{9}$$

For limited case γ=1 one gets d_{xy}-state with order parameter $\Delta_0(T)$ $(0;0;i\sin^2\theta\sin2\phi;0;0)$.

The gap equation has the following form:

$$g^{-1}+\frac{\alpha^2Z^2}{2\beta V}\sum_p\frac{\sin^4\Theta\sin^2 2\phi}{\omega^2+\xi^2+\Delta_0^2\sin^4\Theta\sin^2 2\phi}=0 \tag{10}$$

and gap

$$\Delta^2(T)=\Delta_0^2\sin^4\Theta\sin^2 2\phi \tag{11}$$

Brusov et al.[8] case of equal admixtures of d_{x2-y2} - and d_{xy}-states in our consideration corresponds to the case γ=1/2. The order parameter takes the following form:

$$\Delta_0(T)\left(0;\sin^2\theta\cos2\varphi;i\sin^2\theta\sin2\varphi;0;0\right) \tag{12}$$

The gap equation has the following form:

$$g^{-1}+\frac{\alpha^2Z^2}{2\beta V}\sum_p\frac{\sin^4\Theta}{\omega^2+\xi^2+\Delta_0^2\sin^4\Theta}=0 \tag{13}$$

and gap $\Delta(T)=\Delta_0(T)\sin^2\theta$.

3.2. Equations for collective-modes spectrum in a mixed d-wave state at arbitrary admixture of d_{xy}-state

In the first approximations the spectrum of collective excitations is determined by the quadratic part of S_{eff}, obtained after shift $c_j \rightarrow c_j+c_j^o$. Here c_j^o are the condensate values of c_j of the following form:[5, 11]

http://dx.doi.org/10.5772/59180

$$c_j^0(p) = (\beta V)^{1/2} c\delta_{p0} b_j^0 \text{ and } b_2^0 = 2(1-\gamma), \quad b_3^0 = 2i\gamma$$

with all remaining components of b_j^0 equal to zero.

Excluding terms involving g^{-1} by gap equation, one obtains the following form for the quadratic part of S_h:

$$\begin{aligned} S_H &= \frac{\alpha^2 Z^2}{8\beta V}\sum_p \frac{\left[c^0 Y^*\right]\left[c^{+0} Y\right]}{\omega^2 + \xi^2 + [c^0 Y^*][c^{+0} Y]}\sum_j (1 + 2\delta j1) c_j^+(p) c_j(p) \\ &+ Z^2/4\beta V \sum_{p1+p2=p} \frac{1}{M_1 M_2}\Big\{(i\omega_1 + \xi_1)(i\omega_2 + \xi_2)\Big(\left[c^+(p) Y(p_2)\right] \\ &\left[c(p) Y^*(p_1)\right] + \left[c^+(p) Y(p_1)\right]\left[c(p) Y^*(p_2)\right]\Big) - \Delta^2\left[c^+(p) Y(-p_1)\right] \\ &\left[c^+(-p) Y(-p_2)\right] - \Delta^{+2}\left[c(p) Y^*(-p_1)\right]\left[c(-p) Y^*(-p_2)\right]\Big]\Big\} \end{aligned} \tag{14}$$

Here,

$$\begin{aligned} \left[c Y^*\right] &= c_1(1 - 3\cos^2\theta) + c_2 \sin^2\theta \cos 2\varphi + c_3 \sin^2\theta \sin 2\varphi + \\ &+ c_4 \sin 2\theta \cos\varphi + c_5 \sin 2\theta \sin\varphi. \end{aligned}$$

The quadratic form coefficients are proportional to the sums of the Green's functions of quasi-fermions products. One can go from summation to integration at low temperatures ($T_c - T \sim T_c$) by the following rule:

$$\frac{1}{\beta V}\sum_p \rightarrow \frac{1}{(2\pi)^4}\frac{k_F^2}{c_F}\int d\omega d\xi d\Omega. \tag{15}$$

To evaluate these integrals it is useful to use the Feynman equality:

$$\begin{aligned} &\left[\left(\omega_1^2 + \xi_1^2 + \Delta^2\right)\left(\omega_2^2 + \xi_2^2 + \Delta^2\right)\right]^{-1} = \\ &\int d\lambda\left[\alpha\left(\omega_1^2 + \xi_1^2 + \Delta^2\right) + (1-\lambda)\left(\omega_2^2 + \xi_2^2 + \Delta^2\right)\right]^{-2}. \end{aligned} \tag{16}$$

It is easy to evaluate the integrals with respect to variables ω andξ can also be easy evaluated. Then, they can be evaluated with respect to parameter α and the angular variables.

We obtain the following set of ten equations for the whole spectrum of the collective modes for $(1-\gamma)d_{x^2-y^2} + i\gamma d_{xy}$ state at arbitrary γ after calculating all integrals, except over the angular variables and equating the determinant of the resulting quadratic form to zero:

$$\int_0^1 dx \int d\varphi \Big\{ \frac{\sqrt{\omega^2 + 4\left(1-x^2\right)^2\left[\gamma^2 + \cos^2 2\phi\left(1-2\gamma\right)\right]}}{\omega} \times$$

$$\times \ln \frac{\sqrt{\omega^2 + 4\left(1-x^2\right)^2\left[\gamma^2 + \cos^2 2\phi(1-2\gamma)\right]} + \omega}{\sqrt{\omega^2 + 4\left(1-x^2\right)^2\left[\gamma^2 + \cos^2 2\phi(1-2\gamma)\right]} - \omega} \left(1-3x^2\right)^2 + [\left(1-3x^2\right)^2 -$$

$$-\frac{3}{8}\left(\left(1-3x^2\right)^2 + 3\left(1-x^2\right)^2 \cos^2 2\phi\right)]\ln\left(1-x^2\right)^2\left[\gamma^2 + \cos^2 2\phi\left(1-2\gamma\right)\right] \Big\} = 0$$

$$\int_0^1 dx \int d\varphi \{ \frac{\omega}{\sqrt{\omega^2 + 4\left(1-x^2\right)^2\left[\gamma^2 + \cos^2 2\phi(1-2\gamma)\right]}} \cdot \left(1-3x^2\right)^2 \times$$

$$\times \ln \frac{\sqrt{\omega^2 + 4\left(1-x^2\right)^2\left[\gamma^2 + \cos^2 2\phi\left(1-2\gamma\right)\right]} + \omega}{\sqrt{\omega^2 + 4\left(1-x^2\right)^2\left[\gamma^2 + \cos^2 2\phi(1-2\gamma)\right]} - \omega} + [\left(1-3x^2\right)^2 -$$

$$-\frac{3}{8}\left(\left(1-3x^2\right)^2 + 3\left(1-x^2\right)^2 \cos^2 2\phi\right)]\ln\left(1-x^2\right)^2\left[\gamma^2 + \cos^2 2\phi\left(1-2\gamma\right)\right]\} = 0$$

$$\int_0^1 dx \int d\varphi \{ \frac{\sqrt{\omega^2 + 4\left(1-x^2\right)^2\left[\gamma^2 + \cos^2 2\phi\left(1-2\gamma\right)\right]}}{\omega} \cdot \left(1-x^2\right)^2 \cos^2 2\phi \times$$

$$\times \ln \frac{\sqrt{\omega^2 + 4\left(1-x^2\right)^2\left[\gamma^2 + \cos^2 2\phi\left(1-2\gamma\right)\right]} + \omega}{\sqrt{\omega^2 + 4(1-x^2)^2[\gamma^2 + \cos^2 2\phi(1-2\gamma)]} - \omega} + [\left(1-x^2\right)^2 \cos^2 2\phi -$$

$$-2\left(1-x^2\right)^2 x^2 \cos^2\phi]\ln\left(1-x^2\right)^2\left[\gamma^2 + \cos^2 2\phi\left(1-2\gamma\right)\right]\} = 0$$

$$\int_0^1 dx \int d\varphi \{ \frac{\omega}{\sqrt{\omega^2 + 4\left(1-x^2\right)^2\left[\gamma^2 + \cos^2 2\phi\left(1-2\gamma\right)\right]}} \cdot \left(1-x^2\right)^2 \cos^2 2\phi \times$$

$$\times \ln \frac{\sqrt{\omega^2 + 4\left(1-x^2\right)^2\left[\gamma^2 + \cos^2 2\phi\left(1-2\gamma\right)\right]} + \omega}{\sqrt{\omega^2 + 4\left(1-x^2\right)^2\left[\gamma^2 + \cos^2 2\phi(1-2\gamma)\right]} - \omega} + [\left(1-x^2\right)^2 \cos^2 2\phi -$$

$$-2\left(1-x^2\right)^2 x^2 \cos^2\phi)]\ln\left(1-x^2\right)^2\left[\gamma^2 + \cos^2 2\phi(1-2\gamma)\right]\} = 0$$

$$\int_0^1 dx \int d\varphi \{ \frac{\sqrt{\omega^2 + 4\left(1-x^2\right)^2\left[\gamma^2 + \cos^2 2\phi\left(1-2\gamma\right)\right]}}{\omega} \cdot 4\left(1-x^2\right)^2 x^2 \cos^2\phi \times$$

$$\times \ln \frac{\sqrt{\omega^2 + 4\left(1-x^2\right)^2\left[\gamma^2 + \cos^2 2\phi\left(1-2\gamma\right)\right]} + \omega}{\sqrt{\omega^2 + 4\left(1-x^2\right)^2\left[\gamma^2 + \cos^2 2\phi(1-2\gamma)\right]} - \omega} + [4\left(1-x^2\right)^2 \times$$

$$\times x^2 \cos^2\phi - 2\left(1-x^2\right)^2 x^2 \cos^2\phi]\ln\left(1-x^2\right)^2\left[\gamma^2 + \cos^2 2\phi(1-2\gamma)\right]\} = 0$$

http://dx.doi.org/10.5772/59180

$$\int_0^1 dx \int d\varphi \{ \frac{\omega}{\sqrt{\omega^2 + 4\left(1-x^2\right)^2 \left[\gamma^2 + \cos^2 2\phi\left(1-2\gamma\right)\right]}} \cdot 4\left(1-x^2\right)^2 x^2 \cos^2\phi \times$$

$$\times \ln \frac{\sqrt{\omega^2 + 4\left(1-x^2\right)^2 \left[\gamma^2 + \cos^2 2\phi\left(1-2\gamma\right)\right]} + \omega}{\sqrt{\omega^2 + 4\left(1-x^2\right)^2 \left[\gamma^2 + \cos^2 2\phi\left(1-2\gamma\right)\right]} - \omega} + [4(1-x^2)^2 x^2 \cos^2\phi -$$

$$-2(1-x^2)^2 x^2 \cos^2\phi)] \ln\left(1-x^2\right)^2 \left[\gamma^2 + \cos^2 2\phi\left(1-2\gamma\right)\right] \} = 0$$

$$\int_0^1 dx \int d\varphi \{ \frac{\sqrt{\omega^2 + 4\left(1-x^2\right)^2 \left[\gamma^2 + \cos^2 2\phi(1-2\gamma)\right]}}{\omega} \cdot 4\left(1-x^2\right)^2 x^2 \sin^2\phi \times$$

$$\times \ln \frac{\sqrt{\omega^2 + 4\left(1-x^2\right)^2 \left[\gamma^2 + \cos^2 2\phi\left(1-2\gamma\right)\right]} + \omega}{\sqrt{\omega^2 + 4\left(1-x^2\right)^2 \left[\gamma^2 + \cos^2 2\phi(1-2\gamma)\right]} - \omega} + [4\left(1-x^2\right)^2 x^2 \sin^2\phi -$$

$$-2(1-x^2)^2 x^2 \cos^2\phi] \ln\left(1-x^2\right)^2 \left[\gamma^2 + \cos^2 2\phi\left(1-2\gamma\right)\right] \} = 0$$

$$\int_0^1 dx \int d\varphi \{ \frac{\omega}{\sqrt{\omega^2 + 4\left(1-x^2\right)^2 \left[\gamma^2 + \cos^2 2\phi\left(1-2\gamma\right)\right]}} \cdot 4\left(1-x^2\right)^2 x^2 \sin^2\phi \times$$

$$\times \ln \frac{\sqrt{\omega^2 + 4\left(1-x^2\right)^2 \left[\gamma^2 + \cos^2 2\phi\left(1-2\gamma\right)\right]} + \omega}{\sqrt{\omega^2 + 4\left(1-x^2\right)^2 \left[\gamma^2 + \cos^2 2\phi\left(1-2\gamma\right)\right]} - \omega} + [4\left(1-x^2\right)^2 x^2 \sin^2\phi -$$

$$-2\left(1-x^2\right)^2 x^2 \cos^2\phi)] \ln\left(1-x^2\right)^2 \left[\gamma^2 + \cos^2 2\phi\left(1-2\gamma\right)\right] \} = 0$$

$$\int_0^1 dx \int d\varphi \{ \frac{\sqrt{\omega^2 + 4\left(1-x^2\right)^2 \left[\gamma^2 + \cos^2 2\phi\left(1-2\gamma\right)\right]}}{\omega} \cdot \left(1-x^2\right)^2 \sin^2\phi \times$$

$$\times \ln \frac{\sqrt{\omega^2 + 4\left(1-x^2\right)^2 \left[\gamma^2 + \cos^2 2\phi\left(1-2\gamma\right)\right]} + \omega}{\sqrt{\omega^2 + 4\left(1-x^2\right)^2 \left[\gamma^2 + \cos^2 2\phi\left(1-2\gamma\right)\right]} - \omega} + [\left(1-x^2\right)^2 \sin^2\phi -$$

$$-2\left(1-x^2\right)^2 x^2 \cos^2\phi] \ln\left(1-x^2\right)^2 \left[\gamma^2 + \cos^2 2\phi(1-2\gamma)\right] \} = 0$$

$$\int_0^1 dx \int d\varphi \{ \frac{\omega}{\sqrt{\omega^2 + 4\left(1-x^2\right)^2 \left[\gamma^2 + \cos^2 2\phi\left(1-2\gamma\right)\right]}} \cdot \left(1-x^2\right)^2 \sin^2\phi \times \tag{17}$$

$$\times \ln \frac{\sqrt{\omega^2 + 4\left(1-x^2\right)^2 \left[\gamma^2 + \cos^2 2\phi\left(1-2\gamma\right)\right]} + \omega}{\sqrt{\omega^2 + 4\left(1-x^2\right)^2 \left[\gamma^2 + \cos^2 2\phi(1-2\gamma)\right]} - \omega} + [\left(1-x^2\right)^2 \sin^2\phi -$$

$$-2\left(1-x^2\right)^2 x^2 \cos^2\phi)] \ln\left(1-x^2\right)^2 \left[\gamma^2 + \cos^2 2\phi\left(1-2\gamma\right)\right] \} = 0.$$

We have used the following substitutions: $\cos\theta = x$, $\omega = \omega/\Delta_0$.

The whole spectrum of collective modes in mixed $(1-\gamma)d_{x^2-y^2} + i\gamma d_{xy}$ state of HTSC and arbitrary admixture of d_{xy}-state is determined by equations (17). For interpretation of the sound attenuation and microwave absorption data as well as for identification of the type of pairing and order parameter in unconventional superconductors, knowledge of the collective-mode spectrum could be used. They allow, in particular, evaluation of the extent of admixture of a d_{xy}-state in a mixed state.

Suppose that the dominant state is $d_{x^2-y^2}$-state and admixture of d_{xy}-state is small, say 5–10%; thus, the most interesting case turns out to be the case of small γ. One could in this case expand all expressions in powers of small γ and obtain the corrections to the spectrum of pure $d_{x^2-y^2}$-state, as found previously. [4, 5, 11]

3.3. Equations for collective-modes spectrum in a mixed-d-wave state with equal admixtures of $d_{x^2-y^2}$ - and d_{xy}-states

Brusov et al. [4] supposed equal admixtures of $d_{x^2-y^2}$- and d_{xy}-states – in our consideration this corresponds to the case $\gamma = 1/2$ – and derived the following equations:

$$
\begin{aligned}
&i = 1 \\
&\int_0^1 dx \int d\varphi \left\{ \frac{\sqrt{\omega^2 + 4f}}{\omega} \ln \frac{\sqrt{\omega^2 + 4f} + \omega}{\sqrt{\omega^2 + 4f} - \omega} g_1 + \left(g_1 - \frac{3}{2} f_1 \right) \ln f \right\} = 0 \\
&\int_0^1 dx \int d\varphi \left\{ \frac{\omega}{\sqrt{\omega^2 + 4f}} \ln \frac{\sqrt{\omega^2 + 4f} + \omega}{\sqrt{\omega^2 + 4f} - \omega} g_1 + \left(g_1 - \frac{3}{2} f_1 \right) \ln f \right\} = 0
\end{aligned}
\tag{18}
$$

$$
\begin{aligned}
&i = 2,3,4,5 \\
&\int_0^1 dx \int d\varphi \left\{ \frac{\sqrt{\omega^2 + 4f}}{\omega} \ln \frac{\sqrt{\omega^2 + 4f} + \omega}{\sqrt{\omega^2 + 4f} - \omega} g_i + \left(g_i - \frac{1}{2} g \right) \ln f \right\} = 0 \\
&\int_0^1 dx \int d\varphi \left\{ \frac{\omega}{\sqrt{\omega^2 + 4f}} \ln \frac{\sqrt{\omega^2 + 4f} + \omega}{\sqrt{\omega^2 + 4f} - \omega} g_i + \left(g_i - \frac{1}{2} g \right) \ln f \right\} = 0.
\end{aligned}
\tag{19}
$$

Here,

$$
\begin{aligned}
&g_1 = \left(1 - 3x^2\right)^2; \\
&g_2 = \left(1 - x^2\right)^2 \cos^2 2\varphi; g_3 = g = 4\left(1 - x^2\right) x^2 \cos^2 \varphi; \\
&g_4 = 4\left(1 - x^2\right) x^2 \sin^2 \varphi; g_5 = \left(1 - x^2\right)^2 \sin^2 \varphi, \\
&f_1 = (1/4)\left[\left(1 - 3x^2\right)^2 + 3\left(1 - x^2\right)^2 \cos^2 2\varphi \right]; f = \left(1 - x^2\right)^2.
\end{aligned}
\tag{20}
$$

http://dx.doi.org/10.5772/59180

These equations were solved numerically[4, 11] and the first equations appear to give either Goldstone modes or modes with vanishing energies (of order $0.03\ \Delta_0(T) - 0.08\ \Delta_0(T)$), while five high-frequency modes in each state were obtained from the second equations.

We shall now present results for high-frequency modes (E_i is the energy (frequency) of the i -th branch).

$$\begin{aligned} E_{1,2} &= \Delta_0(T)(1.93 - i\ 0.41); \\ E_3 &= \Delta_0(T)(1.62 - i\ 0.75); \\ E_{4,5} &= \Delta_0(T)(1.59 - i\ 0.83) \end{aligned} \tag{21}$$

Comparison of these results with spectrum of pure $d_{x^2-y^2}$- and d_{xy}-states, obtained by Brusov et al. as follows: [4, 11]

$$\begin{aligned} E_1 &= \Delta_0(T)(1.88 - i\ 0.79); \\ E_2 &= \Delta_0(T)(1.66 - i\ 0.50); \\ E_3 &= \Delta_0(T)(1.40 - i\ 0.68); \\ E_4 &= \Delta_0(T)(1.13 - i\ 0.71); \\ E_5 &= \Delta_0(T)(1.10 - i\ 0.65) \end{aligned} \tag{22}$$

These results led them to conclusion that in spite of the fact that spectra in both pure states, $d_{x^2-y^2}$ and d_{xy}, turn out to be identical, the spectrum in mixed $d_{x^2-y^2}$- and d_{xy}--state is quite different from that in pure states. All modes are non-degenerated in pure states, but two high-frequency modes are twice degenerated in mixed state. The collective modes have higher frequencies in mixed state – from $1.59\ \Delta_0(T)$ up to $1.93\ \Delta_0(T)$, compared to $1.1\ \Delta_0(T)$ up to $1.88\ \Delta_0(T)$ in pure state. In pure d-wave states, damping of collective modes is also bigger than in mixed state (in pure states Im E_i is from 30% to 65% and in mixed state from 20% to 50%). This is because the gap vanishes in pure states along chosen lines while it vanishes just at two points (poles) in mixed state. [4]

Such difference in the spectra of collective modes in pure d -wave states and in mixed d -wave state enables us to probe the symmetry of states using ultrasound and/or microwave absorption experiments. These experiments require high frequencies (in the order of tens of GHz as in the experiment of Feller et al. [16]), but there are no principle restrictions for ultrasound (microwave) frequencies: frequencies of collective modes are proportional to gap $\Delta_0(T)$, and the gap vanishes at T_c, so one could in principle use any frequency approaching T_c.

Note that the case of the $d_{x^2-y^2} + id_{xy}$-state was also considered by Balatsky et al., [17] who studied one of the possible collective modes in this state. They considered a superconducting state with mixed-symmetry-order parameter components, e.g., $d+is$ and $d_{x^2-y^2}+id_{xy}$ and argued for the existence of a new orbital magnetization mode which corresponds to oscillations of relative

phase φ between two components around an equilibrium value of φ = π / 2. The analogue of this mode is the so-called clapping mode of the superfluid A-phase in ^{3}He. The frequency of this mode $\omega_0(B, T)$ depending on the field and temperature for the specific case of magnetic-field-induced d_{xy}-state has been estimated. This mode is tunable with a magnetic field with $\omega_0(B, T) \propto B\Delta_0$, where Δ_0 is the amplitude of gap of the order parameter in d-wave state. The velocity $s(B, T)$ of this mode has been estimated as well.

3.4. $d_{x^2-y^2}$-state of high-temperature superconductors with a small admixture of d_{xy}-state

The whole spectrum of collective modes in mixed $d_{x^2-y^2} + i\varepsilon d_{xy}$ state of HTSC with arbitrary admixture of d_{xy}-state is determined by the above equations (17). For interpretation of the sound attenuation and microwave absorption data as well as for identification of the type of pairing and order parameter in unconventional superconductors knowledge of the collective-mode spectrum could be used. In particular, these experiments allow the estimation in a possible mixed state of the extent of admixture of a d_{xy}-state.

The case of small γ is, however, the most interesting case: one supposes that $d_{x^2-y^2}$-state is the dominant state and the admixture of d_{xy}-state is small, say 3–10%. For this case one can expand all expressions in powers of small γ and obtain the corrections to the equations for the spectrum of pure $d_{x^2-y^2}$-state, which has been found before [11, 13].

Let us consider the case of small admixture of d_{xy}-state (small ε): we suppose that dominant state is $d_{x^2-y^2}$-state and admixture of d_{xy}-state is small, about 3–10%. After expanding of all expressions in powers of small ε we obtain the below corrections.

We use the following notations:

$$\begin{aligned} a &= \left(1 - x^2\right)^2 \cos^2 2\phi; \\ b &= \left(1 - x^2\right)^2 \sin^2 2\phi; \\ a_1 &= a + \omega^2, \end{aligned} \tag{23}$$

Here, we obtain the following expressions:

$$\sqrt{\omega^2 + 4(1-x^2)^2[\cos^2 2\phi + \gamma^2 \sin^2 2\phi]} \approx \sqrt{a_1}\left(1 + \gamma^2 \frac{b}{2a_1}\right) \tag{24}$$

$$\ln f \approx \ln a + \gamma^2 \frac{b}{a} \tag{25}$$

$$\frac{\sqrt{\omega^2 + 4\left(1-x^2\right)^2\left[\cos^2 2\varphi + \gamma^2 \sin^2 2\varphi\right]} + \omega}{\sqrt{\omega^2 + 4\left(1-x^2\right)^2\left[\cos^2 2\varphi + \gamma^2 \sin^2 2\varphi\right]} - \omega} \approx A + \gamma^2 B, \tag{26}$$

http://dx.doi.org/10.5772/59180

where

$$A = \frac{\left(\sqrt{a_1} + \omega\right)^2}{a};$$
$$B = \frac{b}{a^2}\frac{\sqrt{a_1} + \omega}{\sqrt{a_1}}\left[a + \sqrt{a_1}\left(\omega + \sqrt{a_1}\right)\right] \tag{27}$$

$$\ln\frac{\sqrt{\omega^2 + 4\left(1-x^2\right)^2\left[\cos^2 2\phi + \gamma^2 \sin^2 2\varphi\right]} + \omega}{\sqrt{\omega^2 + 4\left(1-x^2\right)^2\left[\cos^2 2\phi + \gamma^2 \sin^2 2\varphi\right]} - \omega} \approx$$
$$\approx \ln\frac{\sqrt{\omega^2 + 4\left(1-x^2\right)^2 \cos^2 2\phi} + \omega}{\sqrt{\omega^2 + 4\left(1-x^2\right)^2 \cos^2 2\phi} - \omega} + \gamma^2 C, \tag{28}$$

where

$$C = \frac{b\left(\sqrt{a_1} + \omega\right)}{\sqrt{a}} + \frac{b}{a}. \tag{29}$$

For other expressions, we obtain, with the accuracy of order γ^2:

$$\frac{\sqrt{\omega^2 + 4\left(1-x^2\right)^2\left[\cos^2 2\varphi + \gamma^2 \sin^2 2\varphi\right]}}{\omega} \times$$
$$\times \ln\frac{\sqrt{\omega^2 + 4\left(1-x^2\right)^2\left[\cos^2 2\varphi + \gamma^2 \sin^2 2\varphi\right]} + \omega}{\sqrt{\omega^2 + 4\left(1-x^2\right)^2\left[\cos^2 2\varphi + \gamma^2 \sin^2 2\varphi\right]} - \omega} \approx$$
$$\frac{\sqrt{\omega^2 + 4\left(1-x^2\right)^2 \cos^2 2\varphi}}{\omega} \ln\frac{\sqrt{\omega^2 + 4\left(1-x^2\right)^2 \cos^2 2\varphi} + \omega}{\sqrt{\omega^2 + 4\left(1-x^2\right)^2 \cos^2 2\varphi} - \omega} + \tag{30}$$
$$+ \frac{\gamma^2}{\omega}\sqrt{a_1}\left(C + \frac{b}{2a_1}\ln\frac{\sqrt{\omega^2 + 4\left(1-x^2\right)^2 \cos^2 2\varphi} + \omega}{\sqrt{\omega^2 + 4\left(1-x^2\right)^2 \cos^2 2\varphi} - \omega}\right);$$

$$\frac{\omega}{\sqrt{\omega^2+4\left(1-x^2\right)^2\left[\cos^2 2\phi+\gamma^2\sin^2 2\phi\right]}}\times$$
$$\times\ln\frac{\sqrt{\omega^2+4\left(1-x^2\right)^2\left[\cos^2 2\phi+\gamma^2\sin^2 2\phi\right]}+\omega}{\sqrt{\omega^2+4\left(1-x^2\right)^2\left[\cos^2 2\phi+\gamma^2\sin^2 2\phi\right]}-\omega}\approx$$
$$\frac{\omega}{\sqrt{\omega^2+4\left(1-x^2\right)^2\cos^2 2\phi+}}\ln\frac{\sqrt{\omega^2+4\left(1-x^2\right)^2\cos^2 2\phi}+\omega}{\sqrt{\omega^2+4\left(1-x^2\right)^2\cos^2 2\phi}-\omega}+ \tag{31}$$
$$+\gamma^2\frac{\omega}{\sqrt{a_1}}\left(C-\frac{b}{2a_1}\ln\frac{\sqrt{\omega^2+4\left(1-x^2\right)^2\cos^2 2\phi}+\omega}{\sqrt{\omega^2+4\left(1-x^2\right)^2\cos^2 2\phi}-\omega}\right).$$

Putting all expressions (23)–(31) into (17) one obtains the whole set of equations for the collective-mode spectrum of mixed $d_{x^2-y^2}+i\varepsilon d_{xy}$ state with small admixture of d_{xy}-state to $d_{x^2-y^2}$-state.

4. Conclusions

In order to solve one of the problems of unconventional superconductivity – the exact form of the order parameter – we consider the mixed $(1-\gamma)d_{x^2-y^2}+i\gamma d_{xy}$ state in HTSC. A full set of equations for the collective-modes spectrum in a mixed d-wave state with an arbitrary admixture of d_{xy}-state has been derived. These equations have been solved for the case of equal admixtures $d_{x^2-y^2}$- and d_{xy}-states by Brusov et al. [4, 11, 14] It has been shown that the difference of collective excitations spectrum in mixed d -wave states and in pure state provide the possibility of probing the symmetry of the state by ultrasound and/or microwave absorption experiments.

The case of small γ is the most interesting case: one supposes that $d_{x^2-y^2}$-state is the dominant state and admixture of d_{xy}-state is small, say 3–10%. In this case all expressions can be expanded in powers of small γ and the corrections to the spectrum of pure $d_{x^2-y^2}$-state, which has been found before, can be obtained. [18]

For identification of the type of pairing and determination of the exact form of the order parameter in unconventional superconductors the results obtained could be quite useful. They allow evaluation of the extent of an admixture of a d_{xy}-state in relation to the spectrum of pure $d_{x^2-y^2}$-state in a possible mixed state. Obtained equations allow the calculation of the whole collective mode. This spectrum could be used for interpretation of the sound attenuation and microwave absorption data. [18]

The results obtained could also allow three quite important questions to be answered: [18]

1. Does the gap disappear along some chosen lines?
2. Is there a pure or mixed d-wave state in HTSC?
3. How huge is the admixture of d_{xy} -state to d_{x2-y2}-state in a possible mixed state?

Author details

Peter Brusov* and Tatiana Filatova

*Address all correspondence to: pnb1983@yahoo.com

Financial University under the Government of Russian Federation, Russia

References

[1] Krishana, K. et al. (1997), Science 277, 83.

[2] Annett, J. F., Goldenfeld, N. D. and Leggett, A. J. (1996), In: Physical Properties of High Temperature Superconductors V, ed. D. M. Ginsberg (World Scientific, Singapore).

[3] Laughlin, R. B. (1998), Phys. Rev. Lett. 80, 5188.

[4] Brusov, P., and P. Brusov (2000), Physica B, 281&282, 949.

[5] Brusov, P. N., Brusova, N. P. (1994), Physica B 194–196, 1479.

[6] Brusov. P. N., Brusova, N. P. (1996), J. Low Temp. Phys., 101, 1003.

[7] Brusov, P. N., Brusova, N. P. and Brusov, P. P. (1996), Czechoslovak Journal of Physics, 46, suppl. s2, 1041.

[8] Brusov, P. N., Brusova, N. P. Brusov, P.P. (1997), J. Low Temp. Phys. 108, 143; Physica B 259–261, 496 (1999).

[9] Brusov, P. N., Brusova, N. P., Brusov, P. P., Harabaev, N. N. (1997), Physica C 282–287, 1881.

[10] Brusov, P. N., Brusova, N. P., Brusov, P. P. (1996), Fiz. Nizk. Temp. 22, 506 [Low Temp. Phys., 22, 389].

[11] Brusov, P. N. (1999), Mechanisms of High Temperature Superconductivity, v.1, 2; Rostov State University Publishing, p. 1389.

[12] Brusov, P. N., Brusov, P.P. (2001), "Collective properties of superconductors with nontrivial pairing", Sov. Phys. JETP, 119, 913–930 [Zh. Eksp. Theor. Phys. v.92, p. 795].

[13] Brusov, P. N., Brusova, N. P. and Brusov, P. P. (1997), The collective excitations of the order parameter in HTSC and heavy fermion superconductors (HFSC) under d-pairing. J. Low Temp. Phys. 108, 143.

[14] Brusov P., Brusov, Majumdar, P. and Orehova, N. (2003), "Ultrasound attenuation and collective modes in mixed $d_{x2-y2}+d_{xy}$ state of unconventional superconductors", Brazilian Journal of Physics, 33, 729–732.

[15] Brusov, P., Brusov, P. and Lee, C. (2004), Collective properties of unconventional superconductors, Int. J. Mod. Phys. B, v.18, 867–882.

[16] Feller J. R., Tsai, C. C., Ketterson, J. B. et al. (2002), Phys. Rev. Lett. 88, 247005.

[17] Balatsky, A. V., Kumar, P. and Schrieffer, J. R. (2000), Phys. Rev. Lett. 84, 4445.

[18] Brusov, P., Brusov, P. (2009) Collective Excitations in Unconventional Superconductors and Superfluids, pp. 860, World Scientific Publishing, Singapore

Chapter 10

Measurements of Stationary Josephson Current between High-T_c Oxides as a Tool to Detect Charge Density Waves

Alexander M. Gabovich, Mai Suan Li,
Henryk Szymczak and Alexander I. Voitenko

Additional information is available at the end of the chapter

http://dx.doi.org/10.5772/59590

1. Introduction

Since an unexpected and brilliant discovery of high-T_c superconductivity in cuprates in 1986 [8], experts have been trying to find the origin of superconductivity in them, but in vain. There are several problems that are interconnected and probably cannot be solved independently. But they are so complex that researchers are forced to consider them separately in order to find the key concepts and express key ideas explaining the huge totality of experimental data. General discussion and the analysis of high-T_c-oxide superconductivity can be found in comprehensive reviews [21, 25, 42, 50, 53, 65, 73, 75, 78, 80, 86, 89, 104]. In particular, the main questions to be solved are as follows: (i) Is superconductivity in cuprates a conventional one based on the Cooper pairing concept? (ii) If the answer to the first question is positive, what is the mechanism of superconductivity, i.e., what are the virtual bosons that glue electrons in pairs? (iii) Which is the symmetry of the superconducting order parameter? This question remains unanswered, although the majority of the researchers in the field think believe that the problem is already resolved (namely, $d_{x^2-y^2}$-one, see, e.g., Refs. [54, 90])? (iv) What is the role of the intrinsic disorder and non-stoichiometry in the superconducting properties [2, 28, 43, 69, 70, 75, 103, 105]? (v) What is the origin of the symmetry loss and, specifically, the emerging nematicity [28, 58, 70, 75, 88, 103]? (vi) What is the origin of the so-called pseudogap [42, 68, 75, 94, 98, 104]? (vii) What is the role of spin- and charge- density waves (SDWs and CDWs) both in the normal and superconducting states of cuprates? The role of various electron spectrum instabilities competing with the Cooper pairing below the critical temperature T_c is a part of the more general problem: How can certain anomalous high-T_c oxide properties above T_c be explained, e.g., the linear behavior of the resistivity [66, 91]? In this connection, a quite reasonable viewpoint was expressed that if one understands the normal state of cuprates, the superconducting state properties will be perceived [42, 46]. Here, it is also worth to mention a possible failure [91, 92] of the

INTECH
open science | open minds

© 2015 The Author(s). Licensee InTech. This chapter is distributed under the terms of the Creative Commons Attribution License (http://creativecommons.org/licenses/by/3.0), which permits unrestricted use, distribution, and eproduction in any medium, provided the original work is properly cited.

Fermi liquid concept belonging to Landau [1] and the role of strong electron correlations [18, 48, 61, 62].

During last decades we have been developing a phenomenological theory to elucidate the influence of CDWs on superconductivity of high-T_c oxides, since the CDWs were observed in a number of those materials [23, 33, 35, 37–39]. We identified the CDW energy gap with the pseudogap mentioned above. Such an identification is based, in particular, on the appearance of CDWs only below the approximate border of the pseudogapped region in $La_{2-x}Sr_xCuO_4$ [14] and $YBa_2Cu_3O_{7-\delta}$ [5, 45]. Moreover, the symmetry of the pseudogap order parameter (isotropic) differs from that for the superconducting one ($d_{x^2-y^2}$) in $Bi_2Sr_2CaCuO_{8+\delta}$ [79], superconductivity in $Bi_2Sr_{2-x}La_xCuO_{6+\delta}$ emerges with doping when the (nodal) pseudogap disappears [72], the pseudogap competes with the superconducting gap at antinodes in $(Bi,Pb)_2(Sr,La)_2CuO_{6+\delta}$ [43], and the interplay of pseudogapping and superconductivity among different members of the oxide family $(Ca_xLa_{1-x})(Ba_{1.75-x}La_{0.25+x})Cu_3O_y$ is not the same for varying dopings x [15]. It is worthy of note that both angle-resolved photoemission spectroscopy (ARPES) and scanning tunnel microscopy (STM) experiments allow one to measure only overall energy gaps whatever their microscopic origin. That is why it is usually difficult to distinguish for sure between superconducting, SDW, and CDW gaps even in the case when they manifest themselves separately in certain momentum ranges each [11, 42].

As for direct experiments confirming the existence of CDWs competing with superconductivity in cuprates, CDWs have been shown to be a more important factor in this sense than SDWs, the remnants of which survive far from the antiferromagnetic state appropriate to zero-doped samples of superconducting families [20]. It is useful to shortly summarize the main new findings in this area.

X-ray scattering experiments in $YBa_2Cu_3O_{6+x}$ revealed the CDW ordering at temperatures lower than those of the pseudogap formation, giant phonon anomalies, and elastic central peak induced by nanodomain CDWs [9, 10, 45, 59]. The CDW correlation length increases with the temperature, T, lowering. However, the competing superconducting order parameter, which emerges below T_c, so depresses CDWs that the true CDW long-range order does not develop, as was shown by Raman scattering [5]. Suppression of CDWs by Cooper pairing was also found in x-ray measurements of $La_{2-x}Sr_xCuO_4$ [14].

The well-known CDW manifestations in $Bi_2Sr_{2-x}La_xCuO_{6+\delta}$ were recently confirmed by complex X-ray, ARPES, and STM studies [13]. Those authors associate CDWs with pseudogapping, but argue that the CDW wave vector connects the Fermi arc tips rather than the antinodal Fermi surface (FS) sections, as stems from the Peierls-insulator scenario [27, 41]. This conclusion, if being true, makes the whole picture even more enigmatic than in the conventional density-wave approach to pseudogaps either in the mean-field approximation or taking into account fluctuations.

The electron-hole asymmetric CDW ordering was demonstrated by STM and resonant elastic x-ray scattering measurements [17] for $Bi_2Sr_2CaCuO_{8+\delta}$ samples, with the pseudogapping in the antinodal momentum region. As was shown in those experiments, CDWs and concomitant periodic crystal lattice distortions, PLDs can be observed directly, whereas their interplay with superconductivity manifestations can be seen only indirectly, e.g., as anticorrelations between T_c and the structural, T_s, or CDW, T_{CDW}, transition temperature.(There is a viewpoint [19] that the strong interrelation between electronic CDW modulations and PLDs [27], inherent, e.g., to the Peierls model of the structural phase transition [41], does not exist, and PLDs can emerge without electronic contributions,

http://dx.doi.org/10.5772/59590

which seems strange in the context of indispensable Coulomb forces.). This fact is well known, say, for superconducting transition metal dichalcogenides [49] or pseudoternary systems $(Lu_{1-x}Sc_x)_5Ir_4Si_{10}$ [102]. Therefore, it seems interesting to propose such studies of superconducting properties, which would demonstrate manifestations of CDW existence, although the CDW gapping is an insulating rather than a superconducting one. In a number of publications, we suggested that certain measurements of the stationary Josephson critical current, I_c, between quasi-two-dimensional CDW superconductors with the $d_{x^2-y^2}$ order parameter symmetry (inherent to cuprates) can conspicuously reveal such dependences that would reflect CDW gapping as well or at least demonstrate that the actual gapping symmetry differs from the pure $d_{x^2-y^2}$ one [29–31, 34, 35]. Below, we present further theoretical studies in this direction, which put forward even more effective experiments.

2. Formulation

Following the dominating idea (see our previous publications [29–31, 34, 35, 95, 96] and references therein) concerning the electron spectrum of high-T_c oxides identified as partially gapped CDW superconductors, CDWSs, we restrict our consideration to the two-dimensional case with the corresponding FS shown in Fig. 1a. The superconducting d-wave order parameter Δ is assumed to span the whole FS, whereas the s-wave mean-field dielectric (CDW) order parameter Σ develops only on the nested (dielectrized, d) FS sections. There are $N = 4$ or 2 of the latter (the checkerboard and unidirectional configurations, respectively), and they are connected in pairs by the CDW-vectors $\mathbf{Q}$'s in the momentum space. The non-nested sections remain non-dielectrized (nd). The orientations of $\mathbf{Q}$'s are assumed to be fixed with respect to the crystal lattice. In particular, they are considered to be directed along the $\mathbf{k}_x$- and $\mathbf{k}_y$-axes in the momentum space (anti-nodal nesting) [39, 67, 74]. The same orientation along $\mathbf{k}_x$- and $\mathbf{k}_y$-axes is also appropriate to Δ-lobes, so that we confine ourselves to the $d_{x^2-y^2}$-wave symmetry of the superconducting order parameter as the only one found in the experiments for cuprates. Hence, the profile of the d-wave superconducting order parameter over the FS is written down in the form

$$\bar{\Delta}(T,\theta) = \Delta(T) f_\Delta(\theta). \tag{1}$$

The function $\Delta(T)$ is the T-dependent magnitude of the superconducting gap, and the angular factor $f_\Delta(\theta)$ looks like

$$f_\Delta(\theta) = \cos 2\theta. \tag{2}$$

In the case $N = 4$, the experimentally measured magnitudes of the CDW order parameter Σ in high-T_c oxides are identical in all four CDW sectors, and the corresponding sector-connecting $\mathbf{Q}$ vectors are oriented normally to each other. Therefore, we assume the CDWs to possess the four- (the checkerboard configuration) or the two-fold (the unidirectional configuration) symmetry [3, 23, 24, 30, 39, 44, 93]. The latter is frequently associated with the electronic nematic, smectic or more complex ordering [16, 22, 26, 28, 52, 70, 83, 84, 88, 97, 99, 100]). The opening angle of each CDW sector, where $\Sigma \neq 0$, equals 2α. Such a profile of Σ over the FS can also be described in the factorized form

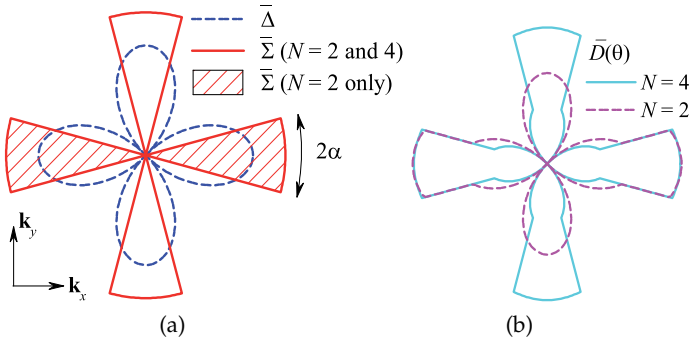

Figure 1. (a) Superconducting, $\bar{\Delta}(\theta)$, and dielectric, $\bar{\Sigma}(\theta)$, order parameter profiles of the partially gapped d-wave charge-density-wave (CDW) superconductor. N is the number of CDW sectors with the width 2α each. (b) The corresponding energy-gap contours (gap roses).

as

$$\bar{\Sigma}(T,\theta) = \Sigma(T) f_{\Sigma}(\theta), \tag{3}$$

where $\Sigma(T)$ is the T-dependent CDW order parameter, and the angular factor

$$f_{\Sigma}(\theta) = \begin{cases} 1 \text{ for } |\theta - k\Omega| < \alpha \text{ (d section)}, \\ 0 \text{ otherwise} \qquad\quad \text{(nd section)}. \end{cases} \tag{4}$$

Here, k is an integer number, and the parameter $\Omega = \pi/2$ for $N = 4$ and π for $N = 2$.

The both gapping mechanisms (superconducting and CDW-driven) suppress each other, because they compete for the same quasiparticle states near the FS. As a result, a combined gap (the gap rose in the momentum space, see Fig. 1b)

$$\bar{D}(T,\theta) = \sqrt{\bar{\Sigma}^2(T,\theta) + \bar{\Delta}^2(T,\theta)}, \tag{5}$$

arises on the FS. The actual $\Delta(T)$- and $\Sigma(T)$-values are determined from a system of self-consistent equations. The relevant initial parameters, besides N and α, include the constants of superconducting and electron-hole couplings recalculated into the pure BCS (no CDWs) and CDW (no superconductivity) limiting cases as the corresponding Δ_0 and Σ_0 order parameters at $T = 0$. It should be emphasized that our model is a simplified, generic one, because real CDWs are complex objects, which behave differently on the crystal surfaces and in the bulk [77]. Thus, it is quite natural that they are not identical for various high-T_c oxides [15]. Nevertheless, the presented model allows the main features of the materials concerned to be taken into account. For brevity, we mark the CDW d-wave superconductor with N CDW sectors as $S^d_{\mathrm{CDW}N}$.

http://dx.doi.org/10.5772/59590

The s-wave BCS superconductor is described in the framework of the standard BCS theory. Its characteristic parameter is the value of the corresponding superconducting order parameter Δ_{BCS} at $T = 0$. Also for the sake of brevity, it will be marked below as S^s_{BCS}.

In the tunnel Hamiltonian approximation, the stationary Josephson critical current is given by the formula [7, 57, 85]

$$I_c(T) = 4eT\sum_{\mathbf{pq}}\left|\widetilde{T}_{\mathbf{pq}}\right|^2\sum_{\omega_n}\mathsf{F}^{+}(\mathbf{p};\omega_n)\mathsf{F}'(\mathbf{q};-\omega_n). \tag{6}$$

Here, $\widetilde{T}_{\mathbf{pq}}$ are the tunnel Hamiltonian matrix elements, $\mathbf{p}$ and $\mathbf{q}$ are the transferred momenta; $e > 0$ is the elementary electrical charge, and $\mathsf{F}(\mathbf{p};\omega_n)$ and $\mathsf{F}'(\mathbf{q};-\omega_n)$ are Gor'kov Green's functions for superconductors to the left and to the right, respectively, from the tunnel barrier (hereafter, all primed quantities are associated with the right hand side electrode). The internal summation is carried out over the discrete fermionic "frequencies" $\omega_n = (2n+1)\,\pi T$, $n = 0, \pm1, \pm2, \ldots$. Below, we consider tunnel junctions of two types: symmetric $S^d_{\mathrm{CDW}N} - I - S^d_{\mathrm{CDW}N}$ between two identical CDWSs, and nonsymmetric $S^d_{\mathrm{CDW}N} - I - S^s_{\mathrm{BCS}}$ between a CDWS as the left electrode and an s-wave BCS superconductor as the right one (here, I stands for the insulator). Expressions for the corresponding Green's functions can be found elsewhere [30, 35]. Since CDWS electrodes are anisotropic, their orientations with respect to the junction plane will be characterized by the angles γ and γ' (the latter appears only in the symmetric case), i.e. the deflections of the "positive" Δ- and Δ'-lobes from the normal $\mathbf{n}$ to the junction (Fig. 2). Accordingly, the angular dependences $f_\Delta(\theta)$ and $f_\Sigma(\theta)$ of the corresponding order parameters (see formulas (2) and (4, respectively) should be modified by changing θ to $\theta - \gamma$ or $\theta - \gamma'$.

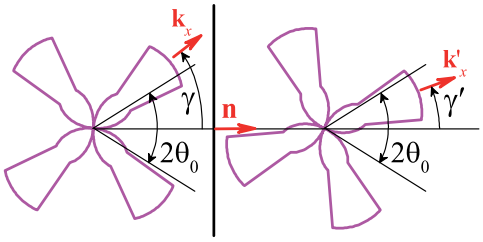

Figure 2. Configuration of symmetric Josephson junction between identical S^d_{CDW4}'s. See further explanations in the text.

An important issue while calculating the Josephson current is tunnel directionality [101], which should be taken into consideration in the tunnel Hamiltonian $\widetilde{T}_{\mathbf{pq}}$. Indeed, if we calculate I_c between, e.g., pure BCS d-wave superconductors, S^d_{BCS}, making no allowance for this factor, formula (6) would produce an exact zero. It is so because, owing to the alternating signs of superconducting lobes, the current contributions from the FS points described by the angles θ and $\theta + \dfrac{\pi}{2}$ would exactly compensate each other in this case. The same situation also takes place in the case of a junction with S^d_{CDW4}. For a junction with S^d_{CDW2}, it is not so, but, in the framework of the general approach, we have to introduce tunnel directionality in this case as well.

Here, we briefly consider three factors responsible for tunnel directionality (see a more thorough discussion in Ref. [31]). First, the velocity component normal to the junction should be taken into account. This circumstance is reflected by the $\cos\theta$-factor in the integrand and an angle-independent factor that can be incorporated into the junction normal-state resistance R_N [51, 64]. Second, superconducting pairs that cross the barrier at different angles penetrate through barriers with different effective widths [12] (the height of the junction barrier is assumed to be much larger than the relevant quasiparticle energies, so that this height may be considered constant). Since the actual θ-dependences of $\widetilde{T}_{\mathbf{pq}}$ for realistic junctions are not known, we simulate the barrier-associated directionality by the phenomenological function

$$w(\theta) = \exp\left[-\left(\frac{\tan\theta}{\tan\theta_0}\right)^2 \ln 2\right], \tag{7}$$

This means that the effective opening of relevant tunnel angles equals $2\theta_0$. The barrier transparency is normalized by the maximum value obtained for the normal tunneling with respect to the junction plane and included into the junction resistance R_N. Hence, $w(\theta = 0) = 1$. The multiplier $\ln 2$ in (7) was selected to provide $w(\theta = \theta_0) = \frac{1}{2}$. Third, we use the model of coherent tunneling [12, 56, 60], when the superconducting pairs are allowed to tunnel between the points on the FSs of different electrodes characterized by the same angle θ.

As a result of the standard calculation procedure [7, 57] applied to formula (6) and in the framework of the approximations made above, we obtain the following formula for the stationary Josephson critical current across the tunnel junction:

$$I_c(T,\gamma,\gamma') = \frac{1}{2eR_N} \times \frac{1}{\pi}\int_{-\pi/2}^{\pi/2} \cos\theta\; w(\theta)\; P(T,\theta,\gamma,\gamma')\mathrm{d}\theta, \tag{8}$$

where [32, 40]

$$P(T,\theta,\gamma,\gamma') = \bar{\Delta}\bar{\Delta}' \int\limits_{\min\{\bar{D},\bar{D}'\}}^{\max\{\bar{D},\bar{D}'\}} \frac{\tanh\frac{x}{2T}\mathrm{d}x}{\sqrt{(x^2-\bar{D}^2)\,(\bar{D}'^2-x^2)}}. \tag{9}$$

Here, for brevity, we omitted the arguments in the dependences $\bar{\Delta}(T,\theta-\gamma)$, $\bar{\Delta}'(T,\theta-\gamma')$, $\bar{D}(T,\theta-\gamma)$, and $\bar{D}'(T,\theta-\gamma')$. Integration over θ in Eq. (8) is carried out within the interval $-\frac{\pi}{2} \le \theta \le \frac{\pi}{2}$, i.e. over the "FS semicircle" turned towards the junction plane. If any directionality and CDW gapping are excluded (so that the integration over θ is reduced to a factor of π) and the angular factors f_Δ and f'_Δ remain preserved, we arrive at the Sigrist–Rice model [81].

http://dx.doi.org/10.5772/59590

3. Results and their discussion

The influence of various problem parameters on the critical stationary Josephson curent in the symmetric, $S^d_{\mathrm{CDW}N} - I - S^d_{\mathrm{CDW}N}$, and nonsymmetric, $S^d_{\mathrm{CDW}N} - I - S^s_{\mathrm{BCS}}$, junctions was analyzed in detail in works [30, 31]. Here, we attract attention to the problem of CDW detection in high-T_c oxides.

The number of problem parameters can be diminished by normalizing the "order parameter" quantities by one of them. For such a normalization, we selected the parameter Δ_0 and introduced the dimensionless order parameters $\sigma_0 = \Sigma_0/\Delta_0$ and $\delta_{\mathrm{BCS}} = \Delta_{\mathrm{BCS}}(T \to 0)/\Delta_0$ (for the superconducting order parameter of CDWS, $\delta_0 = \Delta_0/\Delta_0 = 1$). With regard to experimental needs, we also introduced the reduced temperature $\tau = T/T_c$. Here T_c is the actual critical temperature of the CDWS. In the framework of our theory, it has to be found from the system of equations for the CDWS indicated above. For the Josephson current amplitude I_c, we introduced the dimensionless combination $i_c = I_c e R_N/\Delta_0$.

One more preliminary remark concerns the parameter of effective tunnel directionality θ_0 (see formula (7)). Our calculations [30, 31] showed that its choice is very important. On the one hand, large values of this parameter correspond to thin junctions and large values of the tunnel current, which is beneficial for the experiment. However, in this case, the predicted phenomena become effectively smoothed out up to their disappearance. On the other hand, narrow tunnel cones (small θ_0-values) provide well pronounced effects, but correspond to thick interelectrode layers and, as a result, small tunnel currents. Hence, in the real experiment, a reasonable compromise should be found between those two extremes.

3.1. Electrode rotation

While examining Fig. 2, it becomes clear that the clearest way to prove that electrons in high-T_c oxides undergo an additional pairing of some origin besides the d-wave BCS one is to demonstrate that the gap rose differs from that in the S^d_{BCS} superconductor. The case in question concerns pairing symmetries, which may be different from the d-wave one or/and extend over only certain FS regions. In the framework of the tunnel technique, the most direct way to perform the search is to fix one electrode and rotate the other one (e.g., $\gamma' = \mathrm{const}$ and $\gamma = \mathrm{var}$). In the case of $S^d_{\mathrm{BCS}} - I - S^d_{\mathrm{BCS}}$ junction, the corresponding $i_c(\gamma)$ dependences are known to have a cosine profile stemming from dependence (2) for the superconducting order parameter Δ and, since any other gapping is absent, for the corresponding gap rose ($\tilde{D}(T,\theta) = |\Delta(T,\theta)|$). Any deviations of the gap rose from this behavior will testify in favor of the existence of additional order parameter(s). Certainly, averaging the current over the FS will smooth the relevant peculiarities and making allowance for tunnel directionality will distort them. Nevertheless, the proposed method will be sufficient to detect the competing pairing without its ultimate identification.

In Fig. 3, the corresponding normalized $i_c(\gamma)$ dependences calculated for the symmetric $S^d_{\mathrm{CDW}N} - I - S^d_{\mathrm{CDW}N}$ junction and the CDW geometries $N = 2$ and 4, as well as the reference d-wave BCS curve, are shown. The tunnel directionality parameter $\theta_0 = 10^\circ$ was assumed. A more detailed analysis of $i_c(\gamma)$ dependences and their relations with other problem parameters can be found in work [30]. The results obtained testify that the formulated task is feasible. An attractive feature of this technique is that, instead of the fixed $S^d_{\mathrm{CDW}N}$ electrode, we may use the S^s_{BCS} one as well, which might be more convenient from the experimental point of view.

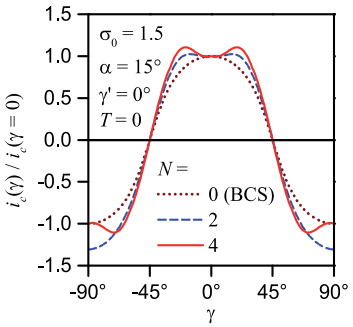

Figure 3. Orientation dependences of the reduced critical Josephson current for the symmetric junction.

3.2. Anomalous temperature dependence of I_c

The measurement of the temperature dependences of the critical Josephson tunnel current $I_c(T)$ seems to be the most easily realizable method of those proposed in this work. The dependence $I_c(T)$ in the symmetric $S^s_{\rm BCS} - I - S^s_{\rm BCS}$ junctions has a monotonic convex shape. Among other things, this fact is associated with the constant sign of order parameter over the whole FS. However, in the case of symmetric $S^d_{\rm BCS} - I - S^d_{\rm BCS}$ junctions, the situation may change. Indeed, for junctions involving $YBa_2Cu_3O_{7-\delta}$, nonmonotonic $I_c(T)$-dependences and even the change of I_c sign, i.e. the transformation of the 0-junction into the π-one or vice versa were observed [47, 87]. Such a phenomenon was not found for other cuprates. However, it is extremely difficult to produce Josephson junctions made of other materials than $YBa_2Cu_3O_{7-\delta}$. Therefore, further technological breakthrough is needed to make sure that the non-monotonic behavior is a general phenomenon inherent to all high-T_c oxides with d-wave superconducting order parameter.

It should be noted that, in the measurements concerned, the electrodes remained fixed, so that the peculiar behavior of $I_c(T)$ could not result from the change of overlapping between the superconducting lobes with different signs. There is an explanation based on the existence of the bound states in the junction due to the Andreev–Saint-James effect [51, 64]. This theory predicts that the current $I_c(T)$ between d-wave superconductors must exhibit a singularity at $T \to 0$. Nevertheless, the latter has not been observed experimentally until now. Probably, this effect is wiped out by the roughness of the interfaces in the oxide junctions [6, 76] and therefore may be of academic interest.

Earlier we suggested a different scenario [36]. Namely, we showed that, at some relative orientations of $S^d_{\rm BCS} - I - S^d_{\rm BCS}$ junction electrodes, one of them can play a role of differential detector, which enables tiny effects connected with the thermally induced repopulation of quasiparticle levels near the FS to be observed. In our approach, no zero-T singularity of the current could arise.

A similar situation takes place for CDWSs. Although we cannot assign a definite sign to the combined gap $\bar{D}$ (see Eq. (5), the corresponding unambiguously signed Δ enters the expression for the calculation of I_c (formulas (8) and 9). In this sense, the FS of the CDWS "remembers" the specific Δ-sign at every of its points and, thus, can also serve as a differential detector of the current at definite electrode orientations. As a result, the dependences $I_c(T)$

both for symmetric $S^d_{\mathrm{CDW}N} - I - S^d_{\mathrm{CDW}N}$ and nonsymmetric $S^d_{\mathrm{CDW}N} - I - S^d_{\mathrm{BCS}}$ junctions can also by nonmonotonic and even sign-changing functions. Unlike the $S^d_{\mathrm{BCS}} - I - S^d_{\mathrm{BCS}}$ junctions, for which the $I_c(T)$-behavior could depend only on the orientation angles of both electrodes (γ and γ'), now the other parameters responsible for the superconducting and combined gaps—these are σ_0 and α—become relevant. In Figs. 4 and 5, the $i_c(\tau)$ dependences are shown for various fixed α and σ_0, respectively, both for the "checkerboard" and "unidirectional" CDW geometry. We would like to attract attention to the fact that those dependences are rather sensitive to the electrode orientations (see the relevant illustration in Fig. 6), so that it might be laborious to find a suitable experimental configuration.

The key issue is that the parameters σ_0 and/or α can be (simultaneously) varied by doping. Hence, doping CDWS electrodes and keeping their orientations fixed, we could change even the character of the $I_c(T)$ dependence: monotonic, nonmonotonic, and sign-changing. Provided the corresponding set of parameters, we could transform the same junction, say, from the 0-state into the π-one by varying the temperature only.

3.3. Anomalous doping dependence of I_c

Now, let the electrode orientations be fixed by the experimentalist [55, 82] and the temperature be zero (for simplicity), but the both parameters α and σ_0 can be varied (by doping). In Figs. 7 and 8, the dependences of the dimensionless order parameters $\delta(0) = \Delta(T = 0)/\Delta_0$ and $\sigma(0) = \Sigma(T = 0)/\Delta_0$ on α and σ_0 are exhibited for both analyzed CDW structures. One can see that, in every cross-section $\alpha = \mathrm{const}$ or $\sigma_0 = \mathrm{const}$, both $\delta(0)$ and $\sigma(0)$ profiles are monotonic. At first glance, the Josephson tunnel current should also demonstrate such a behavior. However, our previous calculations [30, 31, 35] showed that it is so when the orientations of $S^d_{\mathrm{CDW}N}$ electrodes in the $S^d_{\mathrm{CDW}N} - I - S^d_{\mathrm{CDW}N}$ junction are close or rotated by about 90° with respect to each other, i.e. when the superconducting lobes strongly overlap in the momentum space and make contributions of the same sign to the current. But if they are oriented in such a way that mutually form a kind of differential detector for monitoring the states at the gapped and non-gapped FS sections, contributions with different signs cancel each other and more tiny effects become observable. Such a conclusion can already be made from Figs. 4 and 5.

Really, as is illustrated by Figs. 7 and 8, in the limiting cases—$\sigma_0 \to \infty$ for both kinds of CDWs, and, if $\sigma_0 \geq \sqrt{\mathrm{e}}/2 \approx 0.824$ (here, e is the Euler constant), $\alpha \to \pi/4$ at $N = 4$ or $\pi/2$ at $N = 2$ [24]—we have $\delta(0) \to 0$. Then, according to formulas (8) and 9), I_c also vanishes. Therefore, if the current crosses the point $i_c = 0$ at some values of parameters α or σ_0 different from their limiting ones, (i) the current behavior becomes nontrivial, because larger values of α and σ_0, which are accompanied by smaller values of the superconducting order parameter δ, lead to the current enhancement. Nevertheless, as α or σ_0 grows further towards its corresponding limiting values, the current must sooner or later begin to decrease by the absolute value.

This conclusion is confirmed by Figs. 9 and 10, where the dependences $i_c(\sigma_0, \alpha = \mathrm{const})$ and $i_c(\alpha, \sigma_0 = \mathrm{const})$ at $T = 0$ are shown. While analyzing those figures, the following consideration should be taken into account. Namely, we suppose that gradual doping monotonically affects the parameters α and σ_0 of $S^d_{\mathrm{CDW}N}$ superconductors. Specific calculations (Figs. 9 and 10) were made assuming that only one of the control parameters, α

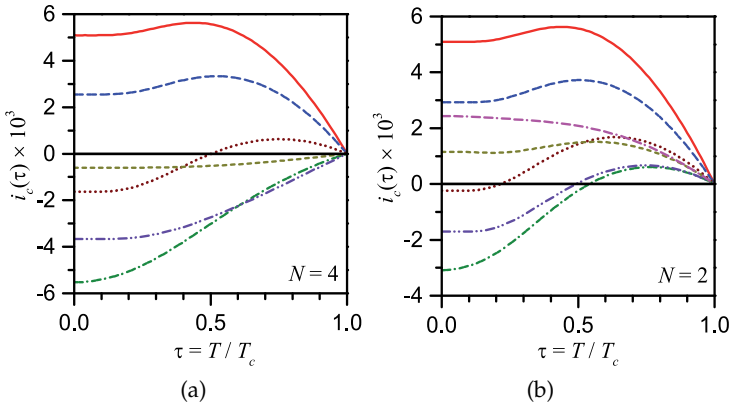

Figure 4. Temperature dependences of the Josephson current for various numbers of CDW sectors $N = 4$ (a) and 2 (b), and their widths $\alpha = 0$ (solid), 5 (dashed), 10 (dotted), 15 (dash-dotted), 20 (dash-dot-dotted), 25 (short-dashed), and 30° (dash-dash-dotted). $\sigma_0 = 1.3$, $\gamma = 15°$, $\gamma' = 45°$, $\theta_0 = 10°$. See further explanations in the text.

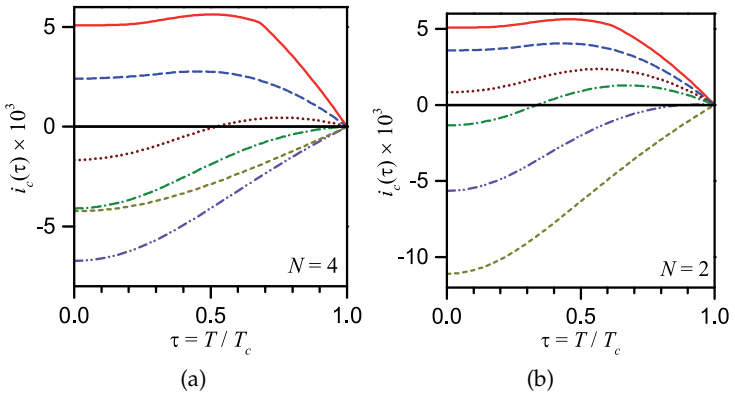

Figure 5. The same as in Fig. 4 but for $\alpha = 15°$ and various $\sigma_0 = 0.9$ (solid), 1 (dashed), 1.1 (dotted), 1.3 (dash-dotted), 1.5 (dash-dot-dotted), and 3 (short-dashed).

or σ_0, changes, which is most likely not true in the real experiment. However, the presented results testify that each of those parameters differently affects the current. Moreover, underdoping is usually accompanied by the increase of both α and Σ (proportional to the structural phase transition temperature, i.e. the pseudogap appearance temperature, T^*) [39, 42, 63, 94]. Therefore, the situation when the doping-induced simultaneous changes in the values of α and Σ_0 would lead to their mutual compensation seems improbable. Accordingly, we believe that the proposed experiments may be useful in one more, this time indirect, technique to probe CDWs in high-T_c oxides. In particular, the oscillating dependences $i_c(\alpha)$ depicted in Fig. 10b, if reproduced in the experiment, will be certain to prove the interplay between the superconducting order parameter and another, competing, one; here, the latter is considered theoretically to be associated with CDWs.

http://dx.doi.org/10.5772/59590

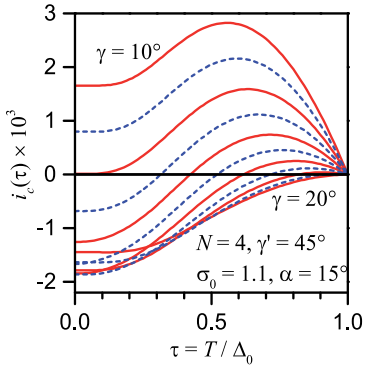

Figure 6. The same as in Fig. 4a but for $\alpha = 15^\circ$ and $\sigma_0 = 1.1$ and various $10^\circ \leq \gamma \leq 20^\circ$.

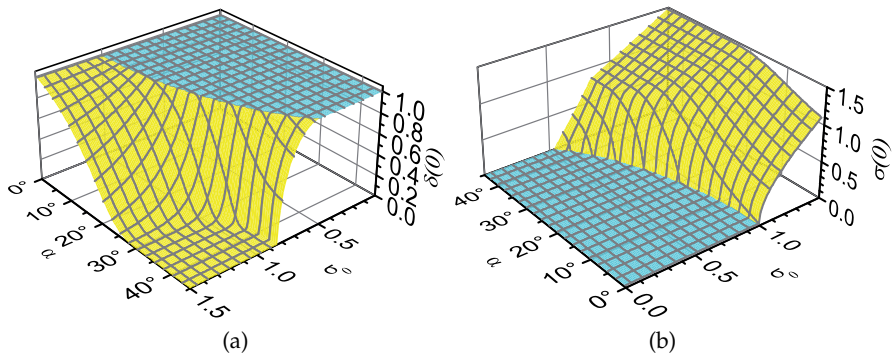

Figure 7. Dependences of the normalized zero-temperature order parameters $\delta(0)$ (a) and $\sigma(0)$ (b) for the S^d_{CDW4} superconductor on α and σ_0.

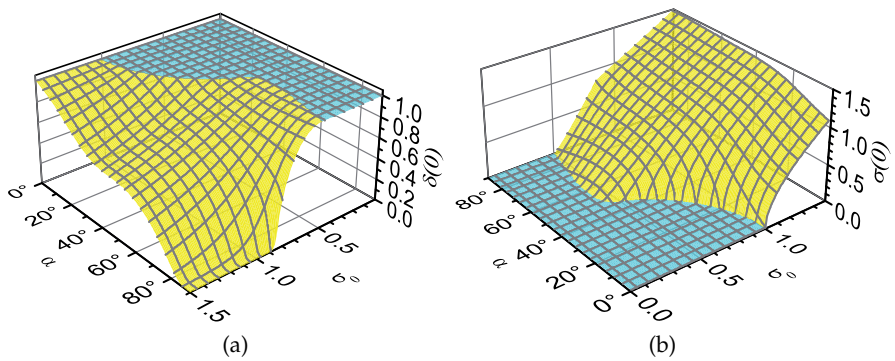

Figure 8. The same as in Fig. 7 but for the S^d_{CDW2} superconductor.

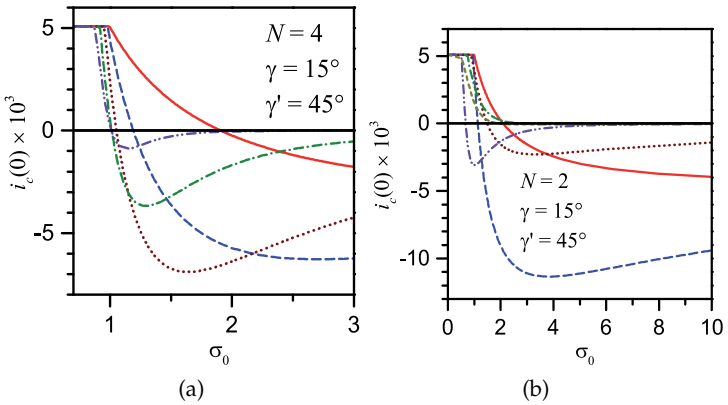

Figure 9. Dependences of the normalized zero-temperature Josephson current on σ_0 for $N = 4$ (a) and $N = 2$ (b) CDW configurations and various α's: (a) $\alpha = 5$ (solid), 10 (dashed), 15 (dotted), 20 (dash-dotted), and 25° (dash-dot-dotted); (b) $\alpha = 5$ (solid), 15 (dashed), 25 (dotted), 35 (dash-dotted), 45 (dash-dot-dotted), and 55° (short-dashed).

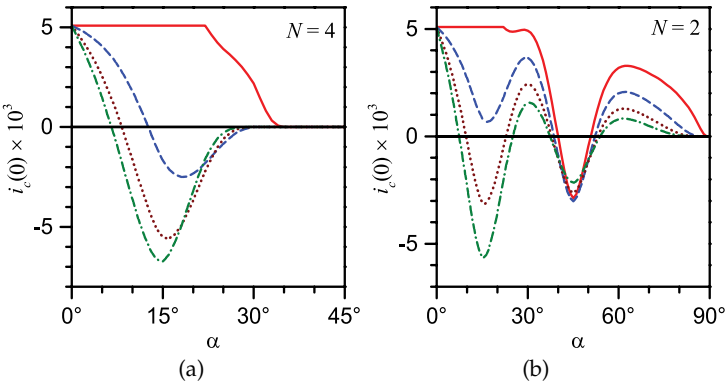

Figure 10. Dependences of the normalized zero-temperature Josephson current on α for $N = 4$ (a) and $N = 2$ (b) CDW configurations and various $\sigma_0 = 0.9$ (solid), 1,1 (dashed), 1.3 (dotted), 1.5 (dash-dotted). $\gamma = 15°$ and $\gamma' = 45°$.

4. Conclusions

In the two-dimensional model appropriate for cuprates, we calculated the dependences of the stationary critical Josephson tunnel current I_c in junctions involving d-wave superconductors with CDWs on the temperature, the CDW parameters, and the electrode orientation angles with respect to the junction plane. It was shown that the intertwining of the CDW and superconducting order parameters leads to peculiar dependences of I_c, which reflect the existence of CDW gapping. The peculiarities become especially salient when the crystal configurations on the both sides of the sandwich make the overall current extremely sensitive to the overlap between the superconducting lobes and the CDW sectors. In this case, the

http://dx.doi.org/10.5772/59590

whole structure can be considered as a differential tool suitable to detect CDWs. Doping serves here as a control process to reveal the CDW manifestations. Such configurations have already been created for $YBa_2Cu_3O_{7-\delta}$ [55, 82] and may be used to check the predictions of our theory.

Acknowledgements

The work was partially supported by the Project N 8 of the 2012–2014 Scientific Cooperation Agreement between Poland and Ukraine. MSL was also supported by the Narodowe Centrum Nauki in Poland (grant No. 2011/01/B/NZ1/01622). The authors are grateful to Alexander Kasatkin (Institute of Metal Physics, Kyiv), and Fedor Kusmartsev and Boris Chesca (Loughborough University, Loughborough) for useful discussion.

Author details

Alexander M. Gabovich*[1], Mai Suan Li[2], Henryk Szymczak[2] and Alexander I. Voitenko[1]

*Address all correspondence to: gabovich@iop.kiev.ua

1 Institute of Physics, National Academy of Sciences of Ukraine, Kyiv, Ukraine

2 Institute of Physics, Polish Academy of Sciences, Warsaw, Poland

References

[1] A A Abrikosov, L P Gor'kov, and I E Dzyaloshinskii. *Methods of Quantum Field Theory in Statistical Physics*. Prentice Hall, Englewood Cliffs, NJ, 1963.

[2] A J Achkar, X Mao, C McMahon, R Sutarto, F He, R Liang, D A Bonn, W N Hardy, and D G Hawthorn. Impact of quenched oxygen disorder on charge density wave order in $YBa_2Cu_3O_{6+x}$. *Phys. Rev. Lett.*, 113(10):107002, 2014.

[3] J W Alldredge, K Fujita, H Eisaki, S Uchida, and K McElroy. Universal disorder in $Bi_2Sr_2CaCu_2O_{8+x}$. *Phys. Rev. B*, 87(10):104520, 2013.

[4] A Avella and F Mancini, editors. *Lectures on the Physics of Strongly Correlated Systems XVII. Seventeenth Training Course in the Physics of Strongly Correlated Systems*. American Institute of Physics, Melville, New York, 2013.

[5] M Bakr, S M Souliou, S Blanco-Canosa, I Zegkinoglou, H Gretarsson, J Strempfer, T Loew, C T Lin, R Liang, D A Bonn, W N Hardy, B Keimer, and M Le Tacon. Lattice dynamical signature of charge density wave formation in underdoped $YBa_2Cu_3O_{6+x}$. *Phys. Rev. B*, 88(21):214517, 2013.

[6] Yu S Barash, H Burkhardt, and D Rainer. Low-temperature anomaly in the Josephson critical current of junctions in *d*-wave superconductors. *Phys. Rev. Lett.*, 77(19):4070–4073, 1996.

[7] A Barone and G Paterno. *The Physics and Applications of the Josephson Effect*. John Wiley and Sons, New York, 1982.

[8] J G Bednorz and K A Müller. Possible high T_c superconductivity in the Ba-La-Cu-O system. *Z. Phys.*, 64(2):189–193, 1986.

[9] E Blackburn, J Chang, A H Said, B M Leu, R Liang, D A Bonn, W N Hardy, E M Forgan, and S M Hayden. Inelastic x-ray study of phonon broadening and charge-density wave formation in ortho-II-ordered $YBa_2Cu_3O_{6.54}$. *Phys. Rev. B*, 88(5):054506, 2013.

[10] S Blanco-Canosa, A Frano, E Schierle, J Porras, T Loew, M Minola, M Bluschke, E Weschke, B Keimer, and M Le Tacon. Resonant x-ray scattering study of charge-density wave correlations in $YBa_2Cu_3O_{6+x}$. *Phys. Rev. B*, 90(5):054513, 2014.

[11] M C Boyer, W D Wise, K Chatterjee, M Yi, T Kondo, T Takeuchi, H Ikuta, and E W Hudson. Imaging the two gaps of the high-temperature superconductor $Bi_2Sr_2CuO_{6+x}$. *Nature Phys.*, 3(11):802–806, 2007.

[12] C Bruder, A van Otterlo, and G T Zimanyi. Tunnel junctions of unconventional superconductors. *Phys. Rev. B*, 51(18):12904–12907, 1995.

[13] R Comin, A Frano, M M Yee, Y Yoshida, H Eisaki, E Schierle, E Weschke, R Sutarto, F He, A Soumyanarayanan, Y He, M Le Tacon, I S Elfimov, J E Hoffman, G A Sawatzky, B Keimer, and A Damascelli. Charge order driven by Fermi-arc instability in $Bi_2Sr_{2-x}La_xCuO_{6+\delta}$. *Science*, 343(6169):390–392, 2014.

[14] T P Croft, C Lester, M S Senn, A Bombardi, and S M Hayden. Charge density wave fluctuations in $La_{2-x}Sr_xCuO_4$ and their competition with superconductivity. *Phys. Rev. B*, 89(22):224513, 2014.

[15] T Cvitanić, D Pelc, M Požek, E Amit, and A Keren. ^{17}O-NMR Knight shift study of the interplay between superconductivity and pseudogap in $(Ca_xLa_{1-x})(Ba_{1.75-x}La_{0.25+x})Cu_3O_y$. *Phys. Rev. B*, 90(5):054508, 2014.

[16] E H da Silva Neto, P Aynajian, R E Baumbach, E D Bauer, J Mydosh, S Ono, and A Yazdani. Detection of electronic nematicity using scanning tunneling microscopy. *Phys. Rev. B*, 87(16):161117, 2013.

[17] E H da Silva Neto, P Aynajian, A Frano, R Comin, E Schierle, E Weschke, A Gyenis, J Wen, J Schneeloch, Z Xu, S Ono, G Gu, M Le Tacon, and A Yazdani. Ubiquitous interplay between charge ordering and high-temperature superconductivity in cuprates. *Science*, 343(6169):393–396, 2014.

[18] E Dagotto. Complexity in strongly correlated electronic systems. *Science*, 309(5732):257–262, 2005.

[19] J Dai, E Calleja, J Alldredge, X Zhu, L Li, W Lu, Y Sun, T Wolf, H Berger, and K McElroy. Microscopic evidence for strong periodic lattice distortion in two-dimensional charge-density wave systems. *Phys. Rev. B*, 89(16):165140, 2014.

[20] A Damascelli, Z Hussain, and Z-X Shen. Angle-resolved photoemission studies of the cuprate superconductors. *Rev. Mod. Phys.*, 75(2):473–541, 2003.

[21] T Das, R S Markiewicz, and A Bansil. Intermediate coupling model of the cuprates. *Adv. Phys.*, 63(3):151–266, 2014.

[22] J C S Davis and D-H Lee. Concepts relating magnetic interactions, intertwined electronic orders, and strongly correlated superconductivity. *Proc. Nat. Acad. Sci. USA*, 110(44):17623–17630, 2013.

[23] T Ekino, A M Gabovich, Mai Suan Li, M Pękała, H Szymczak, and A I Voitenko. d-wave superconductivity and s-wave charge density waves: Coexistence between order parameters of different origin and symmetry. *Symmetry*, 3(4):699–749, 2011.

[24] T Ekino, A M Gabovich, Mai Suan Li, M Pękała, H Szymczak, and A I Voitenko. The phase diagram for coexisting d-wave superconductivity and charge-density waves: cuprates and beyond. *J. Phys.: Condens. Matter*, 23(38):385701, 2011.

[25] Z Fisk and H R Ott, editors. *Superconductivity in New Materials*. Elsevier, Amsterdam, 2011.

[26] E Fradkin, S A Kivelson, M J Lawler, J P Eisenstein, and A P Mackenzie. Nematic Fermi fluids in condensed matter physics. *Annu. Rev. Condens. Matter Phys.*, 1:153–178, 2010.

[27] R H Friend and D Jérome. Periodic lattice distortions and charge-density waves in one-dimensional and 2-dimensional metals. *J. Phys. C*, 12(8):1441–1477, 1979.

[28] K Fujita, C K Kim, I Lee, J Lee, M H Hamidian, I A Firmo, S Mukhopadhyay, H Eisaki, S Uchida, M J Lawler, E-A Kim, and J C Davis. Simultaneous transitions in cuprate momentum-space topology and electronic symmetry breaking. *Science*, 344(6184):612–616, 2014.

[29] A M Gabovich, Mai Suan Li, H Szymczak, and A I Voitenko. *Dc Josephson current between an isotropic and a d-wave or extended s-wave partially gapped charge density wave superconductor*, pages 289–318. In A Gabovich, editor. *Superconductors – Materials, Properties and Applications*. InTech, Rijeka, Croatia, 2012.

[30] A M Gabovich, Mai Suan Li, H Szymczak, and A I Voitenko. Orientation peculiarities of dc Josephson tunneling between d-wave superconductors with charge density waves. *Phys. Rev. B*, 87(10):104503, 2013.

[31] A M Gabovich, Mai Suan Li, H Szymczak, and A I Voitenko. Stationary Josephson current in junctions involving *d*-wave superconductors with charge density waves: the temperature dependence and deviations from the law of corresponding states. *Eur. Phys. J. B*, 87(5):115, 2014.

[32] A M Gabovich, D P Moiseev, A S Shpigel, and A I Voitenko. Josephson tunneling critical current between superconductors with charge- or spin-density waves. *Phys. Status Solidi*, 161(1):293–302, 1990.

[33] A M Gabovich and A I Voitenko. Josephson tunnelling involving superconductors with charge-density waves. *J. Phys.: Condens. Matter*, 9(19):3901–3920, 1997.

[34] A M Gabovich and A I Voitenko. dc Josephson current for *d*-wave superconductors with charge density waves. *Fiz. Nizk. Temp.*, 38(4):414–422, 2012.

[35] A M Gabovich and A I Voitenko. Charge density waves in *d*-wave superconductors: thermodynamics and Josephson tunneling (review article). *Fiz. Nizk. Temp.*, 39(3):301–319, 2013.

[36] A M Gabovich and A I Voitenko. Anomalous temperature dependence of the stationary Josephson tunnel current in junctions between *d*-wave superconductors. *Fiz. Nizk. Temp.*, 40(9):1045–1052, 2014.

[37] A M Gabovich, A I Voitenko, J F Annett, and M Ausloos. Charge- and spin-density-wave superconductors. *Supercond. Sci. Technol.*, 14(4):R1–R27, 2001.

[38] A M Gabovich, A I Voitenko, and M Ausloos. Charge-density waves and spin-density waves in existing superconductors: competition between Cooper pairing and Peierls or excitonic instabilities. *Phys. Rep.*, 367(6):583–709, 2002.

[39] A M Gabovich, A I Voitenko, T Ekino, Mai Suan Li, H Szymczak, and M Pękała. Competition of superconductivity and charge density waves in cuprates: Recent evidence and interpretation. *Adv. Condens. Matter Phys.*, 2010:Article ID 681070, 2010.

[40] A E Gorbonosov and I O Kulik. Temperature dependence of the Josephson current in anisotropic superconductors. *Fiz. Met. Metalloved.*, 23(5):803–812, 1967.

[41] G Grüner. *Density Waves in Solids*. Addison-Wesley Publishing Company, Reading, Massachusetts, 1994.

[42] M Hashimoto, I M Vishik, R-H He, T P Devereaux, and Z-X Shen. Energy gaps in high-transition-temperature cuprate superconductors. *Nature Phys.*, 10(7):483–495, 2014.

[43] Y He, Y Yin, M Zech, A Soumyanarayanan, M M Yee, T Williams, M C Boyer, K Chatterjee, W D Wise, I Zeljkovic, T Kondo, T Takeuchi, H Ikuta, P Mistark, R S Markiewicz, A Bansil, S Sachdev, E W Hudson, and J E Hoffman. Fermi surface and pseudogap evolution in a cuprate superconductor. *Science*, 344(6184):608–611, 2014.

[44] P Hosur, A Kapitulnik, S A Kivelson, J Orenstein, and S Raghu. Kerr effect as evidence of gyrotropic order in the cuprates. *Phys. Rev. B*, 87(11):115116, 2013.

[45] M Hücker, N. B. Christensen, A T Holmes, E Blackburn, E M Forgan, R Liang, D A Bonn, W N Hardy, O Gutowski, M v Zimmermann, S M Hayden, and J Chang. Competing charge, spin, and superconducting orders in underdoped $YBa_2Cu_3O_y$. *Phys. Rev. B*, 90(5):054514, 2014.

[46] N E Hussey. Phenomenology of the normal state in-plane transport properties of high-T_c cuprates. *J. Phys.: Condens. Matter*, 20(12):123201, 2008.

http://dx.doi.org/10.5772/59590

[47] E Il'ichev, M Grajcar, R Hlubina, R. P. J. IJsselsteijn, H E Hoenig, H-G Meyer, A Golubov, M H S Amin, A M Zagoskin, A N Omelyanchouk, and M Yu Kupriyanov. Degenerate ground state in a mesoscopic $YBa_2Cu_3O_{7-x}$ grain boundary Josephson junction. *Phys. Rev. Lett.*, 86(23):5369–5372, 2001.

[48] Yu A Izyumov and E Z Kurmaev. Strongly electron-correlated materials. *Usp. Fiz. Nauk*, 178(1):25–60, 2008.

[49] D Jérome, C Berthier, P Molinié, and J Rouxel. Electronic properties of transition metal dichalcogenides: connection between structural instabilities and superconductivity. *J. Phys. (Paris) Colloq.*, 37:C125–C135, 1976.

[50] H Kamimura and H Ushio. On the interplay of Jahn-Teller physics and Mott physics leading to the occurrence of Fermi pockets without pseudogap hypothesis and d-wave high T_c superconductivity in underdoped cuprate superconductors. *J. Supercond.*, 25(3):677–690, 2012.

[51] S Kashiwaya and Y Tanaka. Tunnelling effects on surface bound states in unconventional superconductors. *Rep. Prog. Phys.*, 63(10):1641–1724, 2000.

[52] H-Y Kee, C M Puetter, and D Stroud. Transport signatures of electronic-nematic stripe phases. *J. Phys.: Condens. Matter*, 25(20):202201, 2013.

[53] B Keimer. *Recent advances in experimental research on high-temperature superconductivity*, pages 9.1–9.24. In Pavarini et al. [71], 2013.

[54] J R Kirtley. Probing the order parameter symmetry in the cuprate high temperature superconductors by squid microscopy. *C. R. Physique*, 12(5-6):436–445, 2011.

[55] J R Kirtley, C C Tsuei, A Ariando, C J M Verwijs, S Harkema, and H Hilgenkamp. Angle-resolved phase-sensitive determination of the in-plane gap symmetry in $YBa_2Cu_3O_{7-\delta}$. *Nature Phys.*, 2(3):190–194, 2006.

[56] R A Klemm. The phase-sensitive *c*-axis twist experiments on $Bi_2Sr_2CaCu_2O_{8+\delta}$ and their implications. *Phil. Mag.*, 85(8):801–853, 2005.

[57] I O Kulik and I K Yanson. *Josephson Effect in Superconducting Tunnel Structures*. Israel Program for Scientific Translation, Jerusalem, 1972.

[58] M J Lawler, K Fujita, J Lee, A R Schmidt, Y Kohsaka, C K Kim, H Eisaki, S Uchida, J C Davis, J P Sethna, and E-A Kim. Intra-unit-cell electronic nematicity of the high-T_c copper-oxide pseudogap states. *Nature*, 466(7304):347–351, 2010.

[59] M Le Tacon, A Bosak, S M Souliou, G Dellea, T Loew, R Heid, K-P Bohnen, G Ghiringhelli, M Krisch, and B Keimer. Inelastic x-ray scattering in $YBa_2Cu_3O_{6.6}$ reveals giant phonon anomalies and elastic central peak due to charge-density-wave formation. *Nature Phys.*, 10(1):52–58, 2014.

[60] M Ledvij and R A Klemm. Dependence of the Josephson coupling of unconventional superconductors on the properties of the tunneling barrier. *Phys. Rev. B*, 51(5):3269–3272, 1995.

[61] P A Lee. From high temperature superconductivity to quantum spin liquid: progress in strong correlation physics. *Rep. Prog. Phys.*, 71(1):012501, 2008.

[62] P A Lee, N Nagaosa, and X-G Wen. Doping a Mott insulator: Physics of high-temperature superconductivity. *Rev. Mod. Phys.*, 78(1):17–85, 2006.

[63] W S Lee, I M Vishik, K Tanaka, D H Lu, T Sasagawa, N Nagaosa, T P Devereaux, Z Hussain, and Z-X Shen. Abrupt onset of a second energy gap at the superconducting transition of underdoped Bi2212. *Nature*, 450(7166):81–84, 2007.

[64] T Löfwander, V S Shumeiko, and G Wendin. Andreev bound states in high-T_c superconducting junctions. *Supercond. Sci. Technol.*, 14(5):R53–R77, 2001.

[65] S Maiti and A V Chubukov. *Superconductivity from repulsive interaction*, pages 3–73. In Avella and Mancini [4], 2013.

[66] E G Maksimov. The problem of high-temperature superconductivity. the current state of the art. *Usp. Fiz. Nauk*, 170(10):1033–1061, 2000.

[67] R S Markiewicz. A survey of the van Hove scenario for high-t_c superconductivity with special emphasis on pseudogaps and striped phases. *J. Phys. Chem. Sol.*, 58(8):1179–1310, 1997.

[68] D K Morr. Lifting the fog of complexity. *Science*, 343(6169):382–383, 2014.

[69] M V Mostovoy, F M Marchetti, B D Simons, and P B Littlewood. Effects of disorder on coexistence and competition between superconducting and insulating states. *Phys. Rev. B*, 71(22):224502, 2005.

[70] L Nie, G Tarjus, and S A Kivelson. Quenched disorder and vestigial nematicity in the pseudogap regime of the cuprates. *Proc. Nat. Acad. Sci. USA*, 111(22):7980–7985, 2014.

[71] E Pavarini, E Koch, and U Schollwöck, editors. *Emergent Phenomena in Correlated Matter Modeling and Simulation, Vol. 3*. Forschungszentrum Jülich, Jülich, 2013.

[72] Y Peng, J Meng, D Mou, J He, L Zhao, Y Wu, G Liu, X Dong, S He, J Zhang, X Wang, Q Peng, Z Wang, S Zhang, F Yang, C Chen, Z Xu, T K Lee, and X J Zhou. Disappearance of nodal gap across the insulator–superconductor transition in a copper-oxide superconductor. *Nat. Commun.*, 4:2459, 2013.

[73] W E Pickett. *Superconductivity: 2D physics, unknown mechanisms, current puzzles*, pages 11.1–11.29. In Pavarini et al. [71], 2013.

[74] N M Plakida. *High-Temperature Cuprate Superconductors. Experiment, Theory, and Applications*. Springer Verlag, Berlin, 2010.

[75] T M Rice, K-Y Yang, and F C Zhang. A phenomenological theory of the anomalous pseudogap phase in underdoped cuprates. *Rep. Prog. Phys.*, 75(1):016502, 2012.

[76] R A Riedel and P F Bagwell. Low-temperature Josephson current peak in junctions with d-wave order parameters. *Phys. Rev. B*, 57(10):6084–6089, 1998.

[77] J A Rosen, R Comin, G Levy, D Fournier, Z-H Zhu, B Ludbrook, C N Veenstra, A Nicolaou, D Wong, P Dosanjh, Y Yoshida, H Eisaki, G R Blake, F White, T T M Palstra, R Sutarto, F He, A F Pereira, Y Lu, B Keimer, G Sawatzky, L Petaccia, and A Damascelli. Surface-enhanced charge-density-wave instability in underdoped $Bi_2Sr_{2-x}La_xCuO_{6+\delta}$. *Nat. Commun.*, 4(7):1977, 2013.

[78] A Sacuto, Y Gallais, M Cazayous, M-A Méasson, G D Gu, and D Colson. New insights into the phase diagram of the copper oxide superconductors from electronic raman scattering. *Rep. Prog. Phys.*, 76(2):022502, 2013.

[79] S Sakai, S Blanc, M Civelli, Y Gallais, M Cazayous, M-A Méasson, J S Wen, Z J Xu, G D Gu, G Sangiovanni, Y Motome, K Held, A Sacuto, A Georges, and M Imada. Raman-scattering measurements and theory of the energy-momentum spectrum for underdoped $Bi_2Sr_2CaCuO_{8+\delta}$ superconductors: Evidence of an s-wave structure for the pseudogap. *Phys. Rev. Lett.*, 111(10):107001, 2013.

[80] S E Sebastian, N Harrison, and G G Lonzarich. Towards resolution of the Fermi surface in underdoped high-T_c superconductors. *Rep. Prog. Phys.*, 75(10):102501, 2012.

[81] M Sigrist and T M Rice. Paramagnetic effect in high T_c superconductors – a hint for d-wave superconductivity. *J. Phys. Soc. Jpn.*, 61(12):4283–4286, 1992.

[82] H J H Smilde, A A Golubov, Ariando, G Rijnders, J M Dekkers, S Harkema, D H A Blank, H Rogalla, and H Hilgenkamp. Admixtures to d-wave gap symmetry in untwinned $YBa_2Cu_3O_7$ superconducting films measured by angle-resolved electron tunneling. *Phys. Rev. Lett.*, 95(25):257001, 2005.

[83] S-Q Su and T A Maier. Coexistence of strong nematic and superconducting correlations in a two-dimensional Hubbard model. *Phys. Rev. B*, 84(22):220506, 2011.

[84] S Sugai, Y Takayanagi, N Hayamizu, T Muroi, R Shiozaki, J Nohara, K Takenaka, and K Okazaki. Superconducting pairing and the pseudogap in the nematic dynamical stripe phase of $La_{2-x}Sr_xCuO_4$. *J. Phys.: Condens. Matter*, 25(47):475701, 2013.

[85] F Tafuri and J R Kirtley. Weak links in high critical temperature superconductors. *Rep. Prog. Phys.*, 68(11):2573–2663, 2005.

[86] F Tafuri, D Massarotti, L Galletti, D Stornaiuolo, D Montemurro, L Longobardi, P Lucignano, G Rotoli, G P Pepe, A Tagliacozzo, and F Lombardi. Recent achievements on the physics of high-T_c superconductor Josephson junctions: Background, perspectives and inspiration. *J. Supercond.*, 26(1):21–41, 2013.

[87] G Testa, E Sarnelli, A Monaco, E Esposito, M Ejrnaes, D-J Kang, S H Mennema, E J Tarte, and M G Blamire. Evidence of midgap-state-mediated transport in 45°

symmetric [001] tilt $YBa_2Cu_3O_{7-x}$ bicrystal grain-boundary junctions. *Phys. Rev. B*, 71(13):134520, 2005.

[88] Y Toda, F Kawanokami, T Kurosawa, M Oda, I Madan, T Mertelj, V V Kabanov, and D Mihailovic. Rotational symmetry breaking in $Bi_2Sr_2CaCu_2O_{8+\delta}$ probed by polarized femtosecond spectroscopy. *Phys. Rev. B*, 90(9):094513, 2014.

[89] J M Tranquada. *Spins, stripes, and superconductivity in hole-doped cuprates*, pages 114–187. In Avella and Mancini [4], 2013.

[90] C C Tsuei and J R Kirtley. *Phase-sensitive tests of pairing symmetry in cuprate superconductors*, pages 869–921. In K H Bennemann and J B Ketterson, editors. *Superconductivity. Vol. 2: Novel Superconductors*. Springer Verlag, Berlin, 2008.

[91] C M Varma, P B Littlewood, S Schmitt-Rink, E Abrahams, and A E Ruckenstein. Phenomenology of the normal state of Cu-O high-temperature superconductors. *Phys. Rev. Lett.*, 63(18):1996–1999, 1989.

[92] C M Varma, Z Nussinov, and W van Saarloos. Singular or non-Fermi liquids. *Phys. Rep.*, 361(5-6):267–417, 2002.

[93] B Vignolle, D Vignolles, M-H Julien, and C Proust. From quantum oscillations to charge order in high-T_c copper oxides in high magnetic fields. *C. R. Physique*, 14(1):39–52, 2013.

[94] I M Vishik, M Hashimoto, R-H Hed, W-S Lee, F Schmitt, D Lu, R G Moore, C Zhang, W Meevasana, T Sasagawa, S Uchida, K Fujita, S Ishida, M Ishikado, Y Yoshida, H Eisaki, Z Hussain, T P Devereauxa, and Z-X Shen. Phase competition in trisected superconducting dome. *Proc. Nat. Acad. Sci. USA*, 109(45):18332–18337, 2012.

[95] A I Voitenko and A M Gabovich. Charge density waves in *d*-wave superconductors. *Fiz. Nizk. Temp.*, 36(12):1300–1311, 2010.

[96] A I Voitenko and A M Gabovich. Charge-density waves in partially dielectrized superconductors with *d*-pairing. *Fiz. Tverd. Tela*, 52(1):20–27, 2010.

[97] M Vojta. Lattice symmetry breaking in cuprate superconductors: stripes, nematics, and superconductivity. *Adv. Phys.*, 58(6):699–820, 2009.

[98] P Wahl. Charting the pseudogap. *Nature Phys.*, 8(7):514–516, 2012.

[99] J Wang and G-Z Liu. Competition between the superconductivity and nematic order in the high-T_c superconductor. *New J. Phys.*, 15(7):073039, 2013.

[100] J-R Wang and G-Z Liu. Additional electron pairing in a d-wave superconductor driven by nematic order. *New J. Phys.*, 15(6):063007, 2013.

[101] E L Wolf. *Principles of Electron Tunneling Spectroscopy*. Oxford University Press, New York, 1985.

http://dx.doi.org/10.5772/59590

[102] H D Yang, P Klavins, and R N Shelton. Competition between superconductivity and charge-density waves in the pseudoternary system $(Lu_{1-x}Sc_x)_5Ir_4Si_{10}$. *Phys. Rev. B*, 43(10):7681–7687, 1991.

[103] K-Y Yang, W-Q Chen, T M Rice, and F-C Zhang. Origin of the checkerboard pattern in scanning tunneling microscopy maps of underdoped cuprate superconductors. *Phys. Rev. B*, 80(17):174505, 2009.

[104] T Yoshida, M Hashimoto, I M Vishik, Z-X Shen, and A Fujimori. Pseudogap, superconducting gap, and Fermi arc in high-T_c cuprates revealed by angle-resolved photoemission spectroscopy. *J. Phys. Soc. Jpn.*, 81(1):011006, 2012.

[105] S Zhou, H Ding, and Z Wang. Correlating off-stoichiometric doping and nanoscale electronic inhomogeneity in the high-T_c superconductor $Bi_2Sr_2CaCu_2O_{8+\delta}$. *Phys. Rev. Lett.*, 98(7):076401, 2007.

Chapter 11

Impurity Effects in Iron Pnictide Superconductors

Yuriy G. Pogorelov, Mario C. Santos and
Vadim M. Loktev

Additional information is available at the end of the chapter

http://dx.doi.org/10.5772/59629

1. Introduction

The recent discovery of superconductivity (SC) with rather high critical temperature in the family of doped iron pnictide compounds [1, 2], has motivated a great interest to these materials (see the reviews [3, 4]). Unlike the extensively studied cuprate family [5], that present insulating properties in their initial undoped state, the undoped LaOFeAs compound is a semimetal. As was established by the previous physical and chemical studies (see, e.g., [6, 7]), this material has a layered structure, where the SC state is supported by the FeAs layer with a 2D square lattice of Fe atoms and with As atoms located out of plane, above or below the centers of square cells (Fig. 1). Its electronic structure, relevant for constructing microscopic SC models, have been explored with high-resolution angle-resolved photoemission spectroscopy (ARPES) techniques [8, 9]. Their results indicate the multiple connected structure of Fermi surface, consisting of electron and hole pockets and absence of nodes in both electron and whole spectrum gaps [8], suggesting these systems to display the so-called extended s-wave (also called $s_{\pm}$-wave) SC order, changing the order parameter sign between electron and whole segments [10].

To study the band structure, the first principles numeric calculations are commonly used, outlining the importance of Fe atomic d-orbitals. The calculations show that SC in these materials is associated with Fe atoms in the layer plane, represented in Fig. 1 by their orbitals and the related hopping amplitudes. The dominance of Fe atomic 3d orbitals in the density of states of LaOFeAs compound near its Fermi surface was demonstrated by the local density approximation (LDA) calculations [10-15]. It was then concluded that the multi-orbital effects are important for electronic excitation spectrum in the SC state, causing formation of two spectrum gaps: by electron and hole pockets at the Fermi surface. To explain the observed SC properties, an unconventional pairing mechanism, beyond the common electron-phonon

INTECH
open science | open minds

© 2015 The Author(s). Licensee InTech. This chapter is distributed under the terms of the Creative Commons Attribution License (http://creativecommons.org/licenses/by/3.0), which permits unrestricted use, distribution, and reproduction in any medium, provided the original work is properly cited.

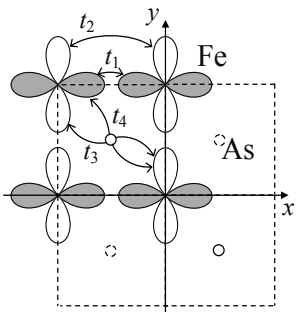

Figure 1. Schematics of a FeAs layer in the LaoFeAs compound with d_{xz} (dark) and d_{yz} (white) Fe orbitals and the Fe-Fe hopping parameters in the minimal coupling model. Note that the hoppings between next near neighbors ($t_{3,4}$) are mediated by the As orbitals (out of Fe plane)

scheme, was suggested for these materials [16-19]. In general, the total of 5 atomic orbitals for each iron in the LaOFeAs compound can be involved, however the ways to reduce this basis are sought, in order to simplify analytical and computational work. Some authors [20, 21] have suggested that it is sufficient to consider only the d_{xz} and d_{yz} orbitals. Building such minimal coupling model based on two orbitals, one is able to adjust the model parameters (energy hopping and chemical potential) to obtain the Fermi surface with the same topology that in the first principles calculations of band structure. Even though it fails to reproduce some finer features of the electronic spectrum [22, 23], this minimal coupling scheme is favored by its technical simplicity to be chosen as a basis for study of impurity effects in LaOFeAs which could be hardly tractable in more involved frameworks.

Having established the SC state parameters, important effects of disorder, in particular by impurities, on the system electronic properties, have been studied for doped iron pnictides. Alike the situation in doped perovskite cuprates, impurity centers can result here either from dopants, necessary to form the very SC state, or from foreign atoms and other local defects. Within the minimal coupling model, an interesting possibility for localized impurity levels within SC gaps in doped LaOFeAs was indicated, even for the simplest, so-called isotopic (or non-magnetic) type of impurity perturbation [24, 25]. This finding marks an essential difference from the traditional SC systems with \emph{s}-wave gap on a single-connected Fermi surface, were such perturbations are known not to produce localized impurity states and thus to have no sizeable effect on SC order, accordingly to the Anderson theorem [26].

In presence of localized quasiparticle states by isolated impurity centers, the next important issue is the possibility for collective behavior of such states at finite (but low enough) impurity concentration. They are expected to give rise to some resonance effects like those well studied in semiconductors at low doping concentrations [27]. This possibility was studied long ago for electronic quasiparticles in doped semiconducting systems [28] and also for other types of quasiparticles in pnononic, magnonic, excitonic, etc. spectra under impurities [29], establishing conditions for collective (including coherent) behavior of impurity excitations. Thus, indirect interactions between impurity centers of certain type (the so-called deep levels at high enough concentrations) in doped semiconductors can lead

http://dx.doi.org/10.5772/59629

to formation of collective band-like states [28, 30]. This corresponds to the Anderson transition in a general disordered system [31], and the emerging new band of quasiparticles in the spectrum can essentially change thermodynamics and transport in the doped material [32]. In this course, the fundamental distinction between two possible types of states is done on the basis of general Ioffe-Regel-Mott (IRM) criterion that a given excitation has a long enough lifetime compared to its oscillation period [32, 33].

Analogous effects in superconductors were theoretically predicted and experimentally discovered for magnetic impurities, both in BCS systems [34-36] and in the two-band MgB_2 system [37, 38]. In all those cases, the breakdown of the Anderson's theorem is only due to the breakdown of the spin-singlet symmetry of an *s*-wave Cooper pair by a spin-polarized impurity. This limitation does not apply to the high-T_c doped cuprates, however their *d*-wave symmetry of SC order only permits impurity resonances in the spectrum of quasiparticles [39, 40], not their true localization, and hinders notable collective effects on their observable properties.

Therefore the main physical interest in SC iron pnictides from the point of view of disorder in general is the possibility for pair-breaking even on non-magnetic impurity [41-43] and for related localized in-gap states [21, 44-46]. This theoretical prediction was confirmed by the observations of various effects from localized impurity states, for instance, in the superfluid density (observed through the London penetration length) [47, 48], transition critical temperature [49, 50] and electronic specific heat [51], all mainly due to an emerging spike of electronic density of states against its zero value in the initial band gap. An intriguing possibility for banding of impurity levels within the SC gap [38, 52], similar to that in the above mentioned normal systems, was recently discussed for doped iron pnictides [53]. Here a more detailed analysis of the band-like impurity states is also focused on their observable effects that cannot be produced by localized impurity states.

We apply the Green function (GF) techniques, similar to those for doped cuprate SC systems [54], using the minimal coupling model by two orbitals for host electronic structure and the simplest isotopic type for impurity perturbation. The energy spectrum near in-gap impurity levels at finite impurity concentrations, emergence of specific branches of collective excitations in this range, and expected observable effects of such spectrum restructuring are discussed. Then specific GFs for SC quasiparticles are used in the general Kubo-Greenwood formalism [55, 56] to obtain the temperature and frequency dependences of optical conductivity. These results are compared with available experimental data and some suggestions are done on possible practical applications.

2. Model Hamiltonian and Green functions

For the minimal coupling model of Fig. 1, the hopping Hamiltonian H_t is written in the local orbital basis as:

$$H_t = -\sum_{\boldsymbol{n},\sigma}\Big[t_1\Big(x_{\boldsymbol{n},\sigma}^{\dagger}x_{\boldsymbol{n}+\delta_x,\sigma} + y_{\boldsymbol{n},\sigma}^{\dagger}y_{\boldsymbol{n}+\delta_y,\sigma} + h.c.\Big) + t_2\Big(x_{\boldsymbol{n},\sigma}^{\dagger}x_{\boldsymbol{n}+\delta_y,\sigma} + y_{\boldsymbol{n},\sigma}^{\dagger}y_{\boldsymbol{n}+\delta_x,\sigma} + h.c.\Big)$$
$$+t_3\Big(x_{\boldsymbol{n},\sigma}^{\dagger}x_{\boldsymbol{n}+\delta_x+\delta_y,\sigma} + x_{\boldsymbol{n},\sigma}^{\dagger}x_{\boldsymbol{n}+\delta_x-\delta_y,\sigma} + y_{\boldsymbol{n},\sigma}^{\dagger}y_{\boldsymbol{n}+\delta_x+\delta_y,\sigma} + y_{\boldsymbol{n},\sigma}^{\dagger}y_{\boldsymbol{n}+\delta_x-\delta_y,\sigma} + h.c.\Big) \quad (1)$$
$$+t_4\Big(x_{\boldsymbol{n},\sigma}^{\dagger}y_{\boldsymbol{n}+\delta_x+\delta_y,\sigma} + y_{\boldsymbol{n},\sigma}^{\dagger}x_{\boldsymbol{n}+\delta_x+\delta_y,\sigma} - x_{\boldsymbol{n},\sigma}^{\dagger}y_{\boldsymbol{n}+\delta_x-\delta_y,\sigma} - y_{\boldsymbol{n},\sigma}^{\dagger}x_{\boldsymbol{n}+\delta_x-\delta_y,\sigma} + h.c.\Big)\Big].$$

where $x_{\boldsymbol{n},\sigma}$ and $y_{\boldsymbol{n},\sigma}$ are the Fermi operators for d_{xz} and d_{yz} Fe orbitals with spin σ on $\boldsymbol{n}$ lattice site and the vectors $\boldsymbol{\delta}_{x,y}$ point to its nearest neighbors in the square lattice. Passing to the operators of orbital plane waves $x_{\boldsymbol{k},\sigma} = N^{-1/2}\sum_{\boldsymbol{n}} e^{i\boldsymbol{k}\cdot\boldsymbol{n}}x_{\boldsymbol{n},\sigma}$ (N is the number of lattice cells) and analogous $y_{\boldsymbol{k},\sigma}$ and defining an "orbital" 2-spinor $\psi_{\boldsymbol{k},\sigma} = (x_{\boldsymbol{k},\sigma}, y_{\boldsymbol{k},\sigma})$, one expands the spinor Hamiltonian in quasimomentum:

$$H_t = \sum_{\boldsymbol{k},\sigma}\psi_{\boldsymbol{k},\sigma}^{\dagger}\hat{h}_t(\mathbf{k})\psi_{\boldsymbol{k},\sigma}. \quad (2)$$

Here the 2×2 matrix

$$\hat{h}_t(\mathbf{k}) = \varepsilon_{+,\boldsymbol{k}}\hat{\sigma}_0 + \varepsilon_{-,\boldsymbol{k}}\hat{\sigma}_3 + \varepsilon_{xy,\boldsymbol{k}}\hat{\sigma}_1 \quad (3)$$

includes the Pauli matrices $\hat{\sigma}_i$ acting on the orbital indices and the energy functions

$$\varepsilon_{\pm,\boldsymbol{k}} = \frac{\varepsilon_{x,\boldsymbol{k}} \pm \varepsilon_{y,\boldsymbol{k}}}{2}, \quad (4)$$

with

$$\varepsilon_{x,\boldsymbol{k}} = -2t_1\cos k_x a - 2t_2\cos k_y a - 4t_3\cos k_x a\cos k_y a,$$
$$\varepsilon_{y,\boldsymbol{k}} = -2t_1\cos k_y a - 2t_2\cos k_x a - 4t_3\cos k_x a\cos k_y a,$$
$$\varepsilon_{xy,\boldsymbol{k}} = -4t_4\sin k_x a\sin k_y a,$$

(a is the distance between nearest neighbor Fe). An optimum fit for the calculated band structure in the minimum coupling model is with the hopping parameters (in $|t_1|$ units): t_1 = –1.0, t_2 = 1.3, $t_3 = t_4$ = –0.85, and with the Fermi energy ε_F = 1.45 [15]. A unitary transformation brings $\hat{h}_t(\boldsymbol{k})$ from orbital to diagonal subband basis:

$$\hat{h}_b(\boldsymbol{k}) = \hat{U}^{\dagger}(\boldsymbol{k})\hat{h}_t(\boldsymbol{k})\hat{U}(\boldsymbol{k}) = \varepsilon_{e,\boldsymbol{k}}\hat{\sigma}_+ + \varepsilon_{h,\boldsymbol{k}}\hat{\sigma}_-, \qquad \hat{U}_{\boldsymbol{k}} = e^{-i\hat{\sigma}_2\theta_{\boldsymbol{k}}/2}. \quad (5)$$

Here $\theta_{\boldsymbol{k}} = \arctan(\varepsilon_{xy,\boldsymbol{k}}/\varepsilon_{-,\boldsymbol{k}})$, $\sigma_\pm = (\sigma_0 \pm\sigma_3)/2$, and the energy eigenvalues:

http://dx.doi.org/10.5772/59629

$$\varepsilon_{h,e}(\boldsymbol{k}) = \varepsilon_{+,k} \pm \sqrt{\varepsilon_{xy,k}^{\ 2} + \varepsilon_{-,k}^{\ 2}}, \tag{6}$$

correspond to the two subbands in the normal state spectrum that respectively define electron and hole pockets of the Fermi surface. There are two segments of each type, defined by the equations $\varepsilon_{e,h}(\boldsymbol{k}) = \mu$, as shown in Fig. 2. We note that both functions $\cos\theta_k$ and $\sin\theta_k$ change their sign around each of these segments, corresponding to their "azimuthal dependencies" around the characteristic points of the 2D Brillouin zone (Fig. 2), so that integrals of these functions with some azimuthal-independent factors over the relevant vicinity of Fermi surface practically vanish and are neglected beside the integrals of fully azimuthal-independent functions in the analysis below.

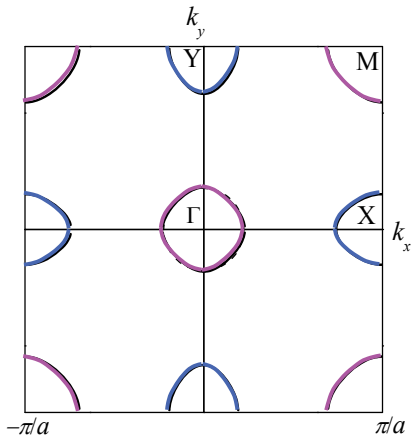

Figure 2. Electron (pink) and hole (blue) segments of the Fermi surface in the normal state of model system with electronic spectrum by Eq. 5. The dashed line around the Γ point marks a circular approximation (see after Eq. 11).

The adequate basis for constructing the SC state is generated by the operators of electron and hole subbands:

$$\begin{aligned} \alpha_{k,\sigma} &= x_{k,\sigma}\cos\theta_k/2 - y_{k,\sigma}\sin\theta_k/2, \\ \beta_{k,\sigma} &= y_{k,\sigma}\cos\theta_k/2 + x_{k,\sigma}\sin\theta_k/2, \end{aligned} \tag{7}$$

giving rise to the "multiband-Nambu" 4-spinors $\Psi_k^{\surd} = (\alpha_{k,\uparrow}^{\surd}, \alpha_{-k,\downarrow}, \beta_{k,\uparrow}^{\surd}, \beta_{-k,\downarrow})$ and to a 4×4 extension of the Hamiltonian Eq. (2) in the form:

$$H_s = \sum_{k,\sigma} \Psi_k^{+} \hat{h}_s(\boldsymbol{k}) \Psi_k, \tag{8}$$

where the 4×4 matrix

$$\hat{h}_s(\boldsymbol{k}) = \hat{h}_b(\boldsymbol{k}) \otimes \hat{\tau}_3 + \Delta_{\boldsymbol{k}} \hat{\sigma}_0 \otimes \hat{\tau}_1,$$

includes the Pauli matrices $\hat{\tau}_i$ acting on the Nambu (particle-antiparticle) indices in Ψ-spinors and $\hat{h}_b(k)$ is defined by Eq. (5). The simplified form for the extended *s*-wave SC order is realized with the definition of the gap function by constant values, $\Delta_{\boldsymbol{k}} = \Delta$ on the electron segments and $\Delta_{\boldsymbol{k}} = -\Delta$ on the hole segments.

The electronic dynamics of this system is determined by the (Fourier transformed) GF 4×4 matrices [58, 29, 54]:

$$\hat{G}_{\boldsymbol{k},\boldsymbol{k}'} = \left\langle\left\langle \Psi_{\boldsymbol{k}} \middle| \Psi_{\boldsymbol{k}'}{}^{\dagger} \right\rangle\right\rangle = i \int_{-\infty}^{0} dt \mathrm{e}^{i\varepsilon t/\hbar} \left\langle \Psi_{\boldsymbol{k}}(t), \Psi_{\boldsymbol{k}'}(0)^{\dagger} \right\rangle, \tag{9}$$

whose energy argument ε is understood as $\varepsilon - i0$ and $\langle A(t), B(0\rangle$ is the quantum statistical average with Hamiltonian H of the anticommutator of Heisenberg operators. From the equation of motion:

$$\varepsilon \hat{G}_{\boldsymbol{k},\boldsymbol{k}'} = \hbar \delta_{\boldsymbol{k},\boldsymbol{k}'} \hat{\sigma}_0 \otimes \hat{\tau}_0 + \left\langle\left\langle \left[\Psi_{\boldsymbol{k}}, H\right] \middle| \Psi_{\boldsymbol{k}'}{}^{\dagger} \right\rangle\right\rangle, \tag{10}$$

the explicit GF for the unperturbed SC system with the Hamiltonian H_s, Eq. (8), is diagonal in quasimomentum, $\hat{G}_{\boldsymbol{k},\boldsymbol{k}'} = \delta_{\boldsymbol{k},\boldsymbol{k}'} \hat{G}^0_{\boldsymbol{k}}$, with the diagonal term:

$$\hat{G}^0_{\boldsymbol{k}} = \frac{\varepsilon \hat{\tau}_0 + \varepsilon_{e,\boldsymbol{k}} \hat{\tau}_3 + \Delta \hat{\tau}_1}{2D_{e,\boldsymbol{k}}} \otimes \hat{\sigma}_+ + \frac{\varepsilon \hat{\tau}_0 + \varepsilon_{h,\boldsymbol{k}} \hat{\tau}_3 - \Delta \hat{\tau}_1}{2D_{h,\boldsymbol{k}}} \otimes \hat{\sigma}_-, \tag{11}$$

where the denominators $D_{i,\boldsymbol{k}} = \varepsilon^2 - \varepsilon_i^2(\boldsymbol{k}) - \Delta^2$ for $i = e, h$. Below we refer energy to the Fermi level ε_F, approximate the segments of Fermi surface by circles of radius k_i around the characteristic points K_i in the Brillouin zone, and linearize the dispersion laws near the Fermi level as $\varepsilon_j(\boldsymbol{k}) = \varepsilon_F + \xi_{j,\boldsymbol{k}}$ with $\xi_{j,\boldsymbol{k}} \approx \hbar v_j(|\boldsymbol{k} - \boldsymbol{K}_j| - k_j)$. Though the Fermi wavenumbers k_j and related Fermi velocities v_j for $j = e, h$ can somewhat differ at given hopping parameters and chemical potential, we shall neglect this difference and consider single values $k_j = k_F$ and $v_j = v_F$.

3. Impurity perturbation and self-energy

We pass to the impurity problem where local perturbation terms due to non-magnetic impurities [24] on random sites $\boldsymbol{p}$ in Fe square lattice with an on-site energy shift V:

$$H_{imp} = V \sum_{\boldsymbol{p},\sigma} \left(x_{\boldsymbol{p},\sigma}{}^{\dagger} x_{\boldsymbol{p},\sigma} + y_{\boldsymbol{p},\sigma}{}^{\dagger} y_{\boldsymbol{p},\sigma} \right), \tag{12}$$

are added to the Hamiltonian H_s. Without loss of generality, the parameter V can be taken positive, and this perturbation is suitably expressed in the multiband-Nambu basis:

$$H_{imp} = \frac{1}{N}\sum_{\boldsymbol{p},\boldsymbol{k},\boldsymbol{k}'} \mathrm{e}^{i(\boldsymbol{k}'-\boldsymbol{k})\cdot\boldsymbol{p}} \Psi_{\boldsymbol{k}}^{\dagger} \hat{V}_{\boldsymbol{k},\boldsymbol{k}'} \Psi_{\boldsymbol{k}'}. \tag{13}$$

through the 4×4 scattering matrix $\hat{V}_{\boldsymbol{k},\boldsymbol{k}'} = V\hat{U}_{\boldsymbol{k}}^{\dagger}\hat{U}_{\boldsymbol{k}'} \otimes \hat{\tau}_3$. From Eq. (5) for $\hat{U}_{\boldsymbol{k}}$, this matrix involves either "intraband" and "interband" elements [41]. The latter scattering could lead to a transition from $s_{\pm}$ to a competing s_{++} SC order (with the same sign of order parameter on both Fermi pockets) under impurity effect [43]. However, as shown below, such a possibility is effectively eliminated for the chosen local perturbation type, due to the specific quasimomentum $\boldsymbol{k}$-dependence of the scattering elements, unlike their constancy postulated in Ref. [43].

Following Refs. [29, 53], the solution for Eq. (10) with the perturbed Hamiltonian $H_s + H_i$ can be obtained in different forms, suitable for different types of states, band-like (extended) or localized. All these forms result from the basic equation of motion:

$$\hat{G}_{\boldsymbol{k},\boldsymbol{k}'} = \delta_{\boldsymbol{k},\boldsymbol{k}'}\hat{G}_{\boldsymbol{k}}^{0} + \frac{1}{N}\sum_{\boldsymbol{p},\boldsymbol{k}''} \mathrm{e}^{i(\boldsymbol{k}''-\boldsymbol{k})\cdot\boldsymbol{p}} \hat{G}_{\boldsymbol{k}}^{0}\hat{V}_{\boldsymbol{k},\boldsymbol{k}''}\hat{G}_{\boldsymbol{k}'',\boldsymbol{k}'}, \tag{14}$$

by specific routines of its iterating for the "scattered" GF's $\hat{G}_{\boldsymbol{k}'',\boldsymbol{k}'}$. Thus, the algorithm, where the next iteration step *never* applies to the scattered GF's already present after previous steps, e.g., to that with $\boldsymbol{k}'' = \boldsymbol{k}$ in Eq. (14), leads to the so-called fully renormalized form (RF), suitable for band-like states. Its result for the most relevant diagonal GF $\hat{G}_{\boldsymbol{k}} \equiv \hat{G}_{\boldsymbol{k},\boldsymbol{k}}$ reads:

$$\hat{G}_{\boldsymbol{k}} = \left[\left(\hat{G}_{\boldsymbol{k}}^{0}\right)^{-1} - \hat{\Sigma}_{\boldsymbol{k}}\right]^{-1}, \tag{15}$$

where the self-energy matrix $\hat{\Sigma}_{\boldsymbol{k}}$ is expressed by the related group expansion (GE):

$$\hat{\Sigma}_{\boldsymbol{k}} = c\hat{T}_{\boldsymbol{k}}\left(1 + c\hat{B}_{\boldsymbol{k}} + \ldots\right). \tag{16}$$

Here $c = \sum_{\boldsymbol{p}} N^{-1}$ is the impurity concentration (per Fe site) and the T-matrix results from all the multiple scatterings by a single impurity:

$$\hat{T}_{\boldsymbol{k}} = \hat{V}_{\boldsymbol{k},\boldsymbol{k}} + \frac{1}{N}\sum_{\boldsymbol{k}'\neq\boldsymbol{k}} \hat{V}_{\boldsymbol{k},\boldsymbol{k}'}\hat{G}_{\boldsymbol{k}'}^{0}\hat{V}_{\boldsymbol{k}',\boldsymbol{k}} + \frac{1}{N^2}\sum_{\boldsymbol{k}'\neq\boldsymbol{k}}\sum_{\boldsymbol{k}''\neq\boldsymbol{k},\boldsymbol{k}'} \hat{V}_{\boldsymbol{k},\boldsymbol{k}'}\hat{G}_{\boldsymbol{k}'}^{0}\hat{V}_{\boldsymbol{k}',\boldsymbol{k}''}\hat{G}_{\boldsymbol{k}''}^{0}\hat{V}_{\boldsymbol{k}'',\boldsymbol{k}} + \ldots. \tag{17}$$

The next term to the unity in the brackets in Eq. (16):

$$\hat{B}_{\boldsymbol{k}} = \sum_{\boldsymbol{n}}\left(\hat{A}_{\boldsymbol{n}}\mathrm{e}^{-i\boldsymbol{k}\cdot\boldsymbol{n}} + \hat{A}_{\boldsymbol{n}}\hat{A}_{-\boldsymbol{n}}\right)\left(1 + \hat{A}_{\boldsymbol{n}}\hat{A}_{-\boldsymbol{n}}\right)^{-1}, \tag{18}$$

describes the effects of indirect interactions in pairs of impurities, separated by vector $\boldsymbol{n}$, in terms of interaction matrices $\hat{A}_{\boldsymbol{n}}=\hat{T}_{\boldsymbol{k}}\sum_{\boldsymbol{k}'\neq\boldsymbol{k}} e^{i\boldsymbol{k}'\cdot\boldsymbol{n}}\hat{G}_{\boldsymbol{k}'}$. Besides this restriction on summation, multiple sums in the products like $\hat{A}_{\boldsymbol{n}}\hat{A}_{-\boldsymbol{n}}$ never contain coincident quasimomenta. Eq. (18) presents the first non-trivial GE term and its other terms omitted in Eq. (16) relate to the groups of three and more impurities [29].

An alternative iteration routine applies Eq. (14) to *all* the scattered GF's, leading to the so-called non-renormalized form (NRF), suitable for localized states:

$$\hat{G}_{\boldsymbol{k}}=\hat{G}^0_{\boldsymbol{k}}+\hat{G}^0_{\boldsymbol{k}}\hat{\Sigma}^0_{\boldsymbol{k}}\hat{G}^0_{\boldsymbol{k}}, \tag{19}$$

The NRF self-energy admits a GE: $\hat{\Sigma}^0_{\boldsymbol{k}}=c\hat{T}^0_{\boldsymbol{k}}\left(1+c\hat{B}^0_{\boldsymbol{k}}+\ldots\right)$, that differs from the RF one by no restrictions in $\boldsymbol{k}$-sums for T-matrix, interaction matrices $\hat{A}^0_{\boldsymbol{n}}=\hat{T}^0_{\boldsymbol{k}}\sum_{\boldsymbol{k}'} e^{i\boldsymbol{k}'\cdot\boldsymbol{n}}\hat{G}^0_{\boldsymbol{k}'}$ and their products.

At the first step, we restrict GE to the common T-matrix level to find the possibilities for localized quasiparticle states and related in-gap energy levels by single impurities [21]. Next, at finite impurity concentrations, formation of (narrow) energy bands of specific collective states near these levels is studied. Finally, the criteria for such collective states to really exist in the disordered SC system follow from the analysis of non-trivial GE terms. We notice that RF for GF's $\hat{G}_{\boldsymbol{k}'}$ in the above interaction matrices is just necessary for adequate treatment of interaction effects within the in-gap bands. To simplify the T-matrix, Eq. (17), note that $\hat{V}_{\boldsymbol{k},\boldsymbol{k}}=V\hat{\sigma}_0\otimes\hat{\tau}_3$ and use the integrated GF matrix:

$$\hat{G}_0=\frac{1}{N}\sum_{\boldsymbol{k}}\hat{U}_{\boldsymbol{k}}\hat{G}^0_{\boldsymbol{k}}\hat{U}^{\dagger}_{\boldsymbol{k}}=\varepsilon\left[g_e\left(\varepsilon\right)\hat{\sigma}_{+}+g_h\left(\varepsilon\right)\hat{\sigma}_{-}\right]\otimes\hat{\tau}_0.$$

This diagonal form (restricted only to the "intraband" matrix elements) follows from the aforementioned cancellation of integrals with $\cos\theta_{\boldsymbol{k}}$ and $\sin\theta_{\boldsymbol{k}}$ in the "interband" matrix elements of $\hat{U}_{\boldsymbol{k}}\hat{G}^0_{\boldsymbol{k}}\hat{U}^{\dagger}_{\boldsymbol{k}}$. This permits to consider below the SC order unchanged under the impurity effects.

The functions $g_j(\varepsilon)=N^{-1}\sum_{\boldsymbol{k}} D_{j,\boldsymbol{k}}{}^{-1}$ for $j=e,h$ are approximated near ε_{F}, $|\varepsilon-\varepsilon_{\mathrm{F}}|\ \delta\ \Delta$, as:

$$g_j\left(\varepsilon\right)\approx-\frac{\pi\rho_j}{\sqrt{\Delta^2-\varepsilon^2}}. \tag{20}$$

Here $\rho_j=m_j a^2/(2\pi\hbar^2)$ are the Fermi densities of states for respective subbands (in parabolic approximation for their dispersion laws), and by the assumed identity of the Fermi segments they can be also considered identical $\rho_j=\rho_{\mathrm{F}}$, so that $g_j(\varepsilon)=g(\varepsilon)=-\pi\rho_{\mathrm{F}}/\sqrt{\Delta^2-\varepsilon^2}$. Omitted terms in Eq. (20) are of higher orders in the small parameter $\varepsilon/\varepsilon_{\mathrm{F}}\ll 1$. Then the momentum independent T-matrix is explicitly written as:

$$\hat{T}(\varepsilon)=\frac{V}{1+v^2}\frac{\varepsilon^2-\Delta^2+v\varepsilon\sqrt{\Delta^2-\varepsilon^2}\hat{\tau}_3}{\varepsilon^2-\varepsilon_0{}^2}, \tag{21}$$

it presents two symmetric poles within the gap, at $\varepsilon=\pm\varepsilon_0=\pm\Delta/\sqrt{1+v^2}$ [21], with the dimensionless impurity perturbation parameter $v=\pi\rho_F V$. Near these poles, Eq. (21) can be approximated as:

$$\hat{T}(\varepsilon)\approx\gamma^2\frac{\varepsilon-\varepsilon_0\hat{\tau}_3}{\varepsilon^2-\varepsilon_0{}^2}, \tag{22}$$

where $\gamma^2=V\Delta v^2/(1+v^2)^{3/2}$ is the effective constant of coupling between localized and band quasiparticles. At finite c, this T-matrix can be used in Eqs. (16) and (15) and then in the formal dispersion equation: $\mathrm{Re}\det\hat{G}_{\boldsymbol{k}}{}^{-1}=0$ [57], to obtain the dispersion laws of perturbed SC system in terms of the normal quasiparticles dispersion $\xi_{\boldsymbol{k}}=\varepsilon_{\boldsymbol{k}}-\varepsilon_F\equiv\xi$. They follow from the general expression: $\mathrm{Re}\left(\tilde{\varepsilon}^2-\Delta^2-\tilde{\xi}^2\right)=0$, with $\tilde{\varepsilon}=\varepsilon\left(1-cVv\sqrt{1-\varepsilon^2/\Delta^2}/\left(\varepsilon^2/\varepsilon_0{}^2-1\right)\right)$ and $\tilde{\xi}=\xi+cV\left(\varepsilon^2/\Delta^2-1\right)/\left(\varepsilon^2/\varepsilon_0{}^2-1\right)$, and display a peculiar multiband structure shown in Fig. 3.

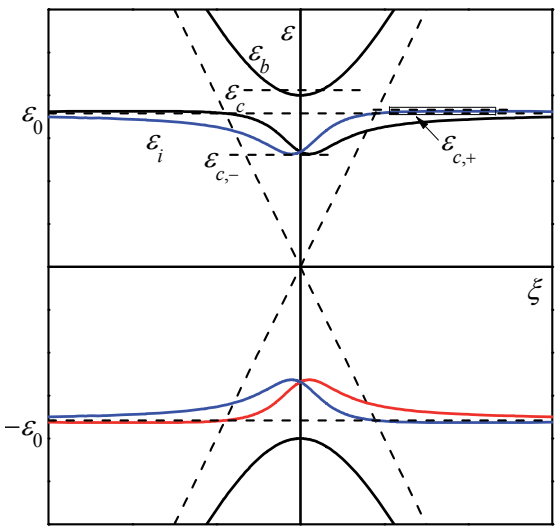

Figure 3. Dispersion laws for band-like quasiparticles in the T-matrix approximation, neglecting their finite lifetime, at a specific choice of impurity parameters $v=1$, $c=0.1\Delta^2/\gamma^2$. The argument ξ composes all specific $\xi_j=\hbar v_F(|\boldsymbol{k}-\boldsymbol{K}_j|-k_F)$ for $\boldsymbol{k}$ near each j-th characteristic point in the Brillouin zone (see in the text), blue lines are for impurity bands near electron-like Fermi segments and red lines do for those near hole-like segments. The single-impurity localized levels are shown with dashed lines. The narrow rectangle around the top of ε_i-band (shown by the arrow) delimits the region in Fig. 5.

First of all, there are modified initial bands

$$\varepsilon_b(\xi) \approx \varepsilon(\xi) + i\Gamma(\xi), \tag{23}$$

whose main difference from the unperturbed SC bands with dispersion $\varepsilon(\xi)=\sqrt{\Delta^2+\xi^2}$ is a finite linewidth $\Gamma(\xi) \sim cV v\xi\Delta/[(1+v^2)(\xi^2+\xi_0^2)]$, $\xi_0^2=\Delta^2-\varepsilon_0^2$, defined by the T-matrix term of the self-energy, Eq. (16). It should be noted that these subbands for opposite signs of their argument ξ in fact refer to excitations around different Fermi segments (by electron and holes), but for clarity all four ε_b bands are set in Fig. 3 in the same ξ-reference. Then from the IRM criterion of band-like states:

$$\xi\frac{\partial}{\partial\xi}\varepsilon_b(\xi) \leftrightarrow \Gamma(\xi), \tag{24}$$

the position of mobility edge ε_c for these bands is estimated as: $\varepsilon_c - \Delta \sim (c/c_1)^2\Delta$, with $c_1 = \pi\rho_F\Delta \ll 1$. Besides the ε_b bands, there appear also four (narrow) in-gap ε_i bands, generated close to ε_0 at finite concentration of impurities, accordingly to:

$$\varepsilon_i(\xi) \approx \varepsilon_0 + c\gamma^2\frac{\xi-\varepsilon_0}{\xi^2+\xi_0^2}, \tag{25}$$

As follows from Eq. (25), the ε_i band has its extrema $\varepsilon_{max} = \varepsilon_0 + c\gamma^2/(\Delta+\varepsilon_0)$ at $\xi_+ = \Delta + \varepsilon_0$ and $\varepsilon_{min} = \varepsilon_0 - c\gamma^2/(\Delta-\varepsilon_0)$ at $\xi_- = \Delta - \varepsilon_0$. The energy and momentum shifts of these extremal points seen in Fig. 3 specify the impurity effect on a multiband initial spectrum, compared to a simpler situation for an impurity level near the edge of a single quasiparticle band [29].

All these spectrum bands would contribute to the overall density of states (DOS) by the related quasiparticles: $\rho(\varepsilon) = (4\pi N)^{-1}$ Im Tr $\sum_{\boldsymbol{k}} \hat{G}_{\boldsymbol{k}}$. More common contributions there come from the ε_b bands and they can be expressed through the Bardeen-Cooper-Schrieffer (BCS) DOS in pure crystal [57]: $\rho_{BCS}(\varepsilon, \Delta) = \rho_F\varepsilon/\sqrt{\varepsilon^2-\Delta^2}$, as follows:

$$\rho_b(\varepsilon) \approx \rho_{BCS}(\varepsilon,\Delta) - \frac{2cv^2\varepsilon\sqrt{\varepsilon^2-\Delta^2}}{\pi\varepsilon_F(1+v^2)(\varepsilon^2-\varepsilon_0^2)}, \tag{26}$$

at $\varepsilon^2 \leftrightarrow \varepsilon_c^2$. The second term in the r.h.s. of Eq. (26) describes a certain reduction of the BCS DOS at energies farther from the gap limits.

More peculiar contributions to DOS come from the ε_i bands, written as:

http://dx.doi.org/10.5772/59629

$$\rho_i(\varepsilon) \approx \frac{\rho_F}{v} \frac{\varepsilon^2 - \varepsilon_0{}^2 - c\gamma^2}{\sqrt{\left(\varepsilon_{max}{}^2 - \varepsilon^2\right)\left(\varepsilon^2 - \varepsilon_{min}{}^2\right)}}, \tag{27}$$

at $\varepsilon_{min}{}^2 \uparrow \varepsilon^2 \uparrow \varepsilon_{max}{}^2$, and presented in Fig. 4.

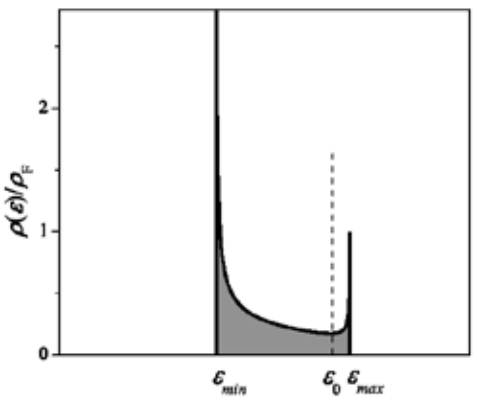

Figure 4. Density of states in the narrow in-gap band near the impurity level ε_0 (dashed line) for the case by Fig. 3.

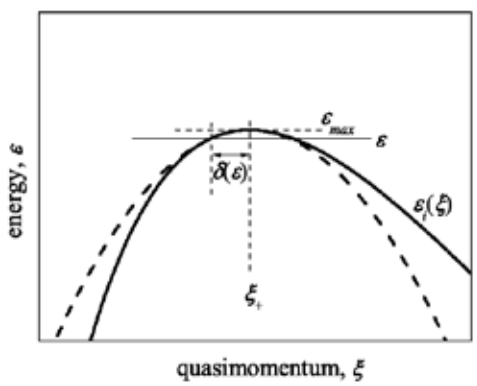

Figure 5. Parabolic approximation (dashed line) for the dispersion law near the top of impurity band (solid line), within the region indicated by a small rectangle in Fig. 3.

Formation of the ε_i bands can have important repercussions in the physical behavior of a disordered SC system and they will be considered below. But before this, we need to analyze the criteria for the considered quasiparticles to really exist, especially in closeness to the limits of corresponding bands and this requires a more involved analysis of non-trivial GE terms for self-energy.

4. Group expansion and Ioffe-Regel-Mott criteria

Let us now study the crossover from band-like to localized states near the limits of ε_i bands, say for definiteness, near its upper limit ε_{max}. Supposing the actual energy $\varepsilon < \varepsilon_{max}$ to be within the range of band-like states, we use the RF self-energy matrix, Eq. (16), up to the GE pair term, $c^2\hat{T}\hat{B}_{\boldsymbol{k}}$, that will add a certain finite imaginary part $\Gamma_i(\varepsilon)$ to the dispersion law $\varepsilon = \varepsilon_i(\xi)$, Eq. (25). Then the IRM criterion for a state at this energy be really band-like (also called extended) is written as:

$$\varepsilon_{max} - \varepsilon \gg \Gamma_i(\varepsilon). \tag{28}$$

To simplify calculation of the scalar function $\Gamma_i(\varepsilon)$, we fix the energy argument in the numerators of T-matrix and interaction matrices at $\varepsilon = \varepsilon_0$, obtaining their forms:

$$\hat{T}(\varepsilon) \approx \frac{\gamma^2 \varepsilon_0}{\varepsilon^2 - {\varepsilon_0}^2}\hat{m}_{+,} \qquad \hat{A}_{\boldsymbol{n}}(\varepsilon) \approx \hat{T}(\varepsilon)\frac{\varepsilon}{N}\sum_{\boldsymbol{k}}\frac{e^{i\boldsymbol{k}\cdot\boldsymbol{n}}}{D_{\boldsymbol{k}}(\varepsilon)}, \tag{29}$$

both proportional to the matrix $\hat{m}_+ = \hat{\sigma}_0 \otimes (\hat{\tau}_0 + \hat{\tau}_3)$ with important multiplicative property: $\hat{m}_+^2 = 2\hat{m}_+$. The $\boldsymbol{k}$-summation (integration) in Eq. (29) is suitably done in polar coordinates over the circular segments of Fermi surface. Here the azimuthal integration only refers to the phase of numerator, resulting in zeroth order Bessel function: $\int_0^{2\pi} e^{ix\cos\theta} d\theta = 2\pi J_0(x)$. Since $x = n(k_F + \xi/\hbar v_F)$ is typically big, $x \gg 1$, the asymptotical formula applies: $J_0(x) \approx \sqrt{2/\pi x}\cos(x - \pi/4)$. Then, for radial integration in ξ around the extremum point ξ_+, it is convenient to decompose this function into fast and slow oscillating factors: $J_0(x) \approx \sqrt{2/(\pi k_+ n)}\cos(k_+ n - \pi/4)\cos[(\xi - \xi_+)n/\hbar v_F]$ with the fast wavenumber $k_+ = k_F + \xi_+/\hbar v_F \approx k_F$, and to write the denominator in the parabolic approximation: $D_\xi(\varepsilon) \approx (\xi - \xi_+)^2 - \delta^2(\varepsilon)$, with $\delta^2(\varepsilon) = 4\Delta(\Delta + \varepsilon_0)^2(\varepsilon_{max} - \varepsilon)/(2c\gamma^2)$ (see Fig. 5). Thus, the interaction matrix $\hat{A}_{\boldsymbol{n}}(\varepsilon) = A_{\boldsymbol{n}}(\varepsilon)\hat{m}_+$ only depends on the distance n between impurities, and, for ε close to ε_{max}, this dependence can be expressed as:

$$A_r(\varepsilon) \approx \sqrt{\frac{r_\varepsilon}{r}}\sin k_\varepsilon r \cos k_F r, \tag{30}$$

where the length scales both for the monotonous decay:

$$r_\varepsilon = \frac{2\pi}{k_F}\left[\frac{\varepsilon_0 \rho_F(\Delta + \varepsilon_0)}{c\delta(\varepsilon)}\right]^2,$$

http://dx.doi.org/10.5772/59629

and for the sine factor: $k_\varepsilon^{-1} = \hbar v_F/\delta(\varepsilon)$, are much longer than k_F^{-1} for the fast cosine. The latter fast oscillation is specific for the interactions mediated by Fermi quasiparticles (like the known RKKY mechanism), unlike the monotonous or slowly oscillating interactions between impurities in semiconductors or in bosonic systems [29].

Now calculation of $\Gamma_i(\varepsilon) = c^2 T(\varepsilon)\ \mathrm{Im}\ B(\varepsilon)$ mainly concerns the dominant scalar part of the GE pair term:

$$B(\varepsilon) \approx \frac{2\pi}{a^2}\int_a^{r_\varepsilon} \frac{rdr}{1-4A_r^{\ 2}(\varepsilon)}, \tag{31}$$

(since the $\boldsymbol{k}$-dependent term in Eq. (18) turns to be negligible beside this). The upper integration imit in Eq. (31) refers to the fact that its integrand only has poles for $r < r_\varepsilon$. With respect to the slow and fast modes in the function, Eq. (30), the integration is naturally divided in two stages. At the first stage, integration over each m-th period of fast cosine, around $r_m = 2\pi m/k_F$, is done setting the slow factors, $\$r \approx r_m$ and $\sin k_\varepsilon r \approx \sin k_\varepsilon r_m$ constant, and using the explicit formula:

$$\mathrm{Im}\int_{-\pi}^{\pi} \frac{dx}{1-4A^2\cos^2 x} = \mathrm{Im}\,\frac{\pi}{\sqrt{1-A^2}}.$$

At next stage, summation of these results in m is approximated by integration in slow variable:

$$\frac{\pi}{k_F}\mathrm{Im}\sum_m \frac{r_m^{\ 3/2}}{\sqrt{r_m - r_\varepsilon \sin^2 k_\varepsilon r_m}} \approx \mathrm{Im}\int_a^{r_\varepsilon} \frac{r^{3/2}}{\sqrt{r - r_\varepsilon \sin^2 k_\varepsilon r}}. \tag{32}$$

Numerical calculation of the latter integral results in:

$$\mathrm{Im}\,B = \frac{r_\varepsilon^{\ 2}}{a^2} f\left(k_\varepsilon r_\varepsilon\right), \tag{33}$$

where the function $f(z)$ is zero for $z < z_0 \approx 1.3585$, and monotonously grows for $z > z_0$, rapidly reaching the asymptotic constant value: $f_{as} \approx 1.1478$, for $z \gg z_0$. Then the IRM criterion, Eq. (28), at ε so close to ε_{max} that $k_\varepsilon\, r_\varepsilon \gg z_0$, is expressed as:

$$\varepsilon_{max} - \varepsilon \gg \frac{c\gamma^2}{\varepsilon_{max} - \varepsilon_0}\frac{r_\varepsilon^{\ 2}}{a^2}, \tag{34}$$

giving an (c-independent) estimate for the range of extended states within the impurity band:

$$\varepsilon_{max} - \varepsilon \gg \Gamma_0 = \frac{\left(v\varepsilon_0\right)^{3/2}}{ak_F}\sqrt{\frac{2\pi\rho_F}{1+v^2}}. \tag{35}$$

Its comparison with the full extension of this band, $\varepsilon_{max} - \varepsilon_{min} = c\gamma^2(1 + v^2)/(v^2\Delta)$, would suggest a possibility for such extended states to really exist if the impurity concentration surpasses the characteristic (small) value:

$$c \gg c_0 = \frac{\left(\pi\rho_F\varepsilon_0\right)^{3/2}}{ak_F}\sqrt{\frac{2v}{1+v^2}}. \tag{36}$$

For typical values of $\rho_F^{-1} \sim 2$ eV, $ak_F \sim 1$, and $\Delta \sim 10$ meV in LaOFeAs system [8, 13, 58], and supposing a plausible impurity perturbation $v \sim 1$, we estimate $c_0 \approx 8\ 10^{-4}$, manifesting important impurity effects already at their very low content.

However, the r. h. s. of Eq. (33) vanishes at $k_\varepsilon r_\varepsilon < z_0$, which occurs beyond the vicinity of the band top:

$$\varepsilon_{max} - \varepsilon > \left(\frac{c_0}{c}\right)^3 \Gamma_0. \tag{37}$$

Under the condition of Eq. (36), this vicinity is yet narrower than Γ_0 by Eq. (35), defining the true, even wider, range of extended states within the impurity band.

Otherwise, for $c \ll c_0$, the impurity band does not exist at all, then we analyze the energy range near the impurity level with the NRF GE and write an approximate criterion for its convergence as $c|B^0| \ll 1$. This calculation is done in a similar way to as before but replacing the interaction function, Eq. (29), by its NRF version:

$$A_r^0\left(\varepsilon\right) \approx \sqrt{\frac{R_\varepsilon}{r}}\mathrm{e}^{-r/r_0}\cos k_F r, \tag{38}$$

with $k_F R_\varepsilon = 2\pi(\varepsilon_0/|\varepsilon - \varepsilon_0|)^2$ and $k_F r_0 = 2\varepsilon_F/\xi_0$. Then the above GE convergence criterion is assured beyond the following vicinity of impurity level:

$$\left|\varepsilon - \varepsilon_0\right| \gg \Gamma_0 \exp\left(-\frac{c_0^{4/3}}{c}\right), \tag{39}$$

defining its broadening due to inter-impurity interactions. Within this range, the DOS function for localized states can be only estimated by the order of magnitude, but outside it is given by:

$$\begin{aligned} \rho_{loc}\left(\varepsilon\right) &\approx \frac{c^2}{c_0^{4/3}}\left|\varepsilon - \varepsilon_0\right|, \quad \text{for} \quad \Gamma_c \ll \left|\varepsilon - \varepsilon_0\right| \ll \Gamma_0, \\ \rho_{loc}\left(\varepsilon\right) &\approx \frac{c^2\varepsilon_0^{\ 4}}{\left|\varepsilon - \varepsilon_0\right|^5}, \quad \text{for} \quad \Gamma_0 \ll \left|\varepsilon - \varepsilon_0\right|, \end{aligned} \tag{40}$$

http://dx.doi.org/10.5772/59629

Notably, the total number of states near the impurity level is

$$\int \rho_{loc}(\varepsilon) d\varepsilon \sim c,$$

alike that of extended states in the impurity band by Eq. (26). The summary of evolution of this area of quasiparticle spectrum in function of impurity concentration is shown in Fig. 7.

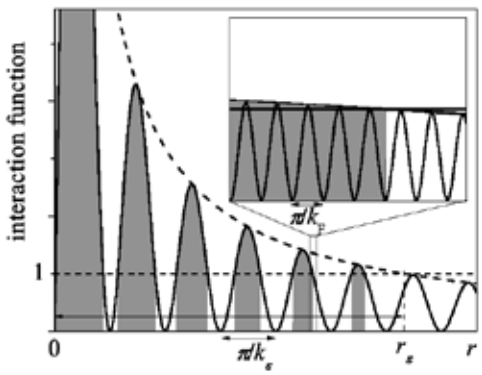

Figure 6. Interaction function $A^2_r(\varepsilon)$ by Eq. 29 at the choice of parameters $\varepsilon_{max} - \varepsilon = 0.1$ and $\Delta/\varepsilon_F = 5\ 10^{-2}$ displays slower sine oscillations (solid line) and the monotonous envelope function (dashed line). The shadowed intervals are those contributing to Im B, accordingly to the condition $(r_\varepsilon/r)\sin^2 k_\varepsilon r > 1$. Inset: the expansion of the rectangle in the main panel shows also faster oscillations by the cosine.

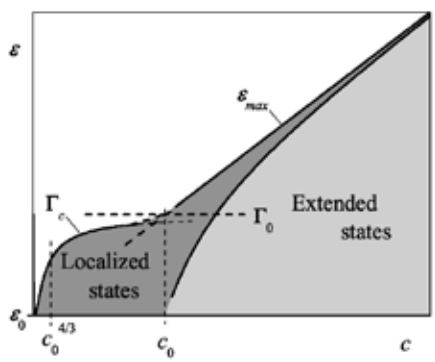

Figure 7. Composition of the energy spectrum near the impurity level ε_0 in function of impurity concentration.

5. Impurity effects on superconducting characteristics

The above results on the quasiparticle spectrum in the disordered SC system can be immediately used for calculation of impurity effects on its observable characteristics. Thus the fundamental SC order parameter Δ is estimated from the modified gap equation:

$$\lambda^{-1} = \int_0^{\varepsilon_D} \mathrm{Im}\ \mathrm{Tr}\ \hat{G}(\varepsilon)\hat{\tau}_1 d\varepsilon, \tag{41}$$

where $\hat{G}(\varepsilon)=N^{-1}\sum_{\boldsymbol{k}} \hat{G}_{\boldsymbol{k}}(\varepsilon)$, $\lambda = \rho_F V_{SC}$ is the (small) dimensionless SC pairing constant, and the Debye energy ε_D restricts the energy range of its action. In absence of impurities, $c = 0$, using of Eq. (11) leads straightforwardly to the known result for the non-perturbed Δ_0 value: λ^{-1} = arccosh (ε_D/Δ_0) and thus $\Delta_0 \approx 2\varepsilon_D\, e^{-1/\lambda}$.

For finite c, contributions to Eq. (41) come both from the main band, Eq. (25), and from the impurity band (or level), Eqs. (26) (or (40)). The latter contribution is ~ c, accordingly to the previous discussion, defining a small correction beside $\lambda^{-1} \gg 1$. But a much stronger c-dependent correction comes from the modified main band (limited to its range of extended states):

$$\int_{\varepsilon_c}^{\varepsilon_D} \frac{d\varepsilon}{\sqrt{\varepsilon^2 - \Delta^2}} = \mathrm{arccosh}\frac{\varepsilon_D}{\Delta} - \mathrm{arccosh}\frac{\varepsilon_c}{\Delta}.$$

For $\varepsilon_c - \Delta \sim (c/c_1)^2\Delta$ (see after Eq. (24)) and $c \grave{} c_1$, the last term is well approximated by:

$$\mathrm{arccosh}\frac{\varepsilon_c}{\Delta} \approx \sqrt{2}\frac{c}{c_1},$$

and leads to the modified gap equation as:

$$\mathrm{arccosh}\frac{\varepsilon_D}{\Delta} - \mathrm{arccosh}\frac{\varepsilon_D}{\Delta_0} \approx \sqrt{2}\frac{c}{c_1}, \tag{42}$$

Its approximate solution for $c \ll c_1$ describes the initial decay of SC order parameter with impurity concentration as:

$$\Delta \approx \Delta_0\left(1 - \sqrt{2}\frac{c}{c_1}\right), \tag{43}$$

and for the values of ρ_F and Δ_0 used above, the estimate of characteristic concentration c_1 is quite low: $c_1 \sim 10^{-2}$ (though higher than c_0 by Eq. (36)), suggesting a very strong impurity effect. With further growing c up to $c \prec c_1$, the value of Δ from Eq. (43) would formally tend to zero as $\approx \Delta_0(c_1/c)^2/2$. However, concentrations $c \sim c_1$ would already correspond to the impurity band as wide as the gap itself; this goes beyond the validity of the present approach and needs a special treatment.

http://dx.doi.org/10.5772/59629

To study another important dependence, that of the SC transition temperature T_c on concentration c, one has, strictly speaking, to extend the above GF techniques for finite temperatures, but a very simple estimate can be done, supposing that the BCS relation $\Delta/T_c \approx 1.76$ still holds in the presence of impurities. Then the r.h.s. of Eq. (44) would also describe the decay of T_c/T_{c0}.

It is of interest to compare the present results with the known Abrikosov-Gor'kov solution for BCS SC with paramagnetic impurities in the Born approximation [59, 60]. In that approximation, the only perturbation parameter is the (constant) quasiparticle lifetime τ. In our framework, τ^{-1} can be related to Im $\Sigma(\varepsilon)$ at a proper choice of energy, $\varepsilon \sim |\Delta - \varepsilon| \sim \Delta$. Then, in the self-consistent T-matrix approximation \cite{psl}, we estimate $\tau^{-1} \sim c\Delta/c_1$ which leads to the relation $\tau T_c \sim c_1/(1.76c)$, reaching at $c \sim c_1$ a good agreement with the Abrikosov-Gor'kov universal criterion for complete SC suppression $\tau T_c < 0.567$.

Also, a notable impurity effect is expected on the London penetration depth $\lambda_L \sim n_s^{1/2}$, as follows from the temperature dependence of superfluid density:

$$n_s(T) = \int_0^\infty \frac{\rho(\varepsilon)d\varepsilon}{e^{\varepsilon/k_BT}+1} \approx n_s^0(T) - \frac{cv^2}{1+v^2}\frac{\Delta}{\varepsilon_F}\sqrt{\frac{k_BT}{\pi\Delta}}e^{-\Delta/k_BT} + \frac{c}{e^{\varepsilon_0/k_BT}+1}. \quad (44)$$

When compared to its unperturbed value in the pure SC system

$$n_s^0(T) = \rho_F \int_\Delta^\infty \frac{\varepsilon d\varepsilon}{\left(e^{\varepsilon/k_BT}+1\right)\sqrt{\varepsilon^2-\Delta^2}} \approx c_1\sqrt{\frac{k_BT}{2\pi\Delta}}e^{-\Delta/k_BT},$$

the effect by the last term in Eq. (45) produces a considerable slowing down of the low-temperature decay of the difference $\lambda(T)/\lambda(0) - 1$ (Fig. 8), in a reasonable agreement with recent experimental observations for SC iron pnictides under doping [47].

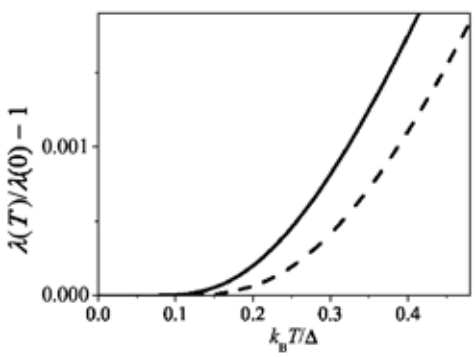

Figure 8. Low-temperature decay of the London penetration depth difference for a SC with impurities (solid line) is slower than that in absence of impurities (dashed line).

Finally, a similar analysis can be applied for the impurity effect on the electronic specific heat in the SC state, whose dependence on inverse temperature $\beta = 1/(k_B T)$ is represented as:

$$C(\beta) = \frac{\partial}{\partial \beta} \int_0^\infty \frac{\varepsilon \rho(\varepsilon) d\varepsilon}{e^{\beta\varepsilon} + 1}, \tag{45}$$

and naturally divided in two characteristic contributions, $C = C_i + C_b$, from ρ_i and ρ_b states:

$$C_i(\beta) \approx c k_B \left[\frac{\beta \varepsilon_0}{2\cosh(\beta\varepsilon_0 / 2)} \right]^2,$$

$$C_b(\beta) \approx k_B (c_1 - c) v (\beta\Delta)^{3/2} \exp(-\beta\Delta).$$

The resulting function $C(\beta)$ deviates from the known low temperature behavior $C_0(\beta) \sim \exp(-\beta\Delta)$ for non-perturbed SC system at $\beta > \ln(c_1/c - 1)/(\Delta - \varepsilon_0)$, where the characteristic exponent is changed to a slower $\sim \exp(-\beta\varepsilon_0)$ as seen in Fig. 9.

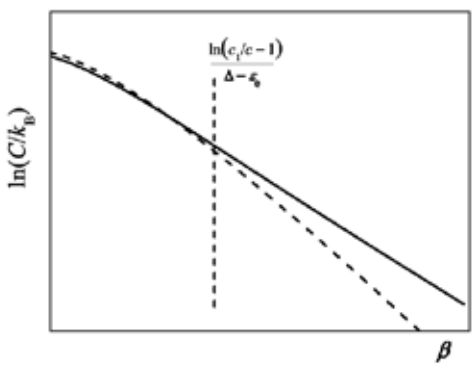

Figure 9. Temperature behavior of specific heat for a SC with impurities presents a crossover from $\beta\Delta$ exponent (dashed line) to $\beta\varepsilon_0$ at low enough temperature (high enough $\beta = 1/(k_B T)$).

The same approach can be then used for other observable characteristics for SC under impurity effect, such as, e.g., heat conductivity, differential conductivity for scanning tunneling spectroscopy or absorption coefficient for far infrared radiation that is done in the next section.

6. Kubo-Greenwood formalism for multiband superconductor

The relevant kinetic coefficients for electronic processes in the considered disordered superconductor follow from the general Kubo-Greenwood formulation [55, 56], adapted here to the

http://dx.doi.org/10.5772/59629

specific multiband structure of Green function matrices. Thus, one of the basic transport characteristics, the (frequency and temperature dependent) electrical conductivity is expressed in this approach as:

$$\sigma(\omega,T)=\frac{e^2}{\pi}\int d\varepsilon\frac{f(\varepsilon)-f(\varepsilon')}{\omega}\int d\boldsymbol{k}v_x(\boldsymbol{k},\varepsilon)v_x(\boldsymbol{k},\varepsilon')\ \mathrm{Tr}\left[\mathrm{Im}\,\hat{G}_{\boldsymbol{k}}(\varepsilon)\mathrm{Im}\,\hat{G}_{\boldsymbol{k}}(\varepsilon')\right], \tag{46}$$

for $\varepsilon' = \varepsilon - \hbar\omega$ and the electric field applied along the x-axis. Besides the common Fermi occupation function $f(\varepsilon) = (e^{\beta\varepsilon} + 1)^{-1}$, the above formula involves the generalized velocity function:

$$\boldsymbol{v}(\boldsymbol{k},\varepsilon)=\left(\hbar\frac{\partial\ \mathrm{Re}\,D_{\boldsymbol{k}}(\varepsilon)}{\partial\varepsilon}\right)^{-1}\nabla_{\boldsymbol{k}}\mathrm{Re}\,D_{\boldsymbol{k}}(\varepsilon). \tag{47}$$

This function is defined in the whole ξ, ε plane in a way to coincide with the physical quasiparticle velocities for each particular band, Eqs. (23, 24), along the corresponding dispersion laws: $\boldsymbol{v}(\boldsymbol{k}, \varepsilon_j(\boldsymbol{k})) = \hbar^{-1}\nabla_k\varepsilon_j(k) = v_{j,k}$, $j = b, i$. The conductivity resulting from Eq. (48) can be then used for calculation of optical reflectivity.

Other relevant quantities are the static (but temperature dependent) transport coefficients, as the heat conductivity:

$$\kappa(T)=\frac{\hbar}{\pi}\int d\varepsilon\frac{\partial f(\varepsilon)}{\partial\varepsilon}\int d\boldsymbol{k}\left[v_x(\boldsymbol{k},\varepsilon)\right]^2\ \mathrm{Tr}\left[\mathrm{Im}\,\hat{G}_{\boldsymbol{k}}(\varepsilon)\right]^2, \tag{48}$$

and the thermoelectric coefficients associated with the static electrical conductivity $\sigma(T) \equiv \sigma(0, T)$ [62], the Peltier coefficient:

$$\Pi(T)=\frac{\hbar e}{\pi\sigma(T)}\int d\varepsilon\frac{\partial f(\varepsilon)}{\partial\varepsilon}\varepsilon\int d\boldsymbol{k}\left[v_x(\boldsymbol{k},\varepsilon)\right]^2\ \mathrm{Tr}\left[\mathrm{Im}\,\hat{G}_{\boldsymbol{k}}(\varepsilon)\right]^2, \tag{49}$$

and the Seebeck coefficient $S(T) = \Pi(T)/T$. All these transport characteristics, though being relatively more complicated from the theoretical point of view than the purely thermodynamical quantities from the previous section, permit an easier and more reliable experimental verification and so could be of higher interest for practical applications of the considered impurity effects in the multiband superconductors.

It is worth to recall that the above formulae are only contributed by the band-like states, that is the energy arguments ε, ε' in Eqs. (47, 49, 50) are delimited by the relevant mobility edges.

This is the main distinction of our approach from the existing treatments of impurity effects on transport in iron pnictide superconductors using the T-matrix approximation to a solution like Eq. (15) for the whole energy spectrum [62], even for its ranges where the very concept of velocity, as Eq. (48), ceases to be valid.

Next, we consider the particular calculation algorithms for the expressions, Eqs. (47, 49, 50), for the more involved case of dynamical conductivity, Eq. (47), that can be then reduced to simpler static quantities, Eqs. (49, 50).

7. Optical conductivity

The integral in Eq. (47) is dominated by the contributions from δ-like peaks of the Im $\hat{G}_{\boldsymbol{k}}(\varepsilon)$ and Im $G_{\boldsymbol{k}}(\varepsilon')$ matrix elements. These peaks arise from the above dispersion laws, Eqs. (23), (24), thus restricting the energy integration to the band-like ranges: $|\varepsilon| > \varepsilon_c$ for the *b*-bands and $\varepsilon_{c,-} < |\varepsilon| < \varepsilon_{c,+}$ for the *i*-bands. Regarding the occupation numbers $f(\varepsilon)$ and $f(\varepsilon')$ at reasonably low temperatures $k_B T \ll \Delta, \varepsilon_0$, the most effective contributions correspond to positive ε values, either from *b*- or *i*-bands, and to negative ε' values from their negative counterparts, *b*' or *i*'. There are three general kinds of such contributions: i) *b*-*b*', due to transitions between the main bands, similar to those in optical conductivity by the pure crystal (but with a slightly shifted frequency threshold: $\hbar\omega \to 2\varepsilon_c$), ii) *b*-*i*' (or *i*-*b*'), due to combined transitions between the principal and impurity bands within the frequency range $\hbar\omega \to \varepsilon_c + \varepsilon_{c,-}$, and iii) *i*-*i*', due to transitions between the impurity bands within a narrow frequency range of $2\varepsilon_{c,-} < \hbar\omega < 2\varepsilon_{c,+}$. The frequency-momentum relations for these processes and corresponding peaks are displayed in Fig. 10. The resulting optical conductivity reads $\sigma(\omega, T) = \sum_\alpha \sigma_\alpha(\omega, T)$ with $\alpha = b\text{-}b', i\text{-}i'$, and *i*-*b*'.

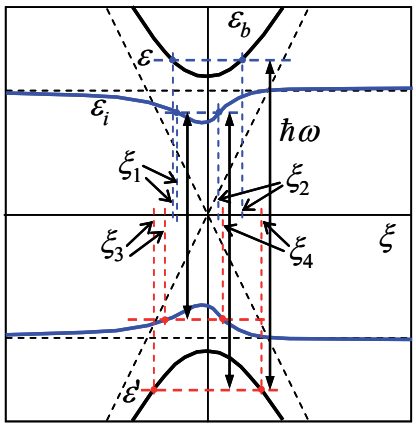

Figure 10. Configuration of the poles ξ_j of GF's contributing to different types of optical conductivity processes (over electronic pocket of the quasiparticle spectrum in Fig. 3).

For practical calculation of each contribution, the relevant matrix Im $\hat{G}_{\boldsymbol{k}}(\varepsilon)$ (within the band-like energy ranges) can be presented as Im $\hat{G}_{\boldsymbol{k}}(\varepsilon)=\hat{N}(\varepsilon,\,\xi)\,\mathrm{Im}\left[D_{\boldsymbol{k}}(\varepsilon)^{-1}\right]$ where the numerator matrix:

$$\hat{N}\left(\varepsilon,\xi\right)=\mathrm{Re}\,\left(\tilde{\varepsilon}+\tilde{\xi}\tau_3+\Delta\tau_1\right), \tag{50}$$

is a smooth enough function while the above referred peaks result from zeros of Re $D_k(\varepsilon)$. Now, the quasimomentum integration in Eq. (47) under the above chosen symmetry of Fermi segments spells as $\int d\varphi\int dk = 2(hv_{\mathrm{F}})^{-1}\int d\varphi\int d\xi$ where the factor 2 accounts for identical contributions from *e*- and *h*-segments. The azimuthal φ-integration contributes by the factor of π (from *x*-projections of velocities) and the most important radial ξ-integration is readily done after expanding its integrand in particular pole terms:

$$v\left(\xi,\varepsilon\right)v\left(\xi,\varepsilon'\right)\,\mathrm{Tr}\left[\,\mathrm{Im}\,\hat{G}\left(\xi,\varepsilon\right)\mathrm{Im}\,\hat{G}\left(\xi,\varepsilon'\right)\right]=\sum_{\alpha}A_{\alpha}\left(\varepsilon,\varepsilon'\right)\delta\left(\xi-\xi_{\alpha}\right), \tag{51}$$

where $v(\xi,\,\varepsilon) = |v_k(\varepsilon)|$ and $\hat{G}(\xi,\,\varepsilon)\equiv\hat{G}_{\boldsymbol{k}}(\varepsilon)$ define the respective residues:

$$A_{\alpha}\left(\varepsilon,\varepsilon'\right)=\pi v_{\alpha}v'_{\alpha}\frac{\tilde{\varepsilon}\tilde{\varepsilon}+\tilde{\xi}\tilde{\xi}'+\Delta^2}{\prod_{\beta\neq\alpha}\left(\xi_{\alpha}-\xi_{\beta}\right)}. \tag{52}$$

Here $v_\alpha \equiv v(\varepsilon,\,\xi_\alpha)$, $v'_\alpha \equiv v(\varepsilon',\,\xi_\alpha)$, and the indices α, β run over all the poles of the two Green functions. As seen from Eqs. (23, 24) and Fig. 10, there can be two such poles of $\hat{G}(\xi,\,\varepsilon)$ related to band-like states with positive ε and respective quasi-momentum values denoted as $\xi_{1,2}(\varepsilon)$. For energies within the *b*-band, $\varepsilon > \varepsilon_c$, they are symmetrical:

$$\xi_{1,2}\left(\varepsilon\right)\approx\pm\sqrt{\varepsilon^2-\Delta^2}, \tag{53}$$

but within the *i*-band, at $\varepsilon_{c,-} < |\varepsilon| < \varepsilon_{c,+}$, their positions are asymmetrical:

$$\xi_{1,2}\left(\varepsilon\right)\approx\frac{c\gamma^2\mp2\varepsilon_0\sqrt{\left(\varepsilon_+-\varepsilon\right)\left(\varepsilon-\varepsilon_-\right)}}{2\left(\varepsilon-\varepsilon_0\right)}. \tag{54}$$

Within the *i*-band, there is a narrow vicinity of ε_0 of ~ $c_0^{1/3}(c_0/c)^3\varepsilon_0$ width where only the ξ_1 pole by Eq. (54) is meaningful and the other contradicts the IRM criterion (so that there is no band-like states with those formal ξ_2 values in this energy range). Analogous poles of $\hat{G}(\xi,\,\varepsilon')$ at negative ε' are referred to as $\xi_{3,4}(\varepsilon')$ in what follows. Taking into account a non-zero Im $D_k(\varepsilon)$ (for the *i*-band, it is due to the non-trivial terms in the group expansion, Eq. (16)), each α-th pole becomes a δ-like peak with an effective linewidth Γ_α but this value turns to be essential only at calculation of static coefficients like Eqs. (49, 50).

Since four peaks in Eq. (47) are well separated, the ξ-integration is done considering them true δ-functions, then the particular terms in $\sigma(\omega, T)$ are given by the energy integrals:

$$\sigma_{\nu}\left(\omega,T\right)=2e^{2}\int_{\varepsilon_{\nu,-}}^{\varepsilon_{\nu,+}}d\varepsilon\frac{f\left(\varepsilon\right)-f\left(\varepsilon'\right)}{\omega}\sum_{\alpha=1}^{4}A_{\alpha}, \tag{55}$$

for $\nu = b\text{-}b'$, $i\text{-}b'$, or $i\text{-}i'$ and the limits $\varepsilon_{\nu,\pm}$ should assure both ε and ε' to be within the band-like ranges. Thus, in the $b\text{-}b'$ term, the symmetry of the poles $\xi_{1,2}(\varepsilon)$ and $\xi_{1,2}(\varepsilon')$ by Eq. (55) and the symmetry of b- and b'-bands themselves defines their equal contributions, then using simplicity of the function $v(\varepsilon, \xi) = \xi/\varepsilon$ and non-renormalized energy $\tilde{\varepsilon} \to \varepsilon$ and momentum $\tilde{\xi} \to \xi$, integration between $\varepsilon_{b\text{-}b',-} = \varepsilon_c$ and $\varepsilon_{b\text{-}b',+} = \hbar\omega - \varepsilon_c$ gives an analytic form $\sigma_{b\text{-}b'}(\omega, T) = \sigma_{b\text{-}b'}(\omega, 0) - \sigma_{b\text{-}b',T}(\omega)$. Here the zero-temperature limit value is:

$$\begin{aligned}\sigma_{b\text{-}b'}\left(\omega,0\right)\approx\sigma_{0}\frac{2\omega_{c}}{\omega^{2}}\Bigg\{&\sqrt{4\omega^{2}-\omega_{c}^{\,2}}\ln\left[2\frac{\omega\left(2\omega-\omega_{c}\right)+\sqrt{\omega\left(\omega-\omega_{c}\right)\left(4\omega^{2}-\omega_{c}^{\,2}\right)}}{\omega_{c}^{\,2}}-1\right]\\&+2\omega\ln\left[2\frac{\omega-\sqrt{\omega\left(\omega-\omega_{c}\right)}}{\omega_{c}}-1\right]-2\sqrt{\omega\left(\omega-\omega_{c}\right)}\Bigg\},\end{aligned} \tag{56}$$

with characteristic scale $\sigma_0 = e^2/\Delta^2$ and simple asymptotics:

$$\sigma_{b\text{-}b'}\left(\omega,0\right)\approx\sigma_{0}\begin{cases}\dfrac{2}{3}\left(\dfrac{\omega}{\omega_{c}}-1\right)^{3/2}, & \omega-\omega_{c}\ll\omega_{c},\\[2ex]\dfrac{32\omega_{c}}{\omega}\ln\dfrac{2\omega}{\omega_{c}}, & \omega\gg\omega_{c},\end{cases}$$

vs the threshold frequency $\omega_c = 2\varepsilon_c/\hbar$, reaching the maximum value $\approx 1.19\sigma_0$ at $\omega \approx 2.12\ \omega_c$ (Fig. 11). The (small) finite-temperature correction to Eq. (57) is:

$$\begin{aligned}\sigma_{b\text{-}b',T}\left(\omega\right)\approx\sigma_{0}\frac{2\omega_{c}^{\,2}\mathrm{e}^{-\beta\Delta}}{\beta\omega\left(\omega-\omega_{c}\right)\sqrt{\Delta}}\Bigg\{&\frac{\sqrt{\hbar\omega}}{\Delta}\left[1-\frac{F\left(\sqrt{\beta\hbar\left(\omega-\omega_{c}\right)}\right)}{\sqrt{\beta\hbar\left(\omega-\omega_{c}\right)}}\right]\\&+\frac{\sqrt{2\Delta}}{\hbar\omega-\Delta}\left[\frac{\sqrt{\pi}}{2}\frac{\mathrm{erf}\left(\sqrt{\beta\hbar\left(\omega-\omega_{c}\right)}\right)}{\sqrt{\beta\hbar\left(\omega-\omega_{c}\right)}}-\mathrm{e}^{-\beta\hbar\left(\omega-\omega_{c}\right)}\right]\Bigg\},\end{aligned} \tag{57}$$

with the Dawson function $F(z) = \sqrt{\pi} e^{-z^2} \mathrm{erf}(iz) / (2i)$ and the error function erf(z) [64].

Calculation of the i-b'-term is more complicated since asymmetry of the i-band poles $\xi_{1,2}(\varepsilon)$ by Eq. (55) and their non-equivalence to the symmetric poles $\xi_{3,4}(\varepsilon')$ of the b'-band analogous to Eq. (54). Also the generalized velocity function within the i-band range:

$$\hbar v\left(\xi,\varepsilon\right) = \frac{c\gamma^2 - \xi\left(\varepsilon - \varepsilon_0\right)}{\varepsilon\left(\varepsilon - \varepsilon_0 - c\gamma^2 / \varepsilon_0\right)}\ , \tag{58}$$

and the energy integration limits: $\varepsilon'_{i\text{-}b',-} = \varepsilon_{c,-}$ and $\varepsilon'_{i\text{-}b',+} = \min\left[\varepsilon_{c,+},\ \hbar\omega - \varepsilon_c\right]$ are more complicated. Then $\sigma_{i\text{-}b'}(\omega, T)$ follows from numerical integration in Eq. (56); as seen in Fig. 11, it has a lower threshold frequency $\omega_{c'} = \varepsilon_c + \varepsilon_{c,-}$ than the b-b'-term. Above this threshold, it grows linearly as ~ $(\omega/\omega_{c'} - 1)c^{5/2}c_0^{-5/3}\sigma_0$ and, for "safe" impurity concentrations $c \ll c_1 \sim c_0^{2/3}$, becomes fully dominated by the b-b' term, Eq. (57) above its threshold ω_c. Finally, the i-i'-term from a similar numerical routine on Eq. (56) within integration limits $\varepsilon_{i\text{-}i',-} = \varepsilon_{c,-}$ and $\varepsilon_{i\text{-}i',+} = \min[\varepsilon_{c,+},\ \hbar\omega - \varepsilon_{c,-}]$, using Eq. (55) for the poles $\xi_{1,2}(\varepsilon)$ and $\xi_{3,4}(\varepsilon')$ and Eq. (59) for generalized velocities. The resulting $\sigma_{i\text{-}i'}(\omega, T)$ occupies a narrow frequency band from $\omega_{i\text{-}i'} = 2\varepsilon_{c,-}/\hbar$ to $\omega_{i\text{-}i',+} = 2\varepsilon_{c,+}/\hbar$ (Fig. 11) with asymptotics near these thresholds in the zero-temperature limit:

$$\sigma_{i\text{-}i'}\left(\omega,0\right) \approx \sigma_0 \frac{16c^{7/2}\gamma^7}{3\sqrt{2}\xi_-^{\ 7}}\left(\frac{\omega - \omega_-}{\omega_-}\right)^{3/2}\ , \tag{59}$$

at $0 < \omega - \omega_- \ll \omega_-$, and alike for $0 < \omega_+ - \omega \ll \omega_+$ with only changes: : $\xi_- \to \xi_+$, $\omega_- \to \omega_+$.

Extrapolation of these asymptotics to the center of impurity band gives an estimate for the maximum of i-i' term: $\sigma_{i\text{-}i',\,max} \sim c^5 c_0^{-10/3}(\xi_+/\xi_-)^{7/2}\sigma_0$. It shows that the narrow i-i' peak of optical conductivity around $\omega \approx 2\varepsilon_0/\hbar$, unlike the "combined" i-b' term, can become as intense as the "main" b-b' intensity, Eq. (58), if the small factor ~ $(c/c_1)^5$ be overweighted by the next factor $(\xi_+/\xi_-)^{7/2}$. It is only possible for *weak* enough impurity perturbation: $v \ll 1$. Then the ratio $\xi_+/\xi_- \approx (2/v)^2 \prec 1$ can really overweight the concentration factor if c reaches ~ $c_1(v/2)^{7/5} \ll c_1$, that is quite realistic within the "safety" range $c \ll 1$. The overall picture of optical conductivity for an example of weakly coupled, $v = 0.25$, impurities at high enough $c = 4c_0$ is shown in Fig. 11. The effect of "giant" optical conductivity by the in-gap impurity excitations could be compared with the known Rashba enhancement of optical luminescence by impurity levels near the edge of excitonic band [64] or with huge impurity spin resonances in magnetic crystals [29], but here it appears in a two-particle process instead of the above mentioned single-particle ones.

To emphasize, the considered impurity features in optical conductivity cannot be simply treated as optical transitions between localized impurity states (or between these and main

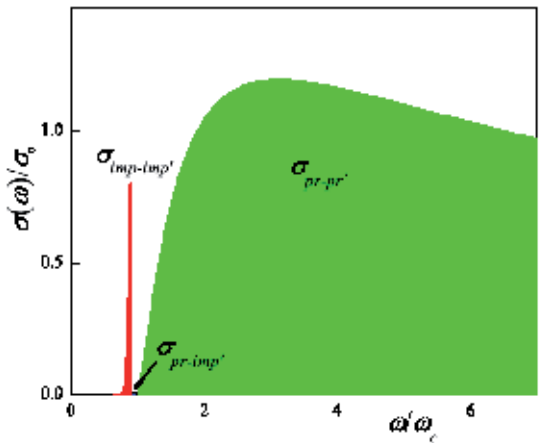

Figure 11. General picture of the optical conductivity showing three types of contributions.

bands) since localized states can not contribute to currents. Such effects only appear at high enough impurity concentrations, $c \gtrsim c_0$, when the impurity banding takes place.

8. Concluding remarks

Resuming, the GF analysis of quasiparticle spectra in SC iron pnictides with impurities of simplest (local and non-magnetic) perturbation type permits to describe formation of impurity localized levels within SC gap and, with growing impurity concentration, their evolution to specific bands of extended quasiparticle states, approximately described by quasimomentum but mainly supported by the impurity centers. Explicit dispersion laws and densities of states are obtained for the modified main bands and impurity bands. Further specification of the nature of all the states in different energy ranges within the SC gap is obtained through analysis of different types of GEs for self-energy matrix, revealing a complex oscillatory structure of indirect interactions between impurity centers and, after their proper summation, resulting in criteria for crossovers between localized and extended states. The found spectral characteristics are applied for prediction of several observable impurity effects.

Besides the thermodynamical effects, expected to appear at all impurity concentrations, that is either due to localized or band-like impurity states, a special interest is seen in the impurity effects on electronic transport in such systems, only affected by the impurity band-like states. It is shown that the latter effects can be very strongly pronounced, either for high-frequency transport and for static transport processes. In the first case, the strongest impurity effect is expected in a narrow peak of optical conductance near the edge of conductance band in non-perturbed crystal, resembling the known resonance enhancement of impurity absorption (or emission) near the edge of quasiparticle band in normal systems. The static transport coefficients at overcritical impurity concentrations are also expected to be strongly enhanced compared to those in a non-perturbed system, including the thermoelectric Peltier and Seebeck coefficients.

The proposed treatment can be adapted for more involved impurity perturbations in SC iron pnictides, including magnetic and non-local perturbations, and for more realistic multiorbital structures of the initial iron pnictide system. Despite some quantitative modifications of the results, their main qualitative features as possibility for new narrow in-gap quasiparticle bands and related sharp resonant peaks in transport coefficients should be still present. The experimental verifications of such predictions would be of evident interest, also for important practical applications, e.g., in narrow-band microwave devices or advanced low-temperature sensors, though this would impose rather hard requirements on quality and composition of the samples, to be extremely pure aside the extremely low (by common standards) and well controlled contents of specially chosen and uniformly distributed impurity centers. This can be compared to the requirements on doped semiconductor devices and hopefully should not be a real problem for modern lab technologies.

Acknowledgements

Y.G.P. and M.C.S. acknowledge the support of this work through the Portuguese FCT project PTDC/FIS/101126/2008. V.M.L. is grateful to the Special Program of Fundumental Research of NAS of Ukraine.

Parts of the chapter are reproduced from the authors' previous publication [53]

Author details

Yuriy G. Pogorelov[1*], Mario C. Santos[2] and Vadim M. Loktev[3]

*Address all correspondence to: ypogorel@fc.up.pt

1 IFIMUP-IN, Departamento de Física, Universidade do Porto, Porto, Portugal

2 Departamento de Física, Universidade de Coimbra, R. Larga, Coimbra, Portugal

3 Bogolyubov Institute for Theoretical Physics, NAN of Ukraine, Kiev, Ukraine

References

[1] Kamihara Y, Hiramatsu H, Hirano M, Kawamura R, Yanagi H, Kamiya T, Hosono H. Iron-Based Layered Superconductor: LaOFeP. J. Am. Chem. Soc. 2006;128:10012–10013. DOI: 10.1021/ja063355c

[2] Kamihara Y, Watanabe T, Hirano M, Hosono H. Iron-based Layered Superconductor La[$O_{1-x}F_x$]FeAs (x=0.05-0.12) with T_c = 26K. J. Am. Chem. Soc. 2008;130:3296-3297. DOI: 10.1021/ja800073m

[3] Sadovskii MV. High-temperature superconductivity in iron-based layered iron compounds. Phys. Uspekhi. 2008;178:1201-1227. DOI: 10.1070/PU2008v051n12ABEH006820

[4] Izyumov YA, Kurmaev EZ. Materials with strong electron correlations. Phys. Uspekhi. 2008;51:23-56. DOI: 10.1070/PU2008v051n01ABEH006388

[5] Ginsberg DM, editor. Physical Properties of High Temperature Superconductors I. World Scientific;1989. 509 p. ISBN: 9971-50-683-1 9971-50-894-X(pbk)

[6] Takahachi H, Igawa K, Arii K, Kamihara Y, Hirano M, Hosono H. Superconductivity at 43K in an iron-based layered compound $LaO_{1-x}F_xFeAs$. Nature 2008;453:376-378. DOI: 10.1038/nature06972

[7] Norman MR. High-temperature superconductivity in the iron-pnictides. Physics 2008;1: 21-26. DOI: 10.1103/Physics.1.21.6

[8] Ding H, Richard P, Nakayama K, Sugawara K, Arakane T, Sekiba Y, Takayama A, Souma T, Takahashi T, Wang Z, Dai X, Fang Z, Chen GF, Luo JL, Wang NL. Observation of Fermi-surface-dependent nodeless superconducting gaps in $Ba_{0.6}K_{0.4}Fe_2As_2$. Europhysics Lett. 2008;83:47001. DOI: 10.1209/0295-5075/83/47001

[9] Kondo T, Santander-Syro AF, Copie O, Liu C, Tillman ME, Mun ED, Schmalian J, Bud'ko SL, Tanatar MA, Canfield PC, Kaminski A. Momentum Dependence of the Superconducting Gap in $NdFeAsO_{0.9}F_{0.1}$. Phys. Rev. Lett. 2008;101:147003. DOI: http://dx.doi.org/10.1103/PhysRevLett.101.147003

[10] Mazin II, Singh DJ, Johannes MD, Du MH. Unconventional Superconductivity with a Sign Reversal in the Order Parameter of $LaFeAsO_{1-x}F_x$. Phys. Rev. Lett. 2008;101:057003. DOI: http://dx.doi.org/10.1103/PhysRevLett101.057003

[11] Luetkens H, Klauss HH, Kraken M, Litterst FJ, Dellmann T, Klingeler R, Hess C, Khasanov R, Amato A, Baines C, Kosmala M, Schumann OJ, Braden M, Hamann-Borrero J, Leps N, Kondrat A, Behr G, Werner J, Buechner B. The electronic phase diagram of the $LaO_{1-x}F_xFeAs$ superconductor. Nature Materials Lett. 2008; DOI: 10.1038/nmat2397

[12] Singh DJ, Du MH. Density Functional Study of $LaFeAsO_{1-x}F_x$: A Low Carrier Density Superconductor Near Itinerant Magnetism. Phys. Rev. Lett. 2008;100:237003. DOI: http://dx.doi.org/10.1103/PhysRevLett100.237003

[13] Haule K, Shim JH, Kotliar G, Correlated Electronic Structure of $LaO_{1-x}F_xFeAs$. Phys. Rev. Lett. 2008;100:226402. DOI: http://dx.doi.org/10.1103/ PhysRevLett100.226402

[14] Xu G, Ming W, Yao Y, Dai X, Zhang SC, Fang Z. Doping-dependent phase diagram of LaOMAs (M=V-Cu) and electron-type superconductivity near ferromagnetic instability. *et al*, Europhys Lett. 2008;82 :67002. DOI : 10.1209/0295-5075/82/67002

[15] Raghu S, Qi XL, Liu CX, Scalapino DJ, Zhang SC. Minimal two-band model of superconducting iron oxypnictides. Phys. Rev. B 2008;77:220503. DOI: http://dx.doi.org/10.1103/PhysRevB.77.220503

[16] Kuroki K, Onari S, Arita R, Usui H, Tanaka Y, Kontani H, Aoki H. Unconventionaol Pairing Originating from the Disconnected Fermi Surfaces of Superconducting $LaFeAsO_{1-x}F_x$. Phys. Rev. Lett. 2008;101:087004. DOI: http://dx.doi.org/10.1103/PhysRevLett.101.087004

[17] Boeri L, Dolgov OV, Golubov AA. Is $LaFeAsO_{1-x}F_x$ an Electron-Phonon Superconductor ? Phys. Rev. Lett. 2008;101:026403. DOI: http://dx.doi.org/10.1103/PhysRevLett.101.026403

[18] Gao Y. Interorbital Pairing and its Physical Consequences in Iron Pnictide Superconductors. Phys. Rev. B 2010;81:104504. DOI: 10.1103/PhysRevB.81.104504

[19] Si Q, Abrahams E. Strong correlations and magnetic frustration in the high Tc iron pnictides. Phys. Rev. Lett. 2008;101:076401. DOI: http://dx.doi.org/10.1103/PhysRevLett.101.076401

[20] Daghofer M, Moreo A, Riera JA, Arrigoni E, Scalapino DJ, Dagotto E. Model for the Magnetic Order and Pairing Channels in Fe Pnictide Superconductors. Phys. Rev. Lett. 2008;101:237004. DOI: http://dx.doi.org/10.1103/PhysRevLett.101.237004

[21] Tsai WF, Zhang YY, Fang C, Hu JP. Impurity-induced bound states in iron-based superconductors with s-wave cos kx cos ky pairing symmetry. Phys. Rev. B 2009;80:064513. DOI: http://dx.doi.org/10.1103/PhysRevB.80.064513

[22] Graser S, Maier TA, Hirschfeld PJ, Scalapino DJ. Near-degeneracy of several pairing channels in multiorbital models for the Fe pnictides. New J. Phys. 2009 ;11:025016. DOI: 10.1088/1367-2630/11/2/025016

[23] Maier TA, Graser S, Scalapino DJ, Hirschfeld PJ. Origin of gap anisotropy in spin fluctuation models of the iron pnictides. Phys. Rev. B 2009;79:224510. DOI: http://dx.doi.org/10.1103/PhysRevB.79.224510

[24] Zhang D. Nonmagnetic Impurity Resonances as a Signature of Sign-Reversal Pairing in FeAs-Based Superconductors. Phys. Rev. Lett. 2009;103:186402. DOI: http://dx.doi.org/10.1103/PhysRevLett.103. 186402

[25] Zhang YY, Fang C, Zhou X, Seo K, Tsai WF, Bernevig BA, Hu J. Quasiparticle scattering interference in superconducting iron pnictides. Phys. Rev. B 2009;80:094528. DOI: http://dx.doi.org/10.1103/PhysRevB.80. 094528

[26] Anderson PW. Theory of dirty superconductors. J. Phys. Chem. Solids 1959;11:26-30. DOI: 10.1016/0022-3697(59)90036-8

[27] Shklovskii BI, Efros AL. Electronic properties of doped semiconductors, Springer-Verlag, 1984, 387 p. DOI: 10.1007/978-3-662-02403-4

[28] Ivanov MA, Pogorelov YG, Electron Properties of Two-Parameter Long-Range Impurity States. Sov. Phys. JETP 1985;61:1033-1039. DOI: 10.1134/0038-5646/85/051033-07

[29] Ivanov MA, Loktev VM, Pogorelov YG, Long-range impurity states in magnetic crystals. Phys. Reports 1987;153:209-330. DOI: 10.1016/0370-1573(87)90103-7

[30] Yamamoto H, Fang ZQ, Look DC. Nonalloyed ohmic contacts on low-temperature molecular beam epitaxial GaAs: Influence of deep donor band. Appl. Phys. Lett. 1990;57:1537-1539. DOI: http://dx.doi.org/10.1063/1.103345

[31] Anderson PW. Absence of Diffusion in Certain Random Lattices. Phys. Rev. 1958;109:1492-1505. DOI: http://dx.doi.org/10.1103/PhysRev.109.1492

[32] Mott NF. Electrons in disordered structures. Adv. Phys. 1967;16:49-144. DOI: 10.1080/00018736700101265

[33] Ioffe AF, Regel AR. Non-crystalline, amorphous and liquid electronic semiconductors. Prog. Semicond. 1960;4:237-291.

[34] Shiba H. Classical Spins in Superconductors. Prog. Theor. Phys. 1968;40:435-451. DOI: 10.1143/PTP.40.435

[35] Rusinov AI. On the Theory of Gapless Superconductivity in Alloys Containing Paramagnetic Impurities. Sov. Phys. JETP 1969;29:1101-1106. DOI: 10.1134/0038-5646/69/061101-06

[36] Maki K. Anomalous Scattering by Magnetic Impurities in Superconductors. Phys. Rev. 1967;153:428-434. DOI: http://dx.doi.org/10.1103/PhysRev.153.428

[37] Gonnelli RS, Daghero D, Ummarino, Calzolari A, Tortello M, Stepanov VA, Zhigadlo ND, Rogacki K, Karpinski J, Bernardini F, Massidda S. Effect of Magnetic Impurities in a Two-Band Superconductor : A Point-Contact Study of Mn-Substituted MgB_2 Single Crystals. Phys. Rev. Lett. 2006;97:037001. DOI: http://dx.doi.org/10.1103/PhysRevLett.97. 037001

[38] Moca CP, Demler E, Janko B, Zarand G. Spin-resolved spectra of Shiba multiplets from Mn impurities in MgB_2. Phys. Rev. B 2008;77:174516. DOI: http://dx.doi.org/10.1103/PhysRevB.77.174516

[39] Balatsky AV, Salkola MI, Rosengren A. Impurity-induced virtual bound states in d-wave superconductors. Phys. Rev. B 1995;51:15547. DOI: http://dx.doi.org/10.1103/PhysRevB.51.15547

[40] Pogorelov YG, Ground state symmetry and impurity effects in superconductors. Sol. St. Commun. 1995;95:245-249. DOI: 10.1016/0038-1098(95)00260-X

[41] Onari S, Kontani H. Violation of Anderson's Theorem for the Sign-Reversing s-Wave State in Iron-Pnictide Superconductors. Phys. Rev. Lett. 2009;103:177001. DOI: http://dx.doi.org/10.1103/PhysRevLett.103.177001

[42] Kontani H, Onari S. Orbital-Fluctuation-Mediated Superconductivity in Iron Pnictides: Analysis of the Five-Orbital Hubbard-Holstein Model. Phys. Rev. Lett. 2010;104157001. DOI: http://dx.doi.org/10.1103/PhysRevLett.104.157001

[43] Efremov DV, Korshunov MM, Dolgov OV, Golubov AA, Hirschfeld PJ. Disorder-induced transition between $s_{\pm}$ and s_{++} states in two-band superconductors. Phys. Rev. B 2011;84:180512. DOI: http://dx.doi.org/10.1103/PhysRevB.84.180512

[44] Senga Y, Kontani H. Impurity Effects in Sign Reversing Fully-Gapped Superconductors: Analysis of FeAs Superconductors. Journ. Phys. Soc. Japan 2008;77:113710. DOI: 10.1143/JPSJ.77.113710

[45] Kariado T, Ogata M. Single-Impurity Problem in Iron-Pnictide Superconductors. Journ. Phys. Soc. Japan 2010;79:083704. DOI: http://dx.doi.org/10.1143/JPSJ.79.083704

[46] Beaird R, Vekhter I, Zhu JX, Impurity states in multiband s-wave superconductors: Analysis of iron pnictides. Phys. Rev. B 2012;86:140507. DOI: http://dx.doi.org/10.1103/PhysRevB.86.140507

[47] Gordon RT, Kim H, Tanatar MA, Prozorov R, Kogan VG. London penetration depth and strong pair breaking in iron-based superconductors. Phys. Rev. B 2010;81:180501. DOI: http://dx.doi.org/10.1103/PhysRevB.81.180501

[48] Kitagawa S, Nakai Y, Iye T, Ishida K, Guo YF, Shi YG, Yamaura K, Takayama-Muromachi E. Nonmagnetic pair-breaking effect in $La(Fe_{1-x}Zn_x)AsO_{0.85}$ studied by ^{75}As and ^{139}La NMR and NQR. Phys. Rev. B 2011;83:180501(R). DOI: http://dx.doi.org/10.1103/PhysRevB.83.180501

[49] Guo YF, Shi YG, Yu S, Belik AA, Matsushita Y, Tanaka M, Katsuya Y, Kobayashi K, Nowik I, Felner I, Awana VPS, Yamaura K, Takayama-Muromachi E. Large decrease in the critical temperature of superconducting $LaFeAsO_{0.85}$ compounds doped with 3% atomic weight of nonmagnetic Zn impurities. Phys. Rev. B 2010;82:054506. DOI: http://dx.doi.org/10.1103/PhysRevB.82. 054506

[50] Li Y, Tong J, Tao Q, Feng C, Cao G, Chen W, Zhang F, Xu Z. Effect of a Zn impurity on Tc and its implications for pairing symmetry in $LaFeAsO_{1-x}F_x$. New J. Phys. 2010 ; 12 :083008. DOI : 10.1088/1367-2630/12/8/083008

[51] Hardy F, Burger P, Wolf T, Fisher RA, Schweiss P, Adelmann P, Heid R, Fromknecht R, Eder R, Ernst D, Löhnheysen Hv, Meingast C. Doping evolution of superconducting gaps and electronic densities of states in $Ba(Fe_{1-x}Co_x)_2As_2$ iron pnictides. Europhys. Lett. 2010;91:47008. DOI: 10.1209/0295-5075/91/47008

[52] Loktev VM, Pogorelov YG. Formation of d-wave superconducting order in a randomly doped lattice. Low Temp. Phys. 2001;27:767-776. DOI: http://dx.doi.org/10.1063/1.1401186

[53] Pogorelov YG, Santos MC, Loktev VM. Specifics of impurity effects in ferropnictide superconductors. Phys. Rev. B 2011;84:144510. DOI: http://dx.doi.org /10.1103/ PhysRevB.84.144510

[54] Pogorelov YG, Santos MC, Loktev VM. Green function study of impurity effects in high-Tc superconductors. In: Carmelo JMP, Lopes dos Santos JMB, Rocha Vieira V, Sacramento PD, editors. Strongly Correlated Systems, Coherence and Entanglement, World Scientific;2007. p. 443-494. ISBN 978-981-270-572-3. cap. 17

[55] Kubo R. Statistical-Mechanical Theory of Irreversible Processes. I. General Theory and Simple Applications to Magnetic and Conduction Problems. J. Phys. Soc. Jpn. 1957 ;12 :570-586. DOI: http://dx.doi.org/10.1143/JPSJ.12.570

[56] Greenwood DA. The Boltzmann Equation in the Theory of Electrical Conduction in Metals. Proc. Phys. Soc. 1958;71:585-596. DOI: 10.1088/0370-1328/71/4/306

[57] Economou EN. Green's Functions in Quantum Physics. Springer, Berlin;2006. 477 p. DOI: 10.1007/3-540-28841-4

[58] Mazin II, Schmalian J. Pairing symmetry and pairing state in ferropnictides: Theoretical overview. Physica C 2009;469:614-627. DOI:10.1016/j.physc.2009.03.019

[59] DeWeert MJ. Proximity-effect bilayers with magnetic impurities: The Abrikosov-Gor'kov limit. Phys. Rev. B 1988;38:732-734. DOI: http://dx.doi.org/10.1103/PhysRevB.38.732

[60] Srivastava RVA, Teizer W. Analytical density of states in the Abrikosov-Gorkov theory. Solid State Commun. 2008;145:512-513. DOI: 10.1016/j.ssc.2007.11.030

[61] Note that this static limit of Eq. (47) only defines the conductivity by normal quasiparticles, seen e.g. in normal resistivity by the magnetic flux flow in the mixed state, but otherwise short circuited by the infinite static conductivity due to supercurrents.

[62] Dolgov OV, Efremov DV, Korshunov MM, Charnukha A, Boris AV, Golubov AA. Multiband Description of Optical Conductivity in Ferropnictide Superconductors. J. Supercond. Nov. Magn. 2013;26:2637-2640. DOI: 10.1007/s10948-013-2150-3

[63] Abramowitz MVL, Stegun IA, editors. Handbook of Mathematical Functions With Formulas, Graphs, and Mathematical Tables. Natl. Bureau of Standards;1964. 1046 p. ISBN 0-486-61272-4 DOI: 10.2307/2008636

[64] Broude, Prikhot'ko AF, Rashba EI. Some problems of crystal luminescence. Sov. Phys. Uspekhi 1959;2:38-49. DOI: http://dx.doi.org/10.1070/PU1959v002n01ABEH003107

Chapter 12

Theory of Flux Cutting for Type-II Superconducting Plates at Critical State

Carolina Romero-Salazar and
Omar Augusto Hernández-Flores

Additional information is available at the end of the chapter

http://dx.doi.org/10.5772/59512

1. Introduction

With the discovery in 1986 of high critical temperature superconductors $T_c \geq 77K$ –which belong to the type-II classification– efforts have been made to recognize which mechanism rules its current carrying capacity in order to expand knowledge of the vortex state and, moreover, devise new and better technological applications. Critical-state phenomenological models for such materials have been a feasible alternative for the theoretical study of the magnetic properties of high- or low-T_c type-II superconductors. Here we present a brief revision of macroscopic critical-state models; following a chronological order, we will begin with the Bean model, moving on with the generalized double-critical state model, the two-velocity hydrodynamic model, and finalizing with the Elliptic Flux-Line Cutting Critical-State Model (ECSM). It will be described further the main features of type-II superconductors, the physical meaning of the critical state and the flux-line cutting phenomenon.

1.1. Type-II superconductor critical state

In 1911 Kammerlingh Onnes discovered the superconductivity of mercury at very low temperature. Nowadays, the characteristics of superconductors are well established: their electric resistance abruptly drops to zero as temperature decreases through a critical temperature value designated as T_c. They show the *Meissner-Ochsenfeld effect*, that is, they completely expel a weak magnetic field as temperature decreases through the transition point. Depending on how this diamagnetic phenomenon is destroyed, superconductors can be classified as type I or II. Type-I superconductors are perfect diamagnets below a critical field H_c. Because their coherence length ξ exceeds the penetration length λ, it is energetically unfavorable for borders to be formed between the normal and superconductive phases. However, when a type-II superconductor is subjected to a magnetic field $\mathbf{H}_a$, free energy can diminish, thus generating normal matter domains that contain trapped flux, with low-energy

INTECH
open science | open minds

© 2015 The Author(s). Licensee InTech. This chapter is distributed under the terms of the Creative Commons Attribution License (http://creativecommons.org/licenses/by/3.0), which permits unrestricted use, distribution, and eproduction in any medium, provided the original work is properly cited.

borders created between the normal core and the superconductive surroundings. When the applied magnetic field exceeds the lower critical field H_{c1}, the magnetic flux penetrates in quantized units Φ_0, forming cylindrical domains called **vortices**. As $\mathbf{H}_a$ increases, vortices will overlap increasing the interior field until the material gently enters the normal state, once $\mathbf{H}_a$ has reached the upper critical field H_{c2}. Between the fields H_{c1} and H_{c2} the superconductor state coexists with the magnetic state in a **mixed state** or **vortex state**.

Another characteristic of superconductors is the presence of a gap, just below the Fermi energy, the energy of conduction electrons. BCS superconductivity theory demonstrated that electrons in the vicinity of the Fermi level are grouped in the so-called Cooper pairs. In addition, the junction of two superconductors –separated by a thin insulating layer– shows the *DC Josephson effect*, in which the superconductor current tunneling is caused by the tunneling of Cooper pairs. This effect demonstrated that the superconductor state is a coherent state, which is associated to a macroscopic uniform-phase wave function; this function corresponds to the order parameter $\kappa = \lambda/\xi$ in the Ginzburg-Landau theory. Finally, they also show the *AC Josephson effect* that describes the relation between the time variation of the macroscopic wave function with the voltage produced across the junction. This voltage arises from the quantized magnetic flux movement, and is identical to the macroscopic voltage observed in type-II superconductors in flux flow state.

Indeed, it is well established that type-II superconductors posses a stationary vortex spatial arrangement only if the total force over each vortex is null. If an electric current is applied with $\mathbf{J}$ density, vortices move at a velocity $\mathbf{v}$ with a direction determined by the Hall angle. If both the Magnus force and the Hall effect on the material are neglected, equilibrium between the Lorentz force $\mathbf{F}_L = \mathbf{J} \times \mathbf{B}$ and the pinning force $\mathbf{F}_p$ will exist:

$$(\mathbf{J} \times \mathbf{B}) - \mathbf{F}_p = 0. \tag{1}$$

In addition to being able to describe the vortex dynamics under the transport current influence, the equation (1) can be used for the time-variable external magnetic case, in absence of transport currents.

Indeed, $\mathbf{F}_p$ opposes the magnetic flux velocity $\mathbf{v}$ due to the local depression of the Gibbs free energy of each vortex. This potential well may be due to inhomogeneities, defects, or material grains. Therefore, magnetic flux movement will occur if the Lorentz force exceed the pinning force. Any electromotive force, even small, causes the vortices to move further into the material, inducing a local current. Initially, this superconductive current flows in regions close to the superconductor surface because pinning centers near the sample surface can catch the vortices in such a way that, in the interior, the Meissner state is preserved, thus the sample is partially penetrated. For higher external magnetic field values, vortices will completely penetrate the material.

1.2. Bean model for a type-II superconductor in critical state

Half a century ago, Charles Bean approached — with great physics intuition and from a macroscopic point of view — the study of the magnetic properties of superconductors made with impure metals or alloys. Bean modeled the spatial distribution of the magnetic flux, for

http://dx.doi.org/10.5772/59512

partial and totally penetrated states, a couple of years before having experimental evidence of the mixed or vortex state predicted by A. A. Abrikosov.

He relied on *Mendelssohn sponge model* to describe the magnetic behaviour of such superconductors, supposing they possessed a filamental structure capable of maintaining a maximum macroscopic current J_c, without energy dissipation in form of Joule heating, that he called it *critical current density*. Due to the J_c dependence on the magnetic field, he considered that such currents were extended into the material, preserving the magnitude J_c.

Bean argued that the macroscopic current is a consequence of the magnetic induction gradient penetrating the material, governed by Ampère's law $\nabla \times \mathbf{B} = \mu_0 \mathbf{J}$. He also argued that the current originates as the Lorentz force drives the magnetic flux into the interior of the material. Therefore, he considered that any local region where an electric field (related to heat dissipation) is perceived during the process of magnetization, it would originated a critical current density J_c which flows in the electric field direction and it keep flowing even if it the electric field was null [6–9]. He synthesized these ideas in the material law:

$$J = J_c(B)\,\mathrm{sign}(E), \tag{2}$$

which is valid for slabs or infinite cylinders subjected to a magnetic field parallel to the superconductor's surface (this is the so-called *parallel geometry*).

To exemplify the Bean model, Figure (1) shows the profile evolution of magnetic induction for a PbBi plate at mixed-state, as it increased (blue curves) or decreased (red curves) the external magnetic field magnitude $\mathbf{H}_a$ parallel to its surface. The hysteresis cycle of the average static magnetization is shown when the $\mathbf{H}_a$ varies a full cycle, from -0.3T to 0.3T. The superconducting plate has a 8mm thickness and a penetration field $\mu_0 H_p = 0.1015$T. We have considered the reliance on B of the critical current density $J_c(B)$.

Subsequently, Bean studied energy dissipation in materials subjected to a magnetic field that rotates in the specimen's plane. He extended his arguments assuming the current density $\mathbf{J}$ and the electric field $\mathbf{E}$ vectors would be parallel to each other [9]. For this case, the material equation can be written as follows:

$$\mathbf{J} = J_c(B)\frac{\mathbf{E}}{E(J)}, \tag{3}$$

where it is necessary to model the $E(J)$ function form. The Bean model, corresponding to the material equation (2) or (3), together with the Ampère's law, have been used to calculate magnetic induction profiles, hysteresis of magnetization cycles, and the energy dissipation of several type-II superconductor materials. In the search for new superconducting alloys that would produce more intense magnetic fields, or a greater current conduction capacity, these materials were simultaneously subjected to a magnetic field and a transport current parallel to each other. It was desirable that the electric current density $\mathbf{J}$ and the magnetic induction $\mathbf{B}$ established a force-free configuration, that is, a zero Lorentz force $\mathbf{F}_L = \mathbf{J} \times \mathbf{B} = 0$. However, experimental evidence showed that even if $\mathbf{F}_L$ could be considered null, a significant voltage

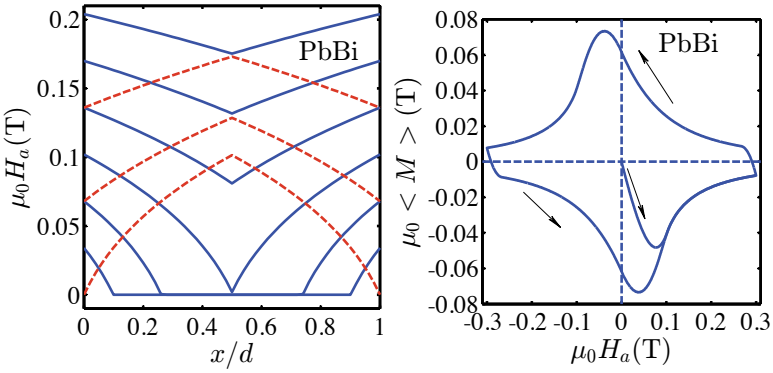

Figure 1. Theoretical curves of a superconductor plate, with thickness $d = 8\text{mm}$ and penetration field $\mu_0 H_p = B_p = 0.1015\text{T}$, obtained with the Bean critical-state model and considering $J_c = J_c(B)$. (Left) Evolution of magnetic induction B as it increases (continuous blue lines) and decreases (red discontinuous lines) the magnitude of the external magnetic field $\mathbf{H}_a$. When $\mu_0 H_a = \mu_0 H_p$, B at the center of the plate is null. (Right) Average static magnetization cycle $\mu_0\langle M\rangle$ against the applied magnetic field $\mu_0 H_a$. Since this material is an irreversible type-II superconductor, $\mu_0\langle M\rangle$ describes a hysteresis.

would arise from the material. Therefore, if the vortex velocity is equal to zero in a force-free configuration, what is going on in this type of configuration? This question could not be answered using the Bean model, so it was considered that another phenomenon might be occurring. The answer to this query is the so-called *flux-line cutting* or *flux crossing*, which will be discussed in the next section.

1.3. Flux-Line cutting

D.G. Walmsley [10] measured the magnetization and the axial resistance of a type-II superconductor –in mixed state and with cylindrical geometry– by subjecting it simultaneously to a magnetic axial field and a transport current, parallel to each other. The objective was to prove under what the Lorentz force density could be null. He found that, at low currents, the potential difference between the extremes of the sample was negligible ($\sim 10\mu$V). However, when the superconducting sample conduced a sufficiently high current, it measured a voltage (or a longitudinal electric field), as well as a paramagnetic moment, that is, a positive average magnetization. He then suggested that the force-free structure could not be established on the material's surface, which originated the flux-flow and, consequently, a voltage in the rest of the material.

He intuited that the measurement of a paramagnetic moment suggested a helicoidal vortex distribution. Nonetheless, the voltage produced by the flux flow would imply a permanent increase in the longitudinal magnetic field. For this reason, he supposed the existence of a non-stationary process in which the magnetic flux lines would continually divide each other, only to reconnect afterward.

As a solution for the flux-flow movement contradiction in a force-free configuration, Clem was the first to suggest that the helicoidal instabilities were precisely the precursors of vortex cutting or crossing; that is, considering the elastic properties of flux lines, he proposed that they could stay fixed but they would be able to bend, calling this phenomenon *flux-line cutting*.

http://dx.doi.org/10.5772/59512

Even though Josephson had already established that cutting or crossing of vortices could not occur because they were energetically too expensive, theoretical calculations done by Brandt, Clem, and Walmsley — using the London and Ginzburg-Landau theories — proved that the threshold of cutting of a pair of rigid flux lines was possible since the characteristics energies of a type-II superconductor.

Subsequently, Brandt and Sudbo extended these results for the case of a pair of twisted flux lines, they considered the tension and interaction between each flux-line or vortex. Given that cutting is energetically plausible, they found that flux-line cutting is an effective disentanglement mechanism of flux lines; and that the cutting energy barrier, in the case of twisted flux lines, is lower for the rigid two-flux-lines case [11, 12]. Several groups, for example, M.A.R. LeBlanc *et. al* [13–15], have done experiments in the last decades that have shown flux-cutting presence in materials with low or high κ, and low or high T_c. In the Clem *et. al* [16–18] and Brandt [19] papers, we can see flux-line cutting diagrams for the case of rigid-vortices arrangement. Furthermore, it includes diagrams for the first theoretical formulations for this often-studied and not completely understood phenomenon.

More recent theoretical studies have studied the scattering dynamics of vortices, and the resulting topology after a collision between two flux lines generated by an applied current. Using the time-dependent Ginzburg-Landau equations, numerical results yielded two generic collision types dependent on the initial angle: one local collision that induces changes in topology through recombination, and a double collision that can occur due to geometrical restrictions. The second case leads to a vortex-crossing type configuration, that is, it seems as if two vortices, while interacting, would cut themselves and join again. This can be seen in the simulations shown in paper [20]. Experiments have been proposed using a magnetic force microscope to monitor vortex-line dynamics and prove if these cut through each other when they are in a liquid-vortex phase [21].

In 2008, A. Palau *et al.* reported results with superconductive heterostructures subjected to an external magnetic field at a θ angle respect to the sample's normal. For this, they designed a device made out of a thin film of low-pinning amorphous material ($Mo_{82}Si_{18}$), sandwiched between two Nb films– a material characterized for strongly pinning the vortices.

They measured the critical current density J_c obtained as a function of θ, the applied field $\mu_0 H_a$, and temperature T. Once obtained, they calculated the balance force between the Lorentz force, the pinning force, and a so-called breaking force. They found that the latter was necessary in order to consider vortex deformation and destabilization. Results showed that the breaking force is independent of B, and that the following cross joining neither limit vortex movement nor increase J_c. Even if a flux-line segment is strongly pinned to the area where Nb material is found, the cut induces other vortex segments to be liberated, thus reducing J_c [22].

Furthermore, Campbell's revision paper can be consulted to know the state of the art about experiments and critical state theories for flux-cutting in superconductors [23]. He included the last proposal of Clem to determine the electric field direction, for the flux transport regime in a type-II superconductor.

Here it is presented three critical state models created for the phenomenological study of type-II superconductors subject to magnetic fields that vary not only in magnitude, but also in direction. All models consider that flux pinning and flux-line cutting govern their answer. It is undeniable that both phenomena can occur in cases when a sample oscillates in presence of a static magnetic field, or when it is subjected to a DC magnetic field and a transversal sweeping magnetic field is superimposed.

2. Other critical state models

2.1. Generalized Double Critical-State Model

LeBlanc *et. al* proposed a model containing two critical-state equations based on their experimental observations on the magnetic response of a disc oscillating at low frequency, in presence of a magnetic field [24]:

$$\frac{dB}{dx} = \pm\frac{F_p(B)}{B}, \qquad \frac{d\alpha}{dx} = \pm k(B)\frac{dB}{dx}. \tag{4}$$

This pair of equations is known as the Double Critical-State Model (DCSM). In their construction, the fact that the magnetic induction B and the orientation α of flux-lines varied spatially was considered. They assumed as well that gradients existed in critical states. In his model, $F_p(B)$ is a parameter that characterizes pinning intensity; k is associated to the shearing coefficient of the flux lattice in the superconductive sample.

Clem and Perez-Gonzalez extended the DCSM based on the assumption that intersection and cross-joining of adjacent non-parallel vortices generate a electric field different to the electric field $\mathbf{E} = \mathbf{B} \times \mathbf{v}$. The latter field is associated to the flux flow with velocity $\mathbf{v}$, for the case in which $\mathbf{J}$ is perpendicular to $\mathbf{B}$. For this, they proposed a pair of constitutive laws of the form:

$$\begin{aligned} J_\perp &= J_{c,\perp}\,\text{sign}\,E_\perp \\ J_\parallel &= J_{c,\parallel}\,\text{sign}\,E_\parallel, \end{aligned} \tag{5}$$

where parameters $J_{c,\perp}$ and $J_{c,\parallel}$ correspond to the depinning and the flux-line cutting thresholds, respectively. They considered that the electric field $\mathbf{E}$ components obey independently the vertical laws:

$$E_\perp = \begin{cases} \rho_\perp[|J_\perp| - J_{c,\perp}]\,\text{sign}\,(J_\perp), & |J_\perp| > J_{c,\perp} \\ 0, & 0 \leqslant |J_\perp| \leqslant J_{c,\perp} \end{cases} \tag{6}$$

$$E_\parallel = \begin{cases} \rho_\parallel[|J_\parallel| - J_{c,\parallel}]\,\text{sign}\,(J_\parallel), & |J_\parallel| > J_{c,\parallel} \\ 0, & 0 \leqslant |J_\parallel| \leqslant J_{c,\parallel}; \end{cases} \tag{7}$$

here, $\rho_\perp$ and $\rho_\parallel$ are the resistivities caused by flux transport and superconductor flux-line cutting, respectively. The group of equations (5)-(7) constitutes the Generalized Double Critical-State Model (GDCSM.) Clem and Perez-Gonzalez did numerical calculations considering as possible values for magnitude J_c all those defined within a rectangular region of $J_{c,\parallel}$ and $J_{c,\perp}$ sides. The model reproduced successfully the experimental distributions

http://dx.doi.org/10.5772/59512

of magnetic induction and magnetization, when the magnetic field oscillates at great amplitudes [25].

The GDCSM was also used to try to reproduce *Magnetization Collapse* and *Paramagnetism*, phenomena encountered when a type-II superconductor is subjected first to a DC magnetic field on which an oscillating low-frequency magnetic field is superposed, perpendicular to the former.

2.2. Two-velocities Hydrodynamic Model (TVHM)

This macroscopic model considers that electrodynamics of a type-II superconductor depends on the translation of vortex planes and the interaction between them. It establishes two vortex subsystems, assuming they posses no elastic properties and that the flux cutting consists of the disappearance of interacting vortices, creating new vortices on a plane with an orientation different to the previous one. Gibbs energy varies through small disturbances on the vortices' coordinates considering the following: 1) magnetic energy; 2) work done by pinning forces given the translation of the vortex network; and 3) the work done by the pinning forces to straighten a vortex after its crossing [26–28]. Thus, the model is conformed by a continuity equation for total vortex density $n(x,t)$, and the average angular distribution $\alpha(x,t)$ of the vortex planes:

$$\frac{\partial n}{\partial t} = -\frac{\partial}{\partial x}\left[n\frac{V_A + V_B}{2}\right], \tag{8}$$

$$\frac{\partial (n\alpha)}{\partial t} = -\frac{1}{2}\frac{\partial [n\alpha(V_A + V_B)]}{\partial x} - \frac{1}{4}\frac{\partial [n\alpha(V_A - V_B)]}{\partial x}, \tag{9}$$

where

$$V_A = V + \frac{U}{2}, \qquad V_B = V - \frac{U}{2}, \tag{10}$$

correspond to the velocities of subsystems A and B, $V(x,t)$ is the mean hydrodynamic velocity, and $U(x,t)$ is the relative velocity. The TVHM requires additionally two equations obtained from force balance conditions in a superconductor, defined for the magnetic induction gradient and for angular distribution:

$$\frac{\partial B}{\partial x} = -\frac{\mu_0 J_{c,\perp}}{2}[F(V_A) + F(V_B)], \tag{11}$$

$$\begin{aligned}\Delta\alpha B\frac{\partial \alpha}{\partial x} + p\sqrt{\frac{n}{8}}[B - \mu_0 H_a\cos(\alpha - \alpha_0)]\Delta\alpha^2\,\mathrm{sign}(V_A - V_B),\\ = -\mu_0 J_{c\perp}[F(V_A) - F(V_B) + p\,\mathrm{sign}(V_A - V_B)],\end{aligned} \tag{12}$$

here p corresponds to the probability that flux-line cutting occurs. Finally, to resolve the equation system (8)-(12) for variables V_A, V_B, $B = n\Phi_0, \alpha$ and $\Delta\alpha$, it is required to introduce a phenomenological equation that relates $\Delta\alpha$ to the mean orientation's spatial derivative of the form:

$$\Delta\alpha = -l\,\mathrm{sign}(V_A - V_B)\,\frac{\partial\alpha}{\partial x}, \tag{13}$$

where l is the vortex mean free path between two successive cuttings or crossings.

3. Theoretical Description of the ECSM

Now we introduce the characteristics of the Elliptic Critical-State Model (ECSM) used in this chapter.

3.1. Geometrical aspects of a superconductor plate

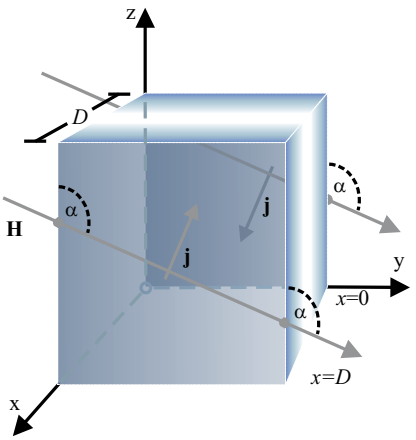

Figure 2. Diagram of a portion of infinite superconducting plate. It is shown, in an instant of time t, the orientation of the external magnetic field $\mathbf{H}_a$, which is always parallel to plane yz.

The study system is a superconducting plate possessing an infinite surface parallel to a plane yz and a finite thickness $0 \leq x \leq D$, as it is shown in Figure (2). The plate is subjected to a magnetic field $\mathbf{H}_a$ parallel to plane yz given by the expression:

$$\mathbf{H}_a = H_{ay}\hat{\mathbf{y}} + H_{az}\hat{\mathbf{z}} = H_a(\sin\alpha_a\hat{\mathbf{y}} + \cos\alpha_a\hat{\mathbf{z}}), \tag{14}$$

where α_a is an angle measured relative to z axis . This problem pertains to the *parallel geometry*. Demagnetization effects are not present, the current density $\mathbf{J}$, electric field $\mathbf{E}$, and magnetic induction $\mathbf{B}$ vectors are all coplanar with their components y and z depending only on variable x and time t. Given the applied magnetic field $\mathbf{H}_a$, local magnetic induction in a superconducting sample is:

http://dx.doi.org/10.5772/59512

$$\mathbf{B} = B(x,t)\hat{\mathbf{e}}_{\parallel} = B(\sin\alpha\hat{\mathbf{y}} + \cos\alpha\hat{\mathbf{z}}). \tag{15}$$

The superconducting current circulates around planes $x =$ constant. In region $x \in [0, D/2)$ it circulates in the opposite direction from the one in region $x \in (D/2, D]$.

Since we are studying flux-line cutting, ECSM postulates that the current density **J** and electric field **E** can possess components both parallel and perpendicular to **B**. The perpendicular component is associated to the flux-pinning effect, while parallel components are associated to flux-line cutting. Therefore, we wish to calculate how large is the force-free component parallel to B of the current density, and if the latter reaches its critical value $J_{c\parallel}$.

It is convenient to work with a reference system that rotates (follows) with the (the) magnetic induction **B**. The current density and electric field components –parallel and perpendicular to **B**– are monitored:

$$\mathbf{J} = J_{\parallel}\hat{\mathbf{e}}_{\parallel} + J_{\perp}\hat{\mathbf{e}}_{\perp}, \qquad \mathbf{E} = E_{\parallel}\hat{\mathbf{e}}_{\parallel} + E_{\perp}\hat{\mathbf{e}}_{\perp}, \tag{16}$$

where the unit vector $\hat{\mathbf{e}}_{\perp}$ is built as $\hat{\mathbf{e}}_{\perp} = \hat{\mathbf{e}}_{\parallel} \times \hat{\mathbf{x}} = \cos\alpha\hat{\mathbf{y}} - \sin\alpha\hat{\mathbf{z}}$.

3.2. Physical considerations for a Type-II superconductor

Type-II superconductor materials are found in vortex state and contain a dense distribution and random pinning centers. When applying a magnetic field $\mathbf{H}_a$, Eq. (14), it is considered that the material is in a critic state (metastable state) when there is a balance between Lorentz force density $\mathbf{F}_L = \mathbf{J}_{c\perp} \times \mathbf{B}$ and the average pinning force. If the perpendicular component of the current overcomes its critical value $J_{c\perp}$, flux transport is begun until another material metastable state is reached. Also, vortex avalanches can occur; however, we will not cover here this phenomenon [29]. In addition, given that a **J** component is parallel to **B**, magnetic flux distribution will depend on flux line cutting, only if $J_{\parallel}$ exceeds its critical value $J_{c\parallel}$. Finally, the magnitude of an applied magnetic field is considered to be much larger than the first critical field H_{c1}, that is, the Meissner currents on the material's surface are neglected.

We are interested in the macroscopic electrodynamics of a type-II superconductor; thus, we work with Maxwell equations, given that low-frequency magnetic fields are considered, displacement current is neglected. In order to establish the critical state, this model considers quasi-stationary electromagnetic fields. This is why first the Faraday law is used, and subsequently stationary solutions are sought. Having chosen a reference system that rotates with magnetic induction **B**, Ampère and Faraday laws are written as follows:

$$-\frac{\partial B}{\partial x} = \mu_0 J_{\perp} \qquad B\frac{\partial \alpha}{\partial x} = \mu_0 J_{\parallel}, \tag{17}$$

$$\frac{\partial E_{\perp}}{\partial x} + E_{\parallel}\frac{\partial \alpha}{\partial x} = -\frac{\partial B}{\partial t}, \qquad E_{\perp}\frac{\partial \alpha}{\partial x} - \frac{\partial E_{\parallel}}{\partial x} = -B\frac{\partial \alpha}{\partial t}. \tag{18}$$

In absence of a demagnetization factor, and considering that the applied magnetic field $\mathbf{H}_a$ is much larger than H_{c1}, the constitutive relation between $\mathbf{B}$ and $\mathbf{H}$ is modeled with the linear approximation $\mathbf{B} = \mu_0\mathbf{H}$, where the Bean-Livingston superficial barrier is neglected. Therefore, the boundary condition is written as follows:

$$\mu_0 H_{ay}(t) = B_y(0;t) = B_y(D;t), \tag{19}$$

$$\mu_0 H_{az}(t) = B_z(0;t) = B_z(D;t). \tag{20}$$

3.3. Elliptic Flux-Cutting Critical-State Model for a type-II superconductor in critical state

The Elliptic Flux-Cutting Critical-State Model (ECSM) [1] considered the presence of an electric field in non-critical states. It models the material as a highly non-linear conductor, using a constitutive relation $\mathbf{E} = \mathbf{E}(\mathbf{J}, \mathbf{B})$, which completes the system of equations (17)-(18). Furthermore, it monitors the electric field's decrease through a vertical law. The model supposes that the material reaches a critical state when the magnetic induction distribution enters a stationary state where the electric field has decreased to zero.

The material law of the elliptic model considers, in contrast to multicomponent Bean and double critical-state models, that the critical current density is a rank-2 tensor determined by the equation:

$$J_i = (\mathcal{J}_c)_{ik}\frac{E_k}{E}, \qquad (\mathcal{J}_c)_{ik} = J_{c,i}(B)\delta_{ik}, \qquad i,k = \perp, \parallel. \tag{21}$$

or, by the vector relation:

$$\mathbf{J} = J_{c\parallel}(B)\frac{\mathbf{E}_{\parallel}}{E} + J_{c\perp}(B)\frac{\mathbf{E}_{\perp}}{E}. \tag{22}$$

In critical state, the magnitude of $\mathbf{J}$, that is, the critical current density $J_c(B,\varphi)$ traces an ellipse on the plane $J_{\parallel} - J_{\perp}$, defined by the equation:

$$J_c(B,\varphi) = \left[\left(\frac{\cos\varphi}{J_{c\parallel}(B)}\right)^2 + \left(\frac{\sin\varphi}{J_{c\perp}(B)}\right)^2\right]^{-1/2}, \tag{23}$$

http://dx.doi.org/10.5772/59512

where the angle φ is measured respect to **B**. Notice that the behaviour of the vortex distribution is a function of the magnitude of **J** and its relative orientation respect to **B**. The model postulates that $J_c(B,\varphi)$ is defined in terms of critical values $J_{c\perp}$ and $J_{c\parallel}$, that is, $J_c(B,\varphi)$ is restricted to the critical ellipse (23). The fact that $J_{\parallel}$ and $J_{\perp}$ are different produces an anisotropy on the plane $J_{\parallel} - J_{\perp}$ because of the external magnetic field $\mathbf{H}_a$ and since such components are associated with different physical phenomena which are still not fully understood. Lastly, a vertical law is used to relate the current density and the electric field magnitudes as:

$$E(J) = \begin{cases} 0, & \text{for} \quad J \leq J_c(B,\varphi), \\ \rho(J - J_c(B,\varphi)), & \text{for } J > J_c(B,\varphi). \end{cases} \tag{24}$$

It can be considered that an electric field can exist in the superconductor only if the current density exceeds its critical value $J_c(B,\varphi)$. Conventionally the parameter ρ acts as a resistivity, however, here it serves as an auxiliary parameter that counteracts the difference $J - J_c(B,\varphi)$. The empirical relation between the critical current density $\mathbf{J}_c$ and magnetic induction **B** used is known as generalized relation, it is an adaptation to such deduced by Y.B. Kim *et al.* [30], and was proposed by M. Xu *et al.* [31], its explicit form is as follows:

$$J_c(B) = J_c(0) / \left[1 + \frac{B}{B^*}\right]^n, \tag{25}$$

where n and B^* are fitting parameters, and the maximum critical current density value $J_c(B=0)$ is defined by the following relation:

$$J_c(0) = \left[\left(1 + \frac{B_p}{B^*}\right)^{n+1}\right] \frac{2B^*}{(n+1)\mu_0 d}. \tag{26}$$

In our case, temperature dependency remains implicit in the parameters election.

All solutions that satisfy the system of equations formed by the Ampère's law (17), the Faraday's law (18), the critical current density $J_c(B,\varphi)$ (23), and the material law (24) establish the superconductor's critical state. Such system is designated the *Elliptic Flux-Cutting Critical-State Model* (ECSM) [1].

4. Results using ECSM for a type-II superconductor in vortex state

Here we present theoretical curves obtained with the ECSM, corresponding to experimental results which depend on vortex dynamics. Specifically, numerical results are shown for magnetic-moment curves and magnetic-induction evolution, using type-II superconductor samples in mixed state, subject to transverse fields, or to a low-frequency rotating field.

4.1. Type-II superconductor plates subjected to transverse DC and AC fields

In this section we present the effect of an AC magnetic field on the static magnetization of a type-II superconductor plate. The purpose was to compare and explain experimental results - obtained by Fisher *et al.*- from YBCO samples subjected to two fields perpendicular to each other, in parallel geometry [28, 33].

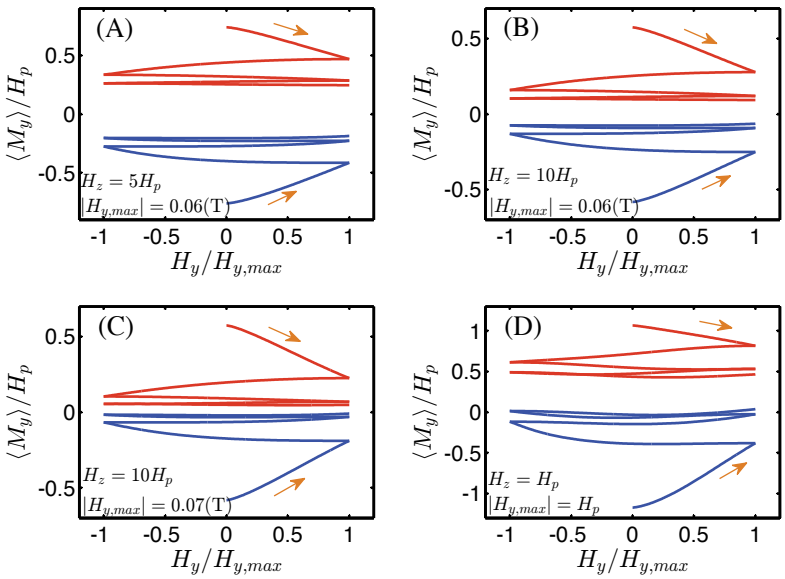

Figure 3. Theoretical average magnetization curves $\langle \mu_0 M_z \rangle$ vs H_y of an YBCO plate. The red (blue) curves were calculated for an initial paramagnetic (diamagnetic) state. In each figure, the magnitude of magnetic fields to which the sample was subjected to is shown: a static one H_z, and one with oscillation amplitude $H_{y,max}$. These fields are perpendicular to each other and coplanar to the specimen. We observe the dependency of $\langle \mu_0 M_z \rangle$ to the first cycles of H_y. Results correspond to a texturized YBCO plate, cooled down on field, a $d = 3$mm thickness and a $\mu_0 H_p = 0.0856$T penetration field. The specimen's larger sides are parallel to the crystallographic plane **ab**.

In the experiments of Fisher *et al.*, plates were cut out from the homogenous part of melt-textured YCBO ingots. This was done in such a way that the larger-sized sides were parallel to the crystallographic **ab** plane, which possesses isotropic properties respect to current conduction capacity. First they applied on the sample an H_z field generated by direct current, with a direction such that it was parallel to the plate's main surface. Afterward they applied a second field H_y, oscillating at low frequencies -of the order 1kOe- coplanar to the sample's surface and perpendicular to the first field. Under this configuration, and depending on the order of magnitude for both fields, they observed phenomena denominated *Magnetization Collapse* and *Paramagnetism*.

Results presented in Figure (3) correspond to a plate with a $d = 3$mm thickness that possesses a penetration field $\mu_0 H_p = 0.0856$T. This last value is very close to the experimental $\mu_0 H_p \sim 0.1$T value for the YBCO samples [33]. The parameters used to model the perpendicular component of current critical density $J_{c\perp}(B)$ (see Eq. 25) are: $n_\perp = 0.5$ y $B^*_\perp = 0.2$T, and a maximum value $J_{c\perp}(0) = 5 \times 10^8 \mathrm{A/m^2}$ (see Eq. 26). The parallel component $J_{c\parallel}(B)$ was

http://dx.doi.org/10.5772/59512

modeled just as $J_{c\perp}(B)$. Therefore, we use $B^*_{\parallel} = B^*_{\perp}$, $n_{\parallel} = n_{\perp}$. The best fitting to the experimental curves was achieved assuming $J_{c\parallel}(0) = 2J_{c\perp}(0)$.

Results for $\langle M_z(H_y)\rangle$ during the first cycles of the oscillating magnetic field H_y are shown in Figure (3). One can observe in (A)-(C) graphics the symmetric reduction of the average magnetization for both the diamagnetic initial state (blue curves) and paramagnetic initial state (red curves). These three cases are characterized by the fact that static magnetic field H_z is greater than H_p ($H_z = 5, 10H_p$), whereas the AC magnetic field oscillates at small amplitudes ($H_{y,max} \ll H_z$). In graphic (D) we appreciate a different behavior of the diamagnetic branch of $\langle M_z(H_y)\rangle$ (blue curve). This is due to the order of magnitude of fields H_z and H_y, which have the same order of magnitude of the sample penetration field H_p. One can observe in graphics (A)-(C) that for the same number of cycles of the oscillating field H_y, the magnetization reduction prevails, however, it is asymmetric. Specifically, the diamagnetic branch of the average magnetization changes sign, this behavior is the so-called paramagnetism. All theoretical results successfully agree with experiments for large ($|H_y| \sim H_z$) and small ($|H_y| \ll H_z$) values of the transverse field amplitude.

The asymmetrical suppression of average magnetization $\langle M_z(H_y)\rangle$ — caused by an AC magnetic field for diamagnetic and paramagnetic initial states as well as the change of sign in its diamagnetic branch — is only possible to reproduce if the effects of flux-line cutting and anisotropy between the perpendicular and parallel components of $\mathbf{J}_c(B)$ are incorporated. Also, it is necessary to consider that the effect of flux-line cutting has greater influence on the sample's magnetic induction behavior than the pinning effect.

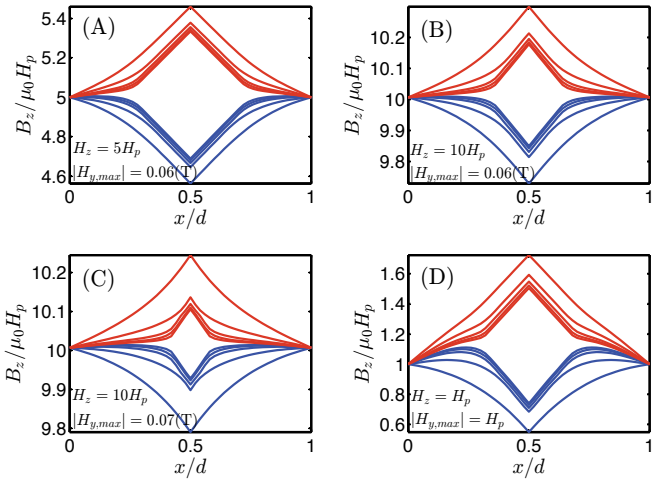

Figure 4. Theoretical magnetic induction curves $B_z/\mu_0 H_p$ vs x/d for a YBCO plate (in Fig. (3) specimen characteristics are specified). The red curves (blue) were calculated for an initial paramagnetic (diamagnetic) state. The magnitude of the static magnetic field H_z, and the amplitude of the oscillating magnetic field $|H_y|$ are shown. In all panels (A)-(D) it is initiated with a magnetic field $H_y = H_{y,max}$, each profile is generated every half cycle of H_y.

We can observe in Figure (4) the evolution of the magnetic induction profiles $B_z(x)$ as H_y ocillates. They correspond to the paramagnetic and diamagnetic branches of the average magnetization $\langle M_z\rangle$ (see Fig.(3). In graphics (A)-(C) we can see the reduction of magnetic

induction component $B_z(x)$ as the transverse field H_y describes small-amplitude cycles ($|H_y| < H_p \ll H_z$). The ECSM predicts that $B_z(x)$ has a tendency towards a fixed distribution (see (A), (B)) or quasi-uniform (see (C)), regardless of the number of cycles. Close to the sample's borders, the distribution $B_z(x)$ collapses to an almost homogeneous value ($B_z \sim B$) as H_y oscillates. However, the graphic (D) shows that when the magnitude of H_z and H_y are comparable to H_p ($|H_y| \sim H_z = H_p$), the slope of $B_z(x)$ changes (conserves) its sign close to the plate borders if the initial state is diamagnetic (paramagnetic). Moreover, B_z collapse areas are not present in the region close to the plate border. Therefore, the average magnetization value $\langle M_z \rangle$, after several H_y cycles becomes positive for the initial diamagnetic state.

In more recent experiments using the magneto-optic technique and Hall sensors, the effect of crossed magnetic fields in the perpendicular geometry was studied [34]. In this case, the sample is pre-magnetized in z-direction. Once the magnetic field along the z-axis is removed, an AC magnetic field, parallel to the sample's *ab* plane, is applied. Experimental results show that in this perpendicular geometry, given the magnitude of external magnetic fields H_y and H_z, only the symmetrical collapse effect of the average magnetization $\langle M_z \rangle$ is present. This occurs regardless of the transverse field H_y magnitude respect to the sample's penetration field $\mu_0 H_p$. It was employed a finite-element numerical model and a power law function $E(J)$. They reproduced the experimental curves of $\langle M_z \rangle$ considering that the flux-line cutting effect is not present in the superconductor dynamics. Indeed, their results do not contradict those obtained with the ESCM, because we have reproduced symmetrical collapse of $\langle M_z \rangle$ in a type-II superconductor with the Bean multicomponent model, which does not consider flux-line cutting.

It has also studied results of magnetization collapse for dissipative states using both ECSM [1] and the **extended ECSM**, the latter proposed by Clem [32]. In the experiments, it was measured the remanent magnetization of a PbBi superconductor disk. First, the disk is magnetized with a single pulse of a H_z field, and subsequently it is subjected to an oscillating magnetic field H_y. Even though the theoretical curves $\langle M_z \rangle$ vs H_y obtained with each model are very similar, the profile evolution of B_z obtained by using the extended ECSM contradicts the cases when the magnitude of fields H_y and H_z are comparable to H_p [5].

4.2. Rotating type-II superconductors in presence of a magnetic field

Another instance in which flux-line cutting occurs is when a superconductor sample rotates or oscillates in presence of an external magnetic field. We will focus on experiments conducted by Cave and LeBlanc [24] where a low-T_c type-II superconductor disk oscillates slowly in presence of a static magnetic field in parallel geometry. Cave and LeBlanc realized extensive research on the magnetic behavior of such sample, for a series of rotation angles, different initial states i.e. magnetic, non-magnetic, diamagnetic, paramagnetic and hybrid, and investigated the energy dissipation during oscillations.

Here we present theoretical calculations both for magnitude and direction of the magnetic induction **B**, as the sample rotates under different angles, also present the average component $\langle B_z \rangle$ and the hysteresis cycles. Results were obtained considering that the parallel and perpendicular components of current density possess a dependency on the magnetic induction of the form:

http://dx.doi.org/10.5772/59512

$$J_{c\perp(\parallel)}(B) = J_{c\perp(\parallel)}(0)\left(1 - \frac{B}{B_{c2}}\right). \tag{27}$$

We used the second critical field $B_{c2} = 0.35$T reported in Ref.[24], and the maximum value of critical current density $J_{c\perp}(0) = 1.6 \times 10^9 \mathrm{A/m}^2$. We found that, with the anisotropy parameter $J_{c\parallel}(0)/J_{c\perp}(0) = 4$, we obtain the best agreement with the experimental curves.

Figures (5) and (6) show the theoretical curves of $\langle B_y(\theta)\rangle$ and $\langle M_z\rangle = \mu_0 H_a - \langle B_z\rangle$ for a non magnetic initial state and four rotation angles $\theta_{max} = 45^o, 120^o, 270^o, 360^o$. All theoretical curves show the main characteristics of the corresponding experimental measurements.

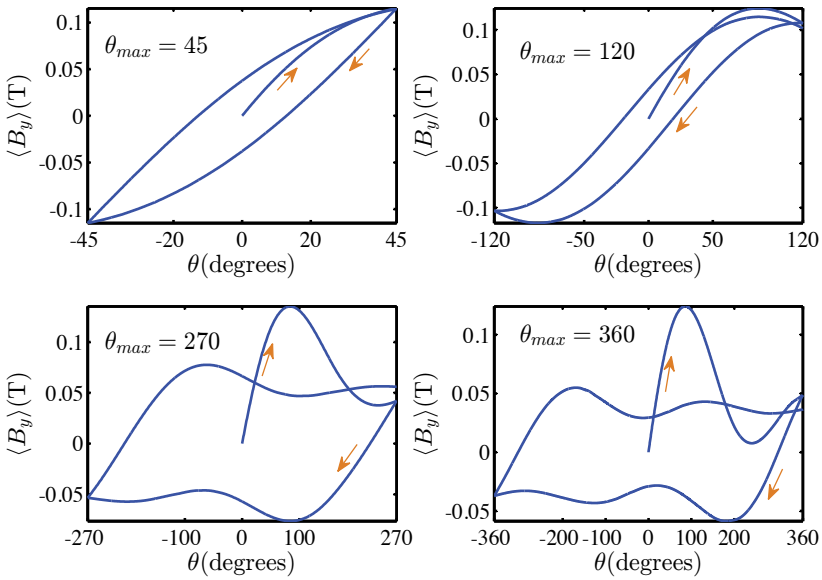

Figure 5. Theoretical curves of $\langle B_z\rangle$ vs θ for a non magnetic initial state for an Nb plate with thickness $d = 0.25$mm, $B_{c2} = 0.25$T , and $J_{c\perp}(0) = 1.6 \times 10^9$A/m^2. The relation $J_{c\parallel}(0)/J_{c\perp}(0) = 4$ was used. Curves are shown for different static external magnetic fields and rotation angles: $\mu_0 H_a = 261$mT and $\theta_{max} = 45^o$; $\mu_0 H_a = 149$mT and $\theta_{max} = 120^o$; $\mu_0 H_a = 172$mT and $\theta_{max} = 270^o$; $\mu_0 H_a = 149$mT and $\theta_{max} = 360^o$.

The most outstanding phenomenon in this experiment is the *magnetic flux consumption*. This phenomenon is analyzed with the help of the spatial evolution distribution of $B(x)$ and $\alpha(x)$ predicted with the ESCM. For instance, Fig. 7 presents the results for an amplitude oscillation $\theta_{max} = 45^o$ of the sample in presence of a static field $\mu_0 H_a = 261$mT. We can observe in the left panel that, as the sample rotates, the two U-shaped minima of the profile of $B(x)$ move away from the surface of the sample, as well as the local magnetic flux reduction. The right panel shows how $\alpha(x)$(B) decreases from a maximum value at the sample's surface to a zero value at the region $0.4 \lesssim x/d \lesssim 0.6$. Therefore, the ECSM can predict the existence of three areas within the material: (1) an exterior area where both flux cutting and flux transport occur, ($\alpha \neq 0$ y $dB/dx \neq 0$); (2) an internal area where only flux transport occurs

($\alpha = 0$ y $dB/dx \neq 0$) and (3) a central area were neither transport flux nor flux cutting occur ($\alpha = dB/dx = 0$).

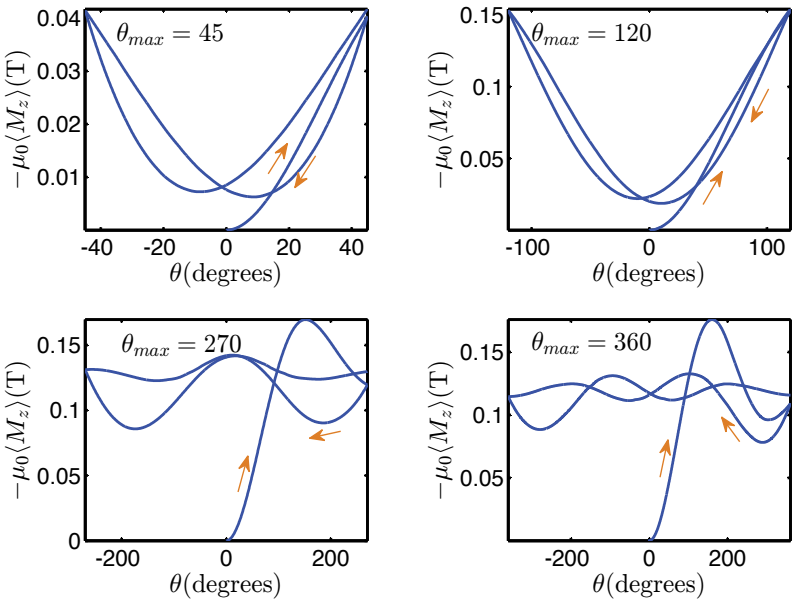

Figure 6. Theoretical curves of $-\mu_0\langle M_z\rangle$ vs θ corresponding to the graphs presented in Fig.(5).

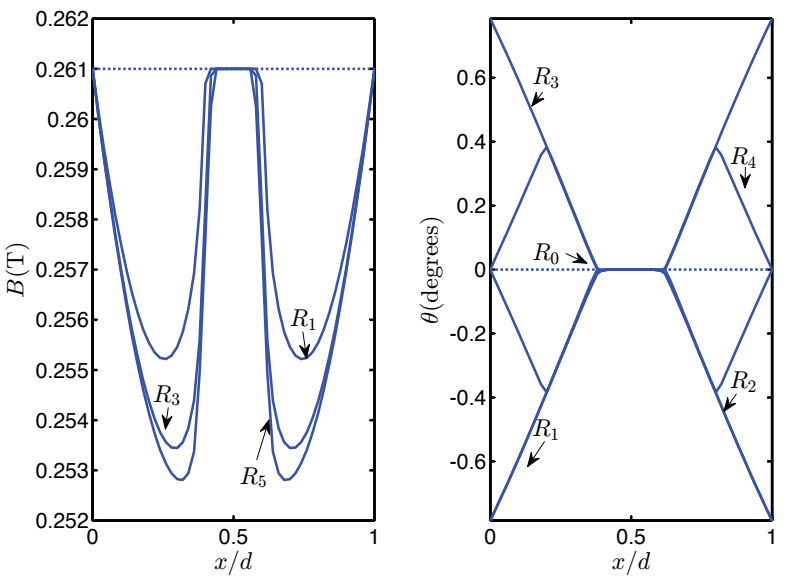

Figure 7. Theoretical curves for the evolution of $B(x)$ vs x/d and $\theta(x)$ vs x/d corresponding to $\mu_0 H_a = 261$mT y $\theta_{max} = 45^o$.

http://dx.doi.org/10.5772/59512

5. Conclusions and expectations

As J.R. Clem [32] emphasized, in contrast with other critical-state models, the Elliptic Flux-line Cutting Critical-state Model (ECSM) contains important new physical characteristics: it considers that the depinning threshold decreases as magnitude $J_{\parallel}$ increases and, in the same way, the flux cutting threshold decreases as magnitude $J_{\perp}$ increases. The model also reproduces the experimentally observed soft angular dependency of $J_c(B)$. In this chapter, we have shown that the ECSM satisfactorily reproduces the response of type-II superconductors subjected to external magnetic field varying in magnitude and direction — when the flux-line cutting effect is considered. Following this line of research, and based on recently results reported [32, 35, 36], the effects of the flux transport will be studied, as well as energy dissipation. This can be achieved incorporating an electric field with a well-defined direction. Our next study will consider the anisotropy in the current carrying capacity, since this characteristic is present in high-T_c superconductors, and flux line cutting as well. It is also desirable to study more complex phenomena in high-T_c superconductors, such as Meissner holes or the turbulent structures that occur in the perpendicular geometry when the external magnetic field is rotated. For this, it is essential to implement the ECSM for the case of finite geometries.

Acknowledgments

This work was supported by SEP-CONACYT under Grant No.CB-2008-01-106433

Author details

Carolina Romero-Salazar* and Omar Augusto Hernández-Flores

School of Sciences, Autonumous University “Benito Juárez" of Oaxaca, Oaxaca, Mexico

*Address all correspondence to cromeros@ifuap.buap.mx

References

[1] Romero-Salazar C. and Pérez-Rodríguez F. Elliptic Fux-line-cutting Critical-state Model. Applied Phyics Letters 2003; 83(25) 5256-5258.

[2] Romero-Salazar C., Pérez-Rodríguez F. Response of Hard Superconductors to Crossed Magnetic Felds: Elliptic Critical-state Model. Physica C. 2004; 404(1-4) 317-321.

[3] Romero-Salazar C., Valenzuela-Alacio L.D., Carballo-Sánchez A.F. and Pérez-Rodríguez F. Flux-Line Cutting in Hard Superconductors. Journal of Low Temperature Physics 2005; 139(1-2) 273-280.

[4] Romero-Salazar C. and Hernández-Flores O.A. Flux-line Cutting in Rotating Type-II Superconductors in Parallel Geometry. Journal of Applied Physics 2008; 103(9), 093907.

[5] Cortés-Maldonado R., De la Peña-Seaman O., García-Vázquez and Pérez-Rodríguez F. On the Extended Elliptic Critical-State Model for Hard Superconductors. Superconductor Sciencie and Technology 2013; 26(12) 125001.

[6] Bean C. P. Magnetization of Hard Superconductors. Physical Review Letters 1962; 8(6) 250-253.

[7] Bean C. P., Schmitt R.W. The Physics of High-Field Superconductors. Science 1963; 140(3562) 26-35.

[8] Bean C. P. Magnetization of High-Field Superconductors. Review of Modern Physics 1964; 36(1) 31-39.

[9] Bean C.P. Rotational Hysteresis Loss in High-Field Superconductors. Journal of Applied Physics 1970; 41(6) 2482-2483.

[10] Walmsley D. G. Force Free Magnetic Fields in a Type-II Superconducting Cylinder. Journal of Physics F: Metal Physics 1972; 2(3) 510-528.

[11] Brandt E.H., Clem J.R., Walmsley D.G. Flux-Line Cutting in Type-II Superconductors. Journal of Low Temperature Physics 1979; 37(1/2) 43-55.

[12] Sudbo A., Brandt E.H. Flux-Line Cutting in Superconductors. Physical Review Letters 1991; 67(22) 3176-3179.

[13] Fillion G., Gauthier R., LeBlanc M.A.R. Direct Evidence of Flux Cutting in Type-II Superconductors. Physical Review Letters 1979; 43(1) 86-89.

[14] LeBlanc M.A.R., LeBlanc D., Golebiowski A., Fillion G. New Observations on the Dynamics of Flus Lines in Type-II Superconductors. Physical Review Letters 1991; 66(25) 3309-3312.

[15] LeBlanc M.A.R., Celebi S., Wang S. X., Plechácêk. Cross-Flow of Flux-Lines in the Weak Link Regime of High-T_c Superconductors. Physical Review Letters 1993; 71(20) 3367-3370.

[16] Clem J. R., Yeh S. Flux-Line-Cutting Threshold in Type II Superconductors. Journal of Low Temperature Physics 1980; 39(1/2) 173-189.

[17] Clem J. R. Steady-State Flux-Line Cutting in Type II Superconductors. Journal of Low Temperature Physics 1980; 38(3/4) 353-370.

[18] Clem J.R. Steady-State Flux-Line Cutting in Type II Superconductors: A Double-Cutting Model. Physica B + C 1981; 107(1-3) 453-545.

[19] Brandt E. H. Continuous Vortex Cutting in Type-II Superconductors with Longitudinal Current. Journal of Low Temperature Physics 1980; 39(1/2) 41-61.

[20] Bou-Diab M., Dodgson M. J. W., Blatter G. Vortex Collisions: Crossing or Recombination? Physical Review Letters 2001; 86(22) 5132-5135.

[21] Nelson D.R. Vortices Weave Tangled Web. Nature 2004; 430() 839-840.

[22] Palau A., Dinner R., Durrell J.H., Blamire M. G. Vortex Breaking and Cutting in Type II Superconductors. Physical Review Letters 2008; 101(9) 097002.

[23] Campbell A.M. Flux Cutting in Superconductors. Superconductor Science and Technology 2011; 24(9) 091001.

[24] Cave J.R., LeBlanc M.A.R. Hysteresis Losses and Magnetic Phenomena in Oscillating Disks of Type II Superconductors. Journal of Applied Physics 1982; 53(3) 1631-1648 .

[25] Pérez-González A., Clem J. R. Magnetic Responde of Type-II Superconductors Subjected to Large-Amplitude Parallel Magnetic Fields Varying in both Magnitude and Direction. Journal of Applied Physics 1986; 58(11) 4326-4335.

[26] Voloshin I. F., Kalinov A. V., Savel'ev S. E., Fisher L. M., Yampol'skii V. A., Pérez Rodríguez F. Electrodynamics of Hard Superconductors in Crossed Magnetic Fields. Journal of Experimental and Theoretical Physics 1997; 84(3) 592-598.

[27] Savel'ev S.E., Fisher L. M., Yampol'skii V. A. Vortex Lattice Kinetics and the Electrodynamics of Rigid Superconductors. Journal of Experimental and Theoretical Physics 1997; 85(3) 507-515.

[28] Fisher L. M., Il'enko K.V., Kalinov A.V., LeBlanc M. A. R., Pérez-Rodríguez F., Savel'ev S. E., Voloshin I. F., Yampol'skii V. A. Suppression of the Magnetic Moment under the Action of a Transverse Magnetic Field in Hard Superconductors. Physical Review B 2000; 61(22) 15382-15391.

[29] Romero-Salazar, C. Morales F., Escudero R., Durán A., Hernández-Flores O.A. Flux Jumps in Hot-Isostatic-Pressed Bulk MgB Superconductors: Experiment and Theory. Physical Review B 2007; 76(10) 104521

[30] Kim Y.B., Hempstead C.F., Strnad A.R. Critical Persistent Currents in Hard Superconductors. Physical Review Letters 1962; 9(7) 306-309.

[31] Xu M., Shi D., Fox R. F. Generalized critical-state model for hard superconductors. Physical Review B 1990;42(16) 10773R-10776R.

[32] Clem J.R. Theory of flux Cutting and Flux Transport at the Critical Current of a Type-II Superconducting cylindrical Wire. Physical Review B 2011; 83(21) 214511.

[33] Fisher L.M., Kalinov A.V., Savel'ev S.E., Voloshin I.F. and Yampol'skii V.A. Paramagnetism of a Hard Superconductor in Crossed Magnetic Fields. Solid State Communications 1997; 103(5) 313-317.

[34] Vanderbemden Ph., Hong Z., Coombs T. A., Denis S., Ausloos M., Schwartz J., Rutel I. B., Hari Babu N., Cardwell D. A., and Campbell A. M. Behavior of Bulk High-temperature Superconductors of Finite Thickness Subjected to Crossed Magnetic Fields: Experiment and Model. Physical Review B 2007; 75(17) 174515.

[35] Clem J. R., Weigand M., Durrell J. H. and Campbell A. M. Theory and Experiment Testing Flux-line Cutting Physics. Superconductor Science and Technology 2011; 24(6) 062002.

[36] Cortés-Maldonado R., Espinosa-Reyes J.E., Carballo-Sánchez A.F., and Pérez-Rodríguez F. Flux-cutting and Flux-transport Effects in Type-II Superconductor Slabs in a Parallel Rotating Magnetic Field. Low Temperature Physics 2011; 37(11), 947.

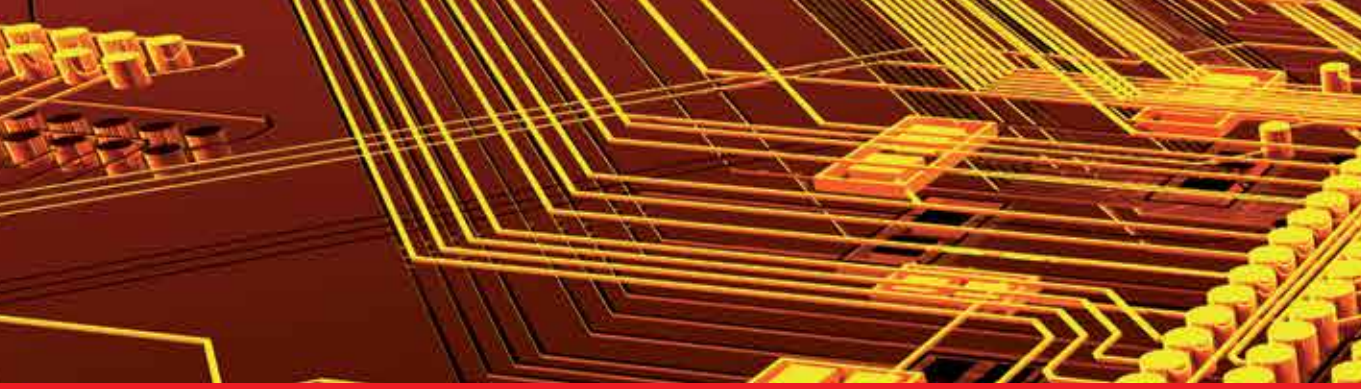

Edited by Alexander Gabovich

The chapters included in the book describe recent developments in the field of superconductivity. The book deals with both the experiment and the theory. Superconducting and normal-state properties are studied by various methods. The authors presented investigations of traditional and new materials. In particular, studies of oxides, pnictides, chalcogenides and intermetallic compounds are included. The superconducting order parameter symmetry is discussed and consequences of its actual non-conventional symmetry are studied. Impurity and tunneling effects (both quasiparticle and Josephson ones) are among topics covered in the chapters. Special attention is paid to the competition between superconductivity and other instabilities, which lead to the Fermi surface gapping.

ISBN 978-953-51-6382-4

Photo by cybrain / iStock

IntechOpen